UNIVERSITÀ
DEGLI STUDI
FIRENZE

DOTTORATO DI RICERCA IN INGEGNERIA INDUSTRIALE

CICLO XXIX

COORDINATORE
Prof. Maurizio DE LUCIA

Development of train parameters estimation algorithms to improve the performance of predictive maintenance systems in railways

Settore Scientifico Disciplinare ING-IND/13

Dottorando
Dott. D'Adamio Pierluca

Tutore
Prof. Allotta Benedetto

Coordinatore
Prof. De Lucia Maurizio

Anni 2013/2016

1

ISBN XXX-XX-XXXX-XXX-X D/XXXX/XXXX/XX

Dedicato a tutte le persone che mi sono state vicine in questi anni...per il vostro sostegno e ascolto

Ringrazio tutte le persone del laboratorio, in primis il Prof. Allotta e Rindi e i miei amici più cari

Un ringraziamento speciale va alla mia famiglia, i miei genitori e mio fratello Giampiero

Summary

The proposed work is aimed at developing accurate train parameters estimation approaches, to get more informations on the vehicle running on the rail, spacing from data about the vertical load (Weigh in Motion systems) to ones on the moving train. More focused, the provided vehicle data concern its speed, vertical axle loads, direction of travel, distance between axles and timetable of the crossing axles to ensure functionalities of dynamical estimations of running loads and aims of train detection. This study allows the formulation of approaches to estimate the quantities above mentioned, starting from the same measurement layout. The developed approaches are flexible against sensors of different typology as load cell, strain gauge or the more efficient Fiber Bragg grating sensors. An analysis of robustness has been involved, concerning the estimation accuracy as a function of the performance of the measurement/acquisition chain, in terms on noise affecting the measure. The performance have been verified in a wide range of speed and vehicle mass showing good results. A comparison between two solutions that involve functionalities of train detection has been done, both on aspects of performance and on the required computational times. The approaches have been stressed, reproducing operating conditions worse than those of a real measurement scenario. A focus has been done on the developed Weigh in Motion algorithm, able to estimate dynamical loads and vehicle centre of mass, for purpose of unbalance loads detection. In order to test the algorithms in the most operating conditions concerning both the vehicle and the measurement chain, in absence of experimental data, simulated track inputs are available thanks a physical model of the infrastructure, composed by vehicle, track and a global contact model that manages their interaction.

Contents

Acronyms List

HBD: *Hot Box Detection*
HWD: *Hot Wheel Detection*
WDD: *Wheel Defect Detection*
WIM: *Weigh in Motion*
AVI: *Automatic Vehicle Identification*
EMI: *Electromagnetic Interference*
FBG: *Fiber Bragg Grating sensors*
TDA: *Time Domain Approach*
FDA: *Frequency Domain Approach*

List of Figures

List of Tables

Preface

Nowadays the trend of industrial companies is to provide tools able to carry out a big data set that, once processed, is useful for the enhancement of maintenance and safety systems. Railway infrastructure contains a wide range of measurement systems: sensor technology has been integrated in railway systems for quite a while. Rail vehicles and the infrastructure are equipped with a large amount of sensors, on which safety mechanism like traffic control as weel as control algorithms on the trains are based. Sensors are getting cheaper and this pushes their usage also in this field: the trend leads towards solutions making use of different sensor data for several kinds of monitoring. Monitoring and alarming are core functions. Diagnostic applications can be added for advanced analysis and decision support. The accuracy of the predictive maintenance system is also related to the performance of sensors [1][2] used in the measurement chain and of embedded unit. Commercial solutions [3] provides different maintenance tools as HBD (*Hot Box Detection*), HWD (*Hot Wheel Detection*), WDD (*Wheel Defect Detection*), WIM (*Weigh in Motion*) systems and supplementary functions as the AVI (*Automatic Vehicle Identification*).

Thanks the improvements in the electronic boards development, several evaluation boards have been brought out by industrial companies [4], [5] to provide additional parameters used to monitoring the state of the running vehicle (see Fig. 1). Beside the progress of available commercial products, there is a wide attention of the railway research on the optimization of the sensor and the signal post processing efficiencies to extract reliable and robust data. There is a development of sensors concerning systems able to detect the presence of train or wheel and systems aimed at estimating the vehicle loads on rail. In particular, nowadays the train detection [6, 7] is performed by two approaches: track circuits [8, 9] and axle counter [6][10]. In order to have less invasive and expensive solutions, axle counters have been widely used as alternative [11][12], equipped of a wheel detector,whose approaches are based on:

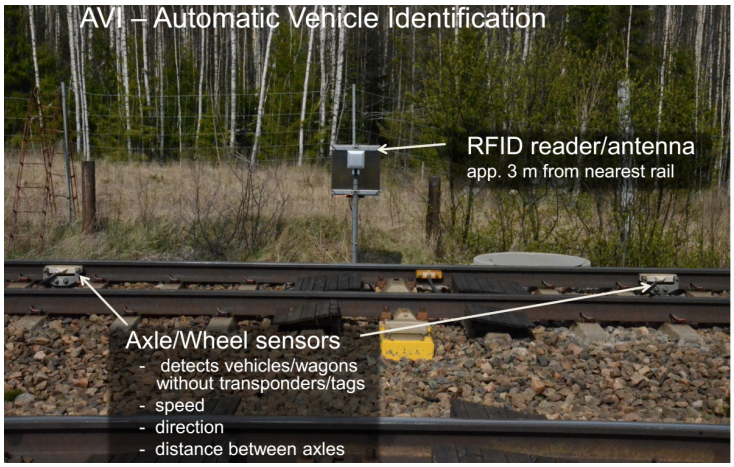

Figure 1: AVI system and axle/wheel detectors

- Rail deformation (strain gauge);
- Acceleration;
- Inductive operating principles (magnetic coils);
- Wavelenght reading (fiber Bragg grating sensors);
- Force.

Strain gauge detects the dynamic load due to the deformation of the rail, but its measure is affected by the electromagnetic interference [13]. Rail contacts with a transmitter coil on one side of the rail and a receiver coil on the other are widely used [14, 15, 16]. The wheel affects the inductive coupling between transmitter and receiver. The devices are mostly designed as double sensors and are often used as counting heads for axle counters. By reading the change of the inducted voltage on the receiver coil due to the wheel presence is possible to detect the presence of the wheel [17]. Other solutions are based on the inductive loops provided only by one element (Fig. 2, [1]).

The advantage for the user lies in its simple design, little mounting work and the fact that no electronics are needed at the rail itself. The wheel detector based on the electromagnetic field involves a simply approach but its reading can be affected by an error due to EMI interference. These limits lead to the development of wheel sensors that are based on other principles of physics. Examples include microwave technology, piezoelectrics, fibre optics or sound technology, but there are few examples of licensable system ready for serial production. However, many recent research works

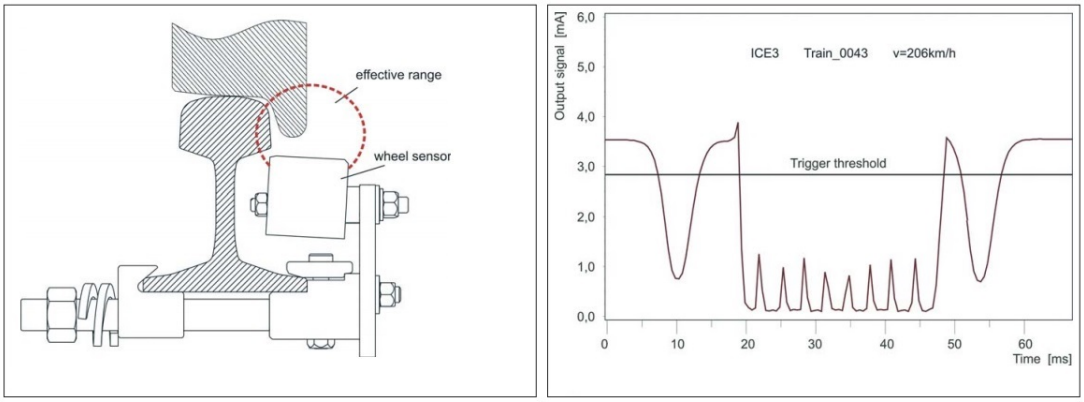

Figure 2: Inductive wheel sensor in the effective range of head of rail and wheel flange

in literature propose a new simple sensor technology, the fiber Bragg grating sensor (FBG) to be free from the EMI interference problem and to enhance the accuracy and reliability of the train detection of the signalling system [18, 19]. Besides, the FBG sensors are immune to electromagnetic interference (EMI). Thanks to this innovative technology, the complexity of the measure system has moved from the sensor part to that of peak reading in the received signal. Chu-liang Wei et al. [18] have developed the X-Crossing and D-Crossing algorithms to compute the number of train axles crossing the measurement station: they have used a cut-off threshold followed by a derivative operation, to extract the useful peak corresponding to the crossing train axles from the received signals. T.K. Ho et al. [7] make the decomposition of the received signals in different frequency band with the Wavelet Transform to study and define the spectral characteristics of the useful signal. Buggy et al. [20] make use of cut-off thresholds and derivative operation to implement the axle counter function. The fiber optic are also widely applied in the field of the structural engineering with good results [21]; in [22][23] the optical sensors are used to measure the dynamic load on bridge with speed higher the 200 km h. Works [24][25][26][27] show the possibility to apply fiber optic to test the line state, wheel flat and the wheel wear, or the local deformation of the rail depending by the traversing load [28]. At the end fiber optic are also used to the speed, acceleration and the weigh in motion systems [29]. Indeed, over the train detection there are many studies concerning problems affecting the line and vehicle safety that can be evaluated through WIM (*Weigh in Motion*) system, able to measure the moving train loads or unbalances also at high speed. WIM systems can be classified on the basis of the type of sensors mounted and the location of their mounting. The classification of the mentioned WIM systems for railways can be performed on the basis of the type

of sensors adopted and also on the location of their mounting. One of the first systems was utilizing strain gauges [30] welded to the neutral axis or mounted on rail foot [31]. Optical fibers can be mounted either to the side of the rail, or to the foot of the rail with the help of special clamps [32]. All the above indicated papers are an important piece of research in this field, but don't provide a general analysis approach and do not meet the question of robustness against the measurement chain performance. Summarizing, the researchers and industrial efforts towards approaches aimed at optimizing the sensor performance and the efficacy of the signal post processing [33] have encouraged this work that is focused on the developing of techniques to extract data concerning the vehicle running on rail for purposes of vehicle maintenance and rail, too (by estimations on possible unbalances loads). Two approaches have been developed to carry out information on the vehicle march through train parameters estimations as speed, direction of travel, distance among train axles and timetable of the crossing axles. In order to provide functionalities useful for safety purposes related to both vehicle and rail a WIM algorithm has been developed. All the approaches have the prerogative to provide a data set in different working conditions concerning the vehicle (wagons or a train composition, different values of car body mass and speed). Studies have also the goal to provide estimation techniques quite flexible against different measurement chains in terms of number of sensing elements, noise affecting the measure and kind of sensing elements (strain gauge, FBGs, force sensor), in order also to do a layout optimization as compromise between the occupied space/cost and the estimation accuracy.

Fig. 3 summarizes the motivation of the work, aimed at developing efficient estimation approaches to enhance and integrate the functionalities guaranteed by WIM and AVI systems.

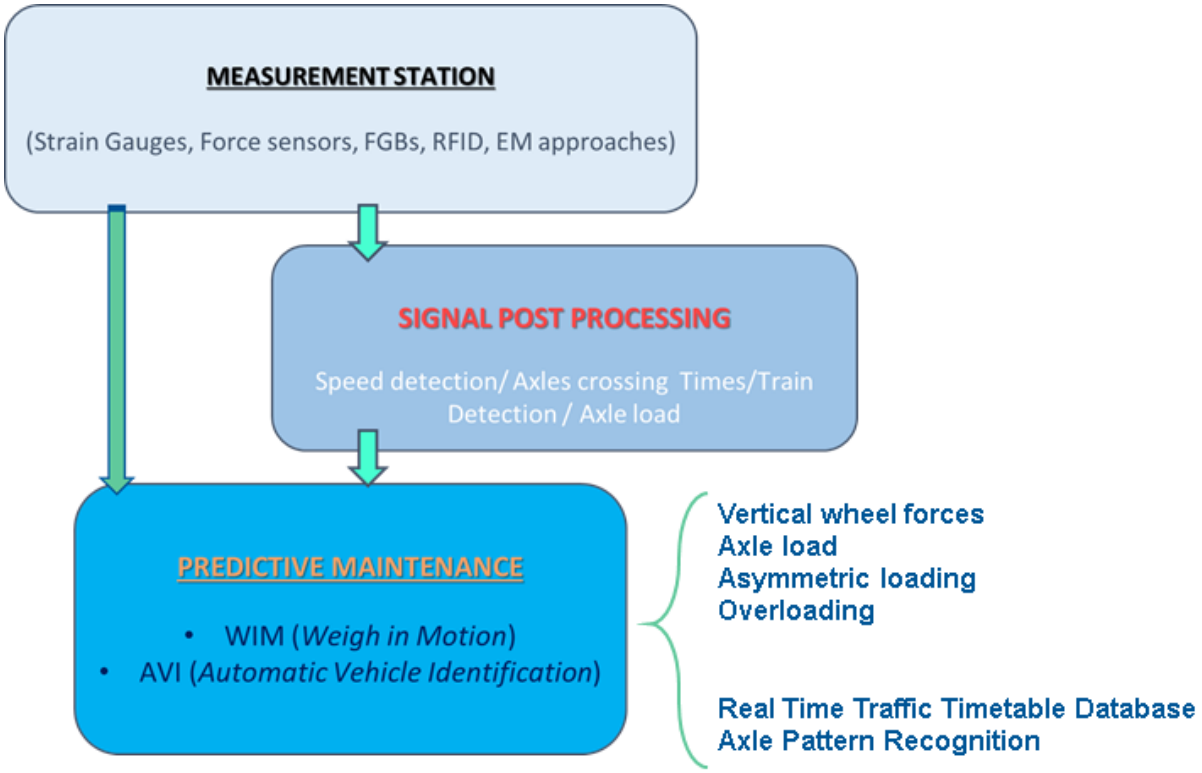

Figure 3: The goal is to provide approaches flexible against different typologies of measurement chains to bring out a data set useful for purposes guaranteed by WIM and AVI systems

Structure of the thesis

This thesis provides estimation approaches of train parameters flexible and robust against operating conditions concerning both the vehicle and the measurement chain.

Chapter 1 shows the general architecture of the approach adopted to test the performance of the algorithms: a physical model of the railway vehicle, a finite element model of the track and a global contact model have been developed to bring outs the inputs useful for the estimation part. The benchmark vehicle is the Manchester Wagon, composed by a car body, two bogies and four wheelsets. The rigid bodies are connected by means of appropriate elastic and damping elements. The infrastructure model has been developed to test the approaches performance in different working conditions regarding both the vehicle and the measurement chain.

Chapter 2 describes the two algorithms developed through time domain or frequency one approaches (TDA/FDA) to detect the train presence computing its speed and crossing time instants and number of crossing axles, starting from the knowledge of the simulated inputs obtained from the physical model described in Chapter 1.

Chapter 3 shows the results of the wide simulation campaign used to test the operation of both algorithms in the computing of the train detection functionalities. The benchmark vehicle is the Manchester Wagon and several measurement layouts are considered in order to check the performance of the estimation algorithms against different working condition concerning the number and spacing among sensing elements. Force sensors displaced on measurement sleepers are used during this training phase. The results on the estimation accuracy on train parameters are shown and a comparison between the TDA and FDA approaches is carried out, concerning their performance, functionalities and the required computational times.

Chapter 4 highlights the performance of the estimation approaches on an experimental data corresponding to a train composition of locomotive and two wagons with a different measurement chain from the one used in the training phase (equipped of strain gauges rather than force sensor). The robustness of the thresholds used to optimize the performance shown in Chapter 3 is verified.

Chapter 5 describes the WIM algorithm able to estimate the vertical loads, starting from the knowledge of vertical force measured on measurement sleepers, obtained from the interaction between the vehicle and track models described in Chapter 1. The WIM algorithm takes in input also the train parameters estimated by the TDA/FDA approaches. The vertical loads on the train axle or wheels and the possible unbalances are computed starting from a formulation based on a Quasi Linearity Hypothesis: the reproducing of the input signals, when experimental data are not available, has been optimized by means of least square minimization (LSQ) techniques. The algorithm is able to estimate also the center of gravity of the vehicle, which accuracy is strictly dependent from that of vertical load estimations.

Chapter 6 describes the results of the WIM algorithm in the estimating of vertical wheel loads and centre of mass in different working condition concerning the vehicle mass and speed and the measurement layout.

Chapter 1

General architecture of the validation model

Chapter Contents

To test the performance of the developed algorithms in a wide range of operating conditions, an accurate validation model has been developed to provide the training set of the input data. The model can bring out:

- force signals [34], rail bending measurements [35];
- signals corresponding to different measurement layouts, in terms of number and position of sensing elements.

In the proposed work, vertical forces obtained from force sensors placed on left and right sides of sleepers have been considered. The general architecture of the system is illustrated in Fig. 1.1 and it is composed by a physical model part and a estimation one. The physical model is structured in:

- 3D multibody model of the vehicle (in the studied case the Manchester Wagon [36], implemented with VI-Rail software, is proposed);

- 3D finite-element model (FEM) of the flexible railway track, developed in Comsol environment.

These two models interact online through a global wheel-rail contact model, developed in previous works [37][38]. At each time integration step, the multibody model provides the kinematic variables (position, orientation and their derivatives) of each wheel; at the same time, the finite-element model (FEM) of the railway track evaluates the position, orientation and their derivatives for each node of the beam that represents the rail. Both the kinematic variables are then sent as inputs to the global contact model, that returns the global contact forces to be applied to the wheel and the rail.
Once the simulation is finished and the vertical forces on the sleepers $F^i_{zr/l}$, with i=1..N_{st} (N_{st} is the minimum i of measurement sleepers included in the measurement

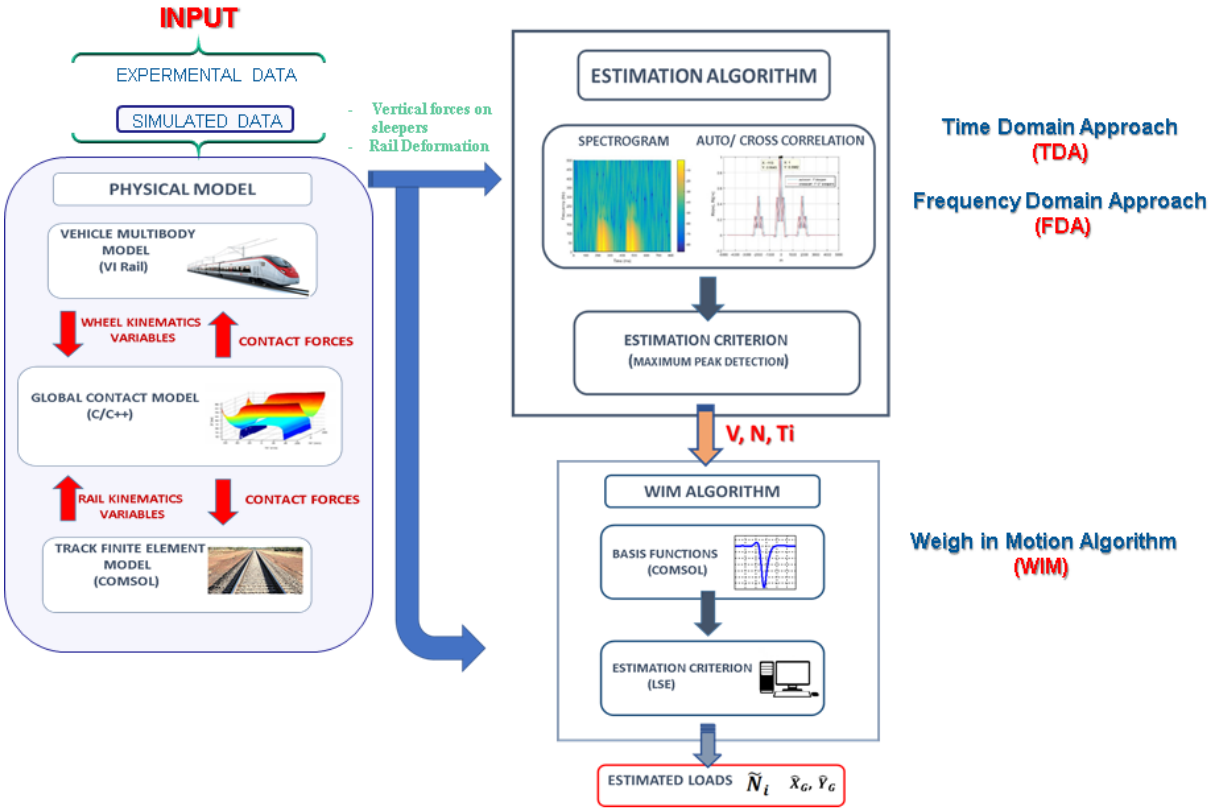

Figure 1.1: General architecture of the system: the physical model provides the training set for the estimation algorithms TDA/FDA, whose estimations are sent in input to the WIM algorithm

station) (indicating the vertical forces on the i-th sleeper measured at the right or left side of the train) are obtained, the estimation part begins. The estimation approaches are:

- Speed, crossing times, train detection estimation algorithms (TDA/FDA);
- WIM algorithm to estimate vertical wheel loads and the vehicle centre of mass.

1.1 Physical model of the railway track

The adopted approach can manage the simulated data in absence of the experimental one: the physical model must contain accurate vehicle and track models. The physical model consists of a 3D finite element model (FEM) of the infrastructure (rail, sleepers and ballast), a 3D multibody model of the vehicle [39] and a contact model describing the interaction between the vehicle wheels and the rail. The vehicle model and the infrastructure one interact online during the simulations by means of the 3D global contact model, specifically developed to improve reliability and accuracy of the wheel-rail contact points detection.

1.1.1 The infrastructure model

Rail and infrastructures are modelled as 3D beams (see Fig. 1.2b), supported by an elastic discrete foundation representing sleepers and ballast (discretized through BEAM elements with two nodes for element and 6 DOFs for each node). The rails are connected through visco-elastic elements to n_{sl} 2D rigid bodies representing the sleepers, which are in turn supported by a visco-elastic foundation including the ballast properties (see Fig. 1.2b). The discretized equation of the rail is defined as:

$$M\ddot{\mathbf{q}}^{\mathbf{l/r}} + C\dot{\mathbf{q}}^{\mathbf{l/r}} + K\mathbf{q}^{l/r} = \mathbf{F}^{l/r} \tag{1.1}$$

in which M, C and K are the mass, damping and stiffness matrices of the track, $\mathbf{q}^{l/r}$ indicates the discretized track displacements and $\mathbf{F}^{\mathbf{l/r}}$ the external applied forces:

$$\mathbf{F}^{l/r} = \mathbf{F_{sl}}^{l/r} + \mathbf{F_c}^{l/r} \tag{1.2}$$

where $\mathbf{F_{sl}}^{l/r}$, $\mathbf{F_c}^{l/r}$ indicate the sleeper forces and the contact forces (provided by the vehicle and the global contact model). The variables of the generic node $\mathbf{q_i}^{l/r} \in R^6$ are the linear displacements $\mathbf{v} \in R^3$ and the rotational displacements $\theta \in R^3$:

$$\mathbf{q_i}^{l/r} = \begin{bmatrix} \mathbf{v_i}^{l/r} \\ \theta_\mathbf{i}^{l/r} \end{bmatrix} \tag{1.3}$$

where vector $\mathbf{v_i}^{l/r}$ includes longitudinal $u_{i_{rail}}^{l/r}$, lateral $v_{i_{rail}}^{l/r}$ and vertical $w_{i_{rail}}^{l/r}$ displacements expressed in the fixed reference system $O_{sys}x_{sys}y_{sys}z_{sys}$. The vector $\theta_\mathbf{i}^{l/r}$ indicates the rotational displacements $\phi_{i_{rail}}^{l/r}$, $\theta_{i_{rail}}^{l/r}$, and $\psi_{i_{rail}}^{l/r}$ expressed in the fixed reference system $O_{sys}x_{sys}y_{sys}z_{sys}$ (see Fig. 1.2a).

In this work the damping of the rail is modelled using the "proportional" or Rayleigh damping; the damping matrix $\mathbf{C}$ is evaluated as a linear combination of the inertia $\mathbf{M}$ and stiffness $\mathbf{K}$ matrices of the structure:

$$\mathbf{C} = \alpha_r \mathbf{M} + \beta_r \mathbf{K}. \tag{1.4}$$

The coefficients α_r and β_r are calibrated in order to fit the typical behaviour expected from experimental results and physical considerations available in literature [39, 40, 41].
In this work the UIC60 rail profile (with cant angle equal to 1/20) has been adopted. The main physical characteristics of the rail beam model are listed in Tab. 1.2a.

Table 1.1: Main characteristics of the rail beam model

Parameter	Value
Young modulus E	$2.1 * 10^{11}$ Pa
Density ρ	$7.8 * 10^3$ kg/m^3
Area of the beam section A	$7.686 * 10^{-3}$ m^2
Momentum of the beam section I	$3.055 * 10^{-5}$ m^4
Rayleigh damping coefficient α_r	30 s^{-1}
Rayleigh damping coefficient β_r	0.003 s
Distance between neutral section and rail foot z_f	-0.172 m
Shear factor k	0.4

The length of the straight track studied in the model is $L = 72$m. The separation distance between two contiguos sleepers is equal to $l = 0.60$m. The sleepers are

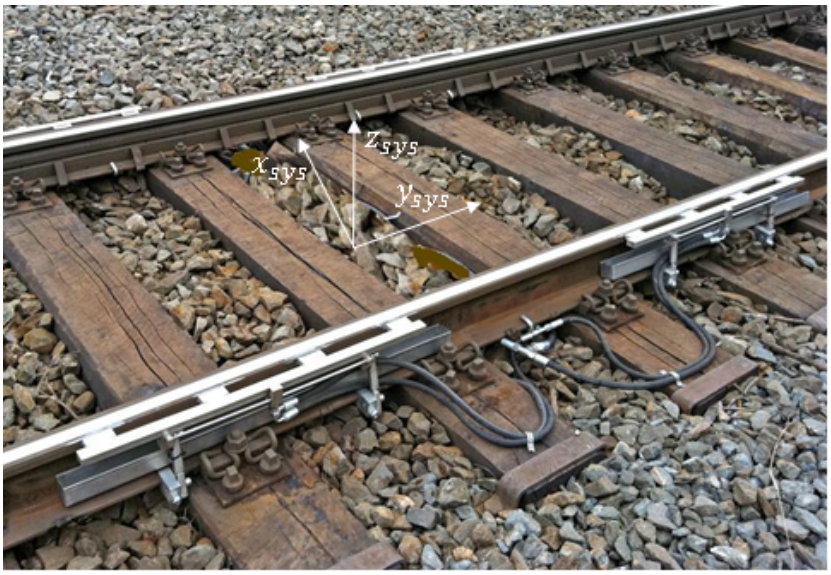

(a) Fixed reference system

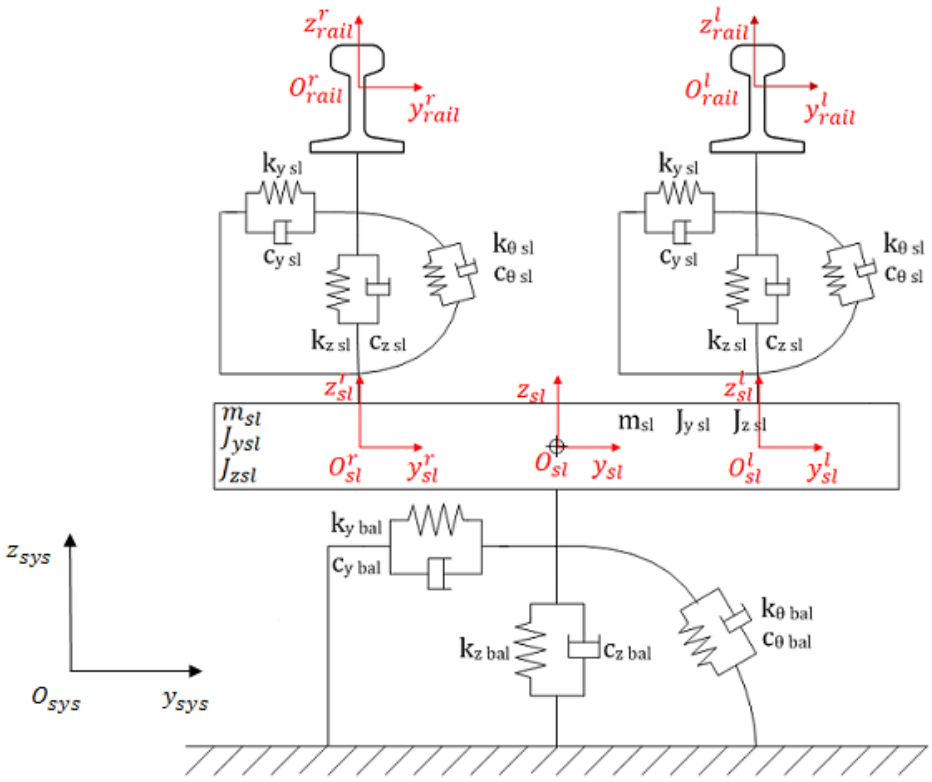

(b) Model of the interaction between rails, sleeper and ballast

Figure 1.2: Reference system and infrastructure model

Table 1.2: Main characteristics of the rail-sleeper-ballast system

(a) Main characteristics of the rail beam model

Parameter	Value
Young modulus E	$2.1 * 10^{11}$ Pa
Density ρ	$7.8 * 10^{3}$ kg/m^3
Area of the beam section A	$7.686 * 10^{-3}$ m^2
Momentum of the beam section I	$3.055 * 10^{-5}$ m^4
Rayleigh damping coefficient α_r	30 s^{-1}
Rayleigh damping coefficient β_r	0.003 s
Distance between neutral section and rail foot z_f	-0.172 m
Shear factor k	0.4

(b) Main characteristics of the sleepers-ballast system

Parameter	Value
Mass of the sleeper m_{sl}	304 kg
Polar inertia of the sleeper J_{sl}	200 kg m^2
Sleeper Lateral Stiffness k_{ysl}	$4.3 * 10^{7}$ N m^{-1}
Sleeper Vertical Stiffness k_{zsl}	$2.5 * 10^{8}$ N m^{-1}
Sleeper Rotational Stiffness $k_{\vartheta sl}$	$1.0 * 10^{7}$ N m
Sleeper Lateral Damping k_{ysl}	$2.4 * 10^{6}$ N s m^{-1}
Sleeper Vertical Damping k_{zsl}	$5.6 * 10^{6}$ N s m^{-1}
Sleeper Rotational Damping $k_{\vartheta sl}$	$1.0 * 10^{5}$ N m s
Ballast Lateral Stiffness k_{ybal}	$3.7 * 10^{7}$ N m^{-1}
Ballast Vertical Stiffness k_{zbal}	$1.0 * 10^{9}$ N m^{-1}
Ballast Rotational Stiffness $k_{\vartheta bal}$	$1.0 * 10^{7}$ N m
Ballast Lateral Damping c_{ybal}	$2.4 * 10^{6}$ N s m^{-1}
Ballast Vertical Damping c_{zbal}	$1.0 * 10^{7}$ N s m^{-1}
Ballast Rotational Damping $c_{\vartheta bal}$	$1.0 * 10^{5}$ N m s
Sleepers distance l	0.6 m
Sleepers total number n_{sl}	121
Beginning of the track L_I	0 m
End of the track L_F	72 m

Table 1.3: Main characteristics of the rail beam model

Parameter	Value
Young modulus E	$2.1 * 10^{11}$ Pa
Density ρ	$7.8 * 10^{3}$ kg/m^3
Area of the beam section A	$7.686 * 10^{-3}$ m^2
Momentum of the beam section I	$3.055 * 10^{-5}$ m^4
Rayleigh damping coefficient α_r	30 s^{-1}
Rayleigh damping coefficient β_r	0.003 s
Distance between neutral section and rail foot z_f	-0.172 m
Shear factor k	0.4

modelled as 2D rigid bodies connected to the rails by means of visco-elastic elements including lateral k_{ysl}, vertical k_{zsl} and rotational $k_{\vartheta sl}$ stiffness and lateral c_{ysl}, vertical c_{zsl} and rotational $c_{\vartheta sl}$ damping properties (see Fig. 1.2b and Tab. 1.2b). The longitudinal position $x_{sl\ p}$ of the $p-th$ 3DOF system modelling the sleepers-ballast ensemble can be expressed as follows:

$$x_{sl\ p} = L_I + (p-1)l, \quad k = 1, 2, ...n_{sl} \tag{1.5}$$

where $x_{sl1} = L_I$, $x_{sl\ n_{sl}} = L_F$ (L_I and L_F are the beginning and the end of the track respectively), l is the distance between two contiguous sleepers and n_{sl} is the total number of sleepers.
The generic 2D sleeper is supported by a flexible foundation characterising the behaviour of the ballast through the lateral k_{ybal}, vertical k_{zbal} and rotational $k_{\vartheta ball}$ stiffness values and lateral c_{ybal}, vertical c_{zbal} and rotational $c_{\vartheta bal}$ damping values (Tab. 1.2b). m_{sl} and j_{sl} indicate the mass and inertia of sleepers.

The 3DOF body modelling the sleepers-ballast ensemble is described by the lateral y_{sl} and vertical z_{sl} translations and the rotation ϑ_{sl} around the $x_{sl} - axis$ of the sleeper reference system expressed in the reference system $O_{sys}x_{sys}y_{sys}z_{sys}$ (see Fig. 1.2a and Tab. 1.2b).

Hence, the dynamic model of the sleeper can be expressed through the following equation:

Table 1.4: Main characteristics of the sleepers-ballast system

Parameter	Value
Mass of the sleeper m_{sl}	304 kg
Polar inertia of the sleeper J_{sl}	200 kg m^2
Sleeper Lateral Stiffness k_{ysl}	$4.3 * 10^7$ N m^{-1}
Sleeper Vertical Stiffness k_{zsl}	$2.5 * 10^8$ N m^{-1}
Sleeper Rotational Stiffness $k_{\vartheta sl}$	$1.0 * 10^7$ N m
Sleeper Lateral Damping k_{ysl}	$2.4 * 10^6$ N s m^{-1}
Sleeper Vertical Damping k_{zsl}	$5.6 * 10^6$ N s m^{-1}
Sleeper Rotational Damping $k_{\vartheta sl}$	$1.0 * 10^5$ N m s
Ballast Lateral Stiffness k_{ybal}	$3.7 * 10^7$ N m^{-1}
Ballast Vertical Stiffness k_{zbal}	$1.0 * 10^9$ N m^{-1}
Ballast Rotational Stiffness $k_{\vartheta bal}$	$1.0 * 10^7$ N m
Ballast Lateral Damping c_{ybal}	$2.4 * 10^6$ N s m^{-1}
Ballast Vertical Damping c_{zbal}	$1.0 * 10^7$ N s m^{-1}
Ballast Rotational Damping $c_{\vartheta bal}$	$1.0 * 10^5$ N m s
Sleepers distance l	0.6 m
Sleepers total number n_{sl}	121
Beginning of the track L_I	0 m
End of the track L_F	72 m

$$M_{sl}\ddot{\mathbf{v}}^p_{sl} + \mathrm{K}_{sl}({\mathbf{v}_{sl}}^{p\,r} - {\mathbf{v}_{rail}}^{p\,r}) + \mathrm{C}_{sl}(\dot{\mathbf{v}}^{p\,r}_{sl} - \dot{\mathbf{v}}^{p\,r}_{rail}) + \mathrm{K}_{sl}({\mathbf{v}_{sl}}^{p\,l} - {\mathbf{v}_{rail}}^{p\,l}) + \\ + \mathrm{C}_{sl}(\dot{\mathbf{v}}^{p\,l}_{sl} - \dot{\mathbf{v}}^{p\,l}_{rail}) + \mathrm{K}_{bal}\mathbf{v}^p_{sl} + \mathrm{C}_{bal}\dot{\mathbf{v}}^p_{sl} = 0 \tag{1.6}$$

where subscript sl refers to the sleeper, subscript bal indicates the ballast properties, subscript $rail$ is related to the rail and l/r refers to the left/right side of the rail. The vector ${\mathbf{v}_{sl}}^p$ includes lateral ${v_{sl}}^p$, vertical ${w_{sl}}^p$ and rotational ϕ^p displacement of the sleeper center of mass expressed in the fixed reference system $O_{sys}x_{sys}y_{sys}z_{sys}$ (see

Fig. 1.2a); M_{sl} is the sleeper mass matrix while K_{sl} and C_{sl} are respectively the stiffness and damping matrices characterising the rail/sleeper visco-elastic connection. The K_{bal} and C_{bal} are respectively the stiffness and damping matrix of the ballast. The vectors $\mathbf{v_{sl}}^{p\ l}$,$\mathbf{v_{sl}}^{p\ r}$ are defined as:

$$\mathbf{v_{sl}}^{p\ r} = \begin{pmatrix} {v_{sl}}^{p\ r} \\ {w_{sl}}^{p\ r} \\ {\phi}^{p\ r} \end{pmatrix} = \begin{bmatrix} {v_{sl}}^{p} \\ {w_{sl}}^{p} - {\phi_{sl}}^{p} \frac{s}{2} \\ {\phi_{sl}}^{p} \end{bmatrix} \tag{1.7}$$

$$\mathbf{v_{sl}}^{p\ l} = \begin{pmatrix} {v_{sl}}^{p\ l} \\ {w_{sl}}^{p\ l} \\ {\phi}^{p\ l} \end{pmatrix}, \mathbf{v_{sl}}^{p\ l} = \begin{bmatrix} {v_{sl}}^{p} \\ {w_{sl}}^{p} + {\phi_{sl}}^{p} \frac{s}{2} \\ {\phi_{sl}}^{p} \end{bmatrix} \tag{1.8}$$

where s indicates the railway gauge among the rails. The vectors $\mathbf{v_{rail}}^{p\ l}$,$\mathbf{v_{rail}}^{p\ r}$ are defined as:

$$\mathbf{v_{rail}}^{p\ r} = \begin{bmatrix} v_{rail}^{p\ r} \\ w_{rail}^{p\ r} \\ \phi_{rail}^{p\ r} \end{bmatrix}, \quad \mathbf{v_{rail}}^{p\ l} = \begin{bmatrix} v_{rail}^{p\ l} \\ w_{rail}^{p\ l} \\ \phi_{rail}^{p\ l} \end{bmatrix}. \tag{1.9}$$

Therefore, each rail-sleeper interaction force is made up of the following components:

$$F_{y\ sl}^{l\ p}(t) = k_{y\ sl}(v_{sl}^{l\ p} - v_{rail}^{l\ p}) + c_{y\ sl}(\dot{v}_{sl}^{l\ p} - \dot{v}_{rail}^{l\ p}) \tag{1.10}$$

$$F_{y\ sl}^{r\ p}(t) = k_{y\ sl}(v_{sl}^{r\ p} - v_{rail}^{r\ p}) + c_{y\ sl}(\dot{v}_{sl}^{r\ p} - \dot{v}_{rail}^{r\ p}) \tag{1.11}$$

$$F_{z\ sl}^{l\ p}(t) = k_{z\ sl}(w_{sl}^{l\ p} - w_{rail}^{l\ p}) + c_{z\ sl}(\dot{w}_{sl}^{l\ p} - \dot{w}_{rail}^{l\ p}) \tag{1.12}$$

$$F_{z\ sl}^{r\ p}(t) = k_{z\ sl}(w_{sl}^{r\ p} - w_{rail}^{r\ p}) + c_{z\ sl}(\dot{w}_{sl}^{r\ p} - \dot{w}_{rail}^{r\ p}) \tag{1.13}$$

$$M_{x\ sl}^{l\ p}(t) = k_{\phi\ sl}(\phi_{sl}^{l\ p} - \phi_{rail}^{l\ p}) + c_{\phi\ sl}(\dot{\phi}_{sl}^{l\ p} - \dot{\phi}_{rail}^{l\ p}) \tag{1.14}$$

$$M_{x\ sl}^{r\ p}(t) = k_{\phi\ sl}(\phi_{sl}^{r\ p} - \phi_{rail}^{r\ p}) + c_{\phi\ sl}(\dot{\phi}_{sl}^{r\ p} - \dot{\phi}_{rail}^{r\ p}) \tag{1.15}$$

where $p = 1, 2, .., n_{sl}$, ${v_{rail}}^{r/l\ p}$, ${w_{rail}}^{r/l\ p}$ and ${\phi_{rail}}^{r/l\ p}$ are the second, third and fourth element of the generic node variables $\mathbf{q_i}^{r/l\ p}$.

1.1.2 The vehicle model

The railway vehicle chosen for the dynamic simulations is the Manchester Wagon, the mechanical structure and elastic and damping characteristics of which are easily

available in literature [36]. The main general characteristics of the vehicle are summarized in Tab. 1.5a while in Tab. 1.5b the inertia properties are shown.

The multibody 3D model of this vehicle has been widely studied and validated in different conditions. The model of the Manchester Wagon, implemented in the Adams VI-Rail environment, is schematically shown in Fig. 1.3a and it lies in seven rigid bodies:

- one car body;
- two bogies;
- four wheelsets.

The rigid bodies are connected by means of appropriate elastic and damping elements; particularly, the vehicle is equipped with two suspension stages. The primary suspensions connect the wheelsets to the bogies (see Fig. 1.3b) and comprise two coil springs and six dampers (longitudinal, lateral and vertical ones), while the secondary suspensions connect the bogies to the coach (see Fig. 1.3c) and consist of the following elements:

- two coil springs;
- four dampers (lateral and vertical ones);
- the traction rod;
- the roll bar (not visible in figure);
- two lateral bumpstops.

Both the suspension stages have been modelled through three-dimensional linear and nonlinear force elements like bushings, dampers, and bumpstops. The main linear stiffness and dumping properties of the suspension stages are summarized in Tab. 1.5c. In this work the ORE S1002 wheel profile has been used.

Table 1.5: Main characteristics of the Manchester Wagon

(a) Main characteristics of the Manchester Wagon

Parameter	Value
Bogie pivot distance	19 000 mm
Bogie wheelbase	2 560 mm
Wheel diameter	920 mm
Height above ToR level of bogie CoG	600 mm
Height above ToR level of coach CoG	1 800 mm
Longitudinal and lateral offset of coach CoG	0 mm

(b) Inertia properties of the multibody model

MBS body	Mass	Roll Inertia	Pitch Inertia	Yaw Inertia
	kg	kgm^2	kgm^2	kgm^2
Car body	32000	56800	1970000	1970000
Bogie	2615	1722	1476	3067
Wheelset	2091	1120	112	1120

(c) Main linear stiffness and damping properties of the Manchester Wagon suspensions

Primary suspension		k_x	3.1E+07 N/m
		k_y	3.9E+06 N/m
		k_z	1.2E+06 N/m
		c_x	1.5E+04 Ns/m
		c_y	2.0E+03 Ns/m
		c_z	4.0E+03 Ns/m
Secondary suspension	Coil spring	k_x, k_y	1.6E+05 N/m
		k_z	4.3E+06 N/m
		k_α, k_β	1.1E+04 Nm/rad
	Traction rod	k_x	5.0E+06 N/m
		c_x	2.5E+04 Ns/m
	Roll bar	k_α	9.4E+05 Nm/rad
	Dampers	c_y	3.2E+04 Ns/m
		c_z	2.0E+04 Ns/m

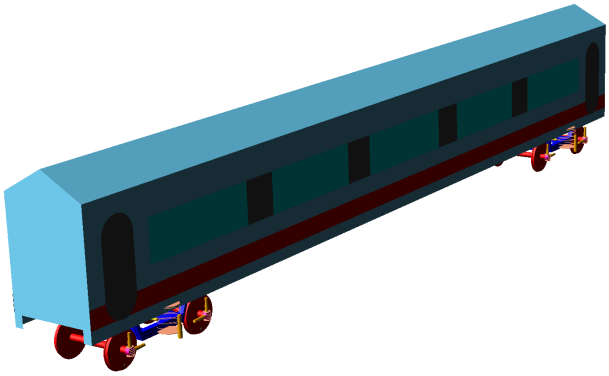

(a) Global view of the multibody model

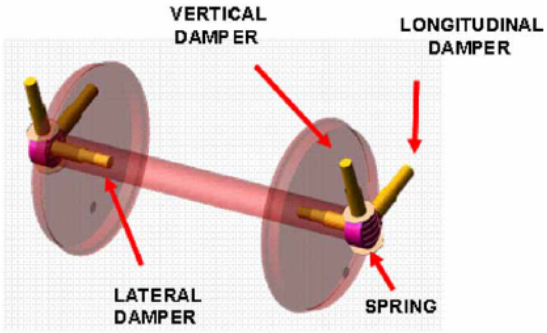

(b) Primary suspensions

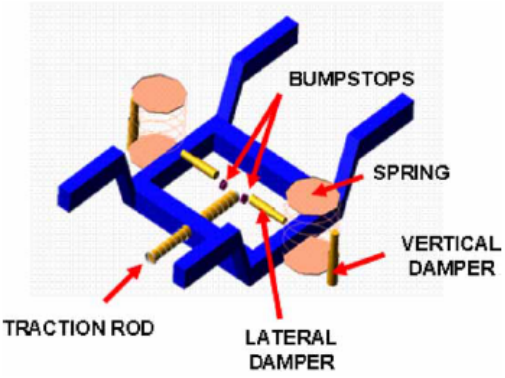

(c) Secondary suspensions

Figure 1.3: Multibody model composition

1.1.3 Global contact model

The vehicle model and the infrastructure model interact online during the simulations by means of a 3D global contact model, developed by the authors in previous works, to improve the reliability and the accuracy of the contact points detection. In particular the used global contact model comprises both the contact points detection [37, 38] and the global contact forces evaluation, based on the theory of Hertz, Kalker [42, 43] and Polach [44]. The vehicle and infrastructure models calculate the wheel kinematics variables (related to each wheel) and the rail kinematics variables (related to each rail node). Starting from these quantities, the global contact model returns the global contact forces to be applied to the wheel and the rail. The global contact model is illustrated in Fig. 1.4.

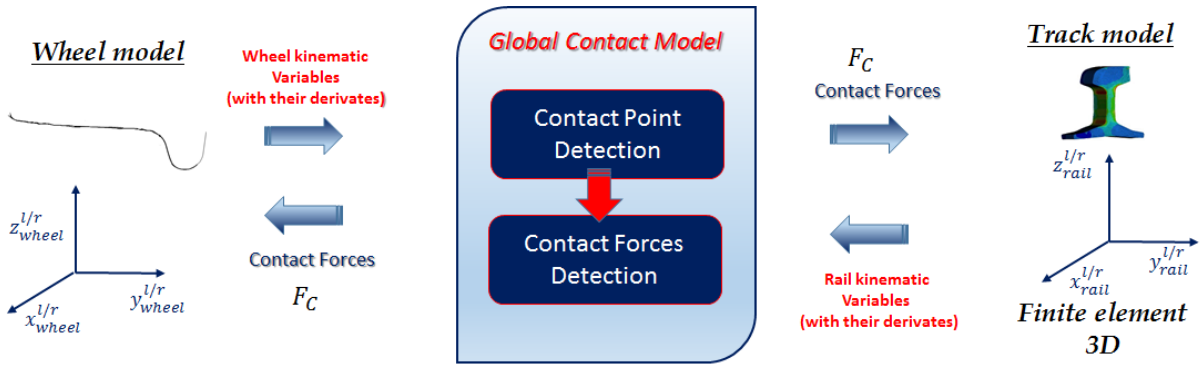

Figure 1.4: Global contact model: interaction between the vehicle model and the finite element 3D model of the track

Chapter 2

Estimation algorithms of train parameters

Chapter Contents

This Chapter describes the estimation approaches developed to involve train detection functionalities by means of the computing of several parameters as vehicle speed, crossing time instants, crossing axles and physical distance between axles. Both of approaches are aimed at bringing out these parameters with methodologies that must be flexible against different measurement chain in terms of number, kind of sensor elements and its performance in terms of noise affecting the measure. Algorithms can manage the experimental data or, in absence of them, simulated track inputs as described in Chapter 1 (see Fig. 1.1). Two approaches have been proposed aimed at detecting the meaning of the input signal peaks also in very badly operating condition, concerning the noise on the input signal. Indeed, the proposed solutions are flexible against different measurement chains and robust against the noise. The aim is the computation of signal local peaks coming from force sensors displaced on measurement sleepers. The first approach is based on auto/cross correlation operations, very useful as denoising techniques and as estimators of the time shift between signals: this way is very useful for the estimation of the crossing time instants and vehicle speed, but becomes quite complicated when it is applied to a long

composite signal and, to overcome this drawback, a frequency domain approach has been adopted, based on spectrograms. The operation of the algorithm is described in Par. 2.2.

2.1 Time domain approach (TDA)

The train detection algorithm aims at computing different train parameters like the crossing times of vehicle on sleepers, vehicle speed and axles number.

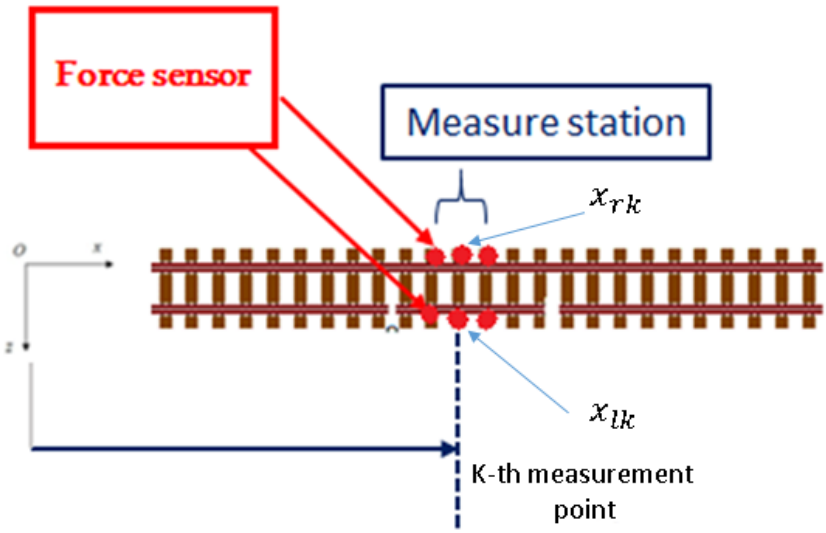

Figure 2.1: Measurement layout composed by three measurement sleepers each one equipped of two force sensors on both left and right sides

The used track inputs are the signals coming from the force sensors located on the left and right side on every sleeper $F^i_{z\,r}$, $F^i_{z\,l}$ (see Fig. 2.1), even if the algorithm can manage different signal input (i.e the vertical forces acting on the sleepers, the rail shear and bending, longitudinal strain and stress on rail). Fig. 2.2 illustrates the right and left vertical forces acting on the first sleeper (vehicle speed $V = 10\text{m}\,\text{s}^{-1}$ and car body mass $M = 10\text{t}$) of the measurement station: there are four peaks related to the four axles of the Manchester Wagon. $F^i_{z\,r}$, $F^i_{z\,l}$ are quite similar because the travel of train is on a rectilinear track. To stress the estimation approaches, very rough operating conditions have been simulated, with the adding of an elevate noise level on the simulated signal amplitude. Fig. 2.2 represents two signals (with or without the added noise), in which a noise has been added on the input signal to obtain a signal input-to-noise ratio equal

to 5 dB (vehicle speed $V = 10\text{m s}^{-1}$ and car body mass $M = 10\text{t}$). The considered signal is the mean between the left and right force input signals $\left(F^i_{zm} = \frac{F^i_{z\,r} + F^i_{z\,l}}{2}\right)$, in order to reject possible disturbances due to the lateral motion of the vehicle.

The technique of auto correlation has been applied because it shows an high robustness against disturbances and noise [45],[46]. Fig. 2.3 shows a scenario in which the autocorrelation is carried out on a force signal, corresponding to four crossing train axles, affected by noise. Considering the measured signal, the noise affects all of its shape, especially its peaks, useful to localize the train axles. Once the autocorrelation is done the noise doesn't affect the signal peaks but mainly its low level, that is not important in the detecting of the main relevant information: this improvement has pushed to use this technique during the algorithm development, based on the signal peaks detection. The operation of the algorithm as speed detector can be summarized in the following points:

- **Simulated track inputs:** starting from the simulated force signals coming from the measurement layout (see Fig. 2.1), their mean is done (in order to reject possible lateral disturbances) and a white noise level is added;
- **Auto/Cross Correlation techniques:** for each noisy signal the auto and cross correlation are applied;
- **Filtering stage:** in order to optimize the estimation accuracy an filter with a cut-off frequency tuned depending by the vehicle speed is performed(see Tab. 2.1);
- **Crossing times and speed detection:** starting from the knowledge of the difference between samples corresponding to the autocorrelation and cross correlation maximums, the vehicle speed are obtained.

Particularly, starting from a measurement layout equipped of three measurement sleepers and considering a couple of force signals, the first step consists in performing the autocorrelation on each obtained signals F^i_{zm} and then in the cross correlation among all the possible pairs of signals F^i_{zm} and F^j_{zm}. The generic expression of the cross-correlation between two signals (i,j) is:

$$\mathbf{R}_{ij}(m) = \sum_{n=0}^{N-m-1} F^i_{zm_{(m+n)}} {F^j_{zm_{(n)}}}^* \tag{2.1}$$

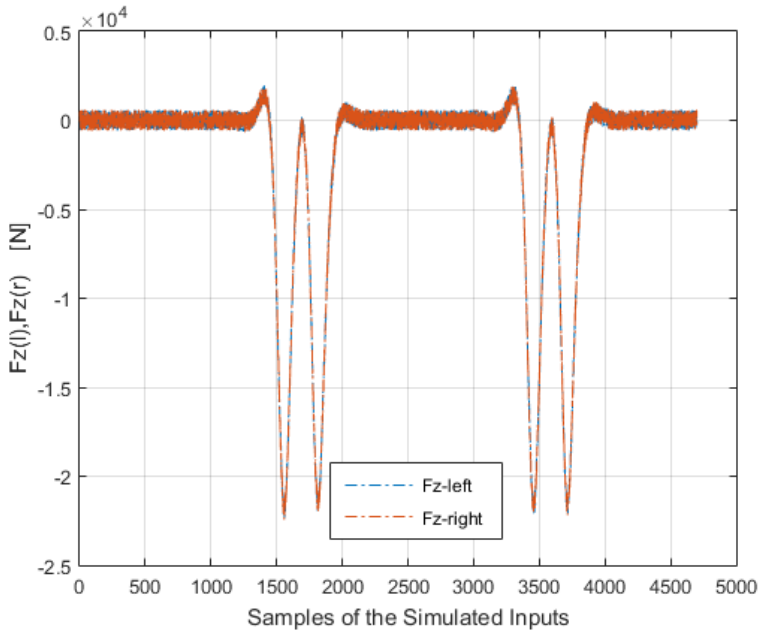

(a) Vertical forces $F^1_{z\,r}$, $F^1_{z\,l}$ acting on the right and left side of the first sleeper of the measurement station (performed at a vehicle speed V=10 $\mathrm{m\,s^{-1}}$) and a car body mass M=10 t

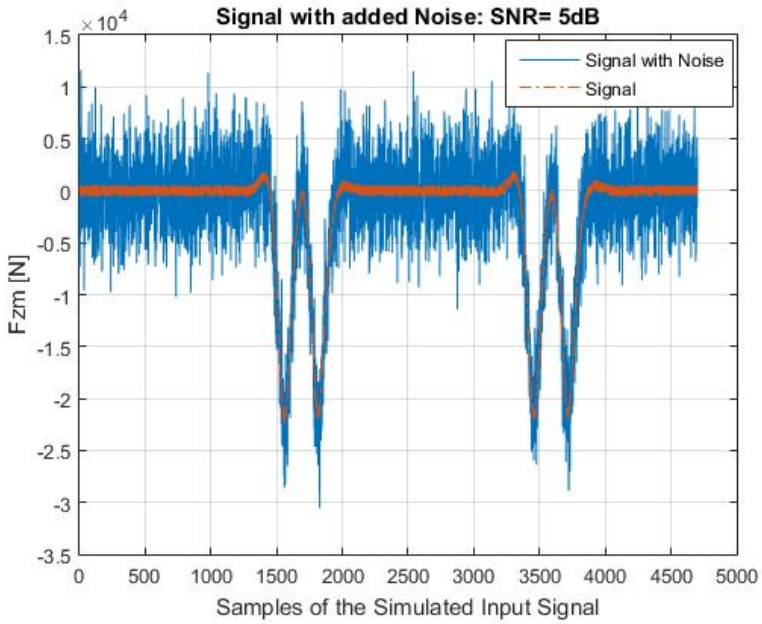

(b) Original input signal F^1_{zm} (red line) and input signal with added noise (green line): Signal-to Noise ratio (SNR)=5 dB performed at a vehicle speed V=10 $\mathrm{m\,s^{-1}}$ and a car body mass M=10 t

Figure 2.2: Input signal

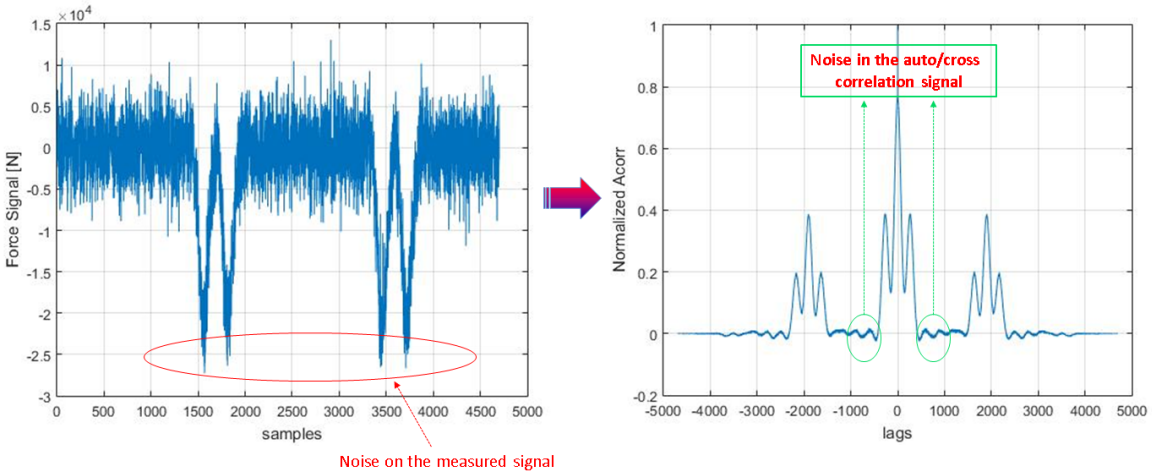

Figure 2.3: Denoising effect obtained with the autocorrelation signal: the noise not affects the local peaks, useful for the train axles detection

digitalized with N samples (m indicates the m-th sample of the correlation signals), where $F^{j}_{zm_{(n)}}{}^{*}$ is the complex conjugate of the discretized signal j and $F^{i}_{zm_{(m+n)}}$ indicates the discretized signal i, shifted of m samples. $R_{ii}(m)$ indicates the auto correlation signal. By means of the correlation operations, it is possible to evaluate the degree of true similarity between all the pairs of signals.
The cut-off frequencies computed for each vehicle speed is summarized in Tab. 2.1.

Table 2.1: Cut off frequencies computed in the full speed range

Speed [m s^{-1}]	f_{cut}[Hz]
2	27
10	35
20	45
30	55
40	65
50	75
60	85
70	95
80	105

Followed the filtering stage, the maximum signal peaks are detected: starting from the difference between the sample corresponding to the maximum value of the

autocorrelation of the signal F_{zm}^{i} and the one corresponding to its cross correlation with the F_{zm}^{j} signal, it is possible to compute the time delay between the F_{zm}^{i}, F_{zm}^{j} signals just multiplying this difference by the sample time integration step Δt. Through this method, the time shifts among all the pairs of input signals can be easily determined. Once known the time delays, the vehicle speed can be computed just dividing the distance between the corresponding sleepers by the time shift previously found for the signals. At the end, the estimation of the vehicle speed is the mean among all the speeds obtained from the previous computed time shifts (see Tab. 2.2).

Table 2.2: Number of speed computing among sleepers

Number Sleepers	Number of speed computing
2	1
3	3
4	6
5	9

An example with two sleepers located at X_i and X_j positions, spaced of d_{ij} apart, is reported:

$$m_i = argmax\ \ R_{ii}(m) \quad m_{ij} = argmax\ \ R_{ij}(m) \tag{2.2}$$

$$\Delta T_{ij} = \Delta t * |m_{ij} - m_i| = t_j - t_i \quad d_{ij} = X_j - X_i \quad V = \frac{d_{ij}}{\Delta T_{ij}} \tag{2.3}$$

where m_i and m_{ij} are the samples corresponding respectively to the maximum value of autocorrelation of i-th sleeper signal R_{ii} and cross correlation R_{ij} between the i-th and the j-th ones; Δt is the sample time and ΔT_{ij} is the time shift between the i-th and the j-th force signals (corresponding to the two sleepers); V represents the vehicle speed, computed dividing d_{ij} by the corresponding time delay ΔT_{ij}. Fig. 2.4a describes the operation of the algorithm as time crossing instants and speed detector [46][45].

Fig. 2.4b shows the shift between signals coming from two sleepers spaced of 9.6 m: just dividing itself with the obtained time shift the vehicle speed is obtained (Hp. T_c=0.001 s).

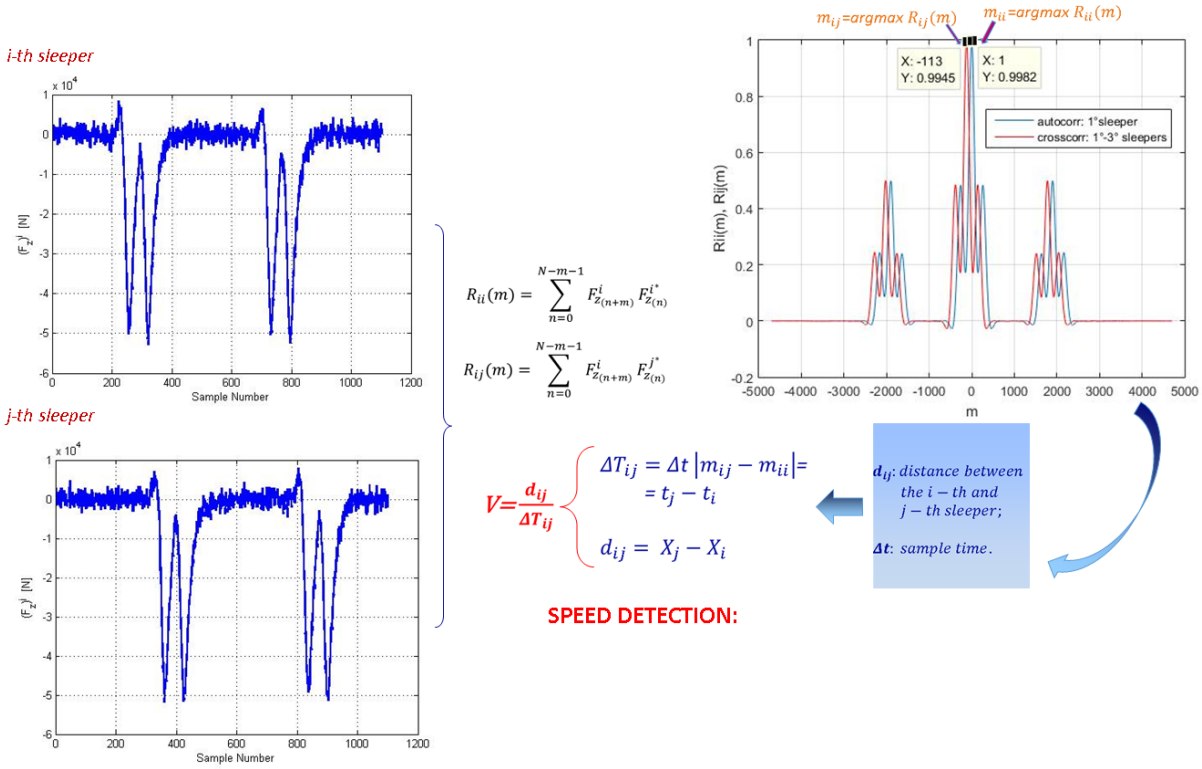

(a) Approach adopted at estimating the crossing time instants on fixed point along the track and at the vehicle speed computing

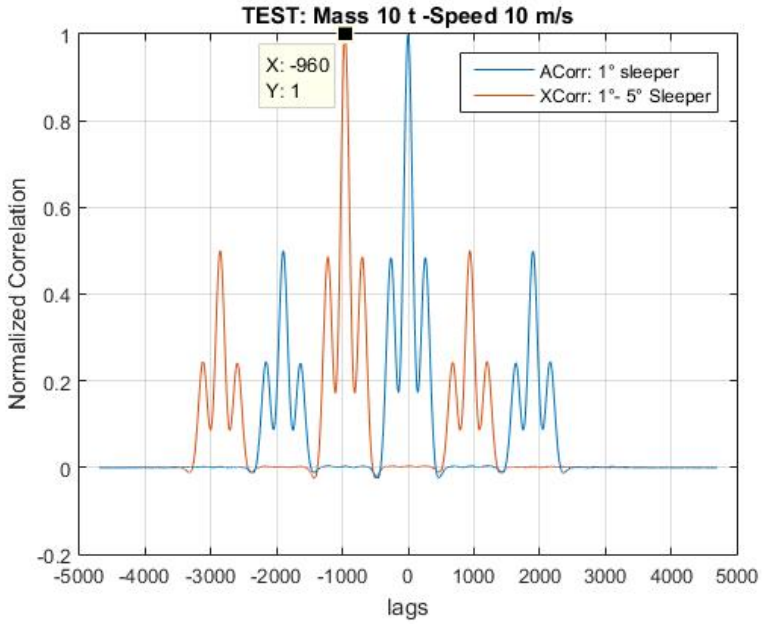

(b) Cross Correlation $R_{1,5}$ between the first sleeper signal F^1_{zm} and the fifth one F^5_{zm} and the auto correlation $R_{1,1}$ of the signal F^1_{zm} (performed at a vehicle speed V=10 m s^{-1} and with a car body mass M=10 t): just dividing the physical distance between the measurement sleepers (9.6 m) and the time shift is possible to obtain the speed vehicle

Figure 2.4: Application of the Cross/Auto correlation techniques as speed and time crossing instants estimator

To compute the crossing times on sleepers it is sufficient to use the signal time shifts among the different sleepers, starting from the first one to the last one:

$$t_i = t_0 + \sum_{j=0}^{i-1} \Delta T_{j,j+1}. \tag{2.4}$$

The method used to test the train detection is still based on the correlation theory because it increases the signals of several orders of magnitude when there is a good degree of true similarity and so it guarantees a better robustness against the input noise and disturbances (Fig. 2.3).

Table 2.3: Correspondence between the auto correlation signal peaks and the number of axles

Distance between axles	Description	Value [mm]
d_{12}	Bogie wheelbase	2 560
d_{13}	Bogie pivot distance	19000
d_{24}	Bogie pivot distance	19000
d_{23}	Distance between bogies	16440
d_{14}	$d_{12} * 2 + d_{23}$	21560

Fig. 2.5a shows the scenarios in which two axles of two different bogies are lost: more focused, if the first and last axles are lost (blue line) there is a local peak that corresponds to the distance between the second and third axles (16.44 m). Otherwise, if the second and fourth or first and third are lost there is a local peak that corresponds to the bogie pivot distance (19 m). Finally, if the second and third axles are lost there is a peak corresponding to the distance between the first and last axles (21.560 m). Fig. 2.5b shows the scenarios in which two axles of the same bogie are lost: in both cases the autocorrelation signal implies the presence of the peak corresponding to the bogie wheelbase distance (2.56 m). The approach used to discuss the Fig. 2.5a is also valid in the scenarios in which one of the vehicle axles is lost (Fig. 2.6), because the signal can be obtained by the combination of each signal showed in Fig. 2.5a. Especially, if the first or forth axles are lost, the local peaks that compare can be obtained with the combination of the blue and green line in Fig. 2.5a.
The same approach is used for Fig. 2.6b. These considerations bring out the idea that

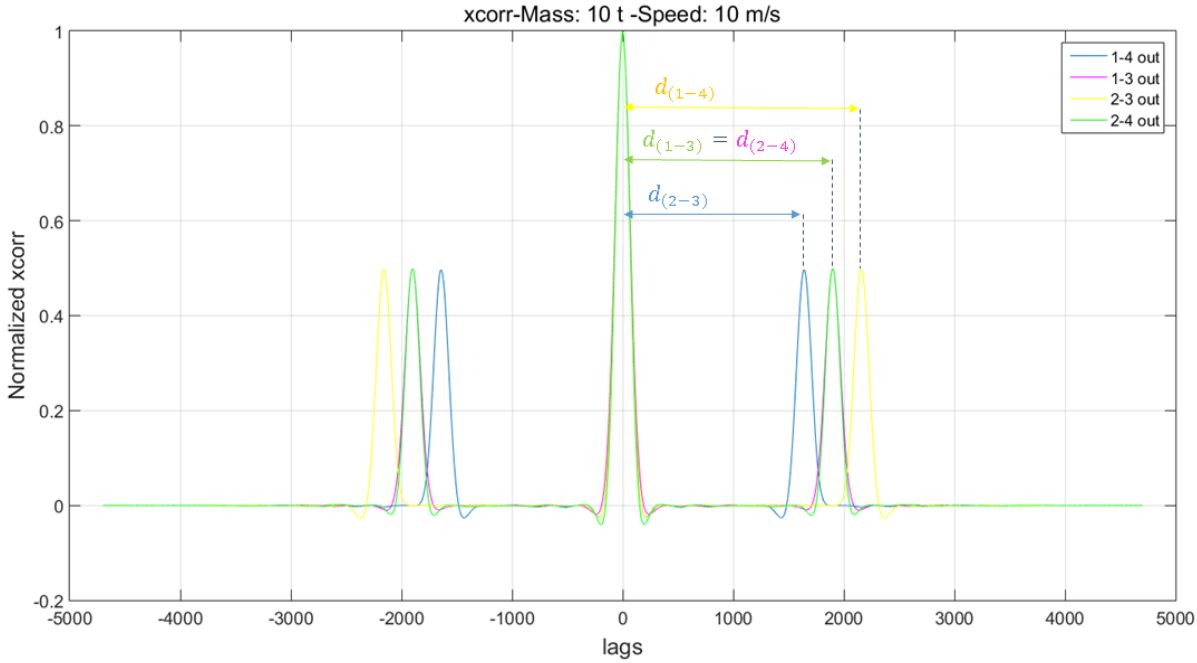

(a) Autocorrelation signal in a scenario in which two axles in two different bogies are lost: the local peaks correspond to the physical distance of the rimaining axles

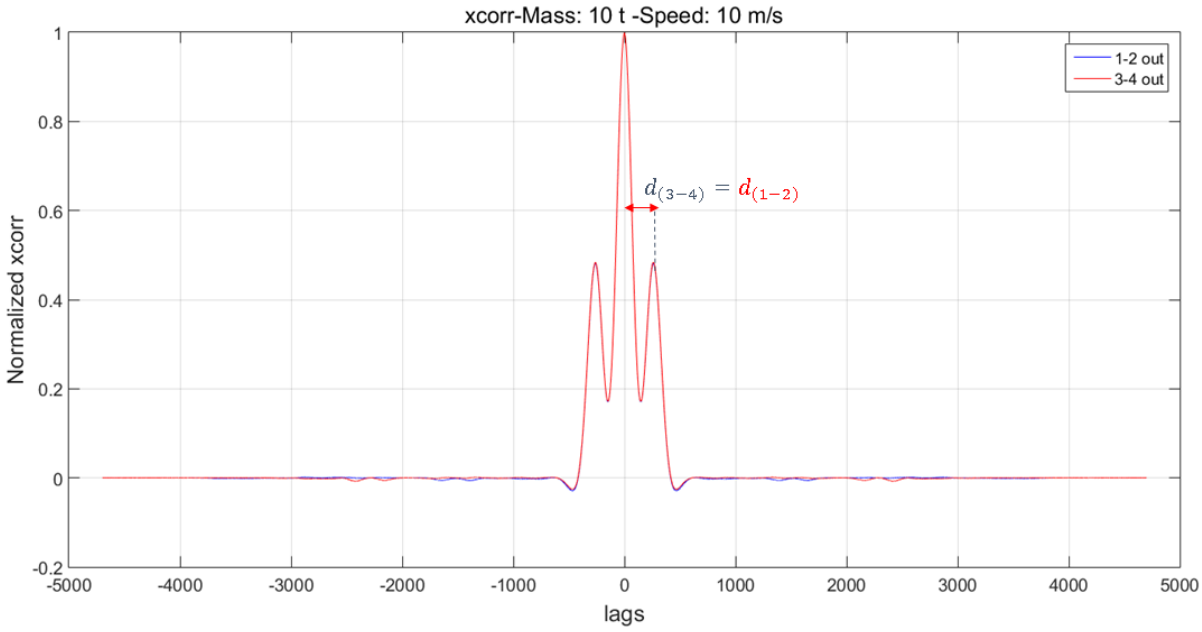

(b) Autocorrelation signal in a scenario in which two axles in the same bogie are lost: the local peaks correspond to the bogie wheelbase distance

Figure 2.5: Autocorrelation signal in a scenario in which two of the fourth train axles are lost

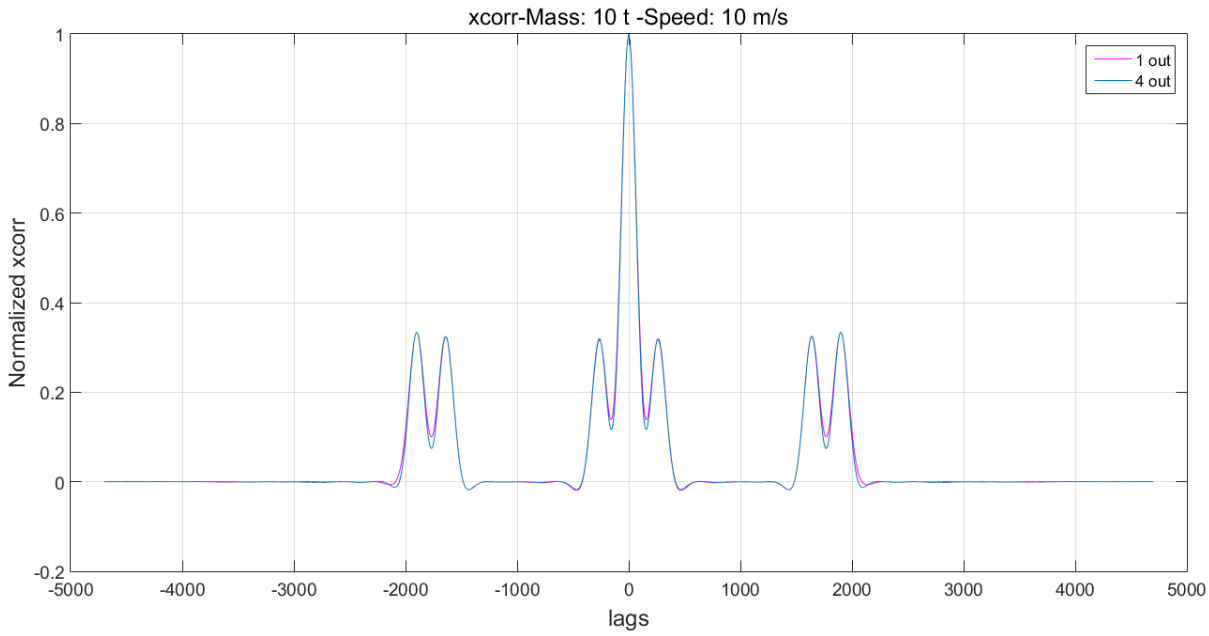

(a) Autocorrelation of the signal if the first or fourth axle are lost: the local peaks are linked with the physical distance of the remaining peaks

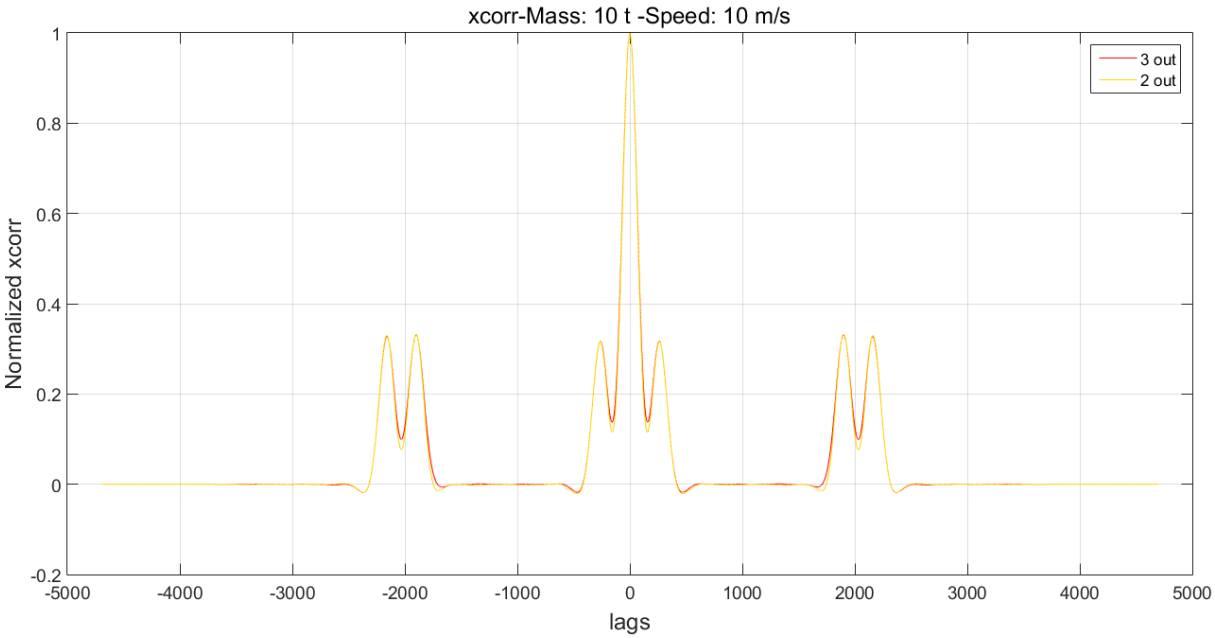

(b) Autocorrelation of the signal if the third or second axle are lost: the local peaks are linked with the physical distance of the remaining peaks

Figure 2.6: Autocorrelation signal in a scenario in which one of the train axle is lost

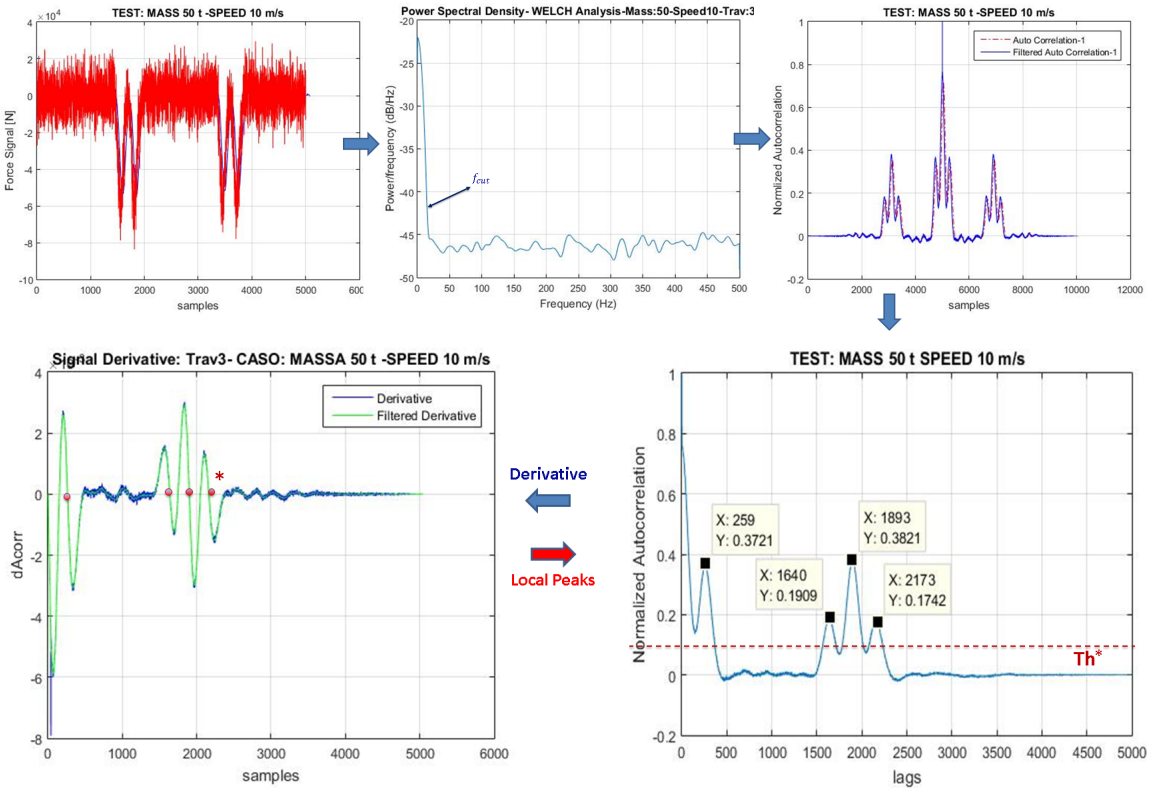

Figure 2.7: Operation of the algorithm as train detector: starting from the noisy input signal, the autocorrelation is done and then filtered. Once the autocorrelation is obtained its derivative is done and smooth to find samples corresponding with autocorrelation local peaks. The traversed axles are at the end computed applying a cut off threshold T_h (0.12)

working on the autocorrelation signal allows to hold the information of the original one with a less noise impact on the local peaks, important for the train detection. The operation of the algorithm to this aim is shown (Fig. 2.7). Starting from the noisy input signal, the autocorrelation and its normalization are carried out (to be free from the force value): then a filtering stage is applied to the autocorrelation signal. The derivative signal is used and filtered with a smooth action to compute local peaks of the autocorrelation signal (that is examined for positive lags) and then applying a cut-off threshold T_h (0.12) the final signal peaks are found (see Fig. 2.7).

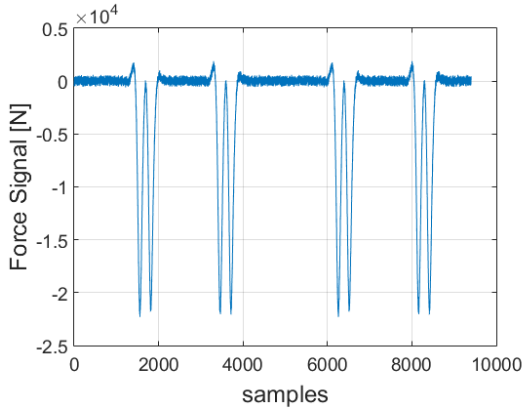

(a) Force signal corresponding to eith train axles

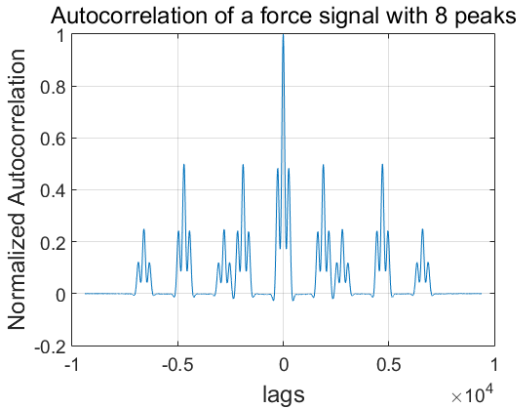

(b) Autocorrelation of a force signal composed by 8 peaks: the signal contains 13 peaks (computed for positive lags)

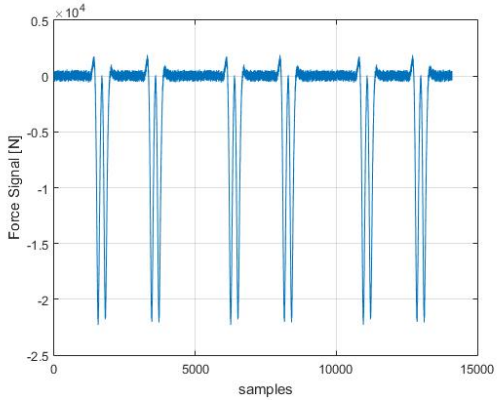

(c) Force signal corresponding to twelve train axles

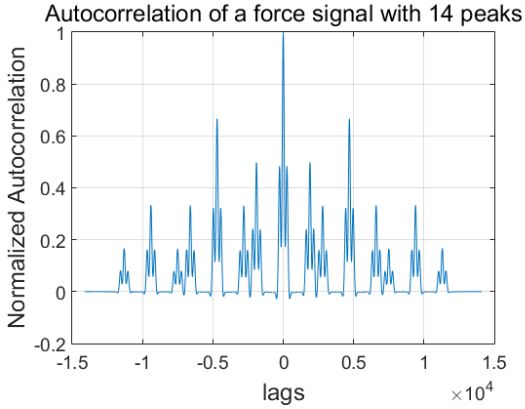

(d) Autocorrelation of a force signal composed by 12 peaks: the signal contains 22 peaks (computed for positive lags)

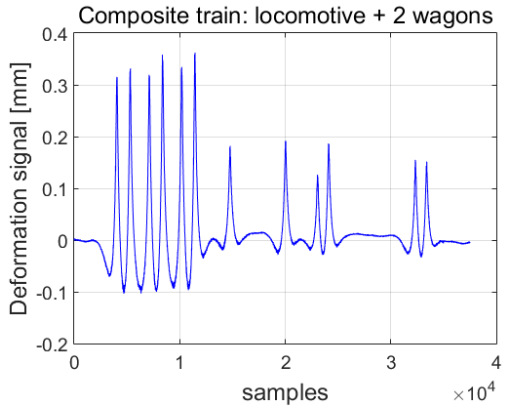

(e) Composite Signal: locomotive and two wagons

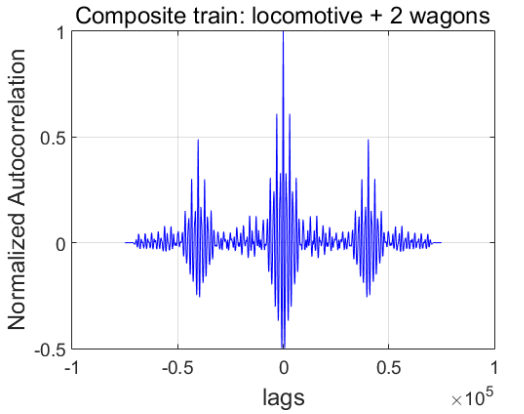

(f) Autocorrelation of a signal corresponding to a composite train

Figure 2.8: Autocorrelation signal evolution with an increasing number of original signal peaks (a,b,c) and with a composite train (e)

As previously said, the auto/cross correlations techniques are very useful to estimate the time shift among signals and so the vehicle speed but the peaks detection becomes quite difficult with a composite signal as well as in a real scenario. Moreover this approach has not shown a sufficient flexibility to trains with different composition if the autocorrelation is applied on the whole input signal (see Fig. 2.8f).
Another significant drawback of the approach concerns the reliability of the vehicle speed detection (see Fig. 2.4), which also depends by the physical distance among sensing elements and the sampling time of the measurement chain. Indeed, in the case in which the theoretical speed needs an accuracy bigger than the one guaranteed by the sampling time, there is an intrinsic error due to the resolution provided by the ratio between these two amplitudes. In particular, starting from the Layout 2 as measurement chain (in which there are two adjacent sleepers spaced of 0.6 m, see Tab. 3.2) is supposed of detecting a train speed of 70 m s^{-1}. Once the cross correlation is performed, the resulting shift between the two signals is $m_{ij} = 892$, where i and j correspond to 1 and 2 respectively: applying the ratio between the physical distance d_{ij} and the product of the sampling time ($T_c = 0.001$s) with m_{ij} the obtained speed is 66.67 m s^{-1} involving an estimation relative error of 4.76 %. This is due to not by the performance of the estimation approach but by the accuracy of the sampling time that must be of 0.00095 s to obtain the correct speed value (see Fig. 2.9): these considerations have involved the developing of new estimation approach based on techniques in the frequency domain.

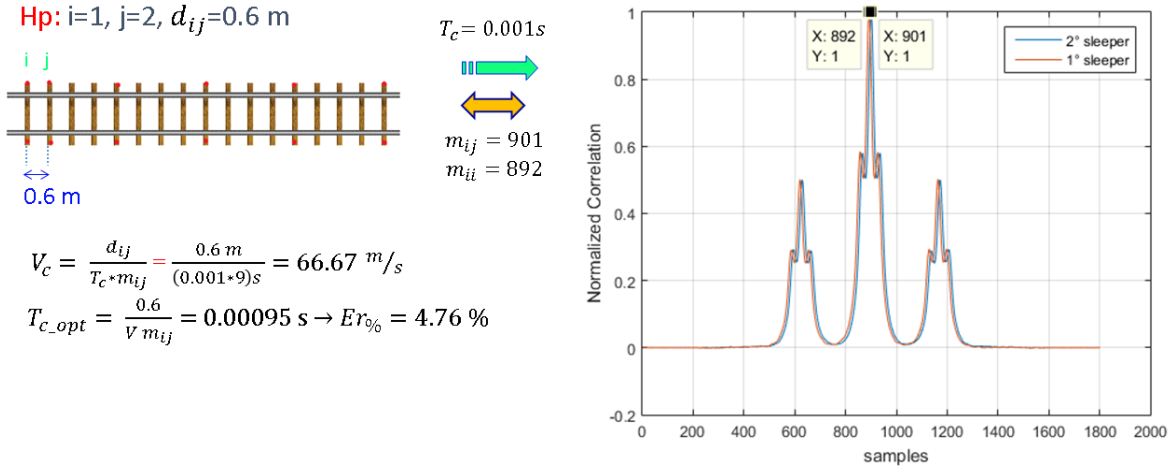

Figure 2.9: Time Domain algorithm- drawback of the approach described in Fig. 2.4 aimed at estimating the vehicle speed

2.2 Frequency domain approach (FDA)

To overcome the time domain problems (see Fig. 2.8), an alternative algorithm has been developed, based on frequency domain techniques with the aim at searching a tool flexible to the composition of the input signal. The new methodology is based on the application of the FFT (Fast Fourier Transform) to identify local peaks due to a train axle from other peaks like noise. Spectrogram is a widely used post processing method to analyze audio/speech and biomedical signals [47][48][49][50]. This approach allows to identify the signal peaks and has also an information of the evolution of the signal in the time domain. The spectrogram settings depends by spectral informations of the analysed signal. Fig. 2.10 shows the input signal (simulated force signal corresponding to a train with 50 t of mass and 80 m s^{-1} of speed) in which the fourth axles are located in the intervals (0.2-0.3) s and (0.45-0.55) s and its power spectral density estimation (PSD): the PSD highlights that the simulated signal, coming from the physical model discussed in Chap. 1, has a bounded bandwith (within 100 Hz). This information may suggest the configuration of spectrograms to get an high time resolution and a low frequency one, due to the no presence of relevant single frequencies that must be detected.

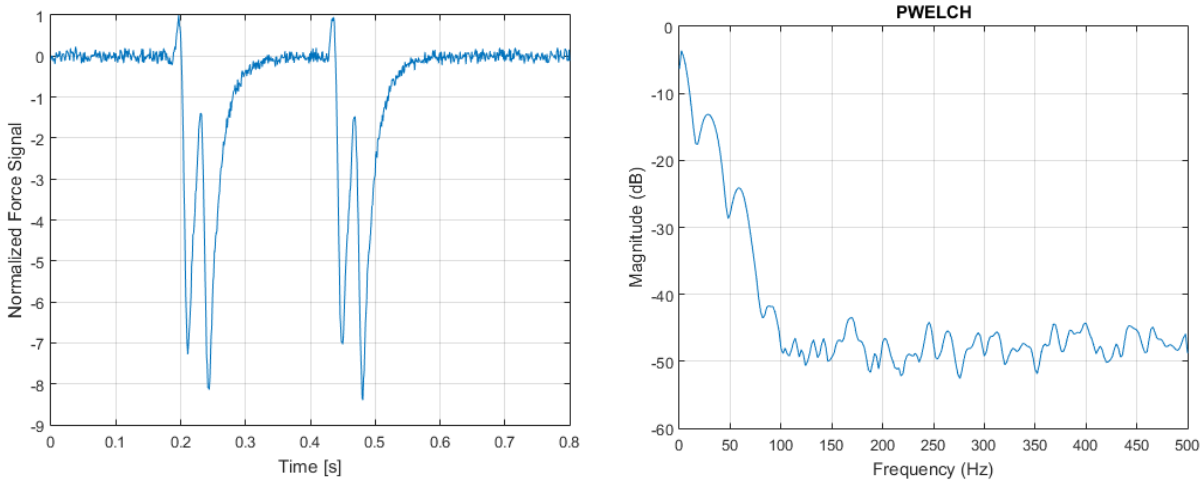

(a) Input Signal

(b) PSD estimation of the input signal

Figure 2.10: Input signal and PSD estimation: axles are present in the time interval of (0.2-0.3) s and (0.45-0.55) s

In particular, to use the spectrogram different parameters must be setted:

- number of FFT points;
- type of window;
- width of the window;
- number of window;
- overlap among windows.

The optimal number of points of the FFT has been carried out by means of the nearest multiple of 2 of the signal size. The choice of the window and its parameters (type,width,number and overlap) is very important and have effects on the good analysis of the signal. Different windows have been evaluated and at the end, in order to do the train detection, the Taylor one (Fig. 2.11) has been used. Taylor windows are similar to Chebyshev ones. Whereas a Chebyshev window has the narrowest possible main lobe for a specified side lobe level, a Taylor window allows to make trade off between the main lobe width and the side lobe level. The Taylor distribution avoids edge discontinuities, so Taylor window side lobes decrease monotonically. The leakage factor is null, setting the side lobes attenuation to 50 dB (Tab. 2.5). Fig. 2.11 shows the evolution of Taylor windows in the time and frequency domains with a different side lobes attenuation: Figs. 2.11a shows how bigger smooth of the lateral ends (left,right) of signal may involve a bigger attenuation of the lateral side lobes (Fig.2.11b). Setting a 50 dB of attenuation (Fig.2.11c) the leakage factor is 0.01 % (very low deformation of the original signal spectrum).

Fig. 2.12 shows spectrograms with an increasing number of samples, from 10 to 100 samples: with the increase of the window size the time resolution decreases and the frequency one increases. Indeed, in Fig. 2.12a the useful frequency information of the input signal is localized in a thin time interval, but there is a high frequency one (low frequency resolution). Increasing the number of window samples (for example 100) the information is more accurate in the frequency domain (amplitude in the (0;-20) dB interval is within 80 Hz), but has a worst definition in the time domain. Considerations regarding the windows size have been carried out in order to detect the train parameters in a wide range of its mass and speed: in particular, with the increase of the vehicle speed the crossing train axles are thinner and so it's important to

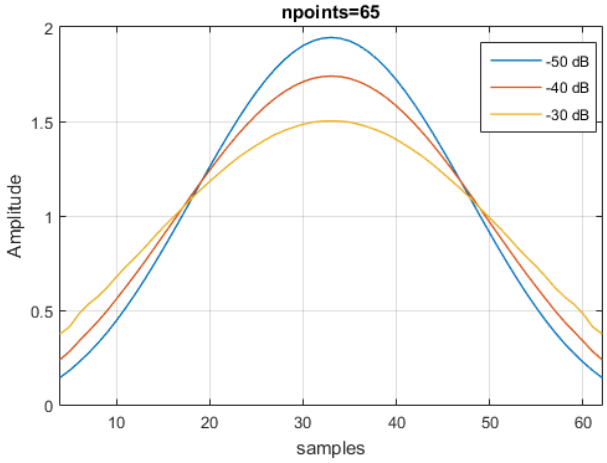

(a) Time domain shape of the Taylor window with different side lobes attenuation (-50 dB, -30 dB)

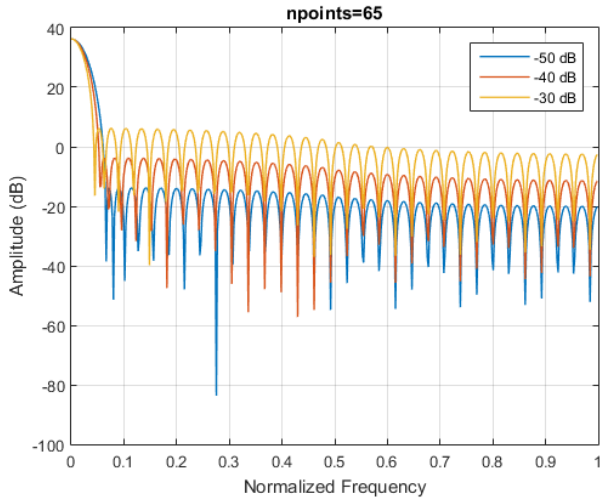

(b) Frequency domain shape of the Taylor window with different side lobes attenuation (-50 dB, -30 dB)

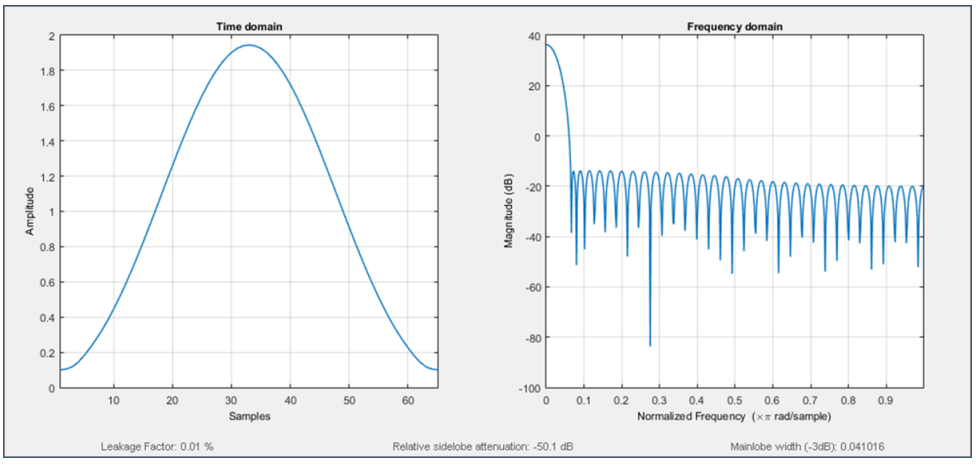

(c) Windows Visualization tool: time domain and frequency one properties of the Taylor windows with -50 dB of side lobes attenuation

Figure 2.11: Setting of the side lobes attenuation of the Taylor windows: (a-b) with the increase of smoothing of the left and right window sides the leakage factor decrease,

use windows with an higher resolution in the time domain. Furthermore, the spectral properties of the signal (Fig. 2.10) suggests that is useful to use spectrogram with an high time resolution, rather than a frequency one. To this aim, the size of windows have been scaled depending by the simulated input: for a speed range of (2-80) $\mathrm{m\,s^{-1}}$ the windows size has been reduced with the increase of the vehicle speed to obtain a bigger time resolution (Fig. 2.13, Tab. 2.4).

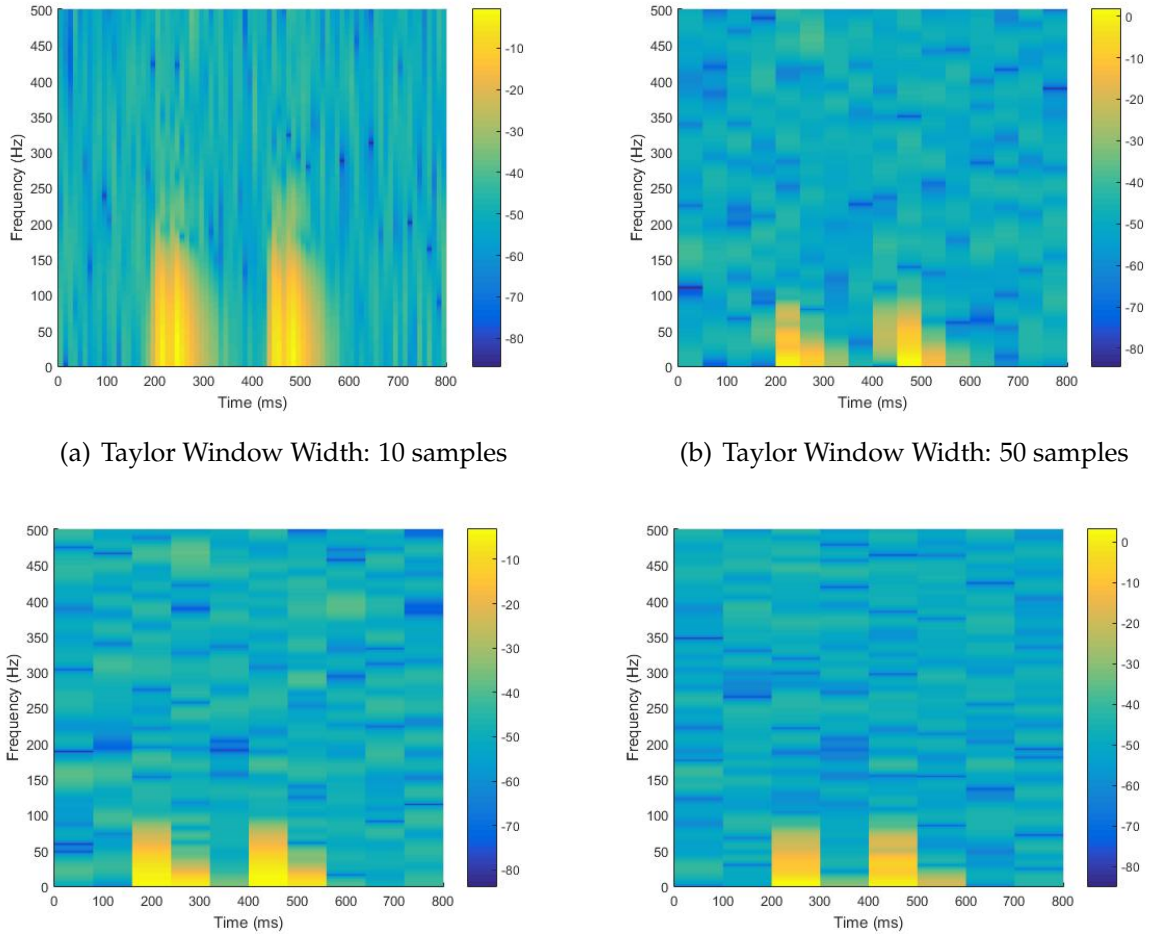

(a) Taylor Window Width: 10 samples

(b) Taylor Window Width: 50 samples

(c) Taylor Window Width: 80 samples

(d) Taylor Window Width: 100 samples

Figure 2.12: Spectrogram applied on the input signal with a different value of window width

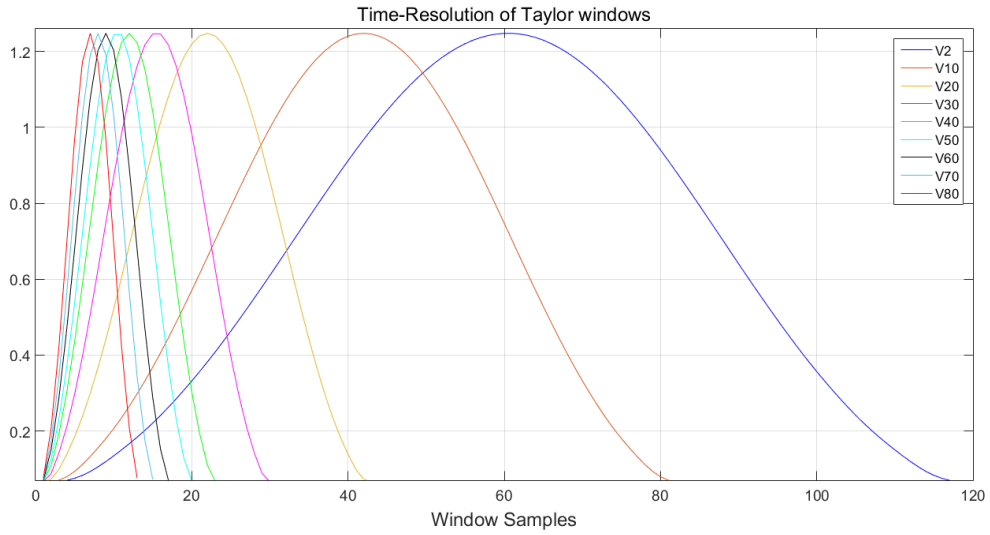

Figure 2.13: Increase of the window time resolution with the increasing of the vehicle speed

Table 2.4: Setting of the Taylor windows size in the full speed range

Speed [m s^{-1}]	Window Size [samples]
2	120
10	83
20	43
30	30
40	23
50	20
60	17
70	15
80	13

Concerning the overlap among windows, two plots of spectrogram have been done with or without the overlap, in order to highlight its effect on the spectrogram analysis.

It's possible to notice the difference in Fig. 2.14 due to the overlap: the presence of overlap gets a detailed analysis. These considerations bring out the idea that using the spectrogram is possible to identify the train axles, involving train detection applications. Moreover, when the window scans the signal, if it superimposes a train axle, the power spectral density assumes a relevant value that, if it is over a threshold, makes possible the axle detection(Fig. 2.15, 2.16). (Fig. 2.15, 2.16).

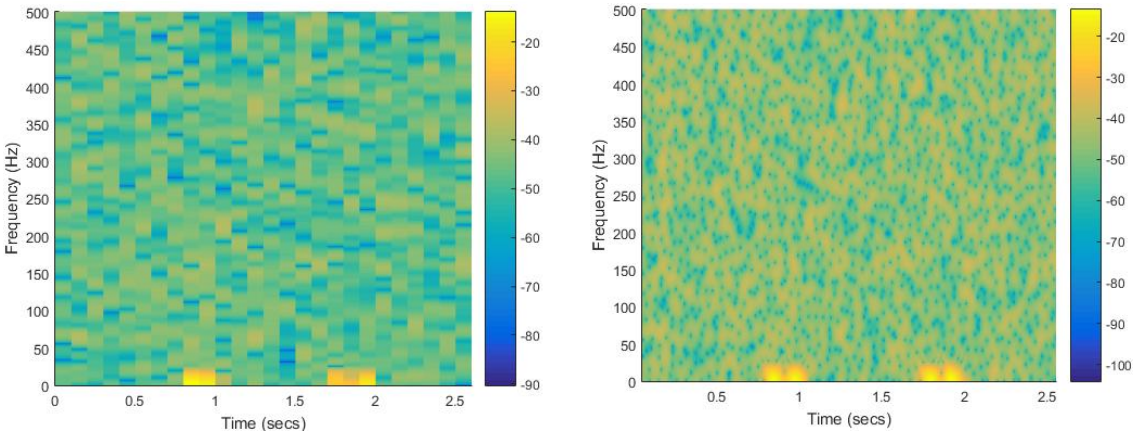

(a) Spectrogram applied without overlap (b) Spectrogram applied with overlap

Figure 2.14: Evaluation of the overlapping among windows: the presence of the overlap involves the train axles detection with bigger accuracy

Fig. 2.17 shows the operation of the algorithm as train axles detection, summarized in the following steps:

- Noise is added to the input signal (when experimental data are not available, see Fig. 1.1);

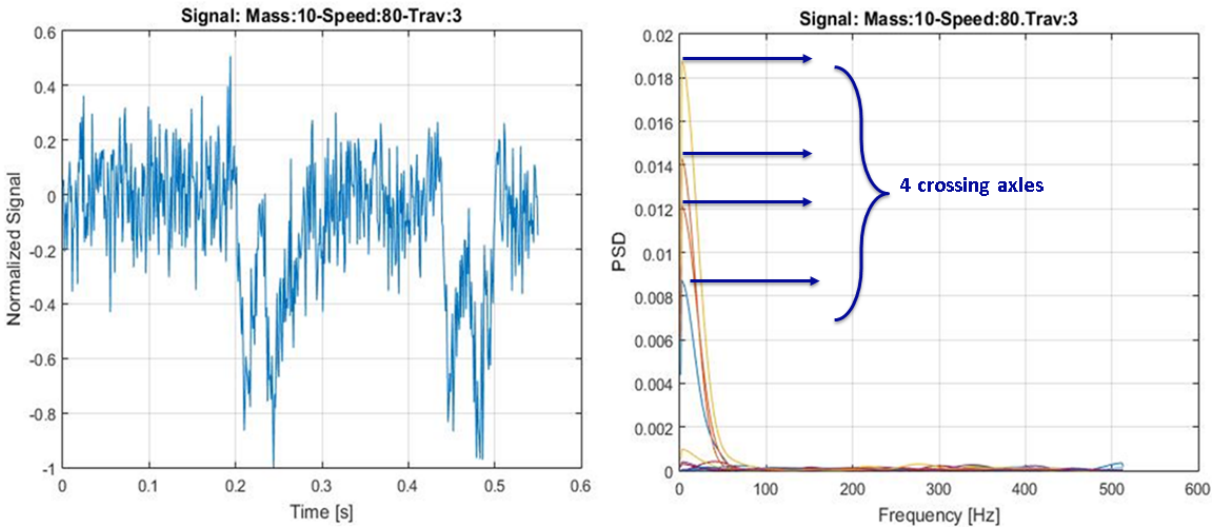

Figure 2.15: Train axles detection: the maximum PSD (power spectral density)value of each spectrogram window is computed and plotted

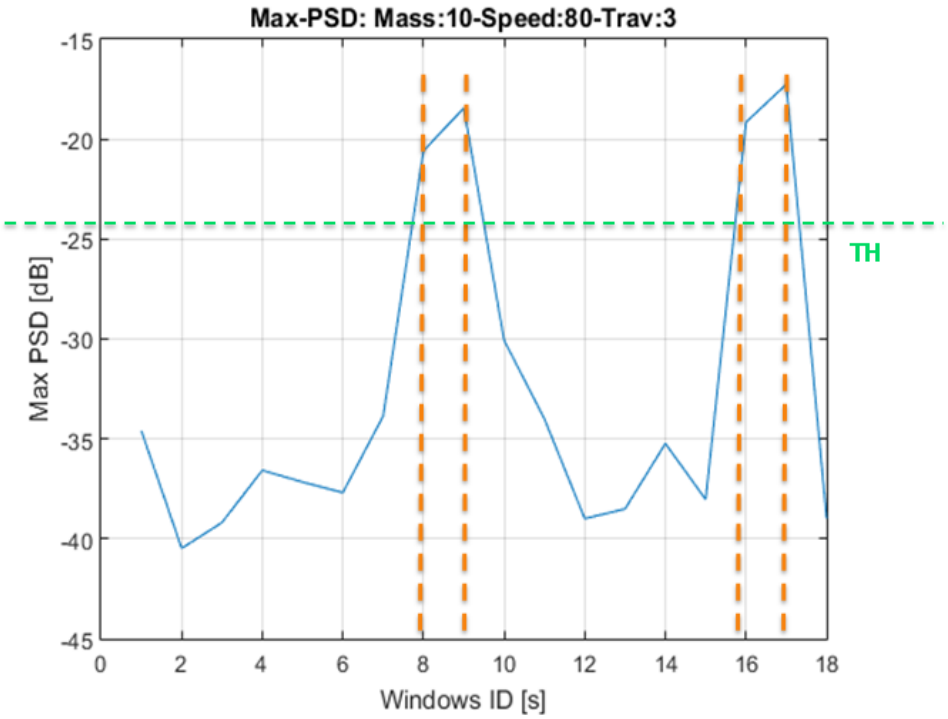

Figure 2.16: Train axles detection: applying the cut-off threshold is possible to detect the four train crossing axles

Table 2.5: Configuration of the spectrogram aimed at the train axles detection

Window	Side Lobes Attenuation (dB)	Number	Overlap [%]	Cut-Off Threshold (dB)
Taylor	-50	40	40	-24

- Normalization of the input signal;
- Calculation of the maximum value of PSD corresponding to the spectrogram windows during the signal scanning;
- Plot of the maximum PSD values for each segment;
- Smooth operation of the signal;
- A cut off threshold (-24 dB) is applied to localize the train axles.

The configuration of the spectrogram used to compute the number of crossing axles is indicated in Tab. 2.5. The spectrogram has been also used to estimate the crossing times instants and the vehicle speed thanks to the central time of windows used to

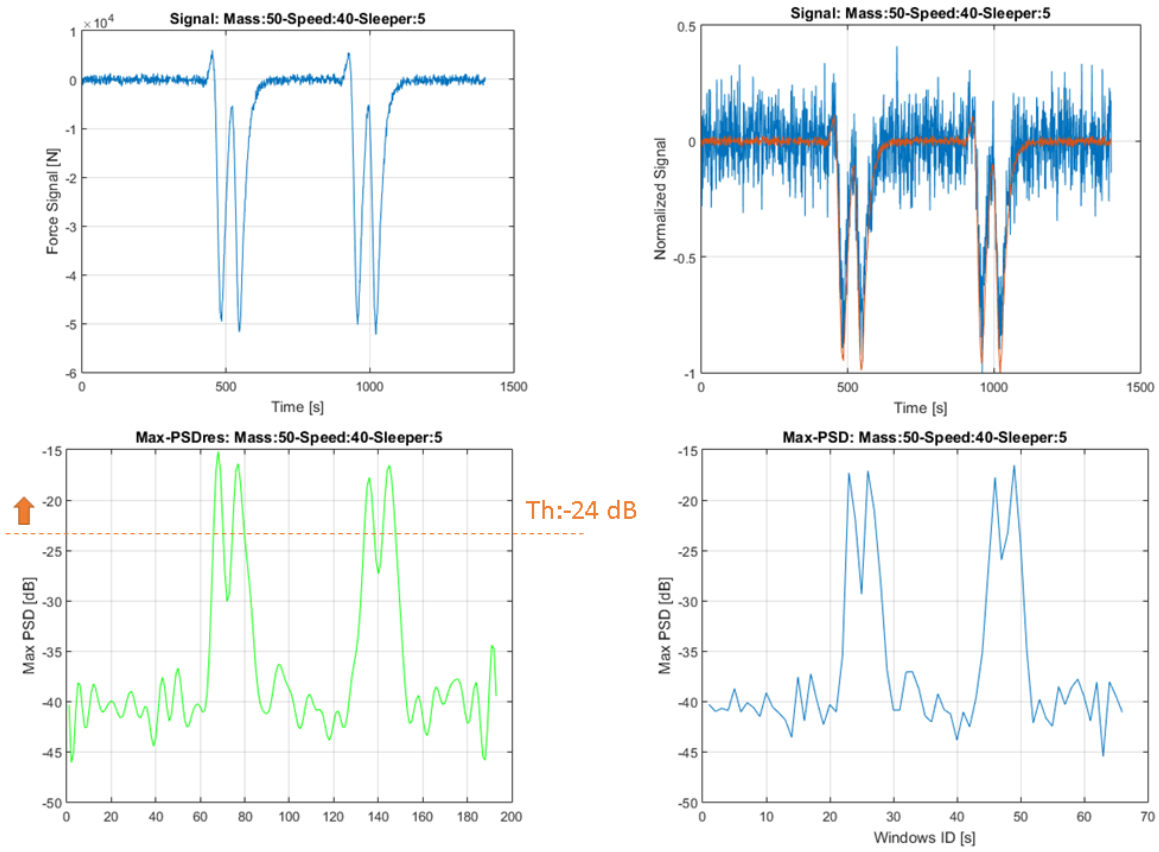

Figure 2.17: Operation of the algorithm as train detector: starting from the simulated force signal, provided by the validation model described in Fig. 1.1, a noise level is added and then the plot of each maximum PSD is used. In this way is possible to separate the useful peaks from the noise ones

decompose the signal. Once the window corresponding with the axle is found, the corresponding central time is an approximation of the time crossing instants (see Fig. 2.18).

To provide an accurate estimation a Bartlett window has been used, which main properties are its leakage factor of 20 % and side lobes attenuation of 20 dB (see Fig. 2.19). The configuration of the spectrogram aimed at estimating the crossing times referred to the train axles is indicated in Tab. 2.6.

The procedure to estimate the axles crossing instants and, as a consequence, the vehicle speed is summarized in the following steps:

- application of the spectrogram (which configuration is indicated in Tab. 2.6);

Table 2.6: Configuration of the spectrogram for the time crossing instants and vehicle speed detection

Window	Number	Overlap
Bartlett	60	90 %

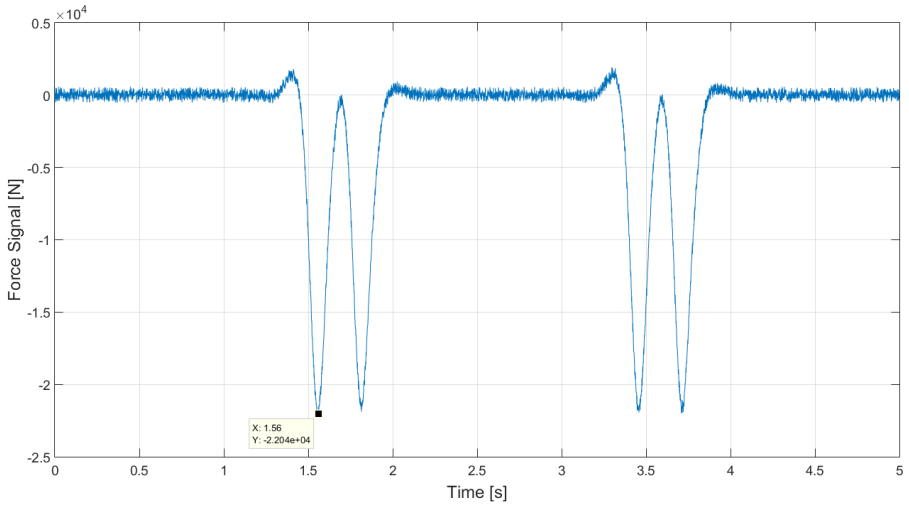

(a) Input Force Signal: the first train axle occurs at 1.56 s

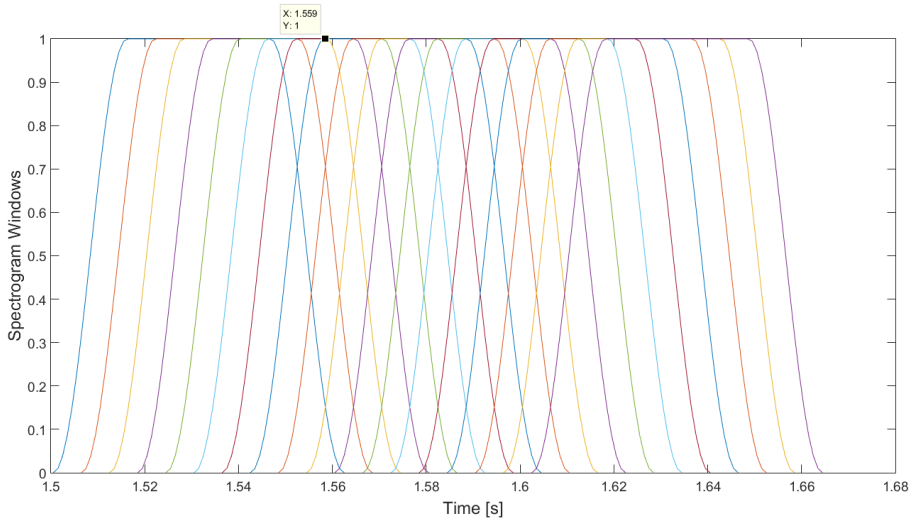

(b) Windows of spectrogram applied to the force signal

Figure 2.18: Application of the spectrogram as estimator of the time crossing instants along the rail in correspondence of the train passage: (b) the central time of the eighth window is the best match of the crossing time corresponding to the first train axle

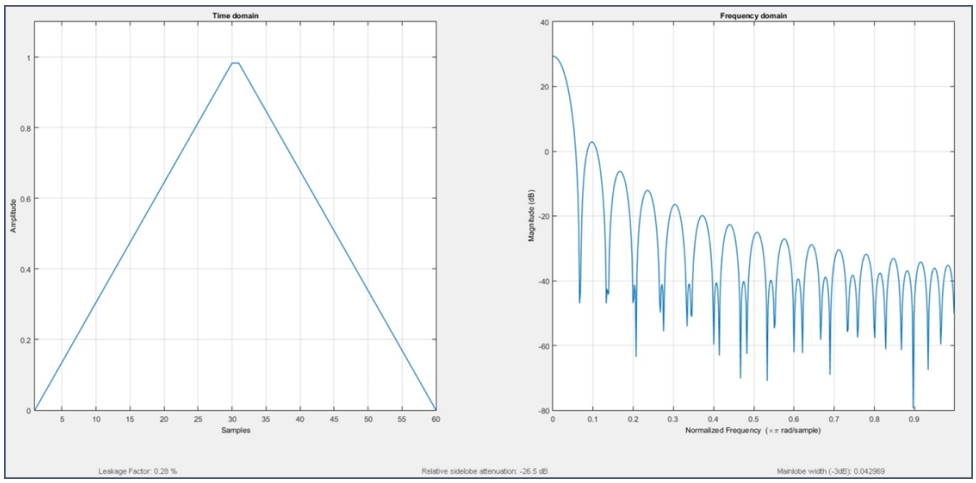

Figure 2.19: Bartlett windows properties in the time domain (left) and in the frequency one (right)

- identification of the windows corresponding to the train axles and reading of the time instants in the centre of each window;
- starting from the knowledge of the measurement layout, for each train axle the time shifts between pairs of measurement sleepers are done;
- the vehicle speed is computed for each pairs, just dividing the physical distance between pairs of measurement sleepers with the corresponding detected time shifts.

Fig. 2.20 shows the operation of the algorithm in the computing of the time shift among sleepers in a reference scenario of three ones. For each sleepers, four time crossing instants are computed with spectrogram, corresponding to the train axles. The frequency approach allows to identify crossing times of each train axle and so the computing number of the vehicle speed is multiplied with the number of train axle. The speed detection for three measurement sleepers can be obtained as:

$$V = \frac{\sum_{i=1}^{n_{axles}} (\frac{dS_{21}}{dTi_{21}} + (\frac{dS_{32}}{dTi_{32}} + (\frac{dS_{13}}{dTi_{13}})}{n_{axles} n_{sleepers}} \tag{2.5}$$

where dTi_{jk} indicates the time shift between the j and k sleepers of the i axle, dS_{jk} indicates the physical distance between the j and k sleepers.
The same approach is used for layout with different number of sensing elements.
Tab. 2.7 compares the number of computing of the vehicle speed done with the TDA

and FDA approaches with a measurement chain equipped of a different number of sensing elements.

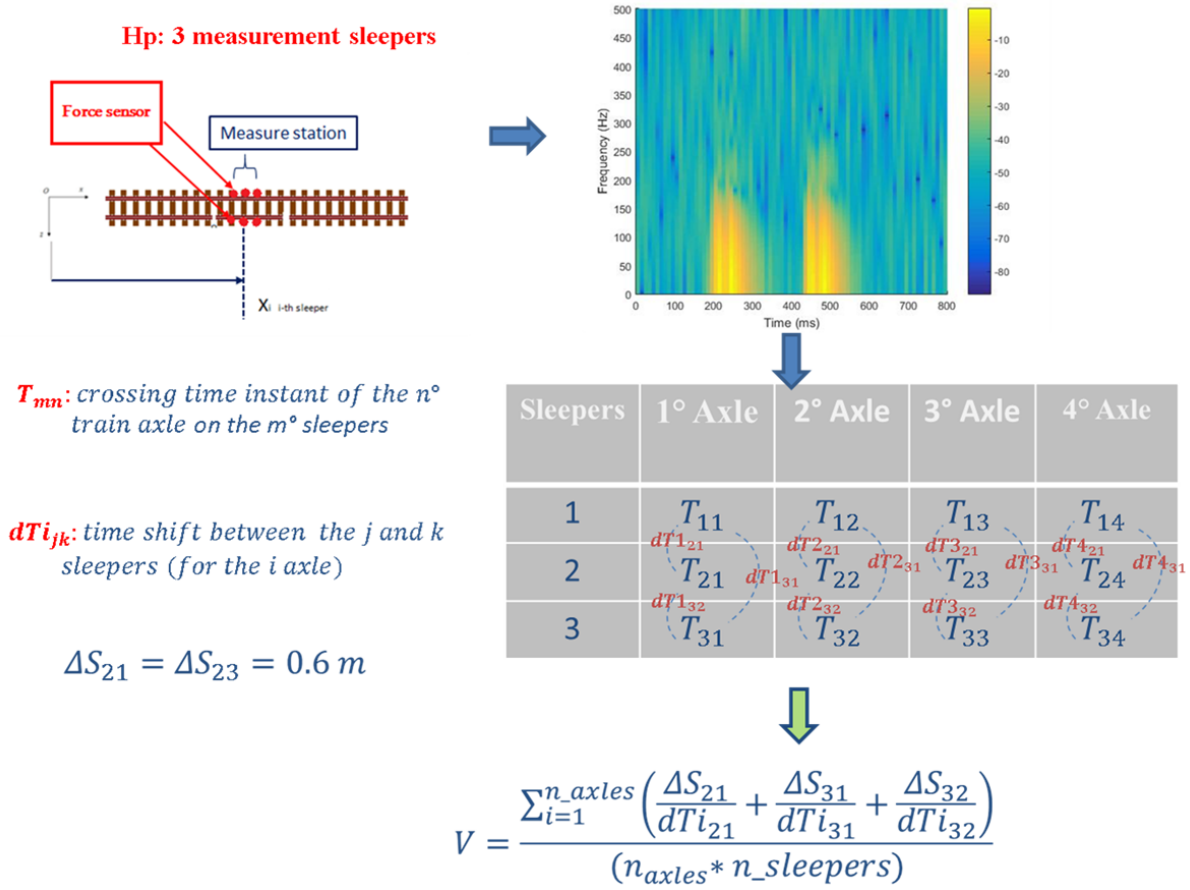

Figure 2.20: Speed computing: for each train axle i the vehicle speed is obtained dividing the physical distance (dS_{jk}) between two sleepers with their time shift dTi_{jk}. At the end the mean among all the obtained vehicle speed estimation is carried out

Table 2.7: Number of speed computing

Number of sleepers	Time Domain Approach (TDA)	Frequency Domain Approach (FDA)
2	1	4
3	3	12
4	6	24
5	9	36

Chapter 3

Results based on input signals coming from the simulation campaign

Chapter Contents

The operation of the two estimation approaches (Time Domain Approach **TDA**, Frequency Domain Approach **FDA**) have been trained with a wide simulation campaign, concerning several vehicle parameters (mass and speed, see Tab. 3.1) and measurement chain ones (number of sensing elements and spacing among them, see Tab. 3.2). In particular, the simulated input signals come from force sensors placed over measurement sleepers at the right an left sides: the resulting force signal is the mean between the right and left detected forces in order to reject possible lateral disturbances. The measurement layout is composed by measurement sleepers spaced among themselves of 0.6 m (Fig. 3.1). Two different levels of white noise (SNR: 4dB or 8 dB, see Fig. 3.2) have been added on the simulated input signal to check the

robustness of the estimation approaches under operating conditions worse than those of a real scenario.

Table 3.1: Simulation Parameters

Parameter	**Min.**	**Max.**	$\mathbf{N_V/N_M}$
Velocity ($m\,s^{-1}$)	2	80	9
Car-body Mass (t)	10	50	5

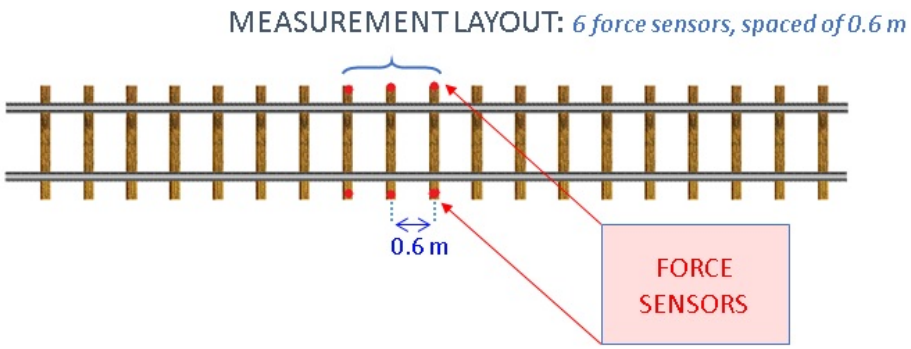

Figure 3.1: Measurement layout equipped of force sensor elements placed over measurement sleepers, spaced of 0.6 m

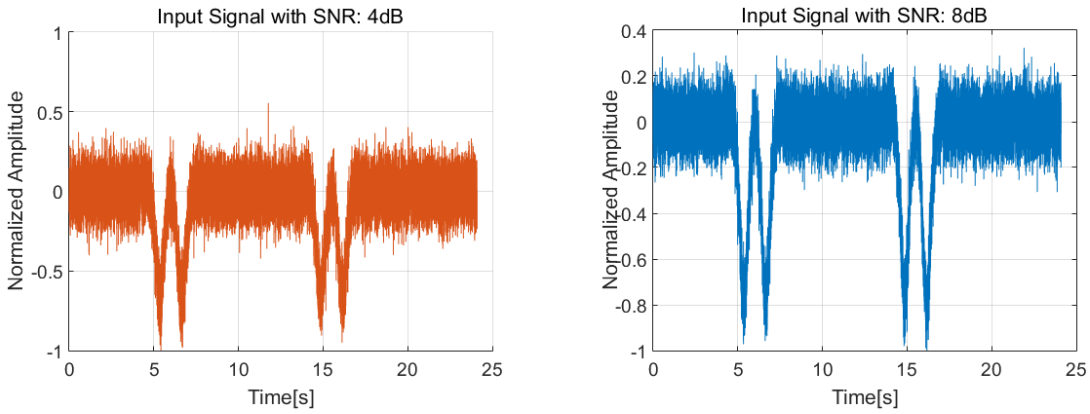

(a) Input Signal with a snr: 4 dB

(b) Input Signal with a snr: 8 dB

Figure 3.2: Noise levels added to the input signal (see also Tab. 3.1) used to test the algorithm performance in the simulation campaign

Several measurement layouts have been proposed for both testing the robustness of the approaches against different measurement chains and to highlight the improvement of the estimation accuracy with the increasing of the sensing elements number. Each measurement layout differs from the other ones for the number of sensing elements or distance among themselves (see Tab. 3.2).

Table 3.2: Measurement layouts used to test the performance of the estimation approaches, composed by a different number of sensing elements and spacing among them

N° Sleepers	Spacing	Occupied space [m]	Sleeper ID	Layout ID
2	0	0.6	[64 65]	Layout 1
2	1	1.2	[64 66]	Layout 2
2	2	1.8	[64 67]	Layout 3
2	3	2.4	[63 67]	Layout 4
3	0	1.2	[64 65 66]	Layout 5
3	1	2.4	[64 66 68]	Layout 6
3	2	3.6	[62 65 68]	Layout 7
3	3	4.8	[60 64 68]	Layout 8
4	0	1.8	[53 64 65 66]	Layout 9
4	1	3.6	[60 62 64 66]	Layout 10
4	2	5.4	[58 61 64 67]	Layout 11
4	3	7.2	[56 60 64 68]	Layout 12
5	0	2.4	[63 64 65 66 67]	Layout 13
5	1	4.8	[60 62 64 66 68]	Layout 14
5	2	5.4	[58 61 64 67 70]	Layout 15
5	3	9.6	[56 60 64 68 72]	Layout 16

The two basilar tasks are the crossing times detection (to compute the vehicle speed) and the trains one: to the first aim, a Monte Carlo analysis has been carried out through several algorithm iterations (see Tab. 3.3), in which, for each one, a white noise is added on the input signal. When the goal is the train detection, the aim is to verify that no estimation errors are involved with a quite big number of crossing axles (in order to be more confident with a realistic scenario).

Table 3.3: Monte Carlo Analysis to evaluate the algorithms performance in estimating of the train parameters

Estimated Amplitude	**Monte Carlo Approach**
Crossing Times (Speed Detection)	[1:2:50 60 70 80 90 100]

3.1 Time Domain Approach (TDA)

The performance analysis involves the definition of several errors: the crossing times and vehicle speed estimations led to the definition of the percentage relative speed error E_v^{sim} [%] and Ti one $E_{T_i}^{sim}$ [%].

$$E_v^{sim} = \frac{|\widehat{V}^{sim} - V|}{V} \qquad E_{T_i}^{sim} = \frac{|\widehat{t_{T_i}}^{sim} - t_{T_i}|}{t_{T_i}} \tag{3.1}$$

where V and t_{T_i} represents the nominal values of the speed and crossing times respectively, and $\widehat{V}^{sim}$, $\widehat{t_{T_i}}^{sim}$ indicate the estimated ones. Errors computed with the Monte Carlo analysis become:

$$E_v^{sim_{iter}} = \sum_{n=1}^{n_{iter}} \frac{E_v^{sim}}{n_{iter}} \qquad E_{T_i}^{sim_{iter}} = \sum_{n=1}^{n_{iter}} \frac{E_{t_{T_i}}^{sim}}{n_{iter}} \tag{3.2}$$

where $E_v^{sim_{iter}}$, $E_{T_i}^{sim_{iter}}$ and n_{iter} are respectively the errors on the speed and crossing times estimations and the number of algorithm iterations.
E.g the Layout 1 is considered which involves two measurement sleepers spaced of 0.6 m: at first an SNR of 8 dB is considered. Results have led out several considerations: in particular Figs.3.3-3.4 highlight the performance in estimating the vehicle speed (that are strictly dependent from those on the time crossing estimation) in the operating

conditions described in Tab. 3.1. Fig. 3.3a is a 3D plot of $E_v^{sim_{iter}}[\%]$ trend with the Monte Carlo approach: errors corresponding to a vehicle speed of 70 $\mathrm{m\,s^{-1}}$ (yellow bars) are quite higher than the other ones, because there is an added error due to the accuracy of the signal sampling time in agree with the considerations developed in Fig. 2.9. Other considerations concern the dependence of estimation accuracy by the vehicle mass: indeed, results have been analysed separately for each speed in Fig. 3.3(b-f) and Fig. 3.4(a-d) to highlight the little different among the trends of $E_v^{sim_{iter}}[\%]$ depending only by the vehicle mass: this is clear because the value of vehicle mass involves a different auto/cross correlation peaks height, that is normalized during the post-processing approach (see Fig. 2.4) and so a little difference among errors depending only by the vehicle mass is expected. These considerations have involved the computing of additional parameters $E_{mTi_k}^{sim}$ and $E_{mV_k}^{sim}$ (Fig. 3.5), defined as:

$$\mathbf{E_m}_{Ti_k}^{sim} = \sum_{M=1}^{n_{mass}} \frac{E_{MTi_k}^{sim}}{n_{mass}} \qquad \mathbf{E_m}_{v_k}^{sim} = \sum_{M=1}^{n_{mass}} \frac{E_{Mv_k}^{sim}}{n_{mass}} \tag{3.3}$$

where $E_{MTi_k}^{sim}$ and $E_{Mv_k}^{sim}$ are the relative crossing times and speed errors corresponding to a vehicle mass $M \in (10-50)$t and speed $k \in (2-80)\mathrm{m\,s^{-1}}$.
As a consequence, for each Monte Carlo iteration, errors become:

$$\mathbf{Em}_{Ti_k}^{sim_{iter}} = \sum_{n=1}^{n_{iter}} \frac{\mathbf{E_m}_{Ti_k}^{sim}}{n_{iter}} \qquad \mathbf{Em}_{v_k}^{sim_{iter}} = \sum_{n=1}^{n_{iter}} \frac{\mathbf{E_m}_{v_k}^{sim}}{n_{iter}} \tag{3.4}$$

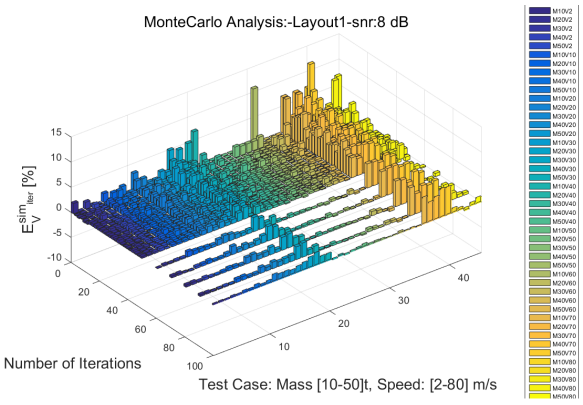

(a) 3D plot diagram of the percentage relative speed errors $E_v^{sim_{iter}}$

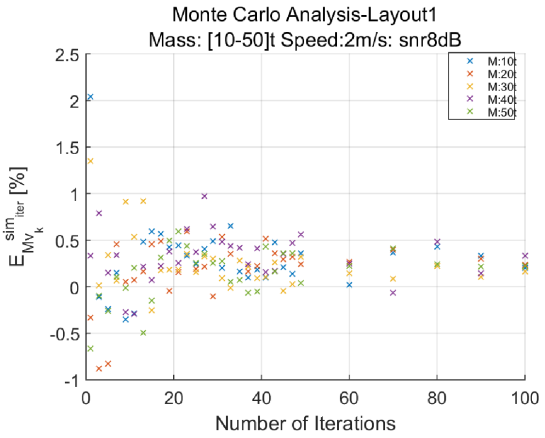

(b) Scatter plot of the percentage relative speed errors $E_{M\,v_k}^{sim}$ with k=2 m s^{-1}

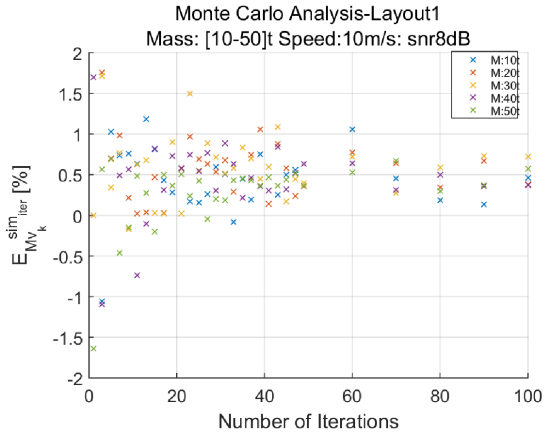

(c) Scatter plot of the percentage relative speed errors $E_{M\,v_k}^{sim}$ with k=10 m s^{-1}

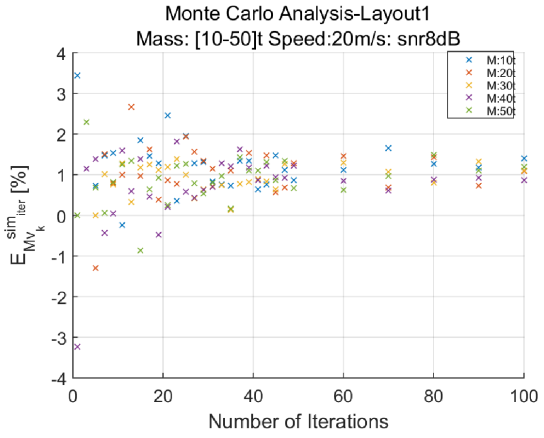

(d) Scatter plot of the percentage relative speed errors $E_{M\,v_k}^{sim}$ with k=20 m s^{-1}

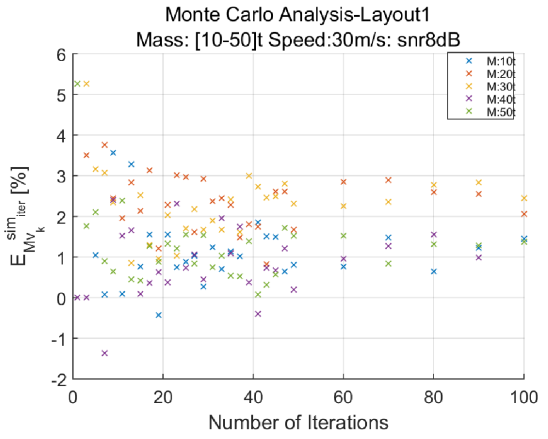

(e) Scatter plot of the percentage relative speed errors $E_{M\,v_k}^{sim}$ with k=30 m s^{-1}

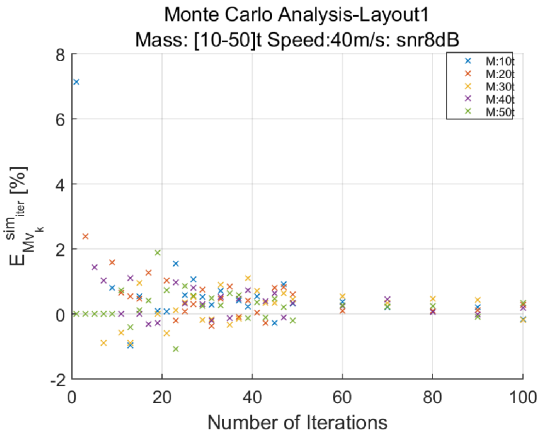

(f) Scatter plot of the percentage relative speed errors $E_{M\,v_k}^{sim}$ with k=40 m s^{-1}

Figure 3.3: Layout1: $E_v^{sim_{iter}}[\%]$ convergence with the Monte Carlo Analysis in all the operating conditions concerning vehicle mass and speed. Focus on error trends for all vehicle mass and a single value of speed (b-f)

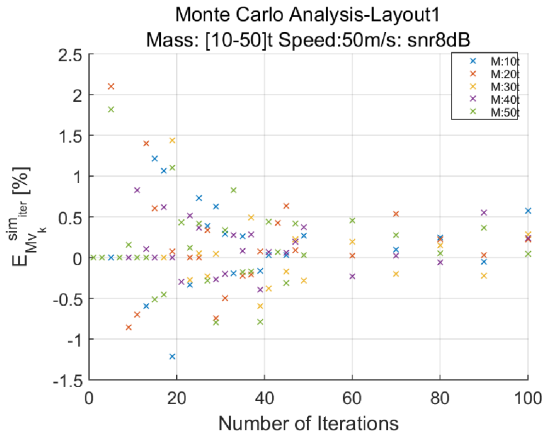

(a) Scatter plot of the percentage relative speed errors $E_M{}_{v_k}^{sim}$ with k=50 m s^{-1}

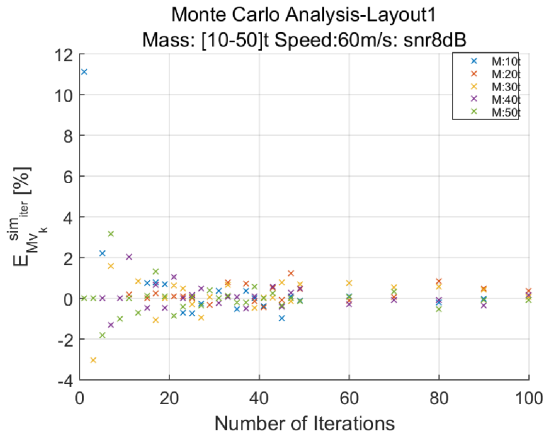

(b) Scatter plot of the percentage relative speed errors $E_M{}_{v_k}^{sim}$ with k=60 m s^{-1}

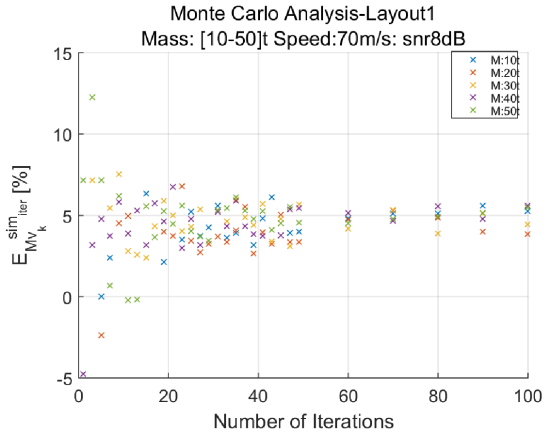

(c) Scatter plot of the percentage relative speed errors $E_M{}_{v_k}^{sim}$ with k=70 m s^{-1}

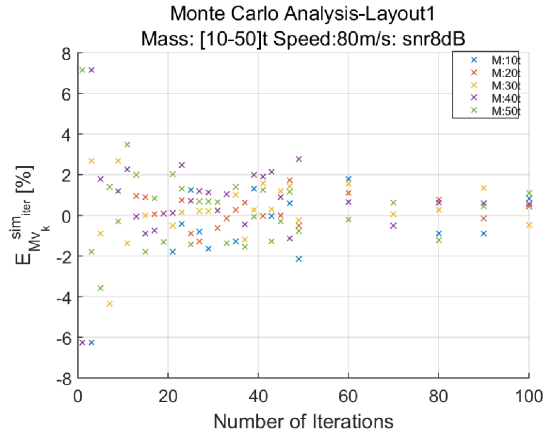

(d) Scatter plot of the percentage relative speed errors $E_M{}_{v_k}^{sim}$ with k=80 m s^{-1}

Figure 3.4: Layout1: Focus on $E_v^{sim_{iter}}[\%]$ trends for each mass and vehicle speed (a-d)

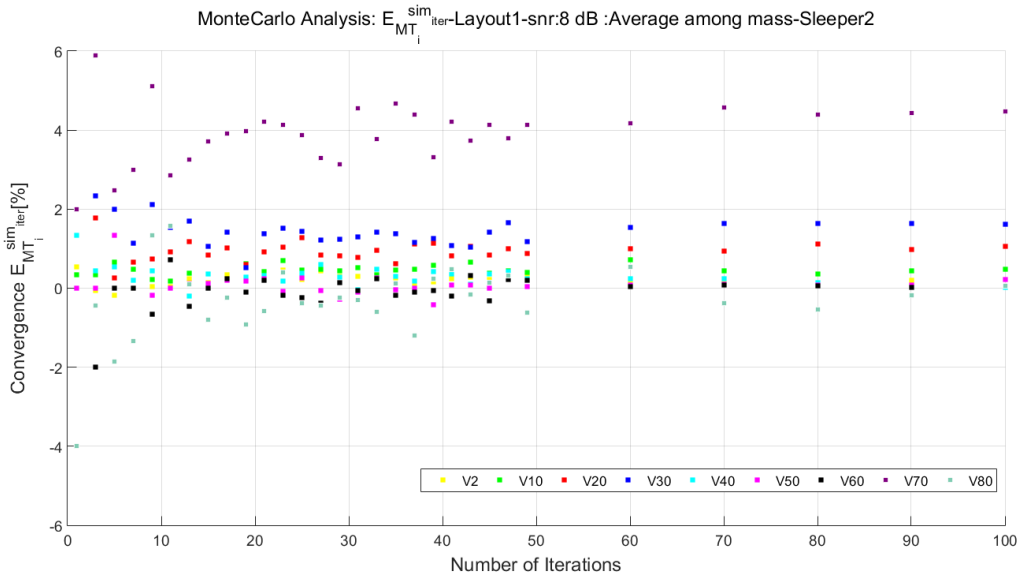

(a) Percentage $Em_{Ti_k}^{sim_{iter}}$ trend with k=(2-80) m s^{-1} on the second measurement sleeper

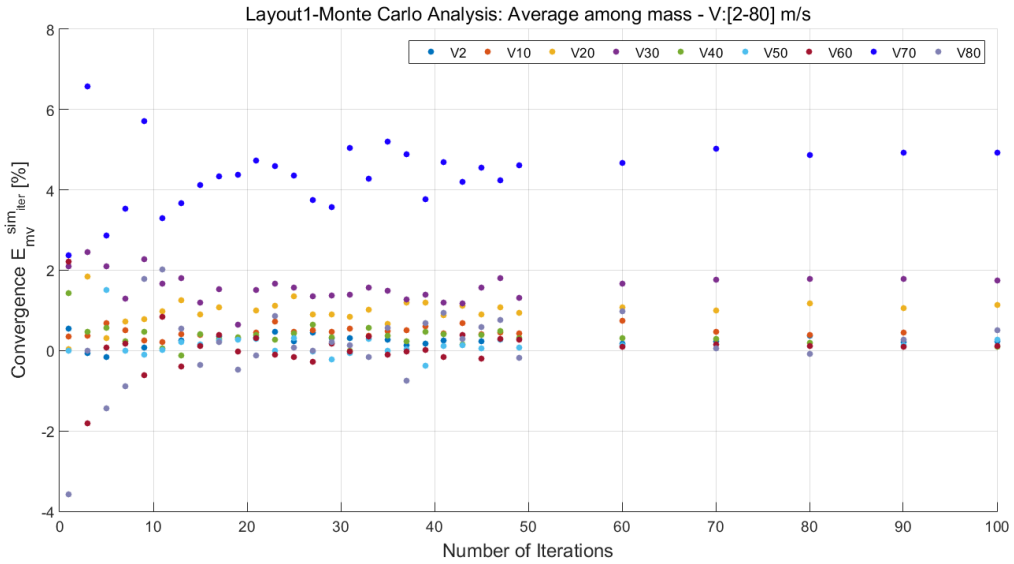

(b) Percentage $Em_{v_k}^{sim_{iter}}$ trend with k=(2-80) m s^{-1}

Figure 3.5: Layout1: Monte Carlo approach-Focus on $Em_{Ti_k}^{sim_{iter}}[\%]$ and $Em_{v_k}^{sim_{iter}}[\%]$ trends for each speed

Fig. 3.5 shows $Em_{Ti_k}^{sim_{iter}}$ and $Em_{v_k}^{sim_{iter}}$ errors. In according with considerations in Fig. 2.4, the accuracy on the speed detection is strictly related to that on the crossing times: indeed, comparing the trend of both errors, their Monte Carlo trends are

quite specular. Same considerations and similar results have been obtained with the other measurement layouts, in which the convergence of the Monte Carlo analysis has been reached, verifying the good operation of the algorithm with a different number of sensing elements and spacing among them. Results have been plotted in the AppendixA, to not overload the reading.

3.1.1 Analysis of the TDA algorithm performance

The Monte Carlo analysis underlines how in all the conditions concerning the vehicle (speed and mass) and measurement layouts (number and spacing among sensing elements) the convergence is reached: this is important in order to establish the good operation of the proposed approach. With the aim at evaluating the algorithm performance a results reportage has been here carried out in correspondence of the reached Monte Carlo convergence: estimation errors on the vehicle speed ${E_{mv}}^{sim_{conv}}[\%]$ and ${E_{M_v}}^{sim_{conv}}[\%]$ are shown in all the operating conditions indicated in Tab. 3.1. Errors on the vehicle speed are strictly linked with those on the crossing times (see Eq. 2.3 and Fig. 2.4). The performance in estimating the vehicle speed are indicated, for both the signal-to-noise ratio of 4 dB and 8 dB. Results are both on the vehicle speed and on the approach abilities to carry out train detection functionalities.

3.1.1.1 Speed detection

Following the estimation errors on the vehicle speed are shown, when the Monte Carlo convergence is reached. Tab. 3.4 summarizes the ${E_{mv}}^{sim_{conv}}[\%]$.

To best understand the effect of the measurement layout on the estimation accuracy, Fig. 3.6 plots the trend of ${E_{mv}}^{sim_{conv}}[\%]$, highlighting an errors amplitude decreasing with an increasing number of sensing elements and spacing among them. More focused, two measurement sleepers involve estimation errors on speed below the 1% if are spaced of 2.4 m, but the best performance is obtained with five measurement sleepers that allow to obtain estimation errors below the 0.4% if are spaced of 2.4m.
Figs. 3.7-3.9 show the trend of ${E_{mv}}^{sim_{conv}}[\%]$ computed among the masses for each layout and the ${E_{M_v}}^{sim_{conv}}[\%]$ values for each speed. All measurement layout involves errors below the 1% for each speed except the one of 70 $\mathrm{m\,s^{-1}}$ that is affected by the intrinsic error due to the accuracy of the sampling time (see Fig. 2.9). Tab.3.5 shows the maximum values of the ${E_{M_v}}^{sim_{conv}}(\%)$ computed for each vehicle speed, with the

indication of vehicle mass corresponding with the maximum error value.

Table 3.4: Convergence $E_{m_v}^{sim_{conv}}[\%]$ reached with 40 iterations (SNR: 8dB)

Layout	Speed $[\mathrm{m\,s^{-1}}]$								
	2	**10**	**20**	**30**	**40**	**50**	**60**	**70**	**80**
1	0.26	0.42	0.87	1.2	0.4	0.12	-0.16	4.69	0.94
2	0.02	0.25	0.35	0.78	0.01	0.18	-0.04	1.22	0.02
3	0.14	0.20	0.29	0.39	0.17	0.03	0.02	1.62	0.39
4	0.08	0.15	0.24	0.41	0.03	0.04	0.05	0.69	0.09
5	0.22	0.34	0.76	1.09	0.15	-0.12	0	2.38	0.2
6	0.11	0.19	0.39	0.44	-0.1	-0.08	-0.03	0.95	-0.11
7	0.05	0.09	0.23	0.34	-0.1	-0.08	-0.03	1.00	-0.1
8	0.05	0.12	0.15	0.29	0.04	0.04	0	0.56	0.02
9	0.18	0.28	0.48	0.94	-0.11	-0.02	-0.24	2.34	0.14
10	0.08	0.17	0.41	0.48	-0.05	0.04	0.02	0.84	0.09
11	0.05	0.12	0.20	0.23	0	-0.03	-0.01	0.85	-0.01
12	0.04	0.06	0.14	0.26	0	0.03	0.03	0.50	0.01
13	0.15	0.20	0.62	0.67	0.08	0.13	0.08	2.00	0.3
14	0.1	0.15	0.30	0.38	-0.03	0.00	0.00	0.70	0
15	0.05	0.05	0.20	0.30	0.02	0.00	0	0.72	0.15
16	0.04	0.07	0.12	0.20	0.03	0.01	0	0.36	0

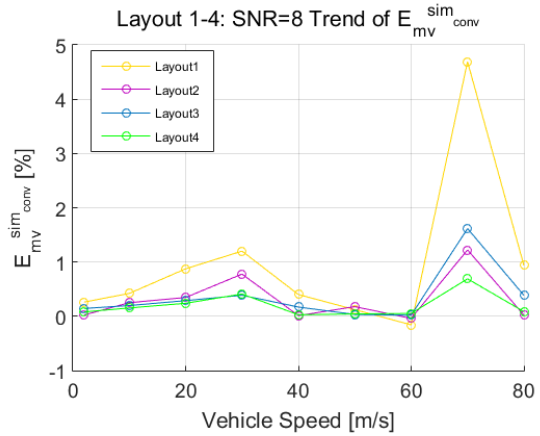

(a) $E_{mv}^{sim_{conv}}(\%)$ trend: the increasing of the spacing between the two sleepers involve a decrement of the estimation error

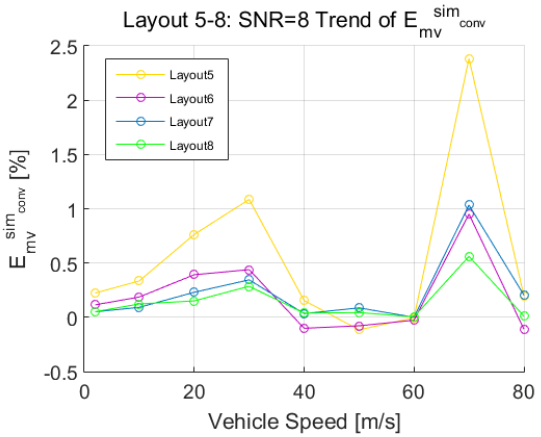

(b) $E_{mv}^{sim_{conv}}(\%)$ trend: the increasing of the spacing among the three sleepers involve a decrement of the estimation error

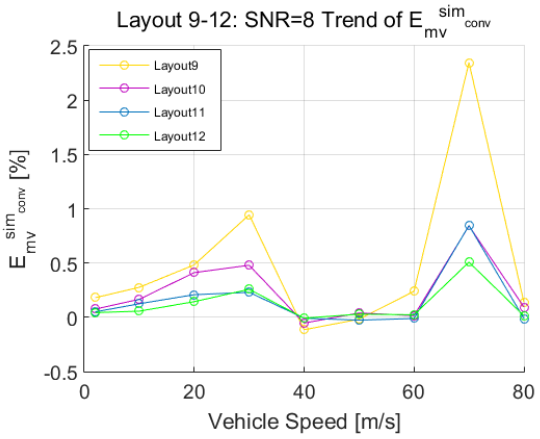

(c) $E_{mv}^{sim_{conv}}(\%)$ trend: the increasing of the spacing among the four sleepers involve a decrement of the estimation error

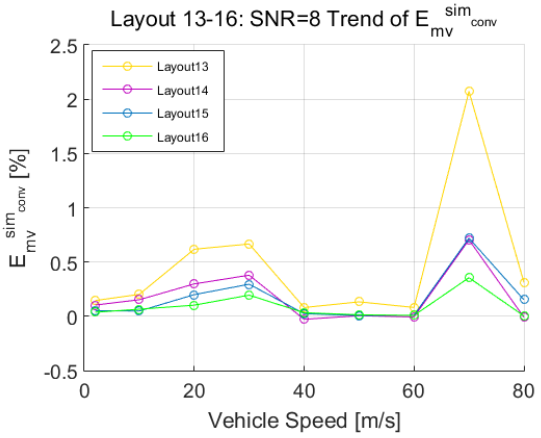

(d) $E_{mv}^{sim_{conv}}(\%)$ trend: the increasing of the spacing among the five sleepers involve a decrement of the estimation error

Figure 3.6: $E_{mv}^{sim_{conv}}(\%)$ trend with different measurement chains: errors are decreasing with the increasing of the number of sensing elements and the spacing among them (from 0.6 m to a maximum one of 2.4 m)

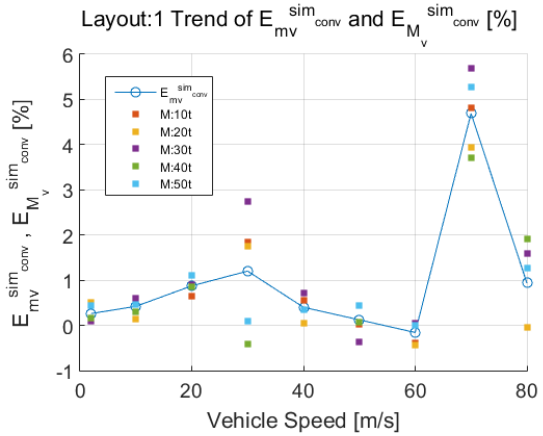

(a) Layout1: $E_{mv}{}^{sim_{conv}}(\%)$ trend (blue line) and $E_{M_v}{}^{sim_{conv}}(\%)$ values

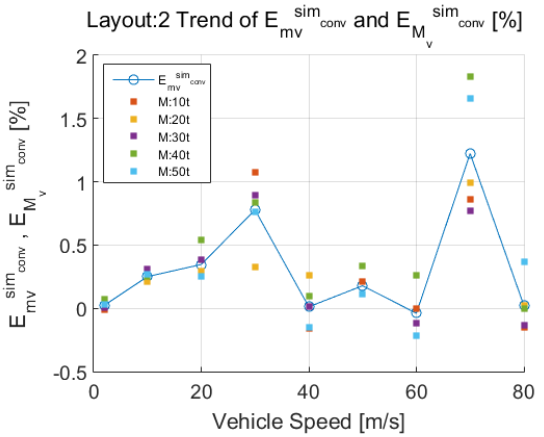

(b) Layout2: $E_{mv}{}^{sim_{conv}}(\%)$ trend (blue line) and $E_{M_v}{}^{sim_{conv}}(\%)$ values

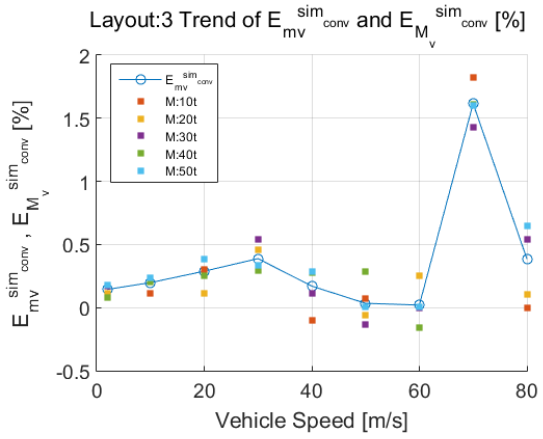

(c) Layout3: $E_{mv}{}^{sim_{conv}}(\%)$ trend (blue line) and $E_{M_v}{}^{sim_{conv}}(\%)$ values

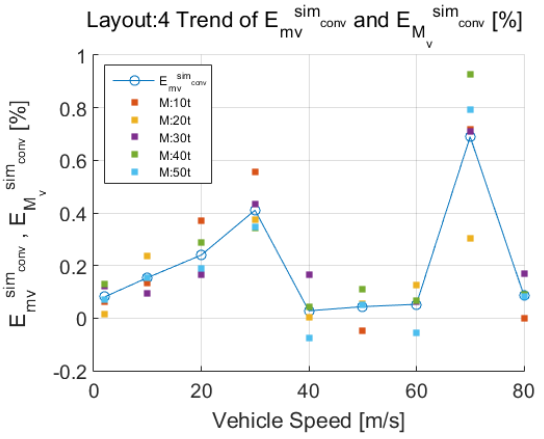

(d) Layout4: $E_{mv}{}^{sim_{conv}}(\%)$ trend (blue line) and $E_{M_v}{}^{sim_{conv}}(\%)$ values

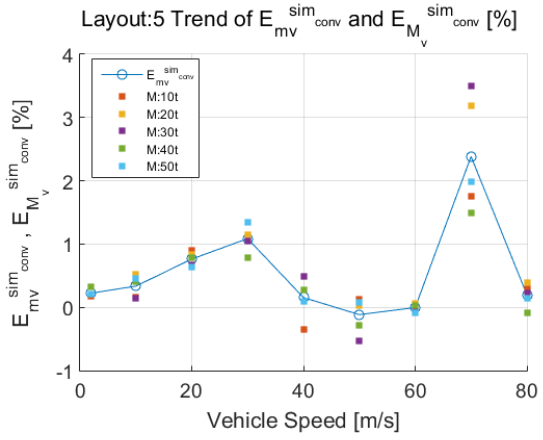

(e) Layout5: $E_{mv}{}^{sim_{conv}}(\%)$ trend (blue line) and $E_{M_v}{}^{sim_{conv}}(\%)$ values

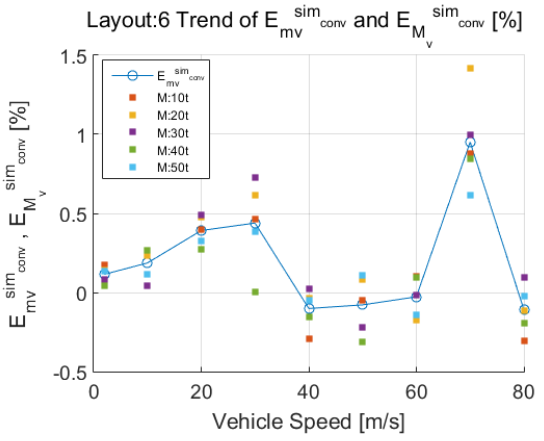

(f) Layout6: $E_{mv}{}^{sim_{conv}}(\%)$ trend (blue line) and $E_{M_v}{}^{sim_{conv}}(\%)$ values

Figure 3.7: $E_{mv}{}^{sim_{conv}}[\%]$ trend and $E_{M_v}{}^{sim_{conv}}[\%]$ values for Layout 1-6: the maximum errors occurs when the vehicle speed is equal to 70 $\mathrm{m\,s^{-1}}$, whose amplitudes are affected also by errors due to the not sufficient accuracy of the sampling time

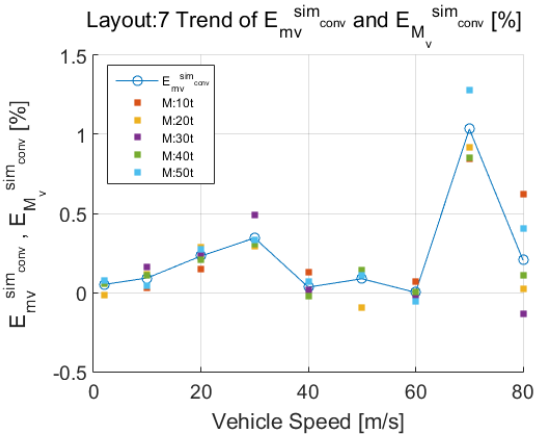

(a) Layout7: $E_{mv}{}^{sim_{conv}}(\%)$ trend (blue line) and $E_{M_v}{}^{sim_{conv}}(\%)$ values

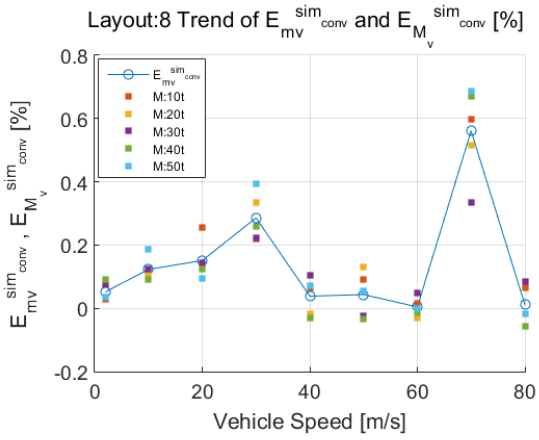

(b) Layout8: $E_{mv}{}^{sim_{conv}}(\%)$ trend (blue line) and $E_{M_v}{}^{sim_{conv}}(\%)$ values

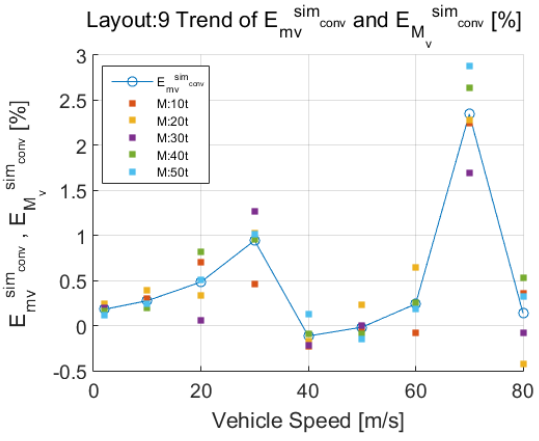

(c) Layout9: $E_{mv}{}^{sim_{conv}}(\%)$ trend (blue line) and $E_{M_v}{}^{sim_{conv}}(\%)$ values

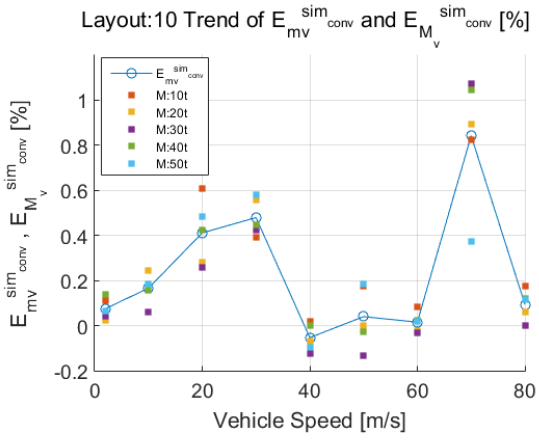

(d) Layout10: $E_{mv}{}^{sim_{conv}}(\%)$ trend (blue line) and $E_{M_v}{}^{sim_{conv}}(\%)$ values

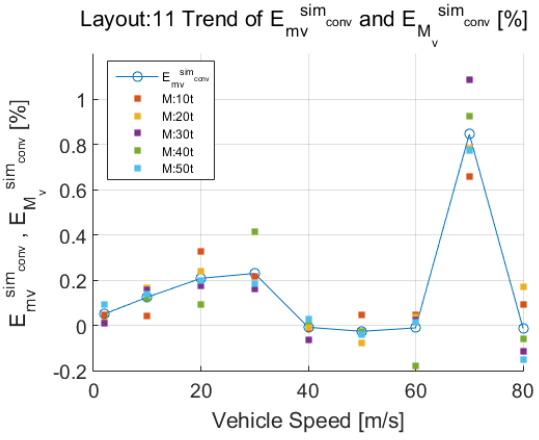

(e) Layout11: $E_{mv}{}^{sim_{conv}}(\%)$ trend (blue line) and $E_{M_v}{}^{sim_{conv}}(\%)$ values

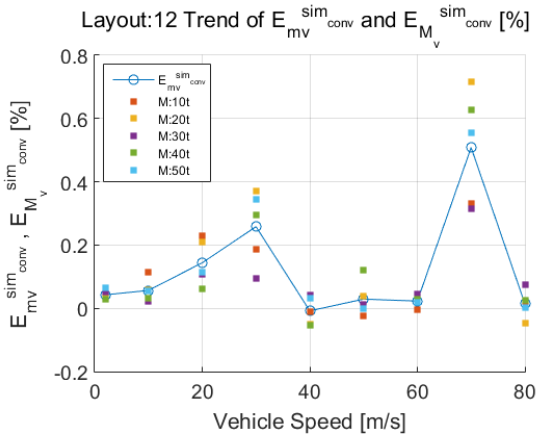

(f) Layout12: $E_{mv}{}^{sim_{conv}}(\%)$ trend (blue line) and $E_{M_v}{}^{sim_{conv}}(\%)$ values

Figure 3.8: $E_{mv}{}^{sim_{conv}}[\%]$ trend and $E_{M_v}{}^{sim_{conv}}[\%]$ values for Layout 7-12: the maximum errors occurs when the vehicle speed is equal to 70 $\mathrm{m\,s^{-1}}$, whose amplitudes are affected also by errors due to the not sufficient accuracy of the sampling time

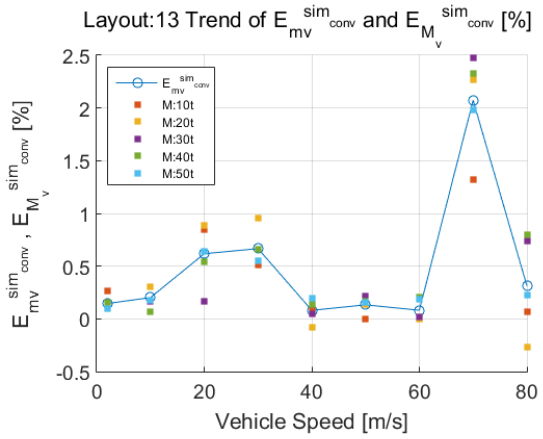

(a) Layout13: $E_{m_v}{}^{sim_{conv}}(\%)$ trend (blue line) and $E_{M_v}{}^{sim_{conv}}(\%)$ values

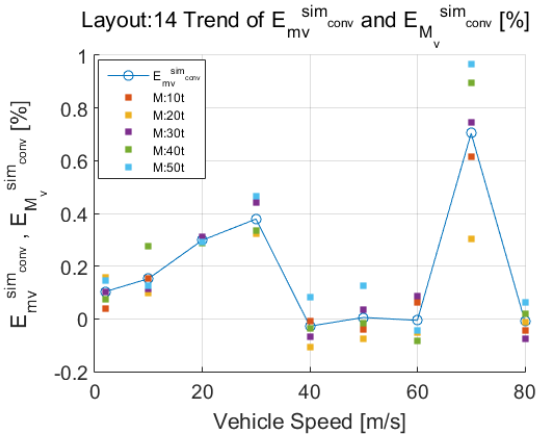

(b) Layout14: $E_{m_v}{}^{sim_{conv}}(\%)$ trend (blue line) and $E_{M_v}{}^{sim_{conv}}(\%)$ values

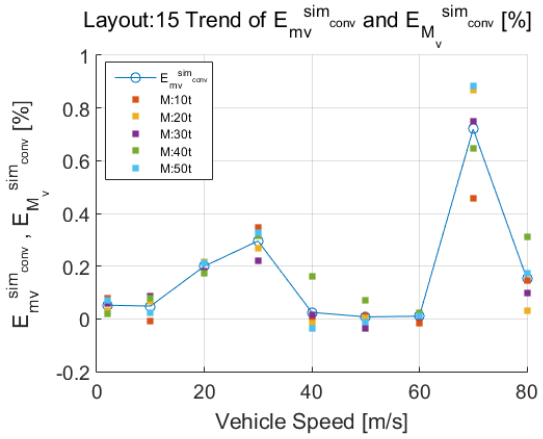

(c) Layout15: $E_{m_v}{}^{sim_{conv}}(\%)$ trend (blue line) and $E_{M_v}{}^{sim_{conv}}(\%)$ values

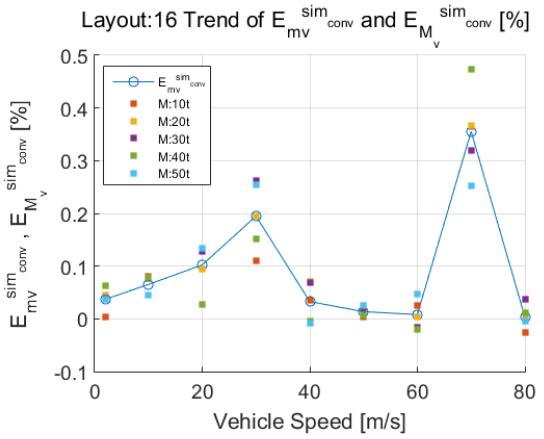

(d) Layout16: $E_{m_v}{}^{sim_{conv}}(\%)$ trend (blue line) and $E_{M_v}{}^{sim_{conv}}(\%)$ values

Figure 3.9: $E_{m_v}{}^{sim_{conv}}[\%]$ trend and $E_{M_v}{}^{sim_{conv}}[\%]$ values for Layout 13-16: the maximum errors occurs when the vehicle speed is equal to 70 $\mathrm{m\,s^{-1}}$, whose amplitudes are affected also by errors due to the not sufficient accuracy of the sampling time

Table 3.5: Maximum ${E_{M_v}}^{sim_{conv}}(\%)$ values computed in the full speed range, with an input SNR of 8 dB

Layout	Speed [m s^{-1}]								
	2	**10**	**20**	**30**	**40**	**50**	**60**	**70**	**80**
1	0.51	0.60	1.1	2.73	0.72	0.44	-0.44	5.69	1.92
	M=20 t	**M=30 t**	**M=50 t**	**M=30 t**	**M=30 t**	**M=20 t**	**M=20 t**	**M=30 t**	**M=40 t**
2	0.07	0.31	0.54	1.07	0.26	0.35	0.26	1.83	0.37
	M=40 t	**M=30 t**	**M=40 t**	**M=10 t**	**M=20 t**	**M=40 t**	**M=40 t**	**M=40 t**	**M=50 t**
3	0.18	0.23	0.39	0.54	0.28	0.28	0.25	1.83	0.65
	M=50 t	**M=50 t**	**M=30 t**	**M=30 t**	**M=50 t**	**M=40 t**	**M=20 t**	**M=10 t**	**M=40 t**
4	0.13	0.24	0.37	0.56	0.17	0.11	0.13	0.93	0.17
	M=40 t	**M=20 t**	**M=10 t**	**M=10 t**	**M=30 t**	**M=40 t**	**M=20 t**	**M=40 t**	**M=30 t**
5	0.32	0.52	0.89	1.35	0.49	0.13	0.06	3.5	0.39
	M=40 t	**M=20 t**	**M=10 t**	**M=50 t**	**M=30 t**	**M=10 t**	**M=20 t**	**M=30 t**	**M=20 t**
6	0.17	0.27	0.49	0.73	-0.29	-0.3	-0.17	1.42	-0.3
	M=10 t	**M=40 t**	**M=30 t**	**M=30 t**	**M=10 t**	**M=40 t**	**M=20 t**	**M=20 t**	**M=10 t**
7	0.08	0.16	0.29	0.49	0.13	0.14	0.07	1.28	0.62
	M=30 t	**M=30 t**	**M=20 t**	**M=30 t**	**M=10 t**	**M=40 t**	**M=10 t**	**M=30 t**	**M=10 t**
8	0.09	0.19	0.26	0.39	0.10	0.13	0.05	0.69	0.08
	M=40 t	**M=50 t**	**M=10 t**	**M=50 t**	**M=30 t**	**M=20 t**	**M=30 t**	**M=50 t**	**M=30 t**
9	0.25	0.40	0.82	1.27	-0.21	0.23	0.65	2.88	0.53
	M=20 t	**M=20 t**	**M=40 t**	**M=30 t**	**M=50 t**	**M=20 t**	**M=20 t**	**M=50 t**	**M=40 t**
10	0.08	0.17	0.41	0.48	-0.05	0.04	0.02	0.84	0.09
	M=40 t	**M=20 t**	**M=10 t**	**M=50 t**	**M=30 t**	**M=50 t**	**M=10 t**	**M=30 t**	**M=10 t**
11	0.09	0.17	0.33	0.41	-0.06	-0.07	-0.17	1.08	0.17
	M=50 t	**M=20 t**	**M=10 t**	**M=40 t**	**M=30 t**	**M=20 t**	**M=40 t**	**M=30 t**	**M=20 t**
12	0.07	0.12	0.23	0.3	-0.05	0.12	0.05	0.72	0.08
	M=50 t	**M=10 t**	**M=10 t**	**M=20 t**	**M=40 t**	**M=40 t**	**M=30 t**	**M=20 t**	**M=30 t**
13	0.26	0.30	0.90	0.96	0.20	0.22	0.20	2.47	0.79
	M=10 t	**M=20 t**	**M=20 t**	**M=20 t**	**M=50 t**	**M=30 t**	**M=40 t**	**M=30 t**	**M=40 t**
14	0.16	0.28	0.31	0.46	-0.11	0.12	0.08	0.97	0.07
	M=20 t	**M=40 t**	**M=30 t**	**M=50 t**	**M=20 t**	**M=50 t**	**M=30 t**	**M=50 t**	**M=30 t**
15	0.08	0.08	0.22	0.35	0.16	0.07	0.02	0.88	0.31
	M=10 t	**M=30 t**	**M=20 t**	**M=10 t**	**M=40 t**	**M=40 t**	**M=20 t**	**M=50 t**	**M=40 t**
16	0.06	0.08	0.13	0.26	0.07	0.03	0.05	0.47	0.04
	M=40 t	**M=10 t**	**M=50 t**	**M=30 t**	**M=20 t**	**M=50 t**	**M=50 t**	**M=40 t**	**M=30 t**

Table 3.6: Convergence of the $E_{m_v}^{sim_{iter}}[\%]$ reached with 40 iterations (SNR: 4dB)

Layout	Speed								
	2	**10**	**20**	**30**	**40**	**50**	**60**	**70**	**80**
1	0.43	2.40	5.84	12.70	2.30	5.80	7.30	27.00	6.50
2	0.27	1.89	3.44	3.70	2.23	2.00	1.08	11.46	2.14
3	0.27	1.40	1.88	3.00	0.83	0.65	2.30	6.80	0.91
4	0.13	0.57	1.55	2.50	-0.40	0.36	0.31	4.76	1.50
5	0.39	2.90	4.40	6.55	2.00	1.06	3.23	15.76	1.20
6	0.22	1.30	2.60	2.65	0.40	-0.33	1.89	8.37	0.60
7	0.12	1.20	1.30	2.14	0.85	0.80	0.50	5.40	1.50
8	0.03	0.28	0.70	1.50	0.40	0.27	0.60	3.27	0.34
9	0.34	1.90	3.34	6.30	1.00	1.69	-0.40	13.84	2.77
10	0.17	0.98	1.82	3.00	1.20	0.35	0.70	7.12	1.20
11	0.06	0.77	1.00	1.38	0.28	-0.095	-0.84	4.39	0.90
12	0.06	0.60	0.93	1.00	0.25	-0.06	0.30	2.74	0.02
13	0.23	0.30	0.56	0.78	0.32	0.43	0.37	2.10	0.38
14	0.12	0.16	0.34	0.29	0.12	0.25	-0.03	0.89	0.05
15	0.08	0.08	0.19	0.32	0.08	0.09	0.05	0.68	0.02
16	0.08	0.07	0.12	0.16	0.05	0.027	0.13	0.43	-0.01

Results are shown also for a SNR of 4 dB to highlight the performance of the approach in very badly conditions. Tab. 3.6 summarizes the results obtained in these operating conditions and highlights how a number of measurement sleepers bigger than three (Layout10-Layout16) may involve estimation errors comparable to those obtained with a lower noise level on the input signal.

In order to best focus the effect of the measurement layout, in terms of the number of sensing elements and spacing among them, Fig. 3.10 shows the trend of $E_{m_v}^{sim_{conv}}(\%)$ studying its shape with the increasing of space among the sensing elements for layout of measurement sleepers equipped of two (Fig. 3.10)a, three (Fig. 3.10b) four (Fig. 3.10c) and five (Fig. 3.10d) measurement sleepers. In particular, although the lower SNR, with five measurement sleepers spaced of almost 1.2 m the $E_{m_v}^{sim_{conv}}(\%)$ are below the 0.5 %.

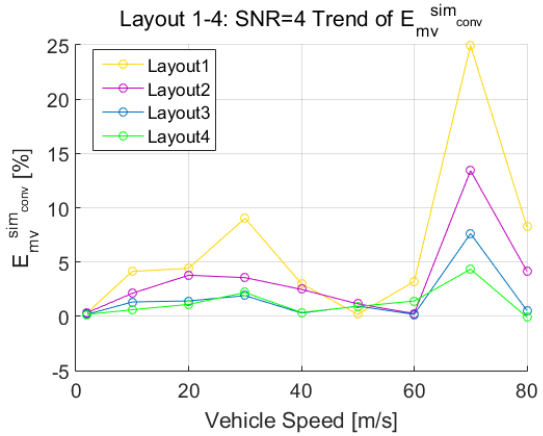

(a) $E_{mv}{}^{sim_{conv}}(\%)$ trend: the increasing of the spacing between the two sleepers involve a decrement of the estimation error

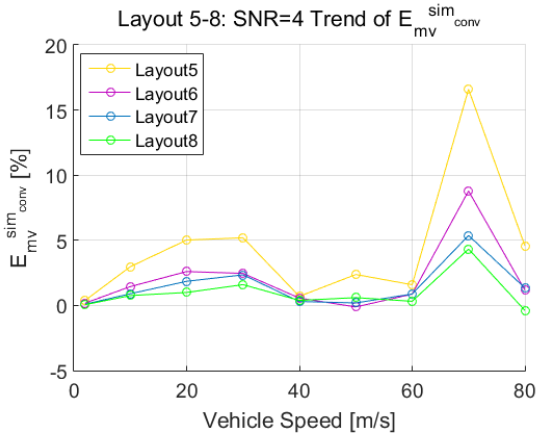

(b) $E_{mv}{}^{sim_{conv}}(\%)$ trend: the increasing of the spacing among the three sleepers involve a decrement of the estimation error

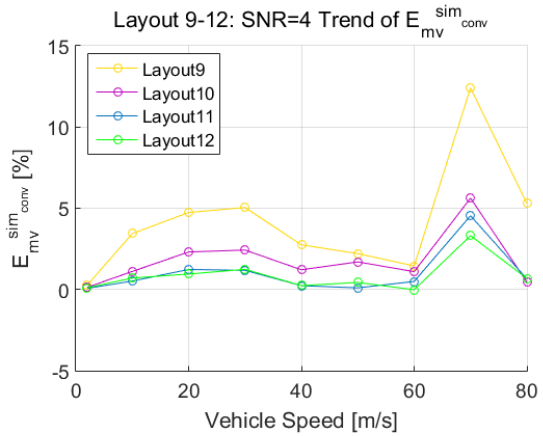

(c) $E_{mv}{}^{sim_{conv}}(\%)$ trend: the increasing of the spacing among the four sleepers involve a decrement of the estimation error

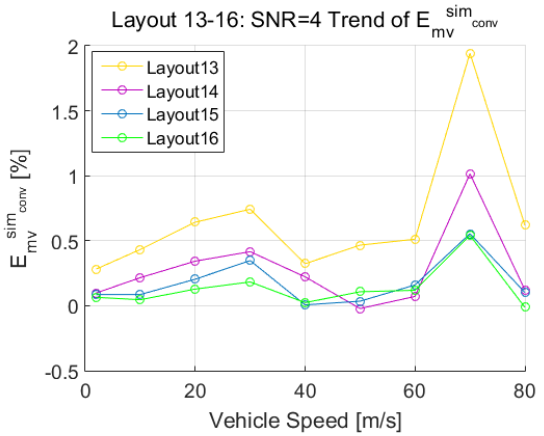

(d) $E_{mv}{}^{sim_{conv}}(\%)$ trend: the increasing of the spacing among the five sleepers involve a decrement of the estimation error

Figure 3.10: $E_{mv}{}^{sim_{conv}}(\%)$ trend with different measurement chains: errors are decreasing with the increasing of the number of sensing elements and the spacing among them (from 0.6 m to a maximum one of 2.4 m)

Following, each values of errors corresponding to the full range of speed and also mass is considered, in order to find for each speed, the maximum estimation error $E_{M_v}{}^{sim_{conv}}(\%)$.

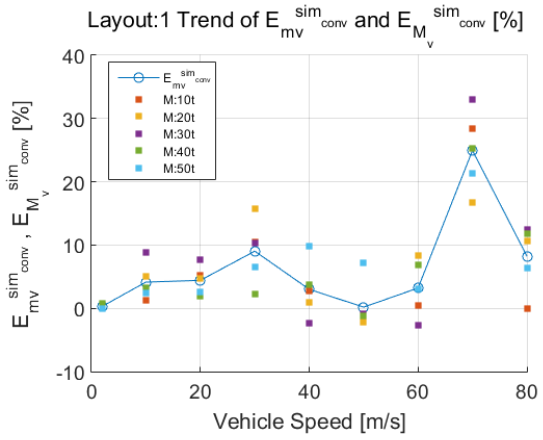

(a) Layout1: $E_{mv}{}^{sim_{conv}}(\%)$ trend (blue line) and $E_{M_v}{}^{sim_{conv}}(\%)$ values

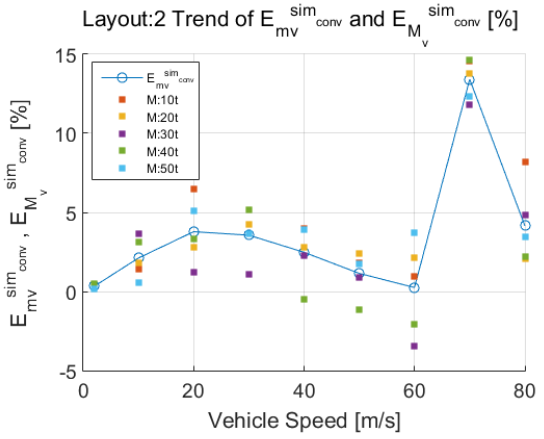

(b) Layout2: $E_{mv}{}^{sim_{conv}}(\%)$ trend (blue line) and $E_{M_v}{}^{sim_{conv}}(\%)$ values

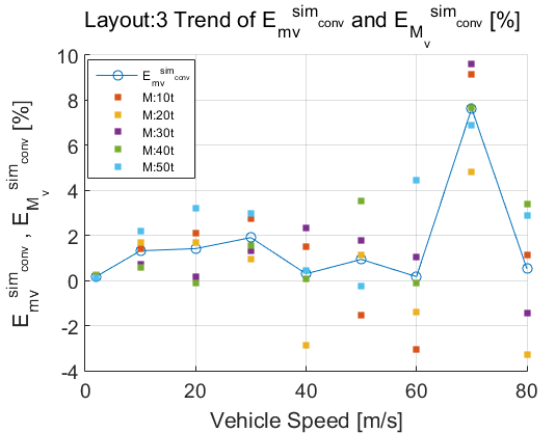

(c) Layout3: $E_{mv}{}^{sim_{conv}}(\%)$ trend (blue line) and $E_{M_v}{}^{sim_{conv}}(\%)$ values

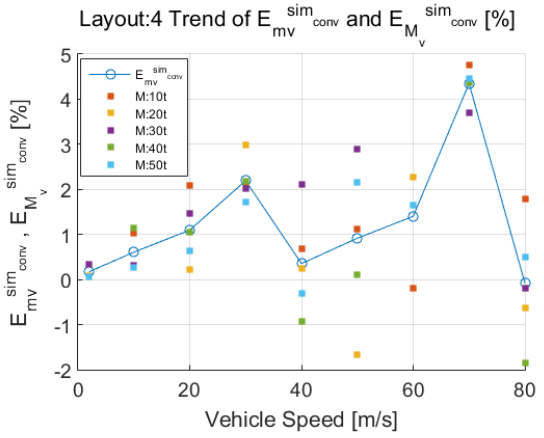

(d) Layout4: $E_{mv}{}^{sim_{conv}}(\%)$ trend (blue line) and $E_{M_v}{}^{sim_{conv}}(\%)$ values

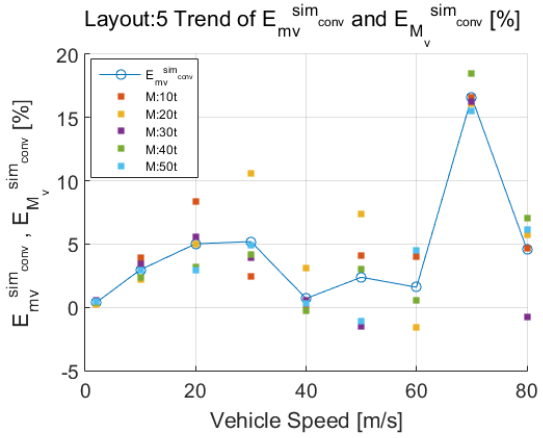

(e) Layout5: $E_{mv}{}^{sim_{conv}}(\%)$ trend (blue line) and $E_{M_v}{}^{sim_{conv}}(\%)$ values

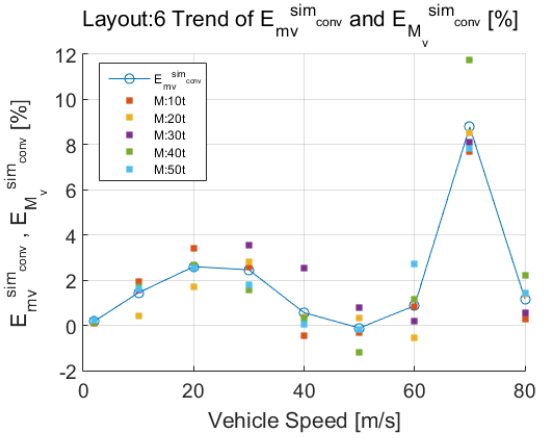

(f) Layout6: $E_{mv}{}^{sim_{conv}}(\%)$ trend (blue line) and $E_{M_v}{}^{sim_{conv}}(\%)$ values

Figure 3.11: $E_{mv}{}^{sim_{conv}}[\%]$ trend and $E_{M_v}{}^{sim_{conv}}[\%]$ values for Layout 1-6: with a SNR of 4 dB errors are huge and the approach is not able to perform accurate estimations

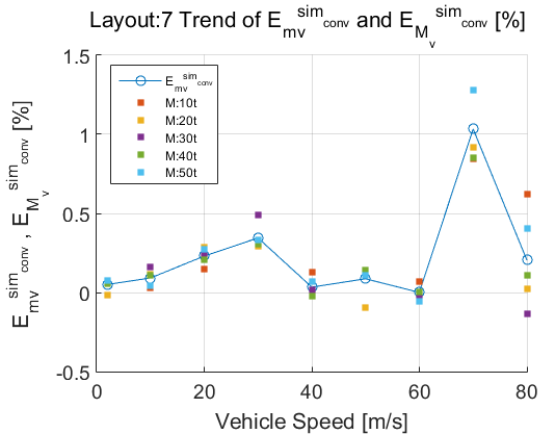

(a) Layout7: $E_{mv}{}^{sim_{conv}}(\%)$ trend (blue line) and $E_{M_v}{}^{sim_{conv}}(\%)$ values

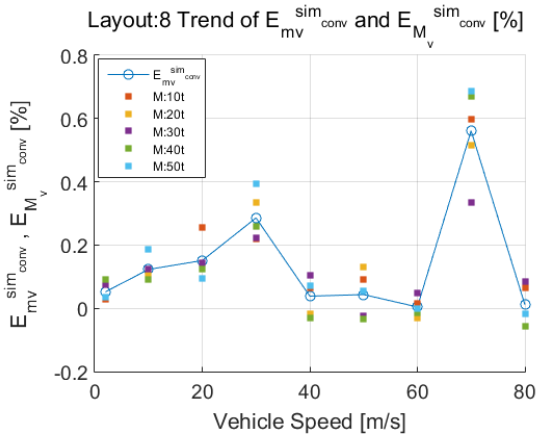

(b) Layout8: $E_{mv}{}^{sim_{conv}}(\%)$ trend (blue line) and $E_{M_v}{}^{sim_{conv}}(\%)$ values

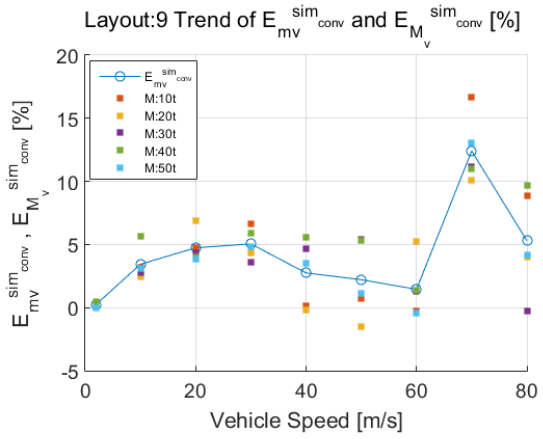

(c) Layout9: $E_{mv}{}^{sim_{conv}}(\%)$ trend (blue line) and $E_{M_v}{}^{sim_{conv}}(\%)$ values

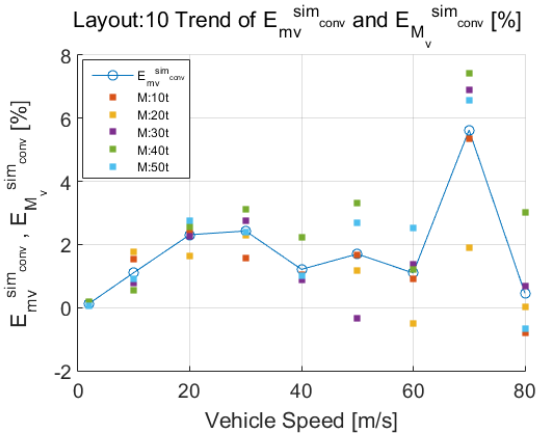

(d) Layout10: $E_{mv}{}^{sim_{conv}}(\%)$ trend (blue line) and $E_{M_v}{}^{sim_{conv}}(\%)$ values

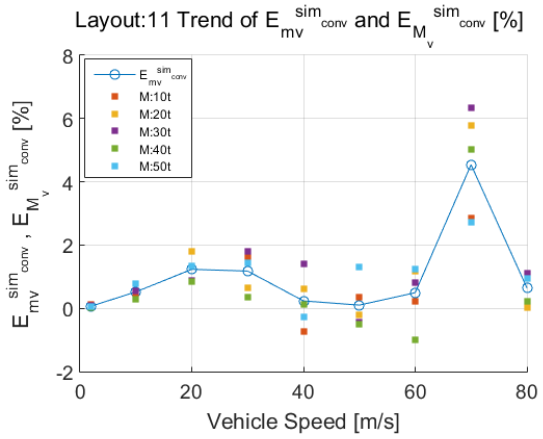

(e) Layout11: $E_{mv}{}^{sim_{conv}}(\%)$ trend (blue line) and $E_{M_v}{}^{sim_{conv}}(\%)$ values

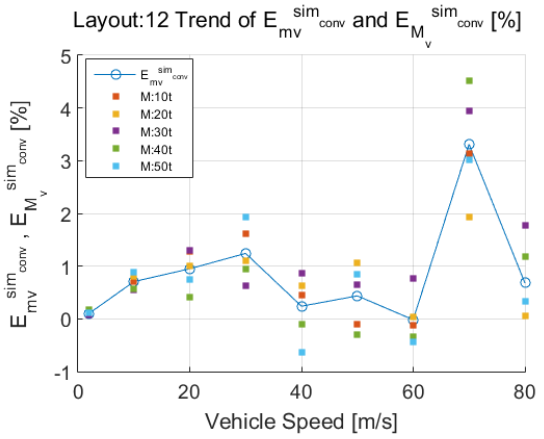

(f) Layout12: $E_{mv}{}^{sim_{conv}}(\%)$ trend (blue line) and $E_{M_v}{}^{sim_{conv}}(\%)$ values

Figure 3.12: $E_{mv}{}^{sim_{conv}}[\%]$ trend and $E_{M_v}{}^{sim_{conv}}[\%]$ values for Layout 7-12: with a SNR of 4 dB errors are big but with the increasing of the number of sensing elements and spacing among them the errors seem to be smaller

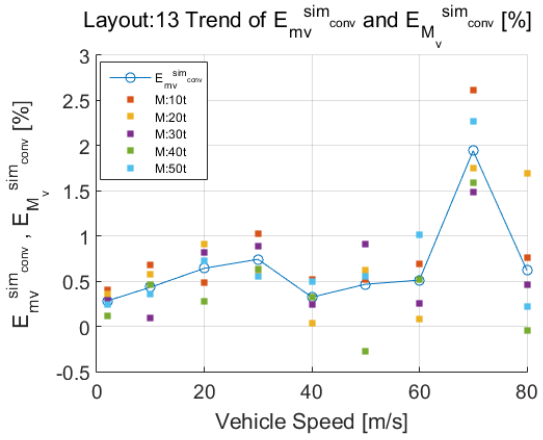

(a) Layout13: $E_{mv}{}^{sim_{conv}}(\%)$ trend (blue line) and $E_{M_v}{}^{sim_{conv}}(\%)$ values

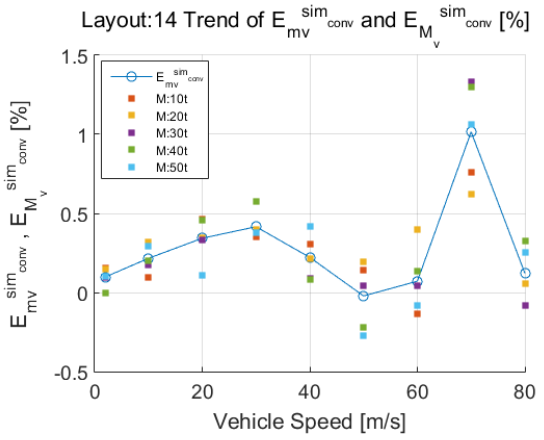

(b) Layout14: $E_{mv}{}^{sim_{conv}}(\%)$ trend (blue line) and $E_{M_v}{}^{sim_{conv}}(\%)$ values

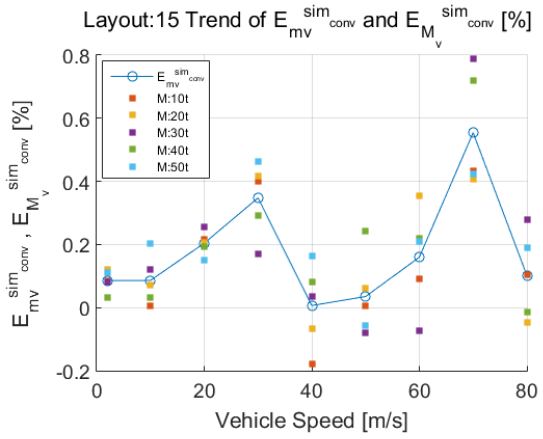

(c) Layout15: $E_{mv}{}^{sim_{conv}}(\%)$ trend (blue line) and $E_{M_v}{}^{sim_{conv}}(\%)$ values

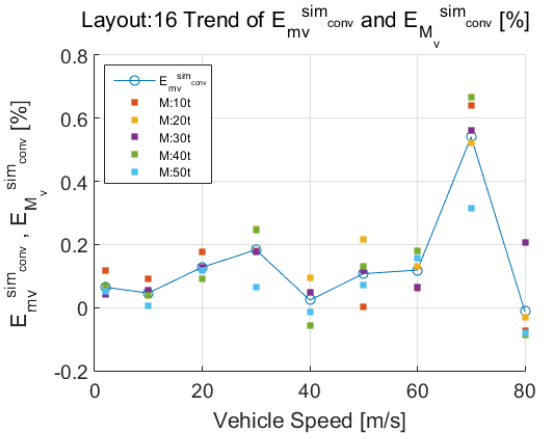

(d) Layout16: $E_{mv}{}^{sim_{conv}}(\%)$ trend (blue line) and $E_{M_v}{}^{sim_{conv}}(\%)$ values

Figure 3.13: $E_{mv}{}^{sim_{conv}}[\%]$ trend and $E_{M_v}{}^{sim_{conv}}[\%]$ values for Layout 13-16: estimation errors are lower thanks to the increasing of the number and spacing among the sensing elements

3.1.1.2 Train detection

The performance of algorithm as vehicle detector is examined in each operating conditions concerning the vehicle and the measurement layout. Results obtained with a SNR of 8 dB and a number of algorithm iterations of 1000 are shown.

$$E_{N\,percent} = \frac{N_{4e}}{N_{iter}} \tag{3.5}$$

where N_{4e} stands for the number of iteration in which the number of the computed crossing axles is not equal to four (number of the Manchester wagon axles) and N_{iter} is the number of algorithm iterations (equal to 1000). Figs. 3.14-3.16 show results on $E_{N\,percent}$ obtained in the full speed and mass ranges, with a SNR of 8 dB and each measurement layouts, highlighting the good operation of the approach in estimating the number of crossing axles within a speed value of 60 m s^{-1}.

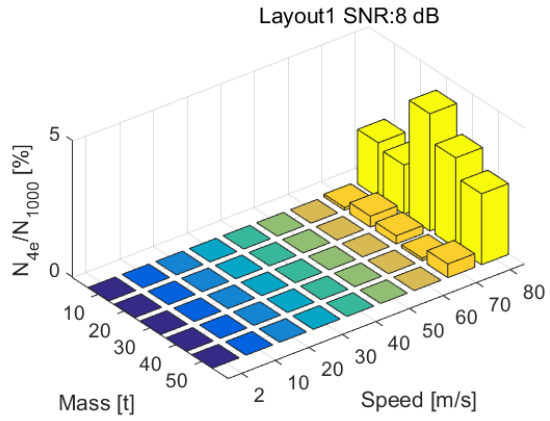

(a) Estimation errors $E_{N\,percent}$ in the full mass and speed range with the Layout 1 and a SNR of 8 dB

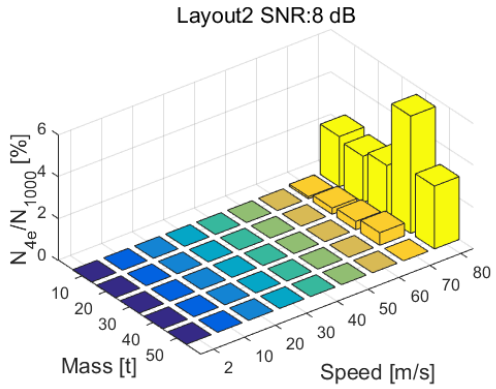

(b) Estimation errors $E_{N\,percent}$ in the full mass and speed range with the Layout 2 and a SNR of 8 dB

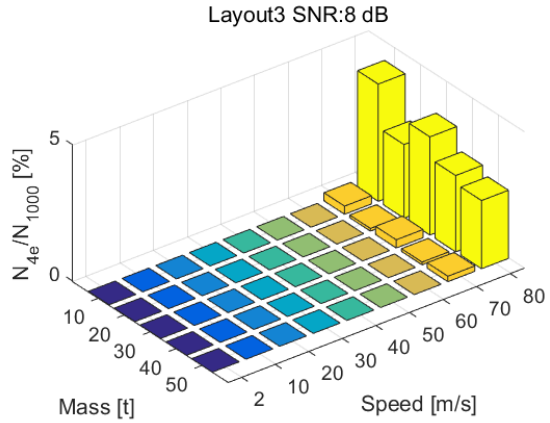

(c) Estimation errors $E_{N\,percent}$ in the full mass and speed range with the Layout 3 and a SNR of 8 dB

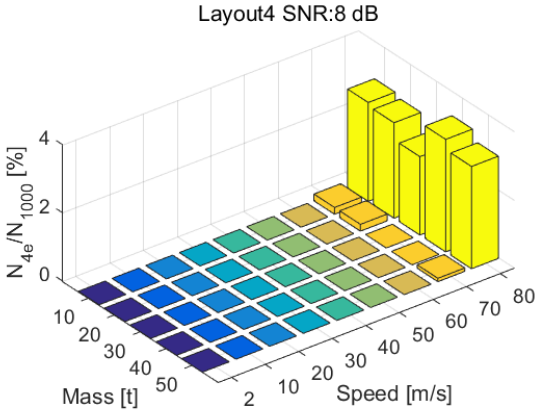

(d) Estimation errors $E_{N\,percent}$ in the full mass and speed range with the Layout 4 and a SNR of 8 dB

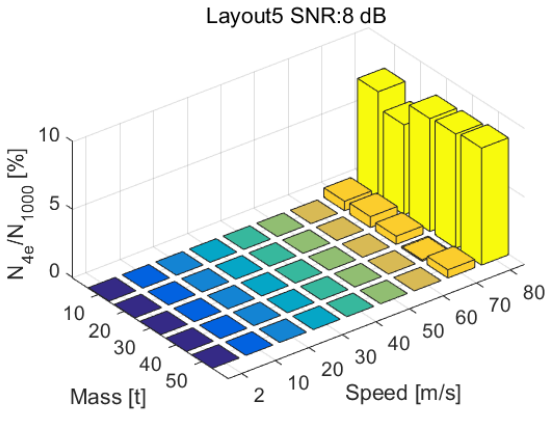

(e) Estimation errors $E_{N\,percent}$ in the full mass and speed range with the Layout 5 and a SNR of 8 dB

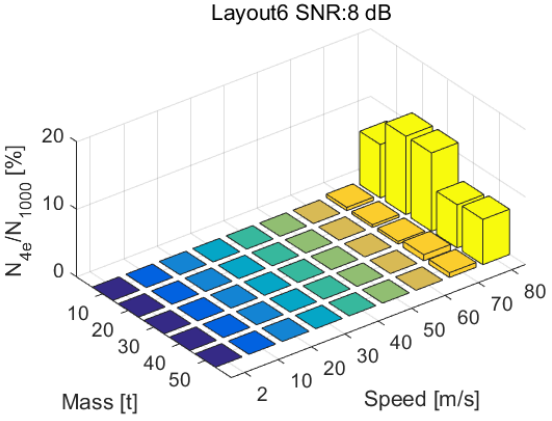

(f) Estimation errors $E_{N\,percent}$ in the full mass and speed range with the Layout 6 and a SNR of 8 dB

Figure 3.14: Estimation errors $E_{N\,percent}$ with Layout 1-6: errors are different from zero for vehicle speed bigger than 60 m s^{-1}

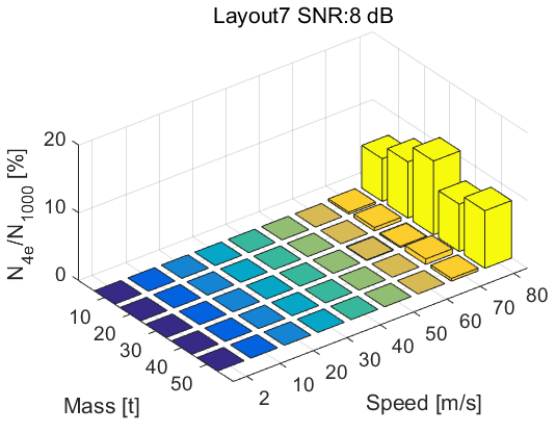

(a) Estimation errors $E_{N\,percent}$ in the full mass and speed range with the Layout 7 and a SNR of 8 dB

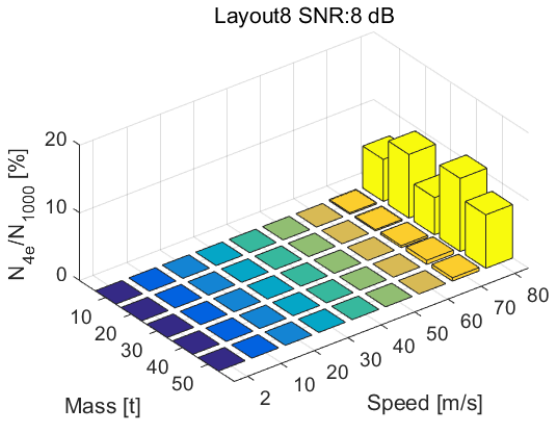

(b) Estimation errors $E_{N\,percent}$ in the full mass and speed range with the Layout 8 and a SNR of 8 dB

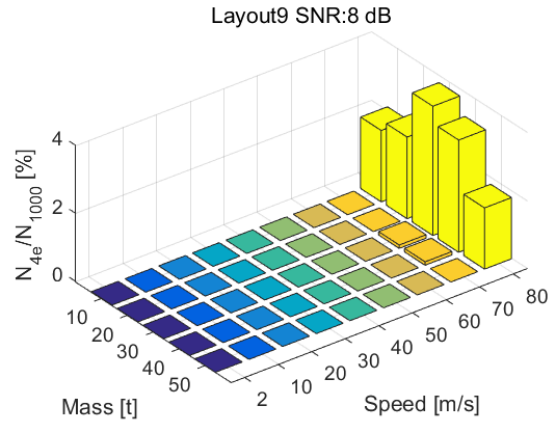

(c) Estimation errors $E_{N\,percent}$ in the full mass and speed range with the Layout 9 and a SNR of 8 dB

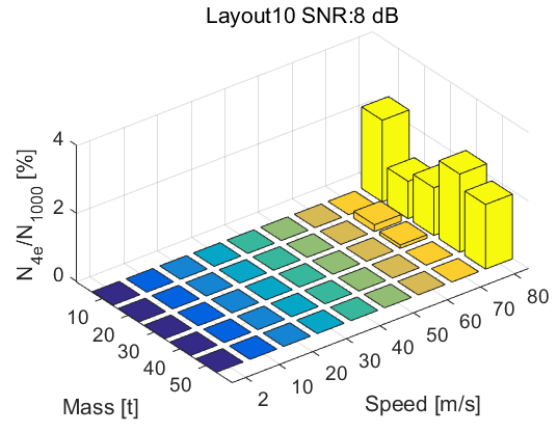

(d) Estimation errors $E_{N\,percent}$ in the full mass and speed range with the Layout 10 and a SNR of 8 dB

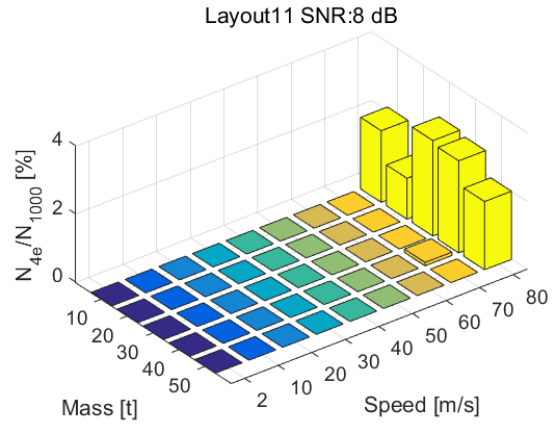

(e) Estimation errors $E_{N\,percent}$ in the full mass and speed range with the Layout 11 and a SNR of 8 dB

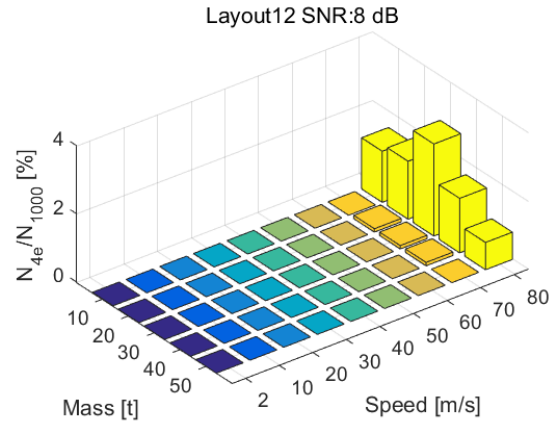

(f) Estimation errors $E_{N\,percent}$ in the full mass and speed range with the Layout 12 and a SNR of 8 dB

Figure 3.15: Estimation errors $E_{N\,percent}$ with Layout 7-12: errors are different from zero for vehicle speed bigger than 60 m s^{-1}

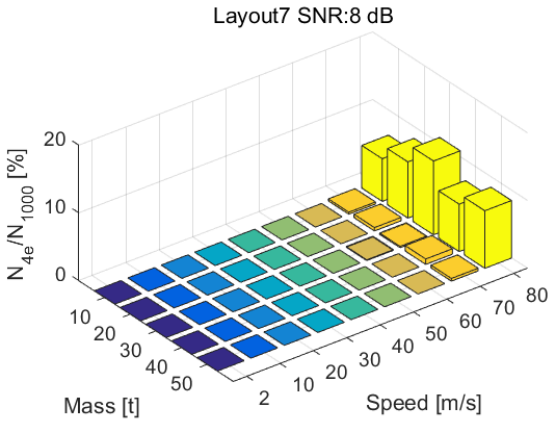

(a) Estimation errors $E_{Npercent}$ in the full mass and speed range with the Layout 13 and a SNR of 8 dB

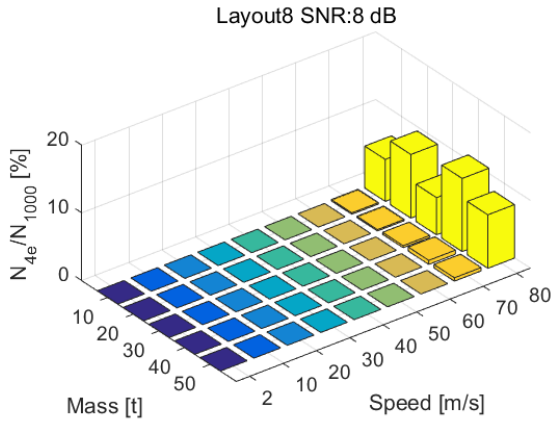

(b) Estimation errors $E_{Npercent}$ in the full mass and speed range with the Layout 14 and a SNR of 8 dB

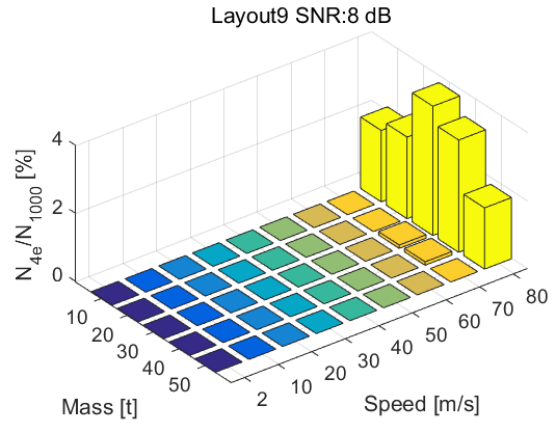

(c) Estimation errors $E_{Npercent}$ in the full mass and speed range with the Layout 15 and a SNR of 8 dB

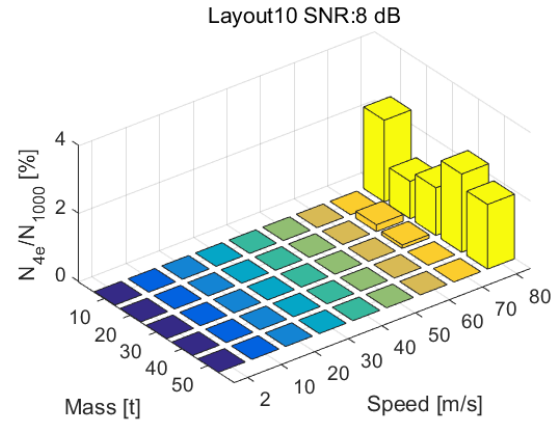

(d) Estimation errors $E_{Npercent}$ in the full mass and speed range with the Layout 16 and a SNR of 8 dB

Figure 3.16: Estimation errors $E_{Npercent}$ with Layout 13-16: errors are different from zero for vehicle speed bigger than 60 m s^{-1}

3.2 Frequency Domain Approach (FDA)

Results on the simulation campaign obtained with the frequency domain algorithm (FDA) are shown, corresponding to different operating conditions concerning the vehicle (see Tab. 3.1) and measurement layouts (see Tab. 3.2). The percentage estimation errors on the vehicle speed and crossing time instants are those indicated in Eq.3.1 and Eq. 3.2 with the difference that the FDA approach allows to detect the time crossing instants of each train axle: to underline this performance, a new error is defined as the maximum crossing time instants one among the ones computed for each train axle:

$$E_{T_{imax}}^{sim_{iter}} = \max_{1 \leq ax \leq 4} (E_{axT_i}^{sim_{iter}}) \tag{3.6}$$

where ax is the index of the train axle and $E_{axT_i}^{sim_{iter}}$ is the crossing time errors on a measurement sleeper referred to the ax-th train axle.
Fig. 3.17 shows a test case in which the trends of $E_{axT_i}^{sim_{iter}}$ are shown: the data have been fit with a spline in order to highlight the trend of errors computed for each crossing axles on the first measurement sleepers (same consideration can be involved for the second one). The maximum errors are those concerning the passage of the first axle and so, in according with Eq. 3.6, these errors are considered. At first the errors

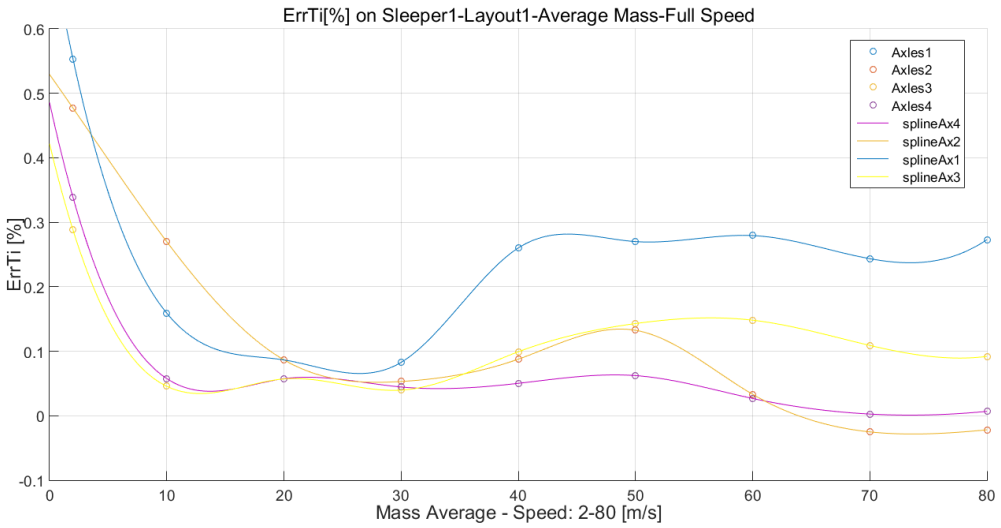

Figure 3.17: $E_{axT_i}^{sim_{iter}}$ trends: the first axle involves the highest estimation error

trends as a function of the Monte Carlo analysis are shown and later the performance of the algorithm are summarized when the convergence is reached.

E.g the Layout1 is considered, which involves two measurement sleepers spaced of 0.6 m. Figs. 3.18-3.20 show the trend of $E_{T_{imax}}^{sim_{iter}}$ on the second sleeper (which involves the bigger errors) in the full speed range (2-80 $\mathrm{m\,s^{-1}}$) and mass one (10-50) t, as a function of the Monte Carlo analysis. Results suggest some considerations on the test case displayed in Fig. 3.18a: it seems that at low vehicle speed as 2 $\mathrm{m\,s^{-1}}$, the algorithm reaches the Monte Carlo convergence just after two algorithm iterations and the errors values are less independent from the vehicle mass than the other test cases, in which there is an overlapping among errors corresponding to different vehicle mass, for each speed (Fig. 3.18b-3.20). To this reason and in order to best localize the number of Monte Carlo iterations involving the convergence, the mean among the errors computed for each mass value is done and displayed in Fig. 3.21.
Error is defined as:

$$Em_{T_{imax}}^{sim_{iter}} = \sum_{M=1}^{n_{mass}} \frac{E_{M}{}_{T_{imax}}^{sim_{iter}}}{n_{mass}} \tag{3.7}$$

where M is the index of the train mass (10-50 t), n_{mass} is the number of simulation parameters about it (5) and $E_{M}{}_{T_{imax}}^{sim_{iter}}$ is the $E_{T_{imax}}^{sim_{iter}}$ computed with the M train mass.

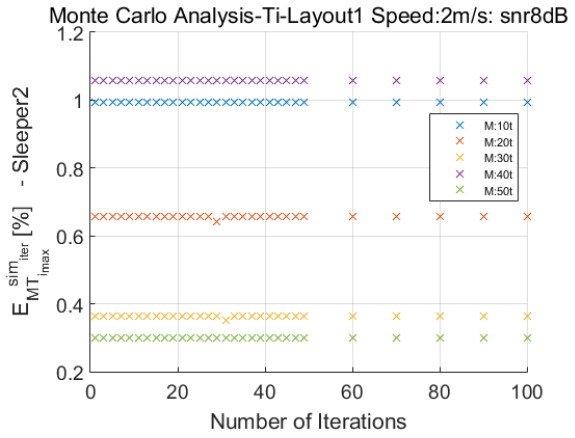

(a) $E_{MT_{imax}}^{sim_{iter}}$ computed for M=(10-50) t and a vehicle speed of 2 $\mathrm{m\,s^{-1}}$: errors are below the 1.1%

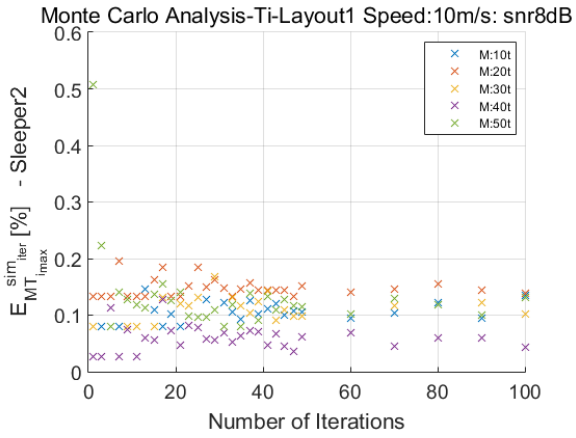

(b) $E_{MT_{imax}}^{sim_{iter}}$ computed for M=(10-50) t and a vehicle speed of 10 $\mathrm{m\,s^{-1}}$: errors are below the 0.2%

Figure 3.18: Layout1: $E_{MT_{imax}}^{sim_{iter}}$ trend in the speed range of (2-10) $\mathrm{m\,s^{-1}}$ and mass M=(10-50) t: errors are depending by the vehicle mass, particularly at low speed of 2 $\mathrm{m\,s^{-1}}$

.

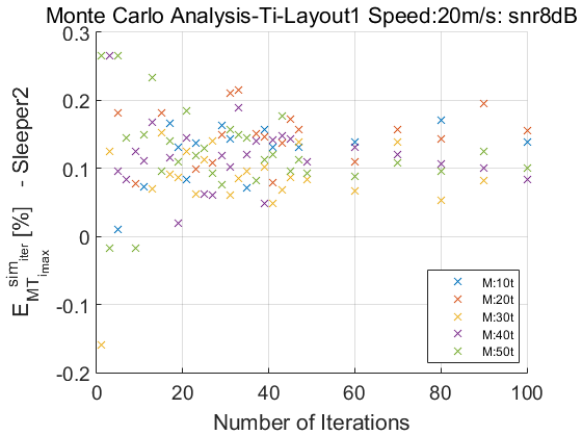

(a) $E_{MT_{imax}}^{sim_{iter}}$ computed for M=(10-50) t and a vehicle speed of 20 $\mathrm{m\,s^{-1}}$: errors are below the 0.3%

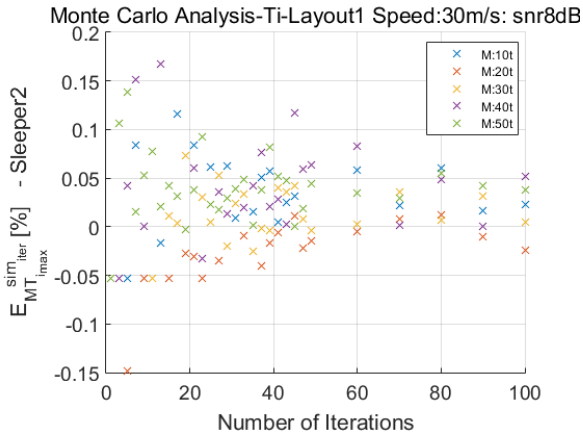

(b) $E_{MT_{imax}}^{sim_{iter}}$ computed for M=(10-50) t and a vehicle speed of 30 $\mathrm{m\,s^{-1}}$: errors are below the 0.2%

Figure 3.19: Layout1: $E_{MT_{imax}}^{sim_{iter}}$ trend in the speed range of (20-30) $\mathrm{m\,s^{-1}}$ and mass M=(10-50) t: errors are not depending by the mass vehicle

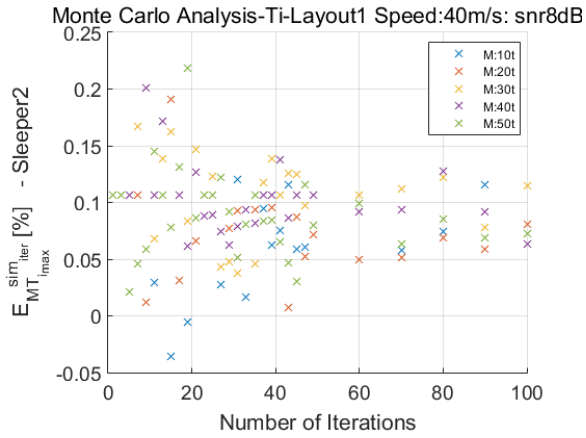

(a) $E_{MT_{imax}}^{sim_{iter}}$ computed for M=(10-50) t and a vehicle speed of 40 m s^{-1}: errors are below the 0.3%

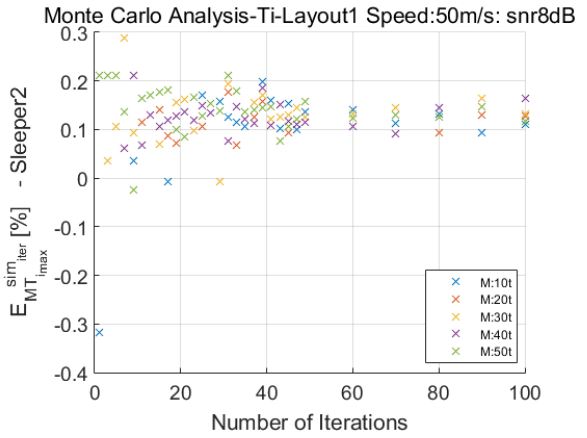

(b) $E_{MT_{imax}}^{sim_{iter}}$ computed for M=(10-50) t and a vehicle speed of 50 m s^{-1}: errors are below the 0.3%

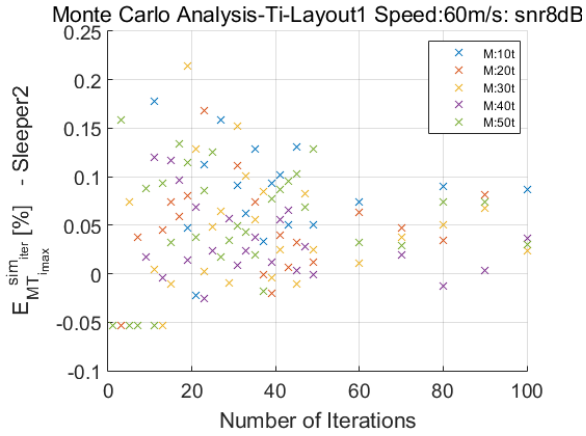

(c) $E_{MT_{imax}}^{sim_{iter}}$ computed for M=(10-50) t and a vehicle speed of 60 m s^{-1}: errors are below the 0.3% and are not depending by the vehicle mass

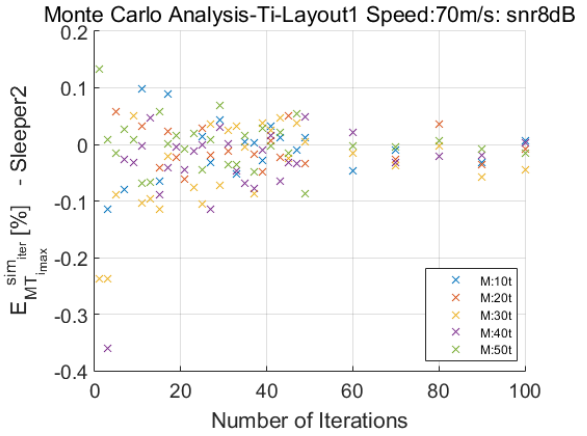

(d) $E_{MT_{imax}}^{sim_{iter}}$ computed for M=(10-50) t and a vehicle speed of 70 m s^{-1}: errors are below the 0.2% and are not depending by the vehicle mass

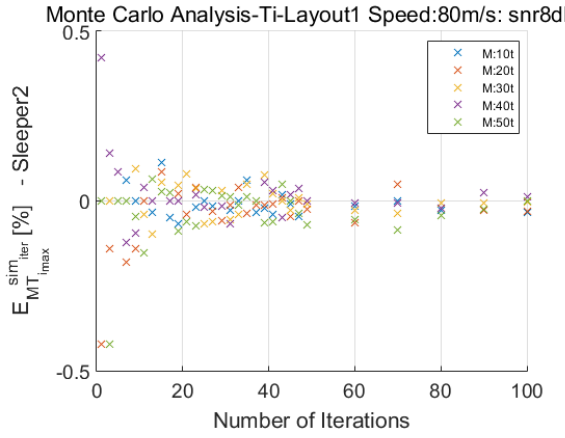

(e) $E_{MT_{imax}}^{sim_{iter}}$ computed for M=(10-50) t and a vehicle speed of 80 m s^{-1}: errors are below the 0.2% and are not depending by the vehicle mass

Figure 3.20: Layout1: $E_{MT_{imax}}^{sim_{iter}}$ trend in the speed range of (40-50) m s^{-1} and mass M=(10-50) t: errors are not depending by the vehicle mass

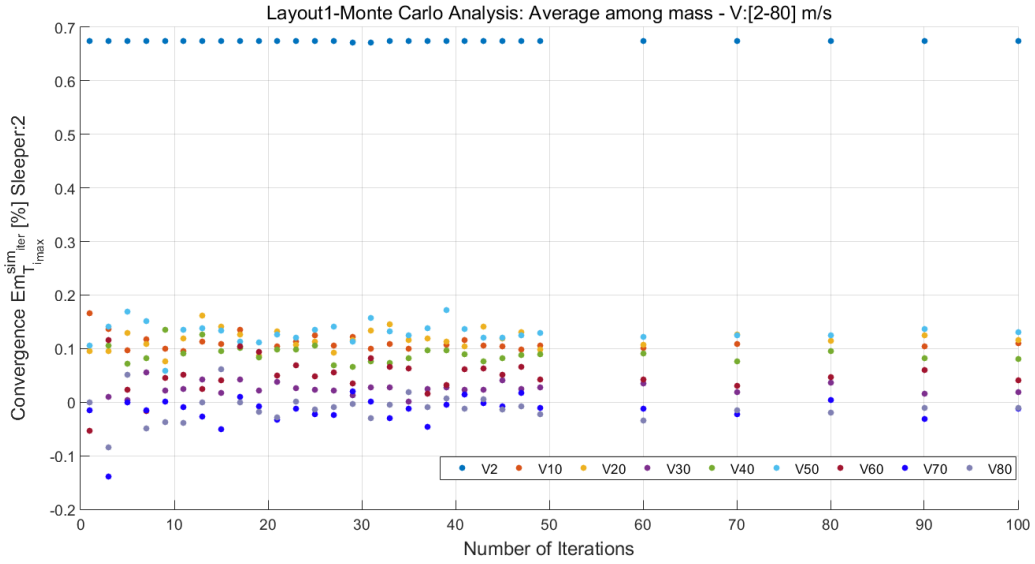

Figure 3.21: Layout1: Monte Carlo analysis on the $Em_{T_{imax}}^{sim_{iter}}$: results show as after 49 iterations the convergence is reached

Fig. 3.21 shows the trend of $Em_{T_{imax}}^{sim_{iter}}$ on the second measurement sleeper (that involves the maximum errors) as a function of the number of algorithm iterations in the Monte Carlo analysis: it underlines how the convergence is reached at about 49 iterations with an exception for the vehicle speed of 2 $\mathrm{m\,s^{-1}}$ in which the errors value has an incredible constant trend just after two algorithm iterations. Considerations and evaluations are also carried out for the speed detection, focusing the attention on the dependence of errors by the vehicle mass and on the convergence of the Monte Carlo analysis. More focused, $E_{M_v}^{sim_{iter}}$ (see Eq. 3.3) and $\mathbf{Em}_{v_k}^{sim_{iter}}$(see Eq. 3.4) are shown, highlighting the not considerable dependence by the vehicle mass (Figs. 3.22-3.23) and the good operation of the approach since the convergence of the Monte Carlo analysis is reached(Fig. 3.24).

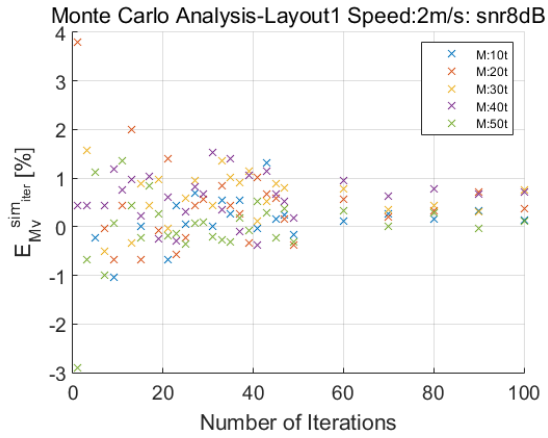

(a) Percentage $E_{M_{v_k}}^{sim_{iter}}$ (with k=2 m s^{-1})

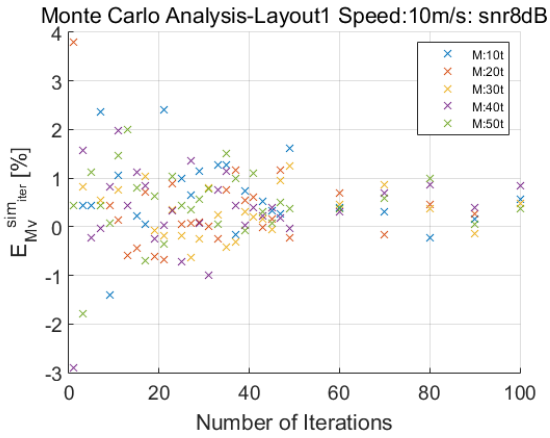

(b) Percentage $E_{M_{v_k}}^{sim_{iter}}$ (with k=10 m s^{-1})

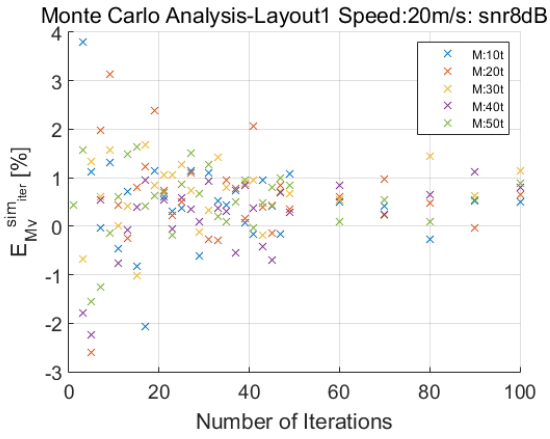

(c) Percentage $E_{M_{v_k}}^{sim_{iter}}$ (with k=20 m s^{-1})

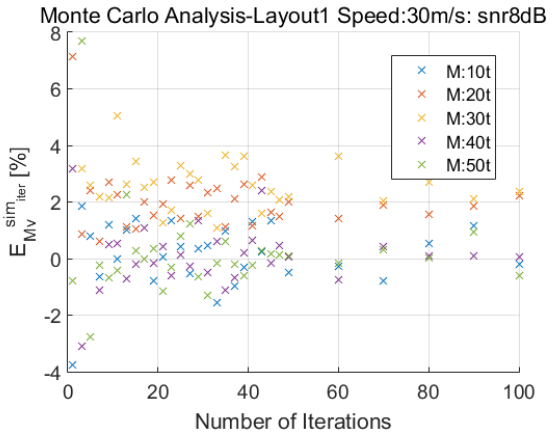

(d) Percentage $E_{M_{v_k}}^{sim_{iter}}$ (with k=30 m s^{-1})

Figure 3.22: Layout1: Speed Estimation-Monte Carlo Analysis with k=(2-30) m s^{-1}, there is no a correlation between errors and the car body mass

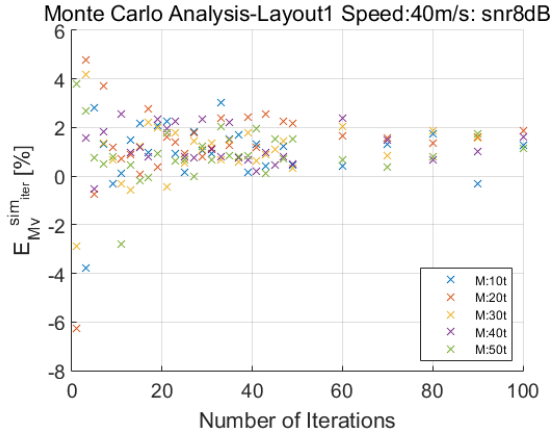

(a) Percentage $E_{M}{}_{v_k}^{sim_{iter}}$ (with k=40 m s^{-1})

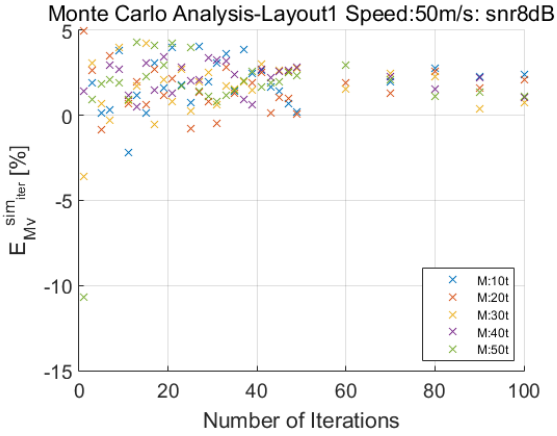

(b) Percentage $E_{M}{}_{v_k}^{sim_{iter}}$ (with k=50 m s^{-1})

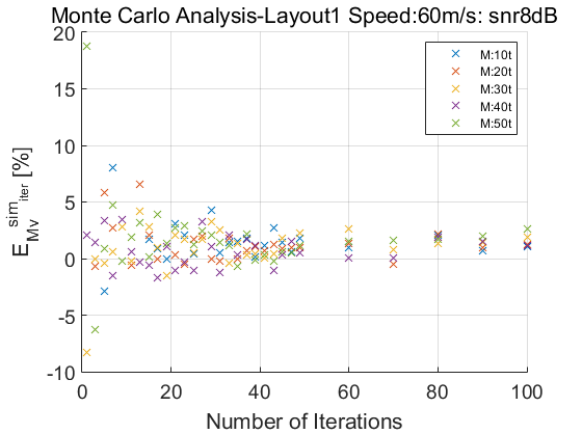

(c) Percentage $E_{M}{}_{v_k}^{sim_{iter}}$ (with k=60 m s^{-1})

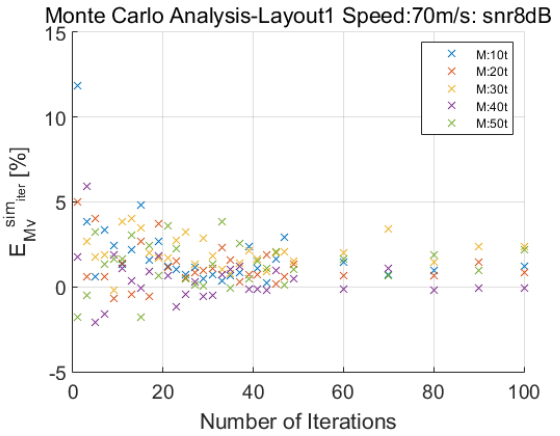

(d) Percentage $E_{M}{}_{v_k}^{sim_{iter}}$ (with k=70 m s^{-1})

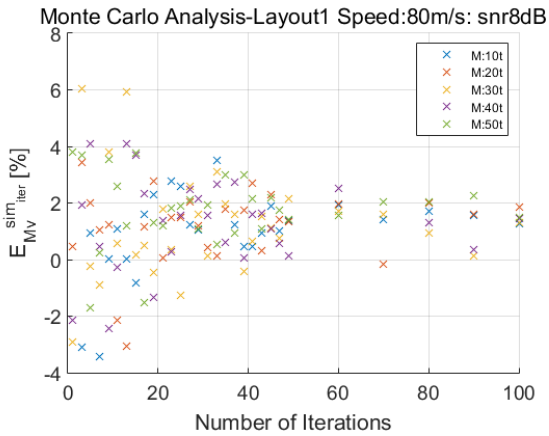

(e) Percentage $E_{M}{}_{v_k}^{sim_{iter}}$ (with k=80 m s^{-1})

Figure 3.23: Layout1: Speed Estimation-Monte Carlo Analysis with k=(40-80) m s^{-1},there is no a correlation between errors and the car body mass

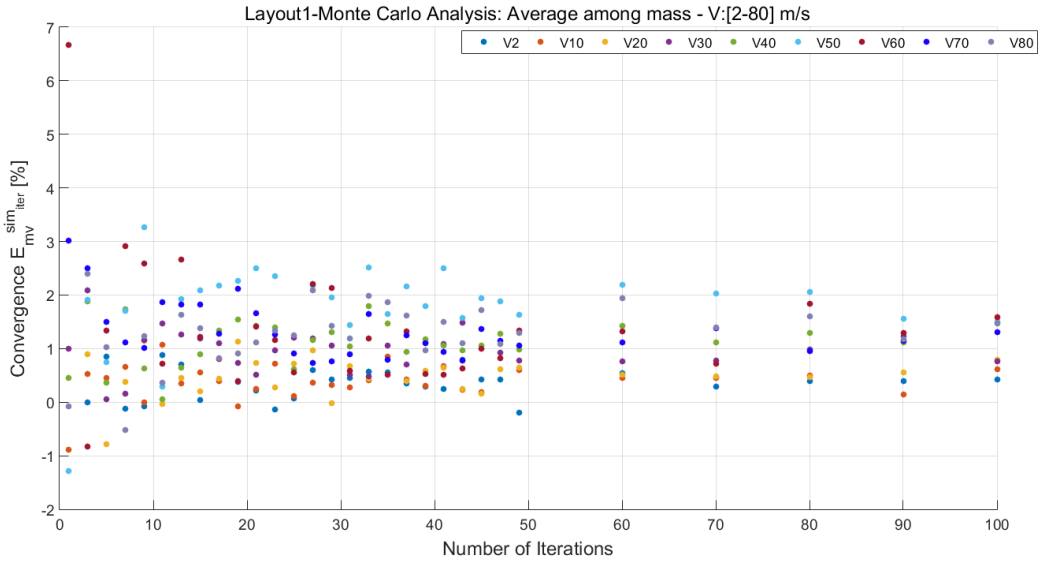

Figure 3.24: Layout1: Monte Carlo convergence of $\mathbf{Em}_{v_k}^{sim_{iter}}$ reached at about 49 iterations

Fig. 3.24 shows the trend of $\mathbf{Em}_{v_k}^{sim_{iter}}$ as a function of the algorithm iterations, highlighting a convergence reached at 49 iterations.
Results have been reported with the other measurement layouts to focus the trend of the estimation errors as a function of the number and spacing among the sensing elements. Layout 2 is considered because it involves accurate estimations (but same good performance have been obtained with the others measurement layouts, see AppendixB) with an occupied space of 1.2 m .

Layout2

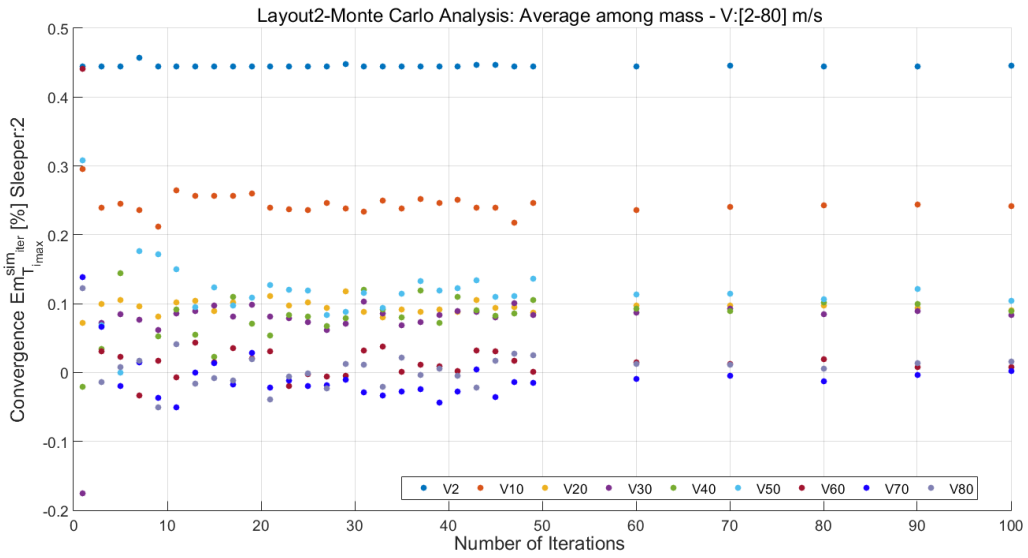

Figure 3.25: Layout2: Monte Carlo analysis on the $Em^{sim_{iter}}_{T_{imax}}$: results show as after 49 iterations the convergence is reached

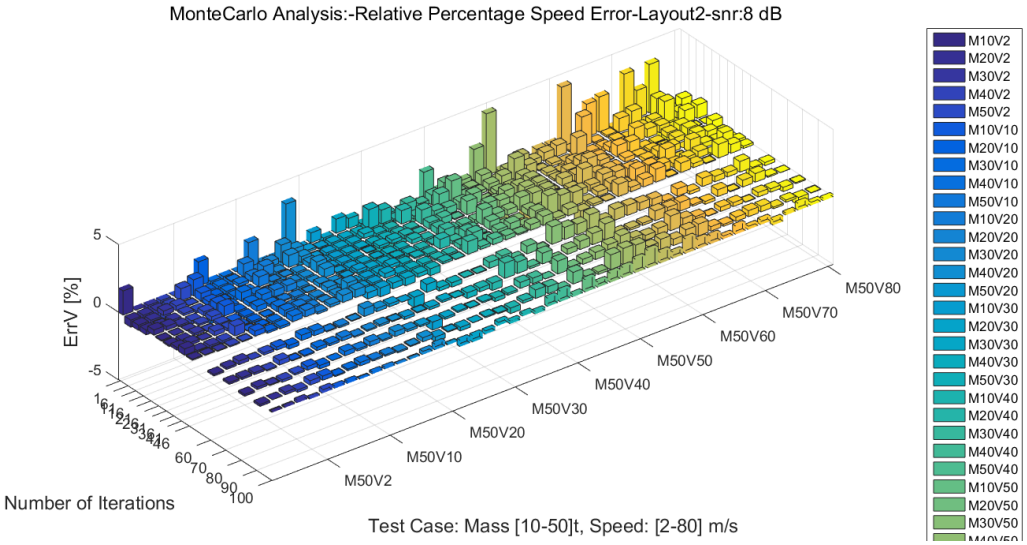

Figure 3.26: Layout2: Percentage $E_V^{sim_{iter}}$ trend in all speed and mass range: results highlight how, for each speed, the value of mass vehicle not involves a relevant effect on the errors

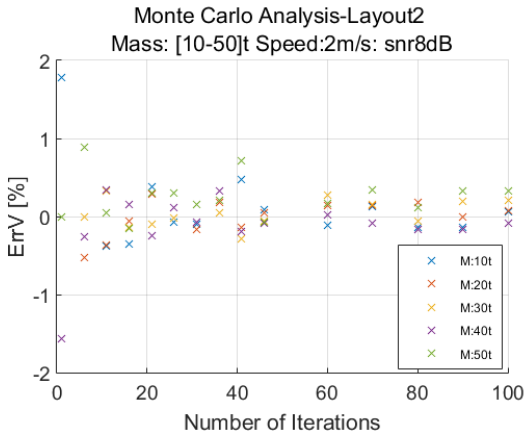

(a) Percentage $E_{M}{}_{v_k}^{sim_{iter}}$ (with k=2 m s^{-1})

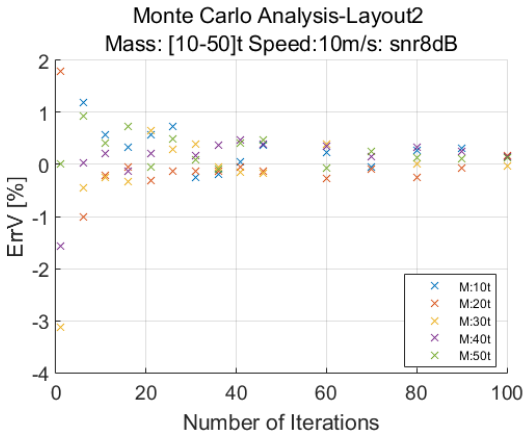

(b) Percentage $E_{M}{}_{v_k}^{sim_{iter}}$ (with k=10 m s^{-1})

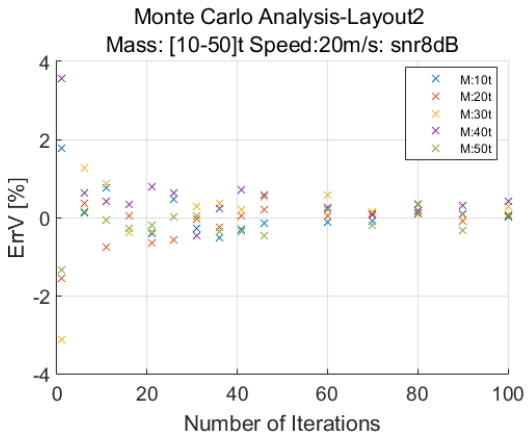

(c) Percentage $E_{M}{}_{v_k}^{sim_{iter}}$ (with k=20 m s^{-1})

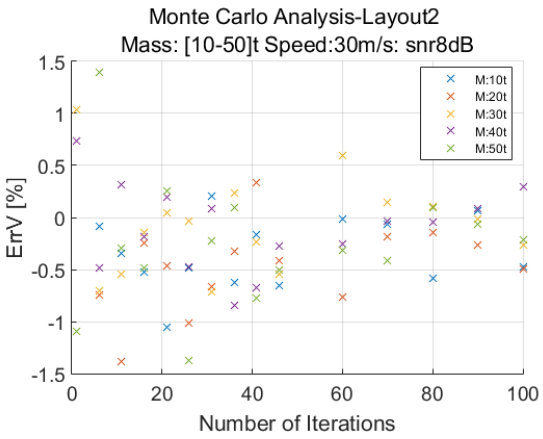

(d) Percentage $E_{M}{}_{v_k}^{sim_{iter}}$ (with k=30 m s^{-1})

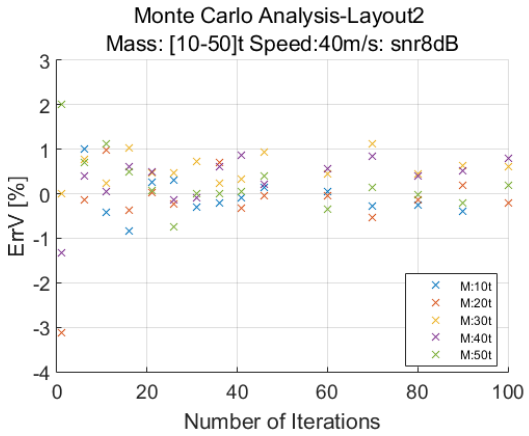

(e) Percentage $E_{M}{}_{v_k}^{sim_{iter}}$ (with k=40 m s^{-1})

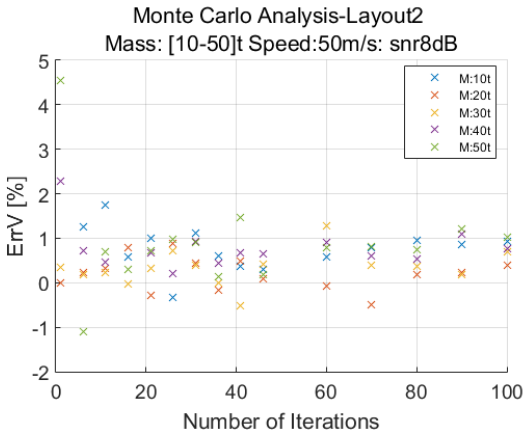

(f) Percentage $E_{M}{}_{v_k}^{sim_{iter}}$ (with k=50 m s^{-1})

Figure 3.27: Layout2: Speed Estimation-Monte Carlo Analysis on $E_{M}{}_{v_k}^{sim_{iter}}$ with k=(2-50) m s^{-1}

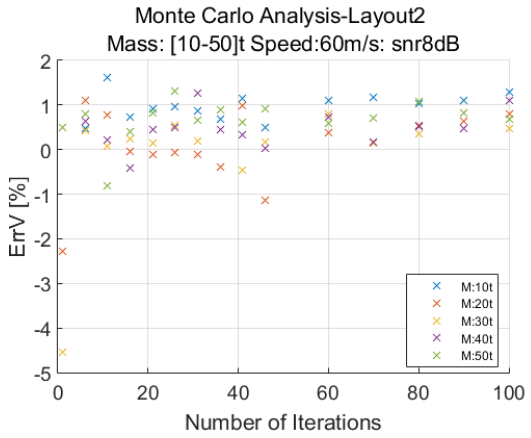

(a) Percentage $E_{M}{}_{v_k}^{sim_{iter}}$ (with k=60 m s^{-1})

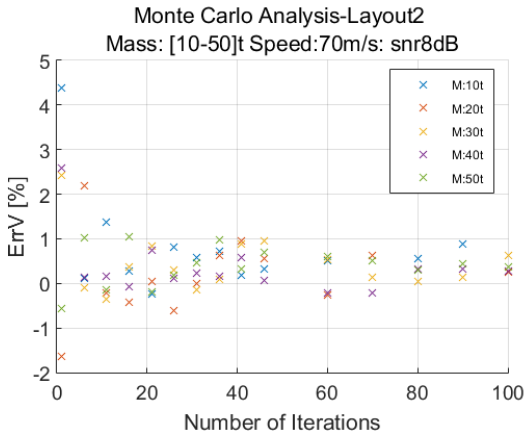

(b) Percentage $E_{M}{}_{v_k}^{sim_{iter}}$ (with k=70 m s^{-1})

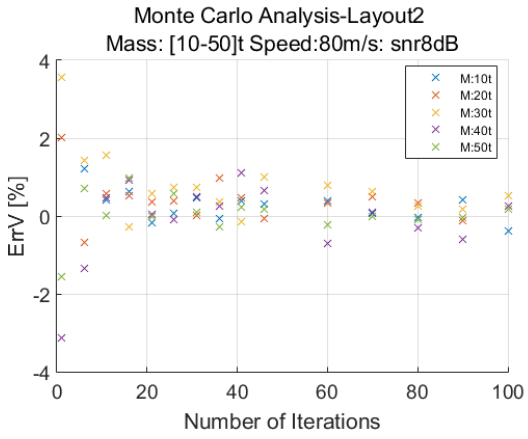

(c) Percentage $E_{M}{}_{v_k}^{sim_{iter}}$ (with k=80 m s^{-1})

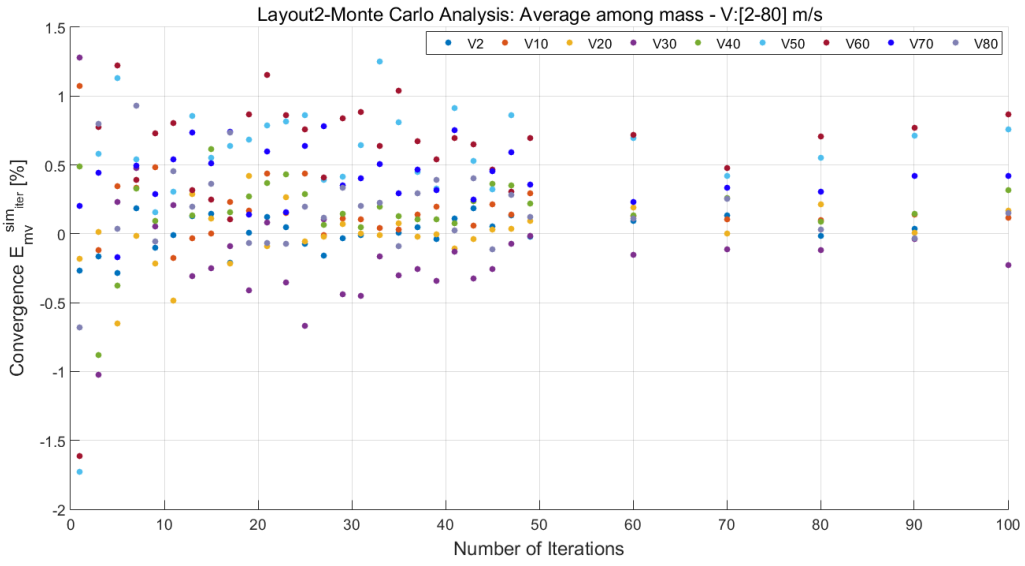

(d) Monte Carlo convergence of $\mathbf{Em}_{v_k}^{sim_{iter}}$ reached at about 50 iterations

Figure 3.28: Layout2: Speed Estimation-Monte Carlo Analysis on $E_{M}{}_{v_k}^{sim_{iter}}$ with k=(60-80) m s^{-1} and (d) Monte Carlo convergence on $\mathbf{Em}_{v_k}^{sim_{iter}}$ in the full speed range

Summering the results, its' clear how the estimation errors on the crossing times are below the 0.5% in the full speed range and the Monte Carlo convergence at low speed as 2 m s^{-1} is reached immediately. As regards the vehicle speed estimation, the increasing of the number of sensing elements involves a better estimation accuracy due to the bigger number of time shifts used to estimate the speed amplitude (see Tab. 2.7, Fig. 2.20).

3.2.1 Analysis of the FDA algorithm performance

The Monte Carlo analysis underlines how in all the conditions concerning the vehicle (speed and mass) and measurement layouts (number and spacing among sensing elements) the convergence is reached: this is important in order to establish the good operation of the proposed approaches. With the aim at evaluating the algorithm performance, a results reportage has been here carried out in correspondence of the reached Monte Carlo convergence: the evaluated estimation errors are on the crossing times ($E_{MT_{imax}}^{sim_{conv}}$ and $Em_{T_{imax}}^{sim_{conv}}$) and on the vehicle speed ($E_{m_v}^{sim_{conv}}$ and $E_{M_v}{}^{sim_{conv}}$). The performance of the FDA approach in estimating the vehicle speed and crossing times have been evaluated also in the full mass range when the Monte Carlo convergence is reached. Results are shown with a SNR from 4 dB to 8 dB to check the approach robustness against a very big noise amplitude on the input signal.

3.2.1.1 Detection of the train axles crossing times on measurement sleepers

The operation of the FDA approach aimed at estimating the train axles crossing time is independent by the number and spacing among the sensing elements, indeed the $E_{mT_{imax}}^{sim_{conv}}$ computed in each measurement layout are quite similar, see Fig. 3.29(a-d). To summarize the performance of the approach and test the robustness against the noise affecting the measure, a comparison between $E_{mT_{imax}}^{sim_{conv}}$ values obtained with a SNR of 4 dB, see Fig. 3.29(e) or a SNR of 8 dB on the input signal is carried out, see Fig. 3.29(f). The comparison between Fig. 3.29e and Fig. 3.29f highlights the robustness of the approach against an high amplitude of noise on the input signal, since estimation errors are not worse with a bigger noise level. Results involve considerations about the dependence between the $E_{MT_{imax}}^{sim_{conv}}$ values and the vehicle mass, that is relevant only at low speed as 2m s^{-1}.

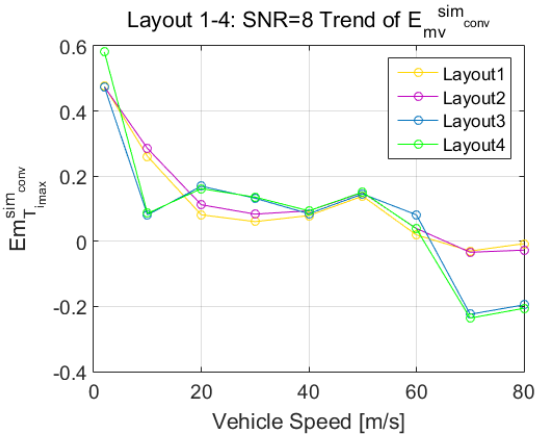

(a) $E_{mT_{imax}}^{sim_{conv}}(\%)$ trend: 2 measurement sleepers

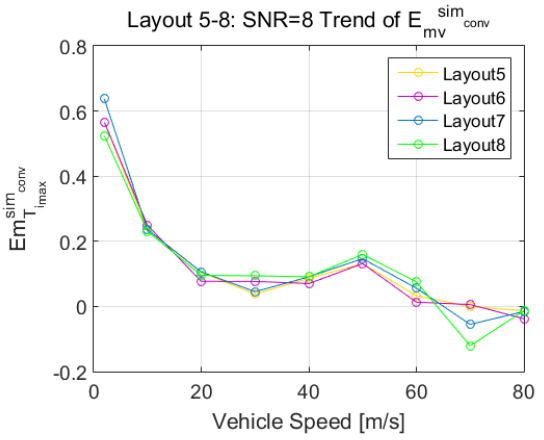

(b) $E_{mT_{imax}}^{sim_{conv}}(\%)$: 3 measurement sleepers

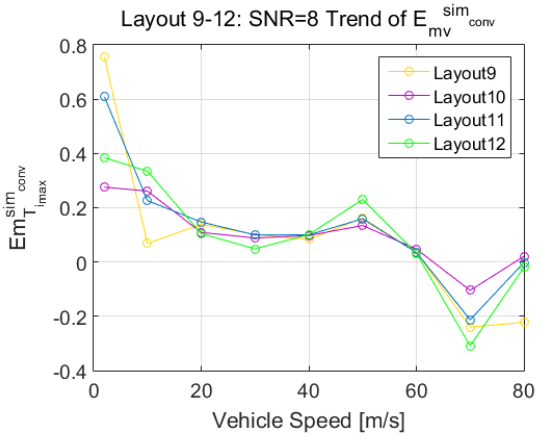

(c) $E_{mT_{imax}}^{sim_{conv}}(\%)$: 4 measurement sleepers

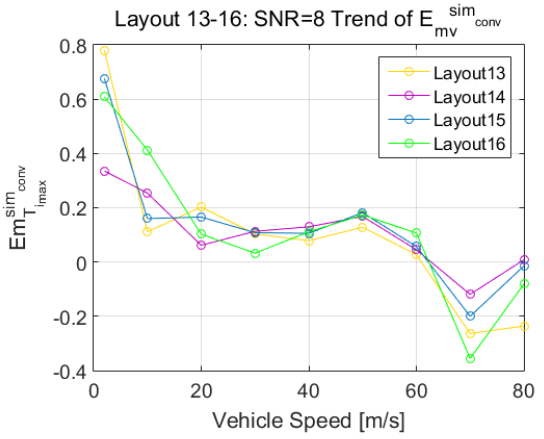

(d) $E_{mT_{imax}}^{sim_{conv}}(\%)$: 5 measurement sleepers

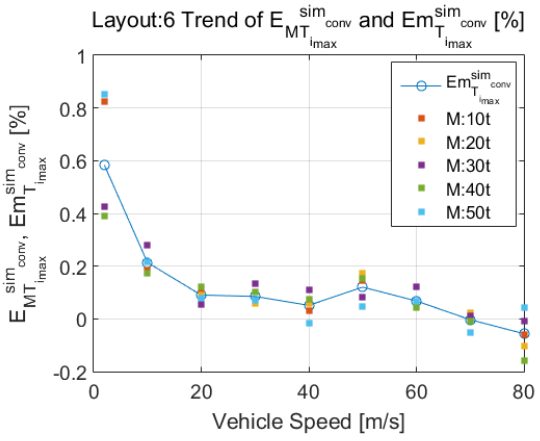

(e) $E_{mT_{imax}}^{sim_{conv}}$ and $E_{MT_{imax}}^{sim_{conv}}(\%)$ trend with SNR of 4 dB

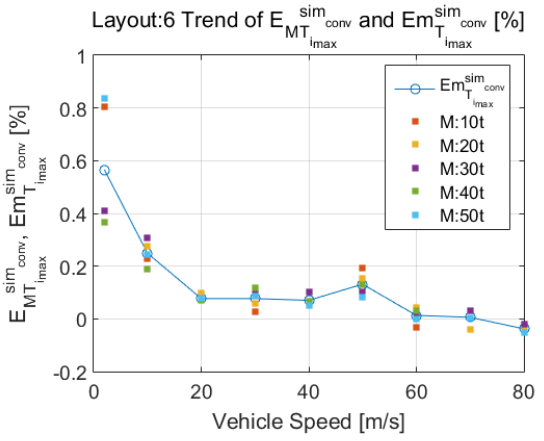

(f) $E_{mT_{imax}}^{sim_{conv}}$ and $E_{MT_{imax}}^{sim_{conv}}(\%)$ trend with SNR of 8 dB

Figure 3.29: (a-d)$E_{mT_{imax}}^{sim_{conv}}$ (%) trends with different measurement chains, (e-f) $E_{mT_{imax}}^{sim_{conv}}$ and $E_{MT_{imax}}^{sim_{conv}}(\%)$ trend with Layout 6

Table 3.7: Layout 6: $E_{mT_{imax}}^{sim_{conv}}[\%]$ and the maximum $E_{MT_{imax}}^{sim_{conv}}[\%]$ for each vehicle speed

					$E_{mT_{imax}}^{sim_{conv}}$ [%]				
SNR					Speed:	[m s^{-1}]			
$[dB]$	**2**	**10**	**20**	**30**	**40**	**50**	**60**	**70**	**80**
4	0.58	0.21	0.09	0.09	0.05	0.12	0.07	0	-0.05
8	0.57	0.25	0.08	0.08	0.07	0.13	0.01	0	-0.04
					$E_{MT_{imax}}^{sim_{conv}}$	[%]			
SNR					Speed:	[m s^{-1}]			
$[dB]$	**2**	**10**	**20**	**30**	**40**	**50**	**60**	**70**	**80**
4	0.85	0.28	0.12	0.13	0.11	0.17	0.12	-0.05	-0.16
	M=50 t	**M=30 t**	**M=40 t**	**M=30 t**	**M=30 t**	**M=20 t**	**M=30 t**	**M=50 t**	**M=40 t**
8	0.84	0.31	0.10	0.12	0.10	0.20	-0.03	-0.04	-0.05
	M=50 t	**M=30 t**	**M=20 t**	**M=40 t**	**M=30 t**	**M=10 t**	**M=20 t**	**M=20 t**	**M=40 t**

Tab. 3.7 summarizes the values of $E_{mT_{imax}}^{sim_{conv}}$ and the maximum values of $E_{MT_{imax}}^{sim_{conv}}$ computed for each vehicle speed, obtained with a SNR from 4dB to 8 dB: results highlight the proximity of errors obtained with 8 dB with the other ones corresponding to a SNR of 4 dB and this involves positive considerations on the robustness of the approach against the white noise on the input signal. Same considerations can be done for the other measurement layouts.

3.2.1.2 Vehicle Speed detection

Tab. 3.8 summarizes results about the $E_{m_v}^{sim_{conv}}[\%]$ trend as a function of the measurement layout (number and spacing among sensing elements): errors are bigger when the measurement layouts are equipped of sensing elements spaced of 0.6 m and are lower with the increasing of the number of sensing elements and spacing among themselves.

Table 3.8: $E_{mv}^{sim_{conv}}[\%]$ (SNR: 8dB)

Layout	Speed: $[\mathrm{m\,s^{-1}}]$								
	2	**10**	**20**	**30**	**40**	**50**	**60**	**70**	**80**
1	0.55	0.45	0.51	2	0.77	2.2	1.31	1.12	1.94
2	0.09	0.13	0.19	-0.15	0.13	0.69	0.72	0.23	0.11
3	0.0	-0.1	0.04	0.28	0.02	0.08	0.13	0.08	0.28
4	0.05	0.0	0.02	0.31	0.07	0.18	0	0.17	0.35
5	0.41	0.34	0.44	0.08	0.66	0.57	1	0.49	0.96
6	0.07	0.14	0.02	0.18	-0.05	0.09	0.16	0.19	0.3
7	0.05	-0.09	0.04	0.06	0.08	0.09	0.19	0.02	0.16
8	0.02	0.02	-0.01	0.14	0.02	0	0.07	0.02	-0.04
9	0.3	0.22	0.45	0.48	0.57	0.81	0.82	0.88	0.78
10	0	0.06	0.11	0.02	0.1	0.19	0.06	0.16	0.17
11	0.02	0.01	0.03	0.08	0.08	0.08	0.13	0.06	0.12
12	0.02	0.02	0.03	0.09	0	0.08	0.04	0.04	0
13	0.2	0.25	0.24	0.38	0.37	0.37	0.86	0.5	0.74
14	0	0.06	0.06	0.15	0.12	0.19	0.13	0.01	0.12
15	0.03	0.04	0.06	0.08	0.03	0.08	0.03	0.07	0.08
16	0.02	-0.02	0.02	0	0.01	0.03	0.05	-0.02	0.03

In order to focus the effect of the measurement layouts on the estimation accuracy, in adding to the Tab. 3.8, the trend of $E_{mv}^{sim_{conv}}$, as a function of the number and spacing among the sensing elements, is carried out in Fig. 3.30.

Fig. 3.30 shows the trend of $E_{mv}^{sim_{conv}}[\%]$ that is lower with the increasing of the number of sensing elements and with a bigger spacing among themselves. Two measurement sleepers involve estimation errors below the 0.5% if the spacing between themselves is bigger than 1.2 m, three measurement sleepers allow to obtain similar results with a spacing bigger than 0.6 m. Layouts with four measurement sleepers allow to obtain estimation errors below the 0.2% with a spacing bigger than 0.6 m and the most performing layouts with 5 measurement sleepers involve estimation errors below the 0.1% with a spacing bigger than 1.2 m. The approach have the worst performance if the spacing among the measurement sleepers is of 0.6 m.

With the aim at evaluating the global performance of the estimation algorithm in the full speed and mass range, Figs. 3.31-3.33 show the trend of $E_{m_v}^{sim_{conv}}(\%)$ with overlapped the values of $E_{M_v}{}^{sim_{conv}}(\%)$ for each vehicle speed, in order to localize the maximum errors.

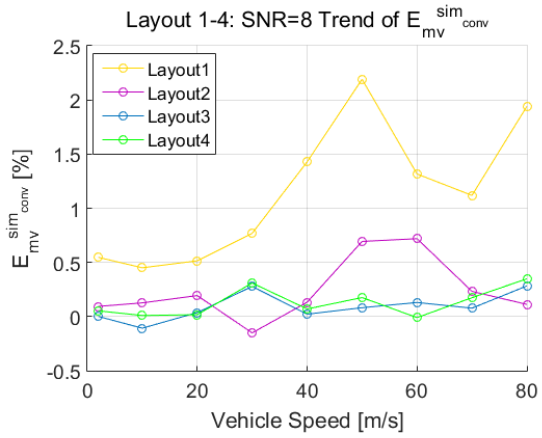

(a) $E_{m_v}^{sim_{conv}}(\%)$ trend: the increasing of the spacing between the two sleepers involves a decrement of the estimation error

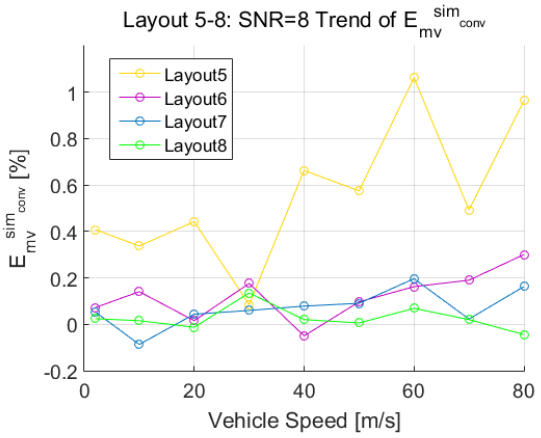

(b) $E_{m_v}^{sim_{conv}}(\%)$ trend: the increasing of the spacing among the three sleepers involves a decrement of the estimation error

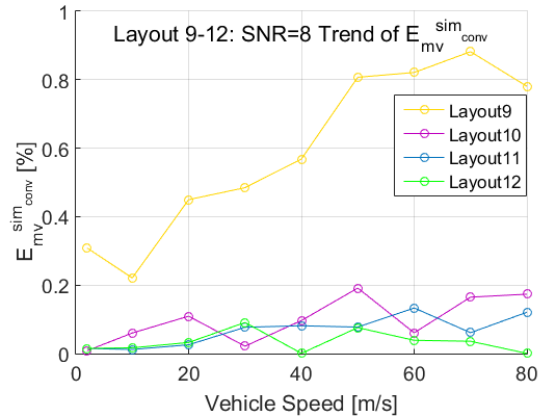

(c) $E_{m_v}^{sim_{conv}}(\%)$ trend: the increasing of the spacing among the four sleepers involves a decrement of the estimation error

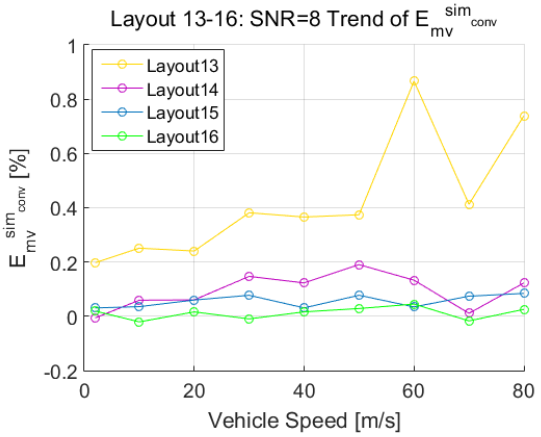

(d) $E_{m_v}^{sim_{conv}}(\%)$ trend: the increasing of the spacing among the five sleepers involves a decrement of the estimation error

Figure 3.30: $E_{m_v}^{sim_{conv}}(\%)$ trend with different measurement chains and noisy input signal (SNR of 8dB): errors are decreasing with the increasing of the number of sensing elements and spacing among them (from 0.6 m to a maximum one of 2.4 m)

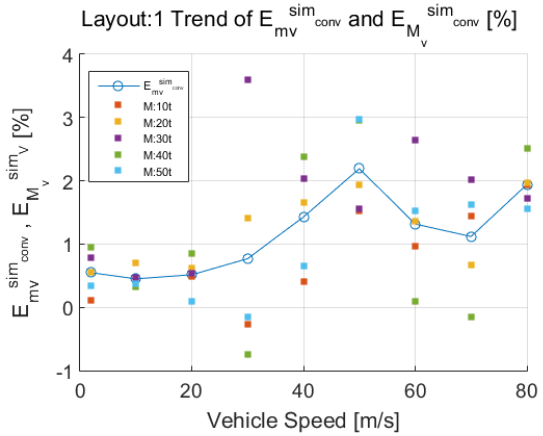

(a) Layout1: $E_{mv}{}^{sim_{conv}}(\%)$ trend (blue line) and $E_{M_v}{}^{sim_{conv}}(\%)$ values

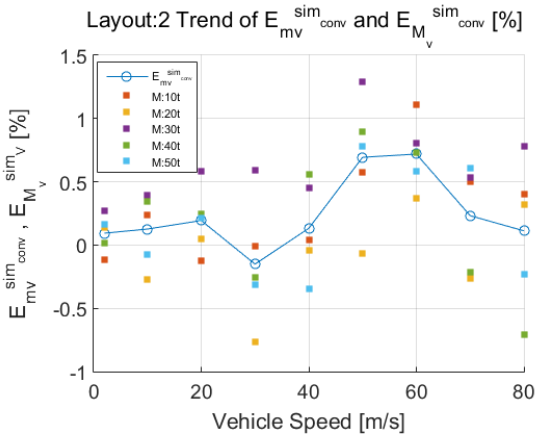

(b) Layout2: $E_{mv}{}^{sim_{conv}}(\%)$ trend (blue line) and $E_{M_v}{}^{sim_{conv}}(\%)$ values

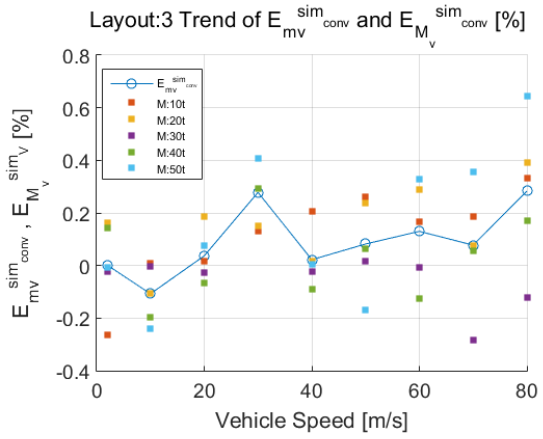

(c) Layout3: $E_{mv}{}^{sim_{conv}}(\%)$ trend (blue line) and $E_{M_v}{}^{sim_{conv}}(\%)$ values

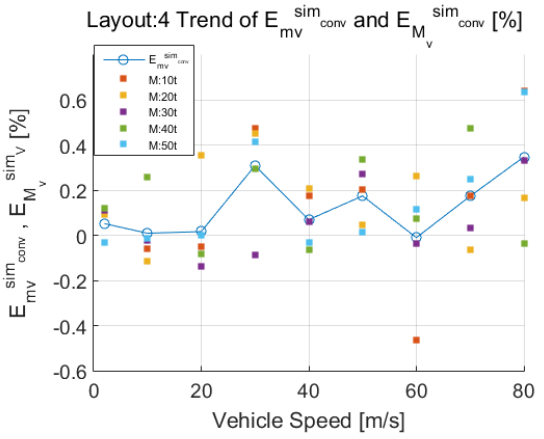

(d) Layout4: $E_{mv}{}^{sim_{conv}}(\%)$ trend (blue line) and $E_{M_v}{}^{sim_{conv}}(\%)$ values

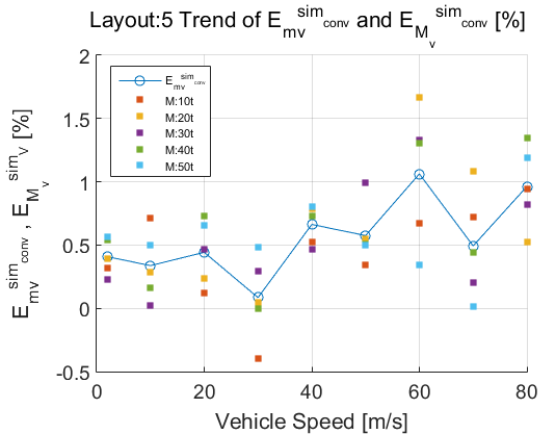

(e) Layout5: $E_{mv}{}^{sim_{conv}}(\%)$ trend (blue line) and $E_{M_v}{}^{sim_{conv}}(\%)$ values

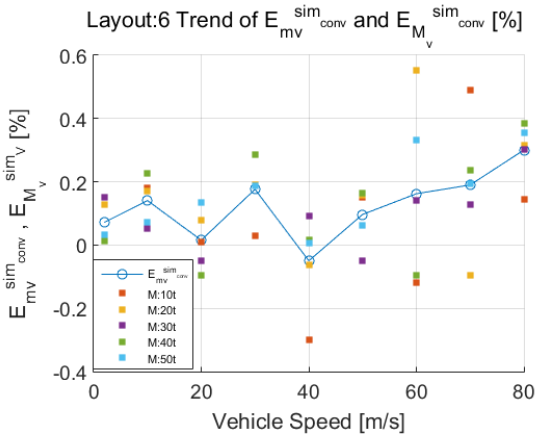

(f) Layout6: $E_{mv}{}^{sim_{conv}}(\%)$ trend (blue line) and $E_{M_v}{}^{sim_{conv}}(\%)$ values

Figure 3.31: $E_{mv}{}^{sim_{conv}}[\%]$ trend and $E_{M_v}{}^{sim_{conv}}[\%]$ values for Layout 1-6

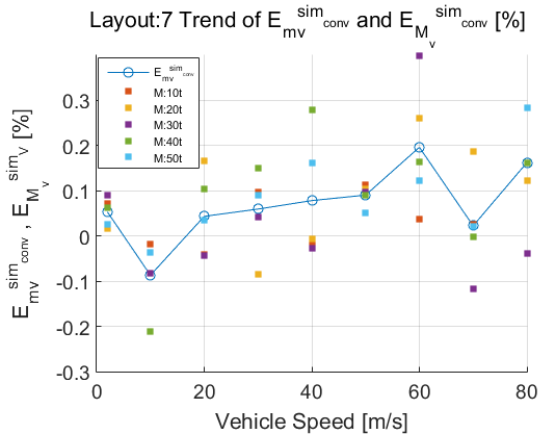

(a) Layout7: $E_{mv}{}^{sim_{conv}}(\%)$ trend (blue line) and $E_{M_v}{}^{sim_{conv}}(\%)$ values

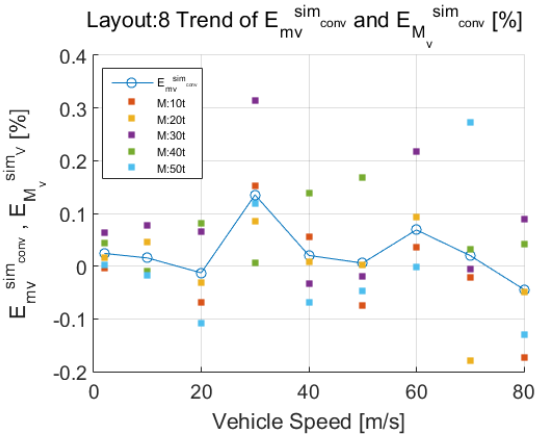

(b) Layout8: $E_{mv}{}^{sim_{conv}}(\%)$ trend (blue line) and $E_{M_v}{}^{sim_{conv}}(\%)$ values

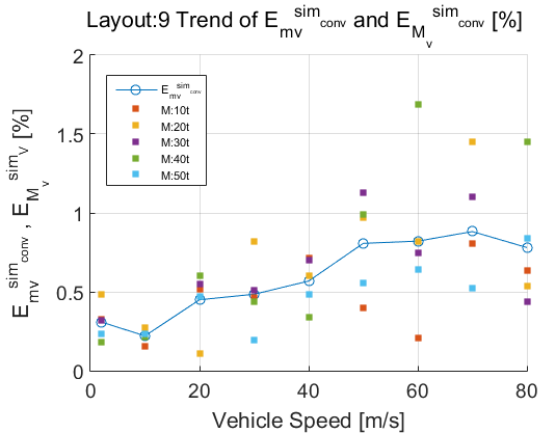

(c) Layout9: $E_{mv}{}^{sim_{conv}}(\%)$ trend (blue line) and $E_{M_v}{}^{sim_{conv}}(\%)$ values

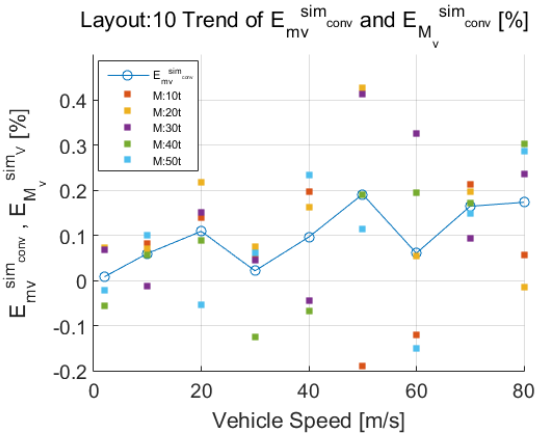

(d) Layout10: $E_{mv}{}^{sim_{conv}}(\%)$ trend (blue line) and $E_{M_v}{}^{sim_{conv}}(\%)$ values

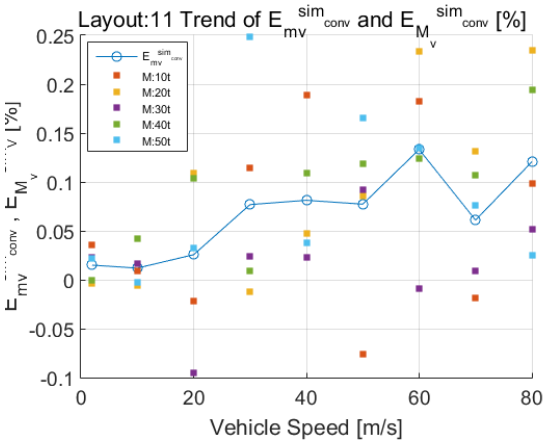

(e) Layout11: $E_{mv}{}^{sim_{conv}}(\%)$ trend (blue line) and $E_{M_v}{}^{sim_{conv}}(\%)$ values

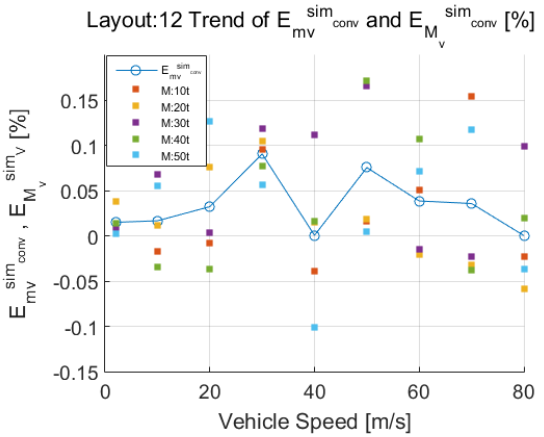

(f) Layout12: $E_{mv}{}^{sim_{conv}}(\%)$ trend (blue line) and $E_{M_v}{}^{sim_{conv}}(\%)$ values

Figure 3.32: $E_{mv}{}^{sim_{conv}}[\%]$ trend and $E_{M_v}{}^{sim_{conv}}[\%]$ values for Layout 7-12

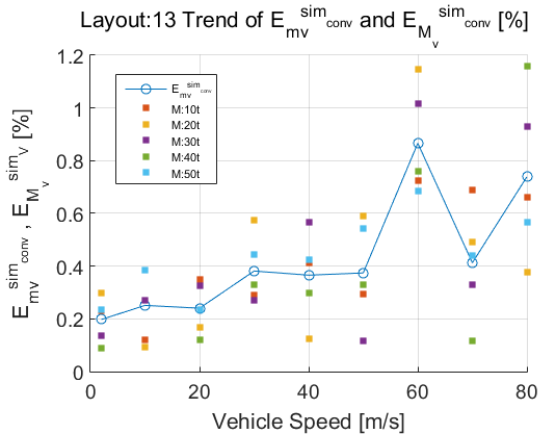

(a) Layout13: $E_{mv}{}^{sim_{conv}}(\%)$ trend (blue line) and $E_{M_v}{}^{sim_{conv}}(\%)$ values

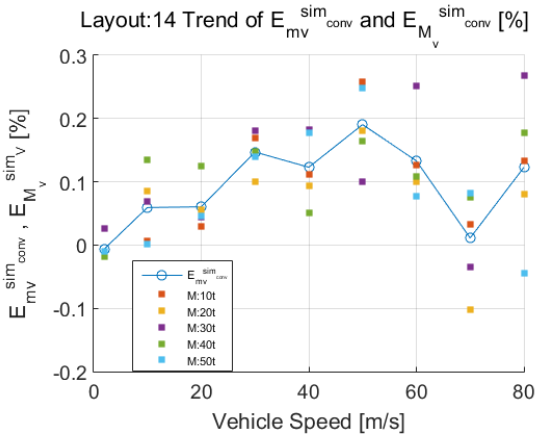

(b) Layout14: $E_{mv}{}^{sim_{conv}}(\%)$ trend (blue line) and $E_{M_v}{}^{sim_{conv}}(\%)$ values

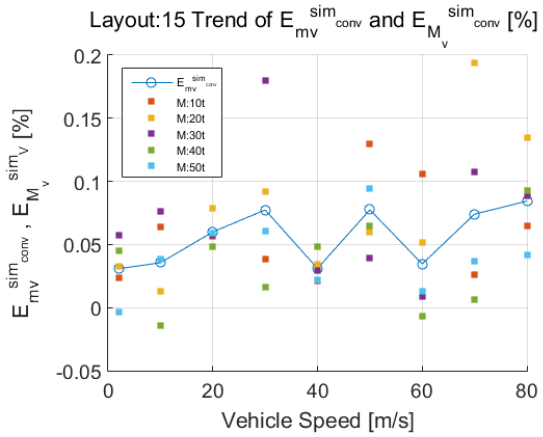

(c) Layout15: $E_{mv}{}^{sim_{conv}}(\%)$ trend (blue line) and $E_{M_v}{}^{sim_{conv}}(\%)$ values

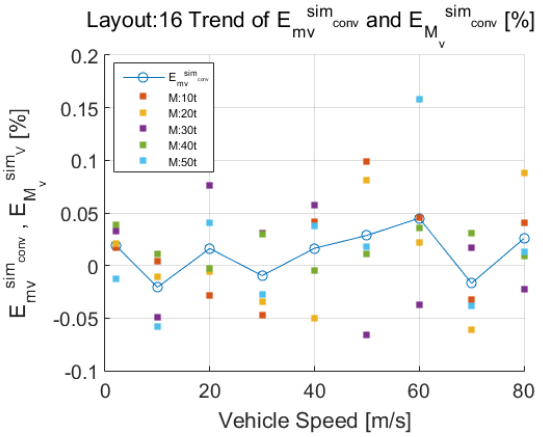

(d) Layout16: $E_{mv}{}^{sim_{conv}}(\%)$ trend (blue line) and $E_{M_v}{}^{sim_{conv}}(\%)$ values

Figure 3.33: $E_{mv}{}^{sim_{conv}}[\%]$ trend and $E_{M_v}{}^{sim_{conv}}[\%]$ values for Layout 13-16

Table 3.9: Maximum ${E_{M_v}}^{sim_{conv}}(\%)$ values computed in the full speed range, with an input SNR of 8 dB

Layout	Speed [m s^{-1}]								
	2	**10**	**20**	**30**	**40**	**50**	**60**	**70**	**80**
1	0.95	0.70	0.84	3.60	2.37	2.98	2.64	2	2.51
	M=40 t	**M=20 t**	**M=40 t**	**M=30 t**	**M=40 t**	**M=50 t**	**M=30 t**	**M=30 t**	**M=40 t**
2	0.27	0.39	0.58	-0.77	0.56	1.28	1.11	0.6	-0.78
	M=30 t	**M=30 t**	**M=30 t**	**M=20 t**	**M=40 t**	**M=30 t**	**M=10 t**	**M=50 t**	**M=30 t**
3	-0.27	-0.24	0.19	0.41	0.20	0.26	0.33	0.36	0.64
	M=10 t	**M=50 t**	**M=20 t**	**M=30 t**	**M=10 t**	**M=10 t**	**M=50 t**	**M=50 t**	**M=50 t**
4	0.12	-0.26	0.35	0.47	0.21	0.34	-0.46	0.48	0.64
	M=40 t	**M=40 t**	**M=20 t**	**M=10 t**	**M=20 t**	**M=40 t**	**M=10 t**	**M=40 t**	**M=10 t**
5	0.57	0.72	0.73	0.48	0.8	0.99	1.67	1.1	1.34
	M=50 t	**M=10 t**	**M=40 t**	**M=50 t**	**M=50 t**	**M=30 t**	**M=20 t**	**M=20 t**	**M=40 t**
6	0.15	0.22	0.13	0.29	-0.3	0.16	0.55	0.49	0.39
	M=10 t	**M=40 t**	**M=30 t**	**M=30 t**	**M=10 t**	**M=40 t**	**M=20 t**	**M=20 t**	**M=10 t**
7	0.09	-0.21	0.17	0.15	0.28	0.11	0.40	0.19	0.28
	M=30 t	**M=40 t**	**M=20 t**	**M=40 t**	**M=40 t**	**M=10 t**	**M=30 t**	**M=20 t**	**M=10 t**
8	0.06	0.08	-0.1	0.32	0.14	0.17	0.22	-0.27	-0.17
	M=30 t	**M=30 t**	**M=50 t**	**M=30 t**	**M=40 t**	**M=40 t**	**M=30 t**	**M=50 t**	**M=10 t**
9	0.48	0.27	0.60	0.82	0.71	1.13	1.68	1.45	1.45
	M=20 t	**M=20 t**	**M=40 t**	**M=20 t**	**M=10 t**	**M=30 t**	**M=40 t**	**M=20 t**	**M=40 t**
10	0.07	0.1	0.22	-0.13	0.24	0.43	0.33	0.21	0.30
	M=20 t	**M=50 t**	**M=20 t**	**M=40 t**	**M=50 t**	**M=20 t**	**M=30 t**	**M=10 t**	**M=40 t**
11	0.04	0.04	0.11	0.25	0.19	0.17	0.23	0.13	0.23
	M=10 t	**M=40 t**	**M=20 t**	**M=50 t**	**M=10 t**	**M=50 t**	**M=20 t**	**M=20 t**	**M=20 t**
12	0.04	0.07	0.13	0.12	0.11	0.17	0.11	0.16	0.1
	M=20 t	**M=30 t**	**M=50 t**	**M=30 t**	**M=30 t**	**M=40 t**	**M=40 t**	**M=10 t**	**M=30 t**
13	0.30	0.39	0.35	0.58	0.57	0.59	1.15	0.69	1.16
	M=20 t	**M=50 t**	**M=10 t**	**M=20 t**	**M=30 t**	**M=20 t**	**M=20 t**	**M=10 t**	**M=40 t**
14	0.03	0.13	0.12	0.18	0.18	0.26	0.26	-0.10	0.27
	M=30 t	**M=40 t**	**M=40 t**	**M=30 t**	**M=30 t**	**M=10 t**	**M=30 t**	**M=20 t**	**M=30 t**
15	0.06	0.08	0.08	0.18	0.05	0.13	0.10	0.19	0.13
	M=30 t	**M=30 t**	**M=20 t**	**M=30 t**	**M=40 t**	**M=10 t**	**M=10 t**	**M=20 t**	**M=20 t**
16	0.04	-0.06	0.08	-0.05	0.06	0.1	0.15	-0.06	0.09
	M=40 t	**M=50 t**	**M=30 t**	**M=10 t**	**M=30 t**	**M=10 t**	**M=50 t**	**M=20 t**	**M=20 t**

In order to check the robustness, results are indicated with a SNR of 4 dB (worst performance of the measurement and acquisition chain). Tab. 3.10 indicates the values of $E_{m_v}^{sim_{conv}}[\%]$ corresponding to the reached convergence of the Monte Carlo analysis (49 iterations).

Table 3.10: $E_{m_v}^{sim_{conv}}[\%]$ (SNR: 4dB)

Layout	Speed: $[\mathrm{m\,s^{-1}}]$								
	2	**10**	**20**	**30**	**40**	**50**	**60**	**70**	**80**
1	0.28	0.45	0.74	1.2	2.06	2.34	2.37	2.67	3.90
2	0.16	0.03	0.12	0.04	0.25	0.50	0.67	0.64	0.9
3	0.05	0.05	0.08	0.05	0.35	0.38	0.22	0.42	0.56
4	0	0.07	0.15	0.22	0.21	0.24	0.18	0.11	0.32
5	0.24	0.36	0.60	0.83	1.2	1.44	1.69	1.48	3
6	0.06	0.04	0.17	0.18	0.12	0.33	0.54	0.41	0.65
7	0.06	0.03	0.08	0.09	0.10	0.12	0.18	0.1	0.32
8	0.02	-0.02	0.05	0.00	0.06	0.11	0.13	0.1	0.082
9	0.48	1.03	1.14	1.48	1.75	2.42	3.06	3.01	4.29
10	0.04	0.1	0.18	0.09	0.32	0.21	0.28	0.44	0.44
11	0.05	0.03	0.06	0.15	0.06	0.06	0.14	0.13	0.22
12	0.01	0.02	0.07	0.06	0.06	0.07	0.13	0.08	0.06
13	0.2	0.35	0.31	0.68	0.83	0.80	1.32	1.34	0.76
14	0.02	0.04	0.08	0.11	0.07	0.31	0.29	0.19	0.33
15	0.03	0.04	0.06	0.08	0.03	0.11	0.17	0.11	0.17
16	0	0.01	0.03	0	0.07	0.07	0.1	0.01	0.05

Tab. 3.10 and Fig. 3.34 summarize the results when the SNR is equal to 4 dB, showing a trend and value of $E_{m_v}^{sim_{conv}}[\%]$ quite similar with which ones obtained with a SNR of 8 dB, as a confirm of the good robustness of the approach against the noise affecting the measurement chain. Two measurement sleepers involve a mean estimation value $E_{m_v}^{sim_{conv}}[\%]$ below the 1% if the sensing elements are spaced of almost 1.2 m, otherwise with a number of sensing elements bigger than three is possible to obtain mean estimation errors below the 0.5%.

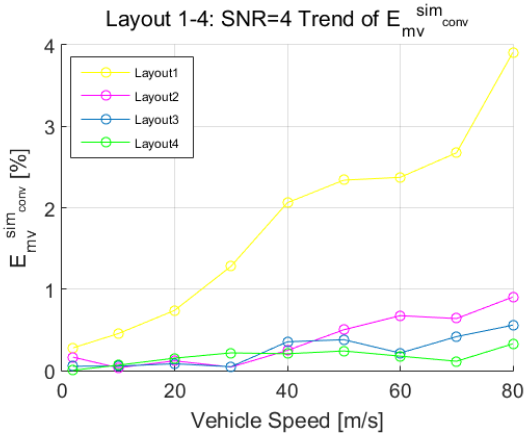

(a) $E_{mv}{}^{sim_{conv}}(\%)$ trend: 2 measurement sleepers

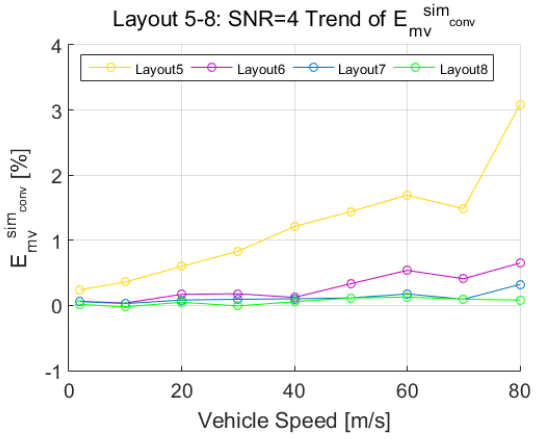

(b) $E_{mv}{}^{sim_{conv}}(\%)$: 3 measurement sleepers

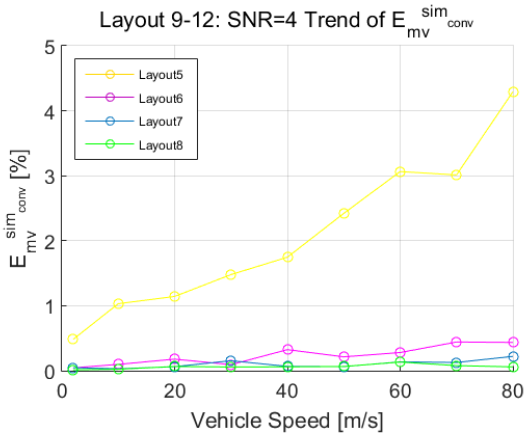

(c) $E_{mv}{}^{sim_{conv}}(\%)$: 4 measurement sleepers

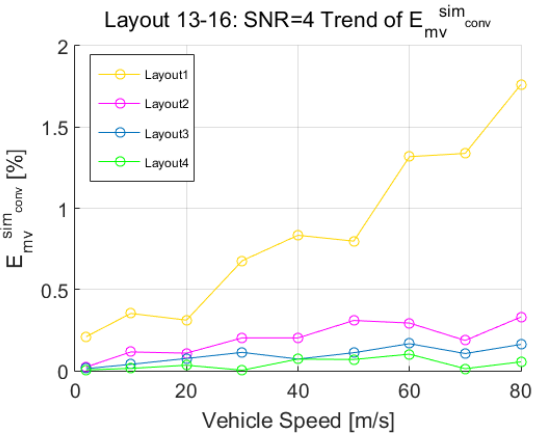

(d) $E_{mv}{}^{sim_{conv}}(\%)$: 5 measurement sleepers

Figure 3.34: $E_{mv}{}^{sim_{conv}}(\%)$ trend with different measurement chains and SNR of 4dB: errors are decreasing with the increasing of the number of sensing elements and spacing among them (from 0.6 m to a maximum one of 2.4 m)

Following, the values of $E_{M_v}{}^{sim_{conv}}(\%)$ are overlapped to the shape of $E_{mv}{}^{sim_{conv}}(\%)$ for each layout, to underline the variation from the mean value and detect the maximum percentage errors for each speed, committed by the estimation algorithm when the operating conditions are very poor (SNR of 4 dB on the input signal). Tab. 3.11 summarizes the maximum values $E_{M_v}{}^{sim_{conv}}(\%)$ for each speed, indicating also the mass value that involves the maximum error.

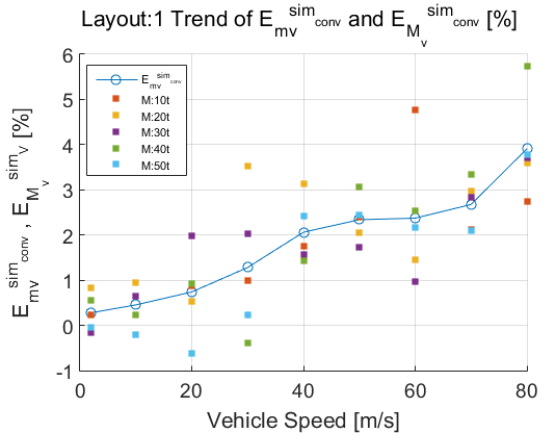

(a) Layout1: $E_{mv}{}^{sim_{conv}}(\%)$ trend (blue line) and $E_{M_v}{}^{sim_{conv}}(\%)$ values

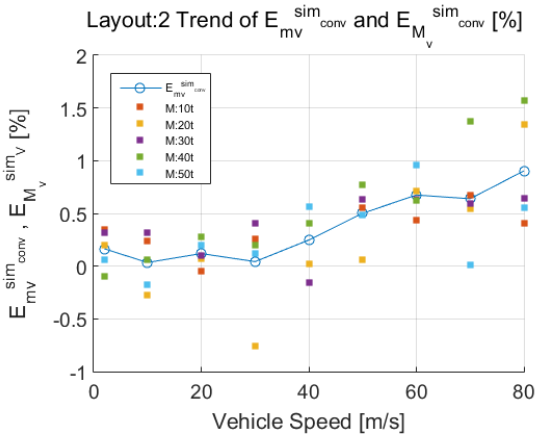

(b) Layout2: $E_{mv}{}^{sim_{conv}}(\%)$ trend (blue line) and $E_{M_v}{}^{sim_{conv}}(\%)$ values

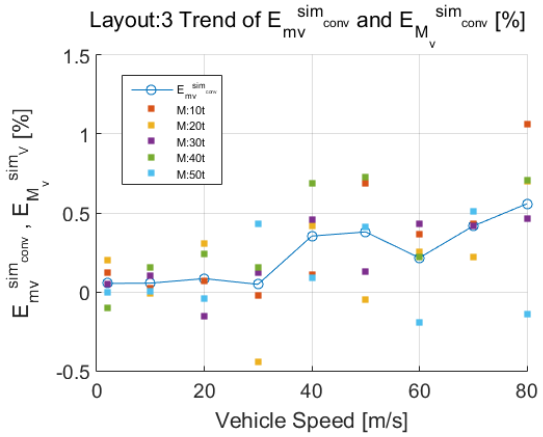

(c) Layout3: $E_{mv}{}^{sim_{conv}}(\%)$ trend (blue line) and $E_{M_v}{}^{sim_{conv}}(\%)$ values

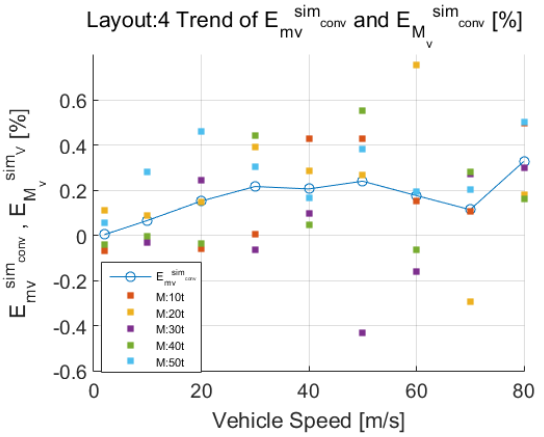

(d) Layout4: $E_{mv}{}^{sim_{conv}}(\%)$ trend (blue line) and $E_{M_v}{}^{sim_{conv}}(\%)$ values

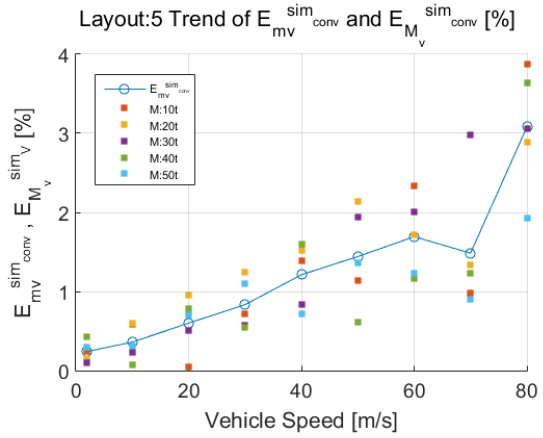

(e) Layout5: $E_{mv}{}^{sim_{conv}}(\%)$ trend (blue line) and $E_{M_v}{}^{sim_{conv}}(\%)$ values

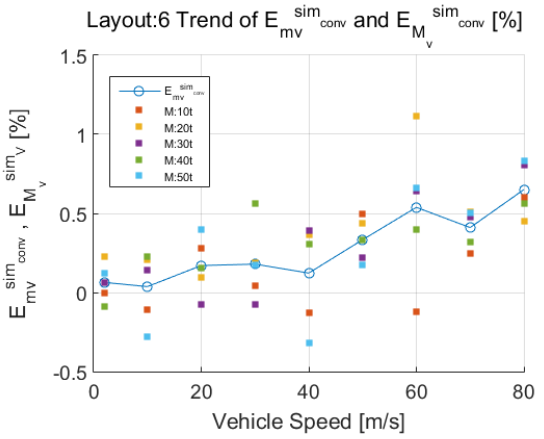

(f) Layout6: $E_{mv}{}^{sim_{conv}}(\%)$ trend (blue line) and $E_{M_v}{}^{sim_{conv}}(\%)$ values

Figure 3.35: $E_{mv}{}^{sim_{conv}}[\%]$ trend and $E_{M_v}{}^{sim_{conv}}[\%]$ values for Layout 1-6 and with a SNR of 4 dB

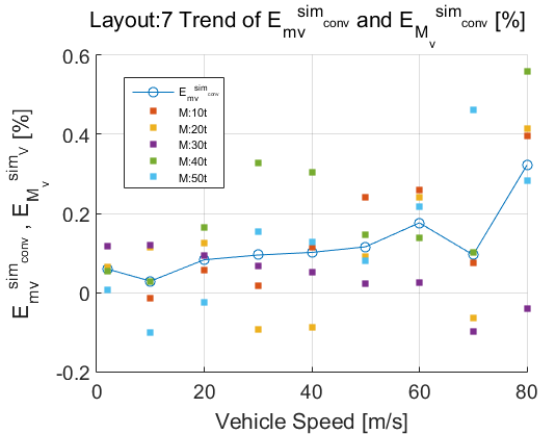

(a) Layout7: $E_{mv}{}^{sim_{conv}}(\%)$ trend (blue line) and $E_{M_v}{}^{sim_{conv}}(\%)$ values

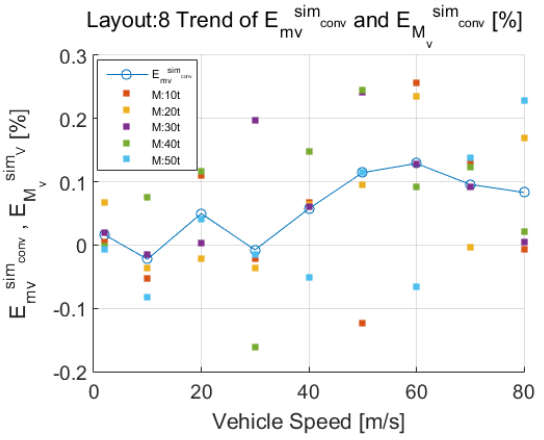

(b) Layout8: $E_{mv}{}^{sim_{conv}}(\%)$ trend (blue line) and $E_{M_v}{}^{sim_{conv}}(\%)$ values

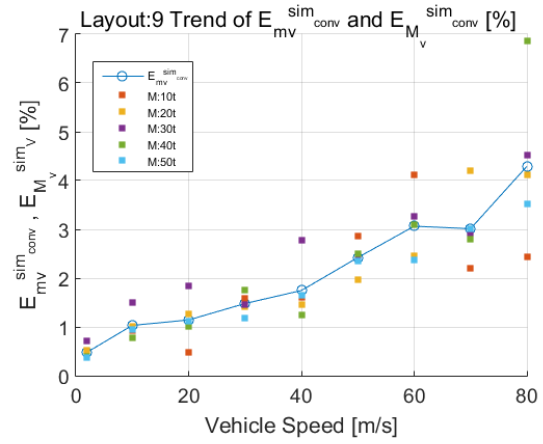

(c) Layout9: $E_{mv}{}^{sim_{conv}}(\%)$ trend (blue line) and $E_{M_v}{}^{sim_{conv}}(\%)$ values

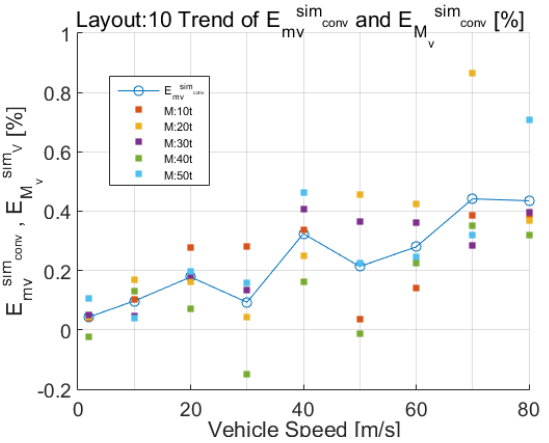

(d) Layout10: $E_{mv}{}^{sim_{conv}}(\%)$ trend (blue line) and $E_{M_v}{}^{sim_{conv}}(\%)$ values

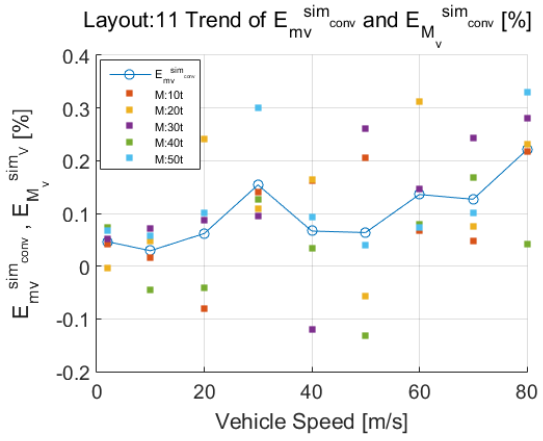

(e) Layout11: $E_{mv}{}^{sim_{conv}}(\%)$ trend (blue line) and $E_{M_v}{}^{sim_{conv}}(\%)$ values

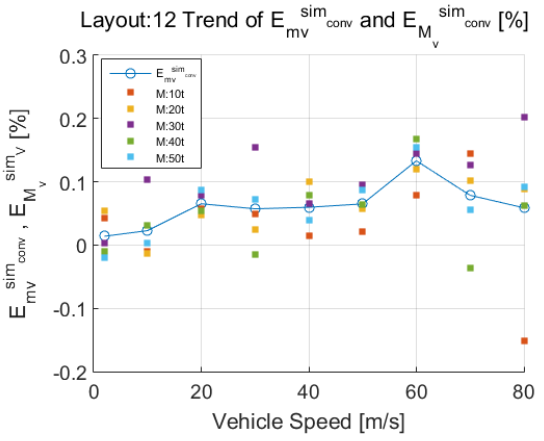

(f) Layout12: $E_{mv}{}^{sim_{conv}}(\%)$ trend (blue line) and $E_{M_v}{}^{sim_{conv}}(\%)$ values

Figure 3.36: $E_{mv}{}^{sim_{conv}}[\%]$ trend and $E_{M_v}{}^{sim_{conv}}[\%]$ values for Layout 7-12 and with a SNR of 4 dB

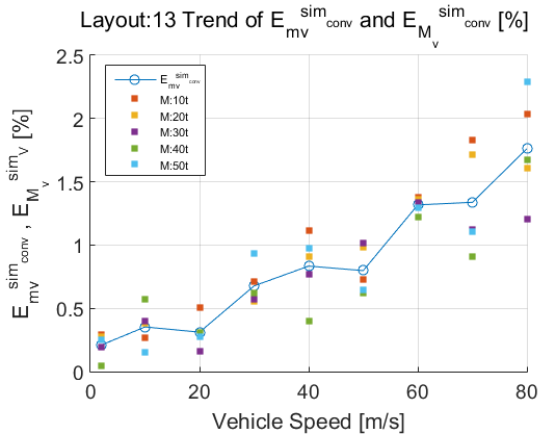

(a) Layout13: $E_{m_v}{}^{sim_{conv}}(\%)$ trend (blue line) and $E_{M_v}{}^{sim_{conv}}(\%)$ values

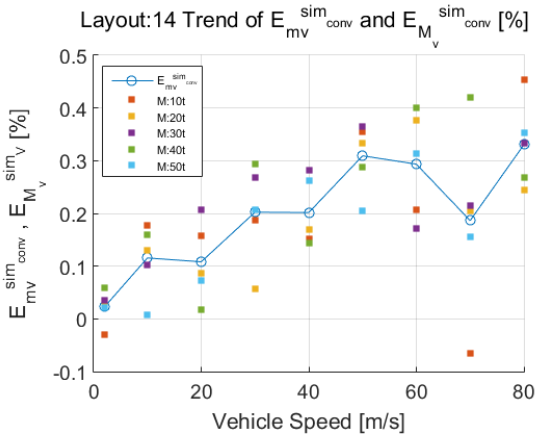

(b) Layout14: $E_{m_v}{}^{sim_{conv}}(\%)$ trend (blue line) and $E_{M_v}{}^{sim_{conv}}(\%)$ values

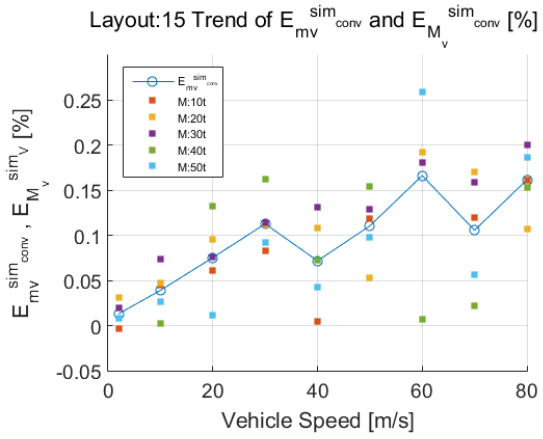

(c) Layout15: $E_{m_v}{}^{sim_{conv}}(\%)$ trend (blue line) and $E_{M_v}{}^{sim_{conv}}(\%)$ values

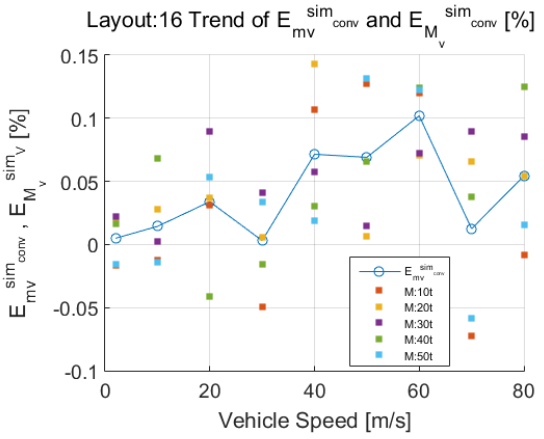

(d) Layout16: $E_{m_v}{}^{sim_{conv}}(\%)$ trend (blue line) and $E_{M_v}{}^{sim_{conv}}(\%)$ values

Figure 3.37: $E_{m_v}{}^{sim_{conv}}[\%]$ trend and $E_{M_v}{}^{sim_{conv}}[\%]$ values for Layout 13-16 and with a SNR of 4 dB

Table 3.11: Maximum ${E_{M_v}}^{sim_{conv}}(\%)$ values computed in the full speed range, with an input SNR of 4 dB

Layout	Speed [m s^{-1}]								
	2	**10**	**20**	**30**	**40**	**50**	**60**	**70**	**80**
1	0.84	0.94	1.98	3.5	3.14	3.07	4.77	3.35	5.74
	M=20 t	**M=20 t**	**M=30 t**	**M=20 t**	**M=20 t**	**M=40 t**	**M=10 t**	**M=40 t**	**M=40 t**
2	0.34	0.31	0.28	-0.76	0.56	0.77	0.95	1.37	1.57
	M=10 t	**M=30 t**	**M=40 t**	**M=20 t**	**M=50 t**	**M=40 t**	**M=50 t**	**M=40 t**	**M=40 t**
3	0.20	0.16	0.30	-0.45	0.69	0.73	0.43	0.51	1.06
	M=20 t	**M=40 t**	**M=20 t**	**M=20 t**	**M=40 t**	**M=40 t**	**M=30 t**	**M=50 t**	**M=10 t**
4	0.11	0.28	0.46	0.44	0.43	0.56	0.76	-0.29	0.50
	M=20 t	**M=50 t**	**M=50 t**	**M=40 t**	**M=10 t**	**M=40 t**	**M=20 t**	**M=20 t**	**M=50 t**
5	0.43	0.60	0.96	1.24	1.60	2.14	2.34	2.98	3.88
	M=40 t	**M=20 t**	**M=20 t**	**M=20 t**	**M=40 t**	**M=20 t**	**M=10 t**	**M=30 t**	**M=10 t**
6	0.23	-0.28	0.39	0.57	0.39	0.50	1.12	0.51	0.83
	M=20 t	**M=50 t**	**M=50 t**	**M=40 t**	**M=30 t**	**M=10 t**	**M=20 t**	**M=20 t**	**M=50 t**
7	0.12	0.12	0.17	0.33	0.30	0.24	0.26	0.46	0.56
	M=30 t	**M=30 t**	**M=40 t**	**M=40 t**	**M=40 t**	**M=10 t**	**M=10 t**	**M=50 t**	**M=40 t**
8	0.068	0.083	0.12	0.20	0.15	0.24	0.26	0.14	0.23
	M=20 t	**M=50 t**	**M=40 t**	**M=30 t**	**M=40 t**	**M=40 t**	**M=10 t**	**M=50 t**	**M=50 t**
9	0.7	1.49	1.84	1.75	2.77	2.85	4.12	4.19	6.87
	M=30 t	**M=30 t**	**M=30 t**	**M=40 t**	**M=30 t**	**M=10 t**	**M=10 t**	**M=20 t**	**M=40 t**
10	0.11	0.17	0.28	0.28	0.46	0.46	0.42	0.87	0.71
	M=50 t	**M=20 t**	**M=10 t**	**M=10 t**	**M=50 t**	**M=20 t**	**M=20 t**	**M=20 t**	**M=50 t**
11	0.07	0.07	0.24	0.30	0.16	0.26	0.31	0.24	0.33
	M=40 t	**M=30 t**	**M=20 t**	**M=50 t**	**M=20 t**	**M=30 t**	**M=20 t**	**M=30 t**	**M=50 t**
12	0.05	0.10	0.09	0.15	0.1	0.1	0.17	0.14	0.20
	M=20 t	**M=30 t**	**M=50 t**	**M=30 t**	**M=20 t**	**M=30 t**	**M=40 t**	**M=10 t**	**M=30 t**
13	0.29	0.57	0.50	0.93	1.11	1.01	1.37	1.83	2.28
	M=10 t	**M=40 t**	**M=10 t**	**M=50 t**	**M=10 t**	**M=30 t**	**M=10 t**	**M=10 t**	**M=50 t**
14	0.06	0.18	0.21	0.29	0.28	0.37	0.40	0.42	0.45
	M=40 t	**M=10 t**	**M=30 t**	**M=40 t**	**M=30 t**	**M=30 t**	**M=40 t**	**M=40 t**	**M=10 t**
15	0.03	0.07	0.13	0.16	0.13	0.15	0.26	0.17	0.20
	M=20 t	**M=30 t**	**M=40 t**	**M=40 t**	**M=30 t**	**M=40 t**	**M=50 t**	**M=20 t**	**M=30 t**
16	0.02	0.07	0.09	-0.05	0.14	0.13	0.12	0.09	0.12
	M=30 t	**M=40 t**	**M=30 t**	**M=10 t**	**M=20 t**	**M=50 t**	**M=40 t**	**M=30 t**	**M=40 t**

3.2.1.3 Train detection

In this section the performance of algorithm in train detection functionalities is examined, with each operating conditions concerning the vehicle and the measurement layout. The estimation approach has led good results with a signal-to-noise ratio both of 4 dB and 8 dB, especially if the measurement layout is composed by almost three sensing elements, for which no estimation errors have been committed. The plotted errors concern a comparison between the ones obtained with a SNR of 4 dB and 8 dB. Performance are shown after 1000 algorithm iterations and the plotted errors are those defined in Eq. 3.5.
Figs. 3.38-3.41 show a comparison between estimated errors with a SNR of 4 dB or 8 dB for the Layout 1-4 (two measurement sleepers). Results with a lower noise level involve errors only when the vehicle speed is 80 $\mathrm{m\,s^{-1}}$ (Layout 3 and 4) or 70 $\mathrm{m\,s^{-1}}$ (Layout 1 and 2), instead with a SNR of 4 dB there are errors at vehicle speeds of 60 and 80 $\mathrm{m\,s^{-1}}$.

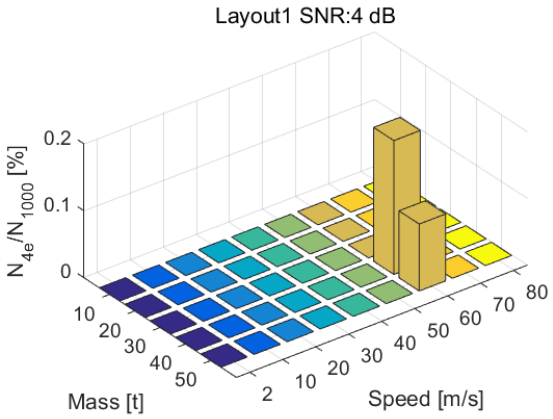

(a) Layout 1-SNR:4 dB- Estimation errors $E_{N\,percent}$:errors are different from zero when the vehicle speed is 60 m s^{-1}

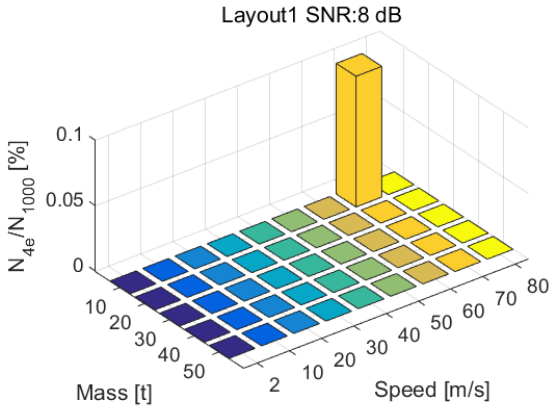

(b) Layout 1-SNR:8 dB- Estimation errors $E_{N\,percent}$:errors are different from zero when the vehicle speed is 70 m s^{-1}

Figure 3.38: Estimation errors $E_{N\,percent}$ with Layout 1 obtained with a SNR of 4 dbB (a) and 8 dB (b)

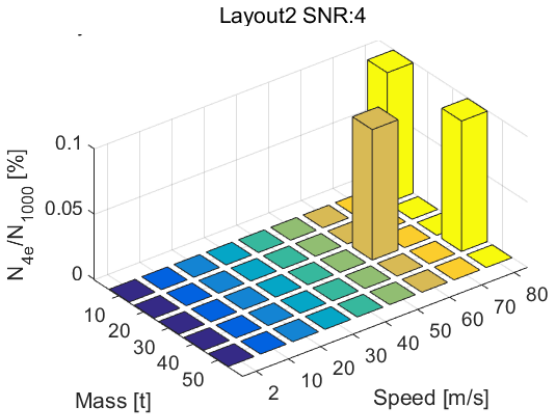

(a) Layout 2-SNR:4 dB- Estimation errors $E_{N\,percent}$:errors are different from zero when the vehicle speed is 60 m s^{-1} and 80 m s^{-1}

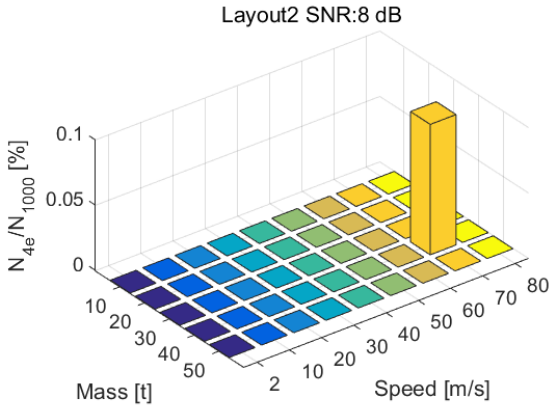

(b) Layout 2-SNR:8 dB- Estimation errors $E_{N\,percent}$:errors are different from zero when the vehicle speed is 70 m s^{-1}

Figure 3.39: Estimation errors $E_{N\,percent}$ with Layout 2 obtained with a SNR of 4 dbB (a) and 8 dB (b)

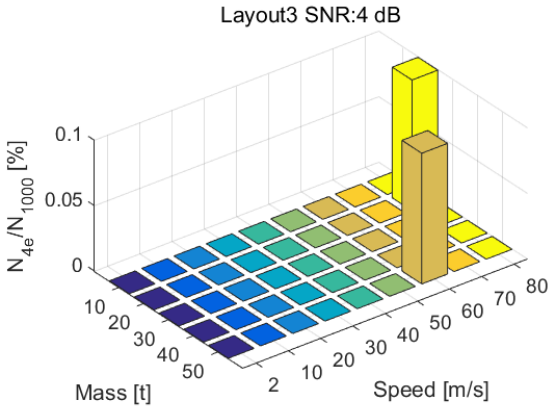

(a) Layout 3-SNR:4 dB- Estimation errors $E_{N\,percent}$:errors are different from zero when the vehicle speed is 60 m s^{-1} and 80 m s^{-1}

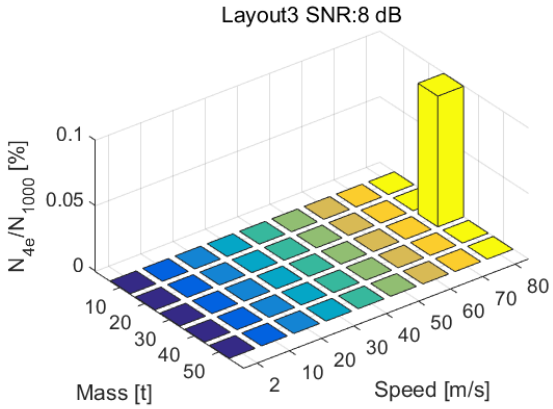

(b) Layout 3-SNR:8 dB- Estimation errors $E_{N\,percent}$:errors are different from zero when the vehicle speed is 80 m s^{-1}

Figure 3.40: Estimation errors $E_{N\,percent}$ with Layout 3 obtained with a SNR of 4 dB (a) and 8 dB (b)

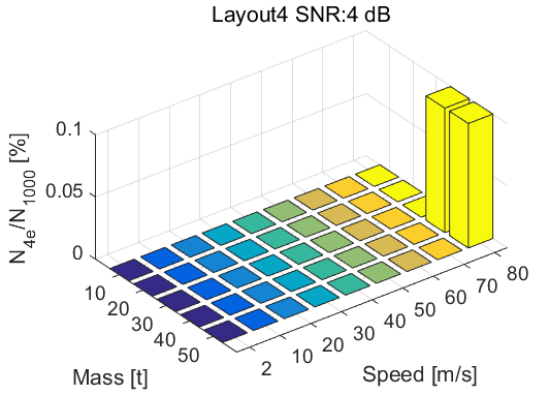

(a) Layout 4-SNR:4 dB- Estimation errors $E_{N\,percent}$:errors are different from zero when the vehicle speed is 80 m s^{-1}

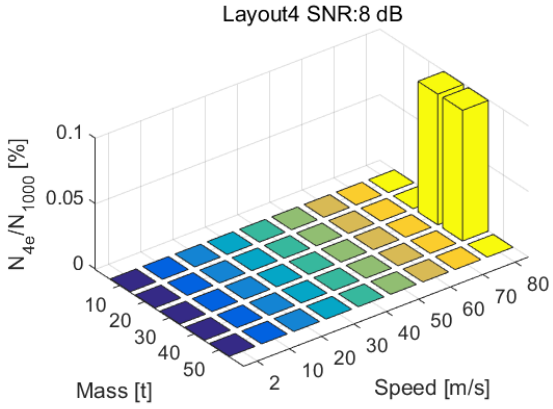

(b) Layout 4-SNR:8 dB- Estimation errors $E_{N\,percent}$:errors are different from zero when the vehicle speed is 80 m s^{-1}

Figure 3.41: Estimation errors $E_{N\,percent}$ with Layout 4 obtained with a SNR of 4 dB (a) and 8 dB (b)

Figs. 3.42-3.43 show results highlighting the good operation of the approach as vehicle detector in the speed range of 2-80 m s^{-1}, with measurement layouts equipped of a number of measurement sleepers bigger than two.

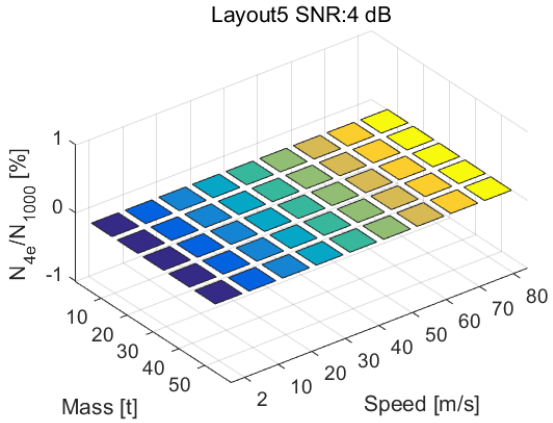

(a) Estimation errors $E_{N\,percent}$ in the full mass and speed range with the Layout 5 and a SNR of 4 dB

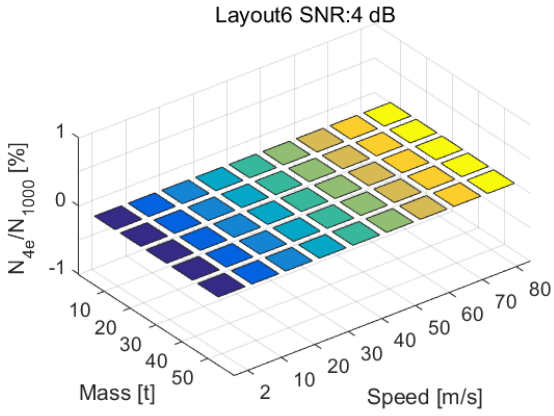

(b) Estimation errors $E_{N\,percent}$ in the full mass and speed range with the Layout 6 and a SNR of 4 dB

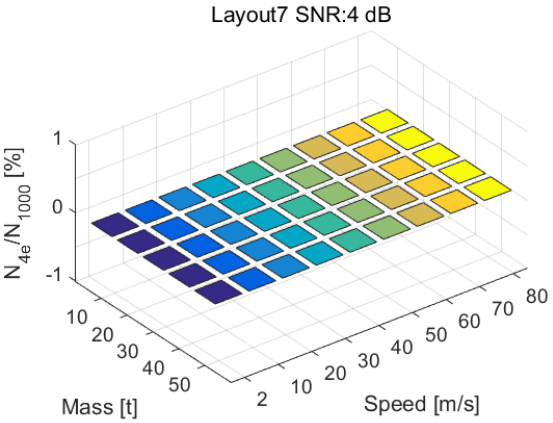

(c) Estimation errors $E_{N\,percent}$ in the full mass and speed range with the Layout 7 and a SNR of 4 dB

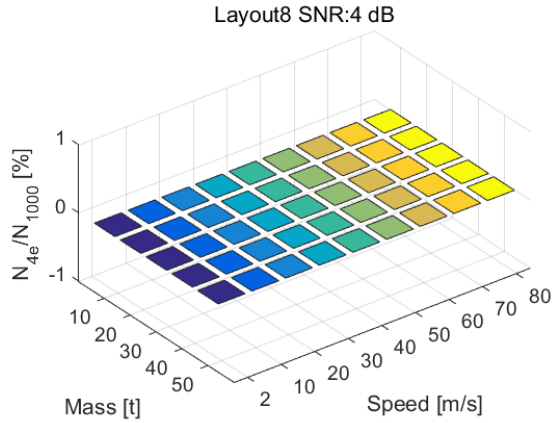

(d) Estimation errors $E_{N\,percent}$ in the full mass and speed range with the Layout 8 and a SNR of 4 dB

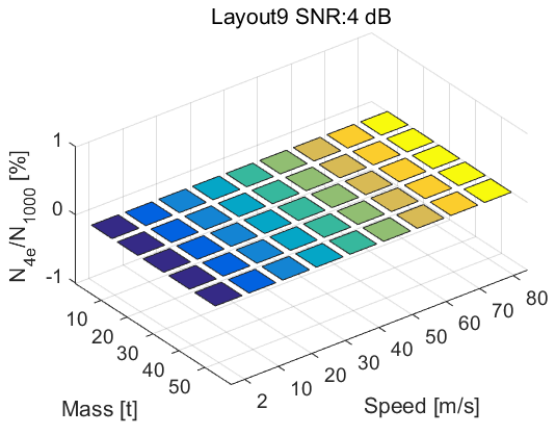

(e) Estimation errors $E_{N\,percent}$ in the full mass and speed range with the Layout 9 and a SNR of 4 dB

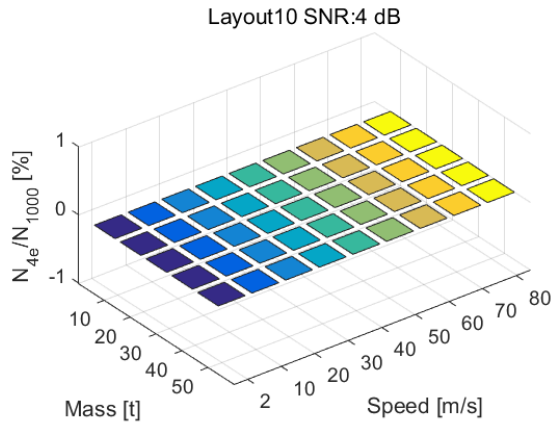

(f) Estimation errors $E_{N\,percent}$ in the full mass and speed range with the Layout 10 and a SNR of 4 dB

Figure 3.42: Estimation errors $E_{N\,percent}$ with Layout 5-10: errors are different from zero for vehicle speed bigger than 60 m s^{-1}

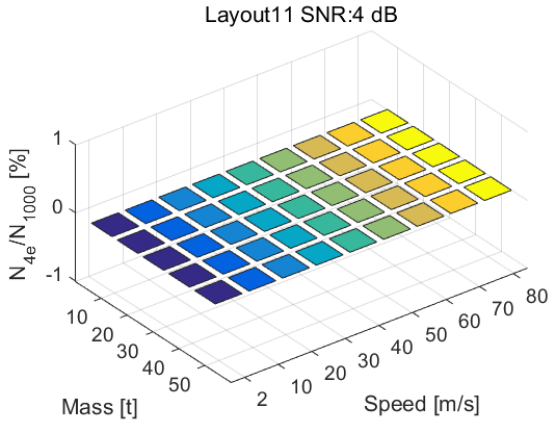

(a) Estimation errors $E_{N\,percent}$ in the full mass and speed range with the Layout 11 and a SNR of 4 dB

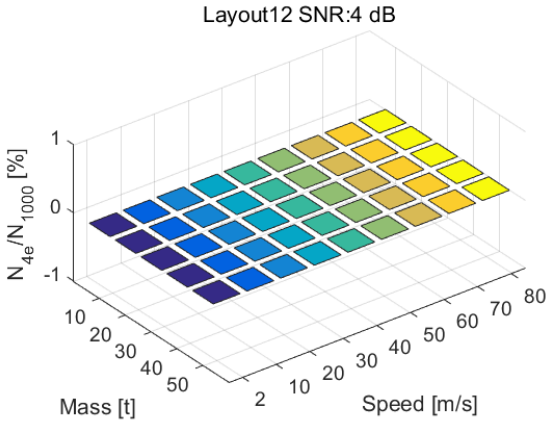

(b) Estimation errors $E_{N\,percent}$ in the full mass and speed range with the Layout 12 and a SNR of 4 dB

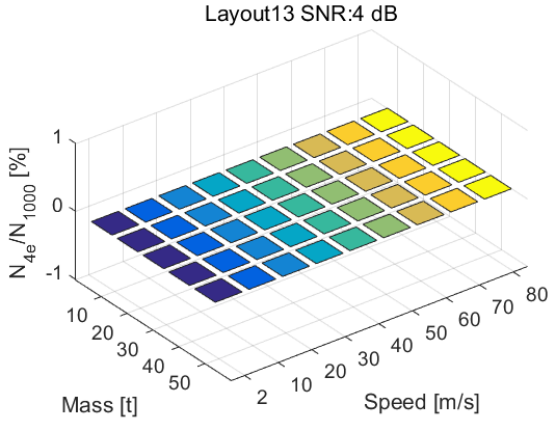

(c) Estimation errors $E_{N\,percent}$ in the full mass and speed range with the Layout 13 and a SNR of 4 dB

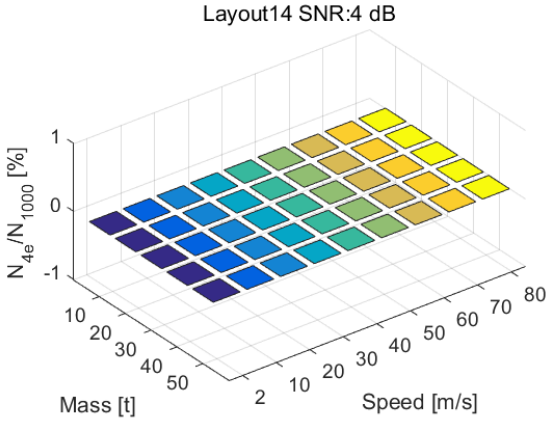

(d) Estimation errors $E_{N\,percent}$ in the full mass and speed range with the Layout 14 and a SNR of 4 dB

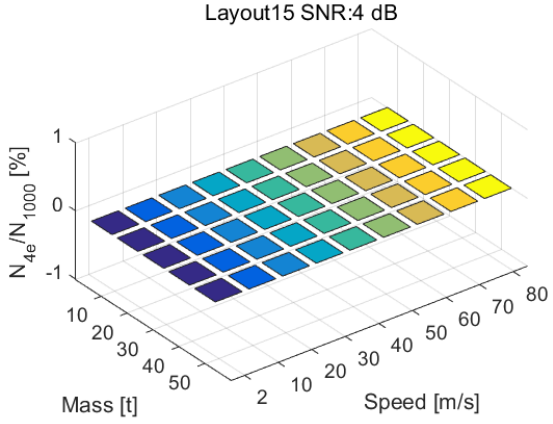

(e) Estimation errors $E_{N\,percent}$ in the full mass and speed range with the Layout 15 and a SNR of 4 dB

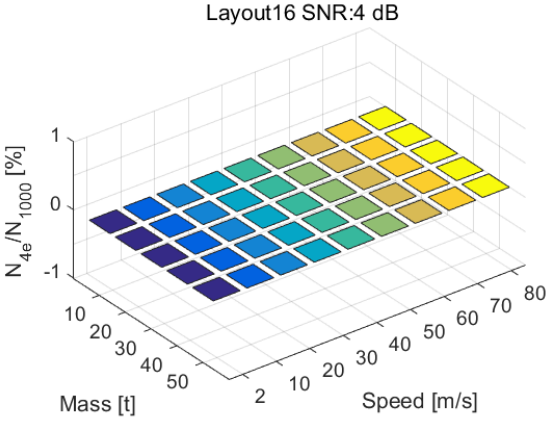

(f) Estimation errors $E_{N\,percent}$ in the full mass and speed range with the Layout 16 and a SNR of 4 dB

Figure 3.43: Estimation errors $E_{N\,percent}$ with Layout 11-16: no errors are committed

3.3 Comparison between the TDA/FDA approaches

In this paragraph a comparison between the two estimation approaches has been carried out under several points of view:

- performance in the estimation of train parameters;
- required computational time.

3.3.1 Performance in the train parameters estimations

One of the main purposes involves the study of the best measurement layout as compromise between installation and maintenance cost and the estimation accuracy. To this aim, the goal is to find the shorter layout that allows an high estimation accuracy. Results (see Figs. 3.6 and 3.30) highlight how configurations equipped of a bigger number of sensing elements and spacing among them provide lower estimation errors and so, in order also to do a comparison of the two approaches, a focus on the performance obtained with layouts 2, 3 and 6 is done, whose lengths are of 1.2, 1.8 and 2.4 m respectively.
Fig.3.44 shows the comparison between the TDA/FDA approaches in estimating of the $E_{m_v}^{sim_{conv}}[\%]$ in the full speed range: in both cases error trends are not constant against the speed value and FDA led lower estimation errors at low and high speeds, instead TDA involves better estimations in the speed range of (40-60) $\mathrm{m\,s^{-1}}$. Fig.3.45 shows the situation with the Layout 3 composed by still two sensing elements but spaced of 1.8 m: both approaches involve errors quite constant with the increasing of the vehicle speed and TDA is better than FDA only in the speed range of (50-60) $\mathrm{m\,s^{-1}}$. Layout 6 (Fig. 3.46) shows a FDA error trend more constant with the varying of the vehicle speed rather than that obtained with the TDA approach, which however led a little bit lower estimation error in the speed range of (40-60) $\mathrm{m\,s^{-1}}$. As observed in the previous chapter, all speed estimations done by the TDA approach at the vehicle speed of 70 $\mathrm{m\,s^{-1}}$ are affected by additional errors that have led bigger global $E_{m_v}^{sim_{conv}}[\%]$ values.

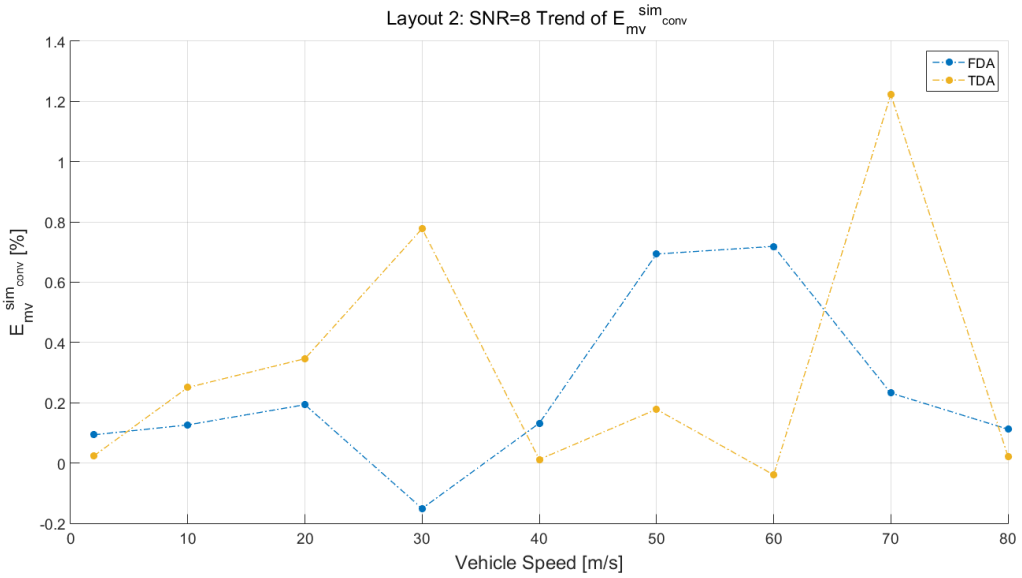

Figure 3.44: Comparison between TDA/FDA approaches in the estimating of the vehicle speed $E_{mv}^{sim_{conv}}[\%]$ with a measurement layouts equipped with 2 sensing elements spaced of 1.2 m

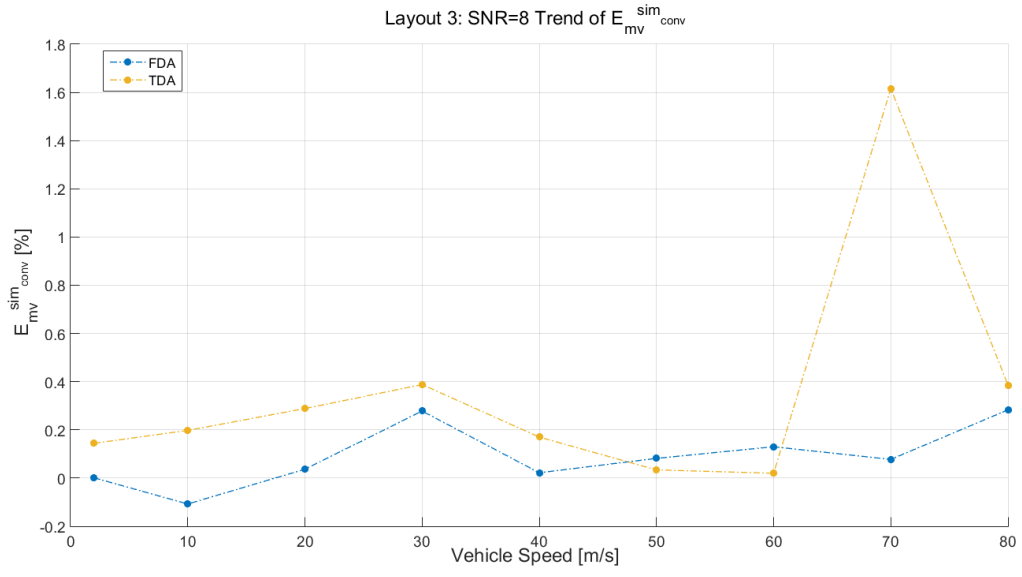

Figure 3.45: Comparison between TDA/FDA approaches in the estimating of the vehicle speed $E_{mv}^{sim_{conv}}[\%]$ with a measurement layouts equipped with 2 sensing elements spaced of 1.8 m

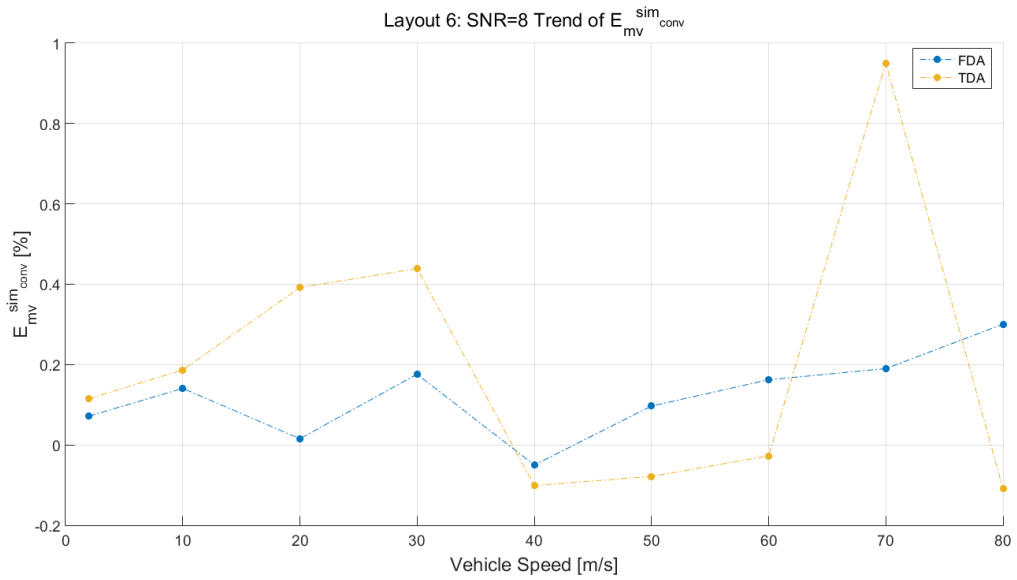

Figure 3.46: Comparison between TDA/FDA approaches in the estimating of the vehicle speed $E_{m_v}{}^{sim_{conv}}[\%]$ with a measurement layouts equipped with 3 sensing elements spaced of 1.2 m

Following, a comparison between the estimation approaches is performed evaluating the errors $E_{M_v}{}^{sim_{conv}}(\%)$ in the full range and using the three measurement layouts above discussed. Fig. 3.47 shows the trend of errors for each mass and speed value and discourage the usage of the Layout 2 due to the wide range in which, at the same speed, errors referred to different vehicle mass differ from each other. Increasing the spacing among sensing elements, errors computed by the two approaches are lower and there is a little bit difference between them since FDA involves errors below the 0.5 % in the full mass and speed ranges and the TDA has led quite similar results, except those affected by errors due to also the intrinsic performance of the measurement chain. Layout 6 shows an operation of the approach quite similar to that obtained with the Layout 3, although the adding of a measurement sleeper. As a consequence, the best configuration of the measurement layout as a compromise between the occupied space, maintenance cost and estimation accuracy is that equipped of two measurement sleepers spaced of 1.8 m, that involves a maximum estimation error about the half of the one obtained with the same number of sensing elements spaced of 1.2 m (Layout 2). Concerning the other train parameters, the FDA has led the estimation also of the crossing times of each train axles and this is a very important in order of monitoring the railway traffic on the rail for purposes of vehicle safety and maintenance.

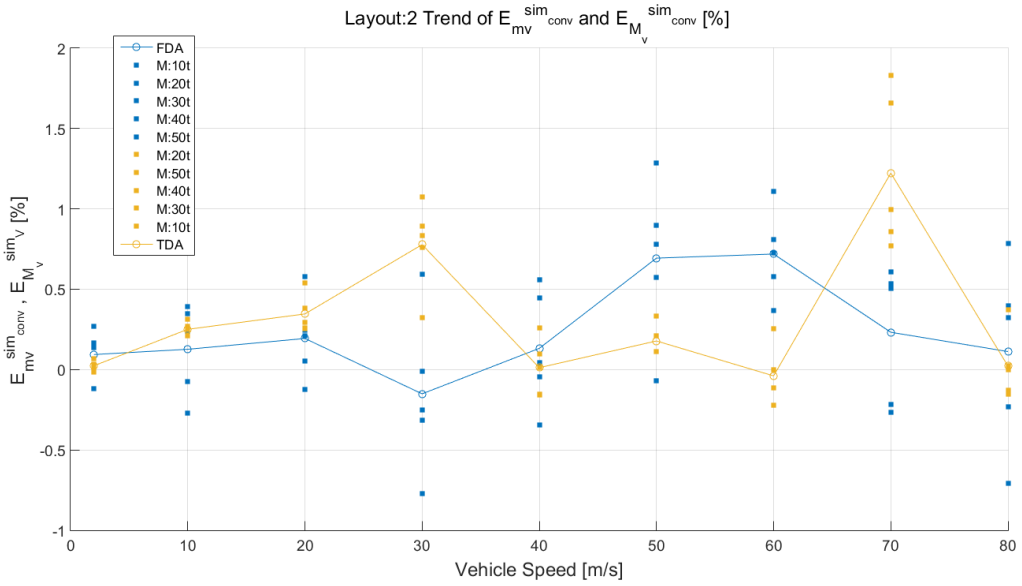

Figure 3.47: Comparison between TDA/FDA approaches in the estimating of the vehicle speed for each vehicle mass with measurement layouts equipped of 2 sensing elements spaced of 1.2 m

In agree with the above considerations, Fig. 3.50 shows the maximum errors committed among those corresponding to each train axle and each measurement sleepers of the Layout 3 (quite similar results have been obtained with the others operating conditions concerning the measurement chain). More focused, estimation errors are quite low and errors related to different vehicle mass are very close especially with speed bigger than 2 $\mathrm{m\,s^{-1}}$.

The train detection analysis has led different performance since the TDA offers best results with a SNR of 8 dB and a speed range between 2 to 60 $\mathrm{m\,s^{-1}}$ in all the measurement layouts, instead the FDA allows no errors with a SNR of 8 dB (but also with SNR of 4dB) and measurement layouts equipped of almost three measurement sleepers. In general, the FDA approach has involved estimations on train parameters more robust against the noise that may affect the measured input signal. However, to compare the two estimation approaches in the train detection, results on the estimation errors computed with the Layout 3 and a SNR of 8 dB are indicated in Fig. 3.51, which highlights as with the FDA approach errors are committed only with a vehicle speed of 80 $\mathrm{m\,s^{-1}}$.

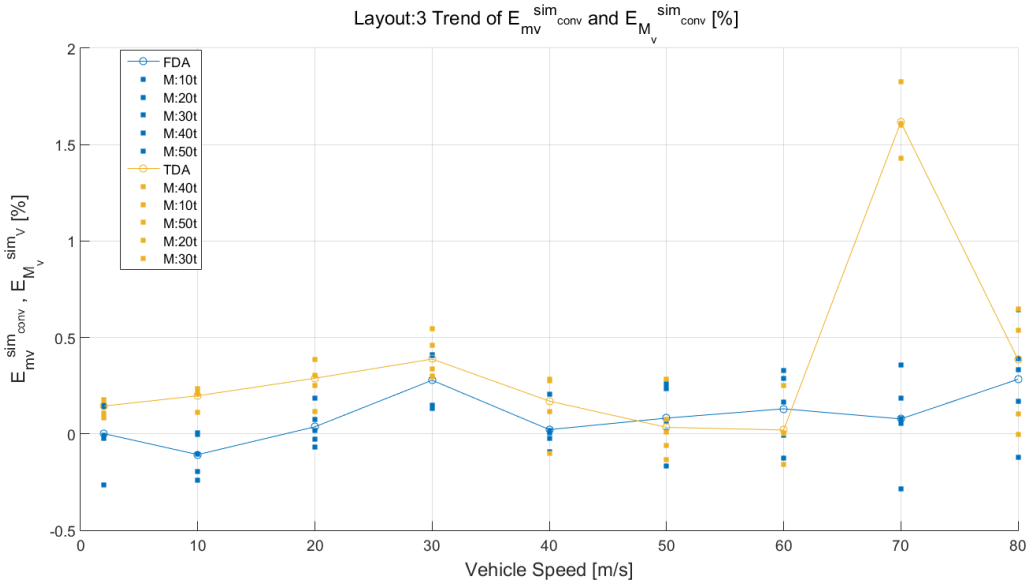

Figure 3.48: Comparison between TDA/FDA approaches in the estimating of the vehicle speed for each vehicle mass with measurement layouts equipped of 2 sensing elements spaced of 1.8 m

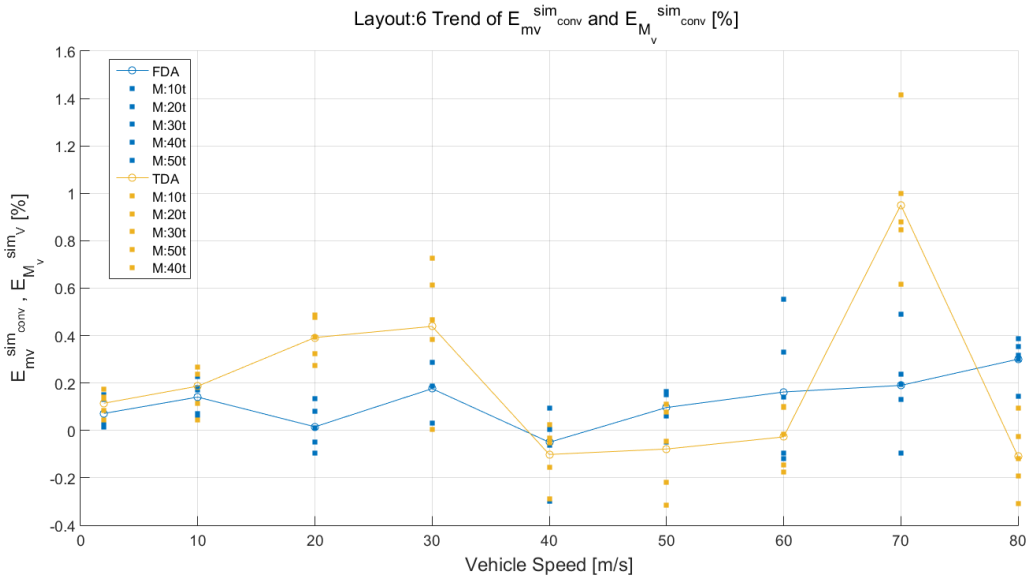

Figure 3.49: Comparison between TDA/FDA approaches in the estimating of the vehicle speed for each vehicle mass with measurement layouts equipped of 3 sensing elements spaced of 1.2 m

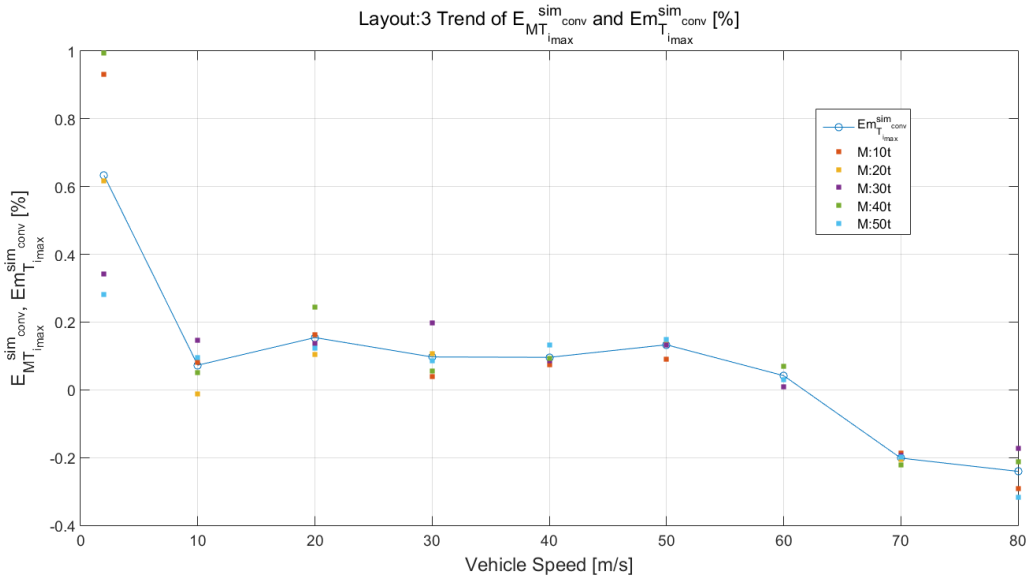

Figure 3.50: Layout 3: $E_{mT_{imax}}^{sim_{conv}}[\%]$ and the $E_{MT_{imax}}^{sim_{conv}}$ for each vehicle speed

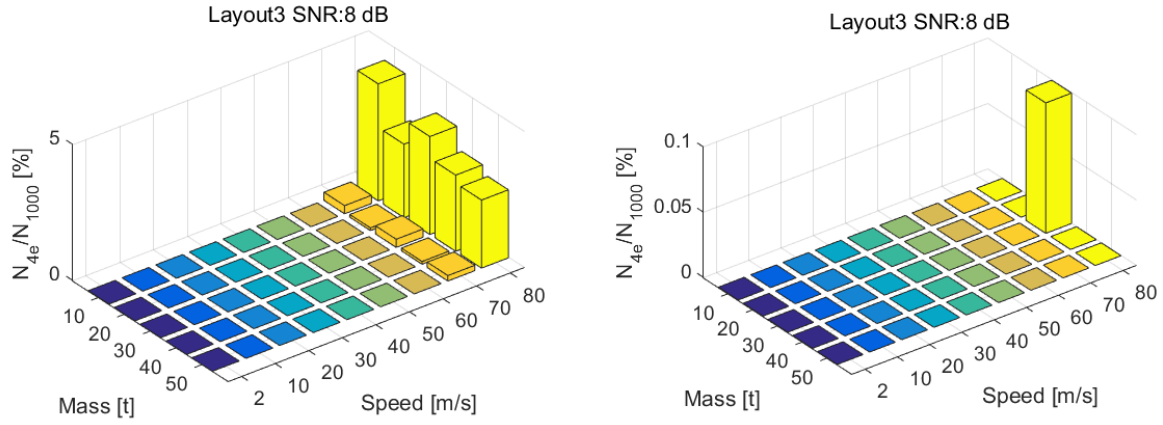

(a) TDA (b) FDA

Figure 3.51: Estimation errors $E_{Npercent}$ in the full mass and speed range with the Layout 3 and a SNR of 8 dB, after 1000 trains passed on the measurement layout

3.3.2 Computational Times

The processor adopted in the simulation campaign is a Intel(R) Core(TM) i7-4700HQ CPU 2.4 GHz. To introduce the analysis of the required computational times in the execution of the two algorithm is important to highlight step by step their operation. More focused the operations done in TDA (*Time Domain Algorithm*)/TDF (*Frequency Domain Algorithm*) approaches are listed below.

TDA Approach

1**)** *Reading of simulated signals coming from the measurement layout*;
2**)** *Adding of white noise on each simulated signal*;
3**)** *The time shifts between signals are computed by means of auto and cross correlation approaches*;
4**)** *Starting from the time shifts previously obtained, the vehicle speed estimations are performed, as described in Fig. 2.4*;
5**)** *The mean value of the vehicle speed is computed*;
6**)** *Post processing of the autocorrelation signal to detect train axles (Train detection), as described in Fig. 2.7*.

FDA Approach

1**)** *Reading of simulated signals coming from the measurement layout*;
2**)** *Adding of white noise on each simulated signal*;
3**)** *Computing of the crossing times of train axles on each measurement sleepers by using the spectrogram analysis*;
4**)** *Computing for each crossing axle of the vehicle speed using the time shifts previously estimated and the physical distance between the measurement points, as described in Fig. 2.20*;
5**)** *The mean value of the vehicle speed is computed*;
6**)** *Post processing of the signal to detect train axles (Train detection) as indicated in Fig. 2.17*.

Once the operation of the two algorithms are summarized, the mean computational times employed to estimate the crossing times, vehicle speed and number of crossing axles are indicated in Tabs. 3.12, 3.13. Obviously the global computational times increase with the increasing of the number of measurement sleepers: in order to compare the computational times required by both approaches Tab. 3.14 summarizes the ratio between the employed times, split for the estimated train parameter. In addition, Tab. 3.14 highlights how the FDA implies a bigger computational time both

in the train detection and in the vehicle speed computing. It also true that FDA allows to extract more informations from the simulated track inputs, by means of the detection of each axle (approach suitable for the wheel detection and traffic timetable purposes): these informations are not available with the TDA approach. This explains also the bigger computational time required in the speed computing (see also Tab. 2.7).

Table 3.12: Mean computational times required by the Time Domain Algorithm (TDA), applied to a single Manchester wagon

Layout (*N* **sleepers)**	**TDA** [s]	**Train Crossing Times & Speed Detection** [s]	**Train Detection** [s]
Layout1 (2)	0.266	0.046	0.057
Layout5 (3)	0.321	0.069	0.075
Layout9 (4)	0.367	0.094	0.095
Layout13 (5)	0.441	0.131	0.114

Table 3.13: Mean computational times required bu the Frequency Domain Algorithm (FDA), applied to a single Manchester wagon

Layout (*N* **sleepers)**	**FDA** [s]	**Train Crossing Times & Speed Detection** [s]	**Train Detection** [s]
Layout1 (2)	0.822	0.353	0.183
Layout5 (3)	1.011	0.507	0.208
Layout9 (4)	1.219	0.681	0.233
Layout13 (5)	1.429	0.838	0.253

Table 3.14: Comparison between computational times required by the two estimation algorithms

Parameter	Ratio Value
$T_{alg_{FDA}}/T_{alg_{TDA}}$	$(3 \div 3.5)$
$T_{axle_{FDA}}/T_{axle_{TDA}}$	$(2.2 \div 3.2)$
$T_{TiV_{FDA}}/T_{TiV_{TDA}}$	$(6.5 \div 6.7)$

Chapter 4

Results based on experimental input signal

Chapter Contents

This Chapter has the aims to evaluate the operation of the trained algorithms in a real scenario, concerning the measurement layout and the features of the acquired signal. Moreover is important to check its flexibility against a train composition and a measurement layout equipped with sensors different from the force ones used in the training phase. These capabilities are mandatory prerogatives of innovation offered by the proposed approaches. Fig. 4.1 summarizes the training phase used to calibrate the algorithms parameters in a wide range of operating conditions and the test phase used to check the trained algorithms in a real scenario.

The train configuration is described in Tabs. 4.1,4.2: it is composed by a locomotive and two wagons. Tab. 4.2 indicates the number of axles composing the vehicle (locomotive, first and second wagons), their inter space and the nominal load. The features of the measurement chain and the experimental data measured by sensors are indicated in Tab. 4.3: differently from the force sensors simulated in the training phase, the experimental measurement chain is equipped of two strain gauges.

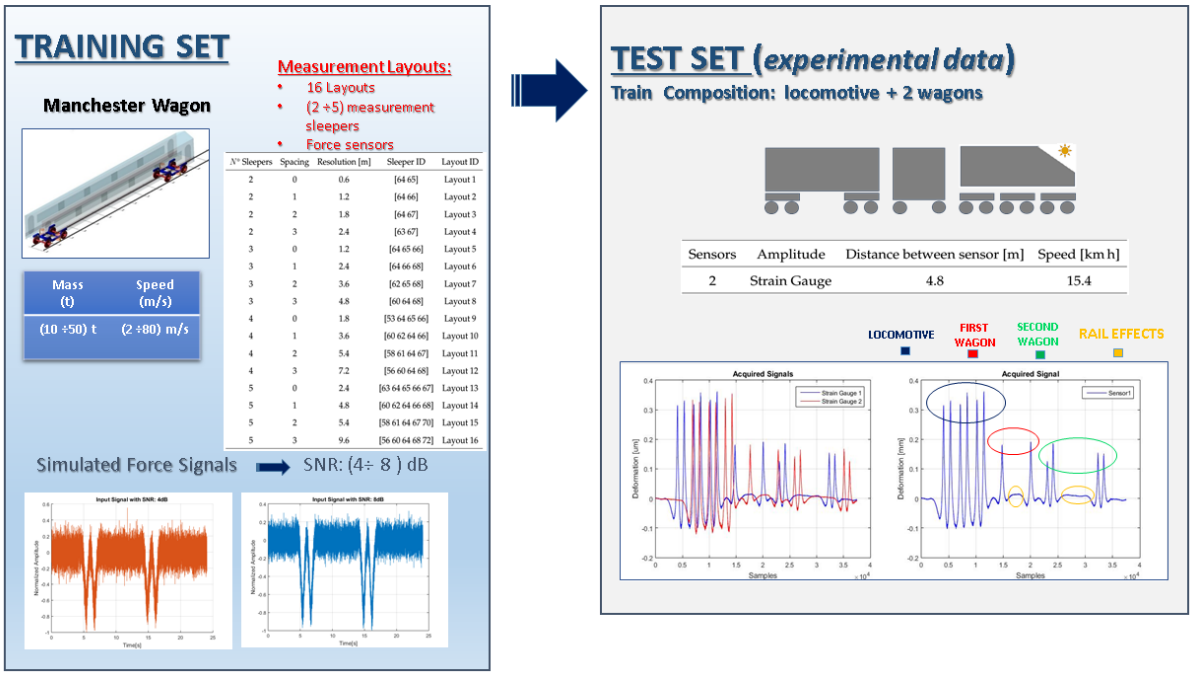

Figure 4.1: Procedure to test the performance of estimation algorithms on an experimental data: after the training phase in which a wide range of operating conditions regarding the vehicle and measurement chain have been simulated, the algorithm performance has been verified on a complete train composition

Table 4.1: Benchmark train composition

Vehicle	Wheelset	Prim. susp	Sec. susp	Axle load t	Bogie dist. m	Wheelbase [m]
Locomotive	b-b-b	yes	17.7	5.25	2.15	
First Wagon	1-1	yes	no	8.0	-	9
Second Wagon	2-2	yes	yes	7.8	15.8	1.8

Table 4.2: Train composition

Number of Wagon	Axle Number	Interspace [mm]	Nominal Load [t]
1) Locomotive	1	0	106
	2	2150	
	3	5250	
	4	7400	
	5	10500	
	6	12650	
2) First wagon	7	0	16
	8	9000	
3) Second wagon	9	0	31
	10	1800	
	11	15800	
	12	17600	

Table 4.3: Features of the measurement chain

Sensors	Amplitude	Distance between sensor [m]	Speed [km h]
2	Strain Gauge	4.8	15.4

The real scenario may involve undesired local peaks like those due to the back effect of rail traversed by train (see Fig. 4.2, [51]): is important testing the reliability of algorithms that must not detect these undesired peaks as train axles.

Results of the two estimation algorithms have been shown in order to check their robustness and flexibility to train with difference composition and measurement layout equipped of sensing elements different from those used in the training phase.

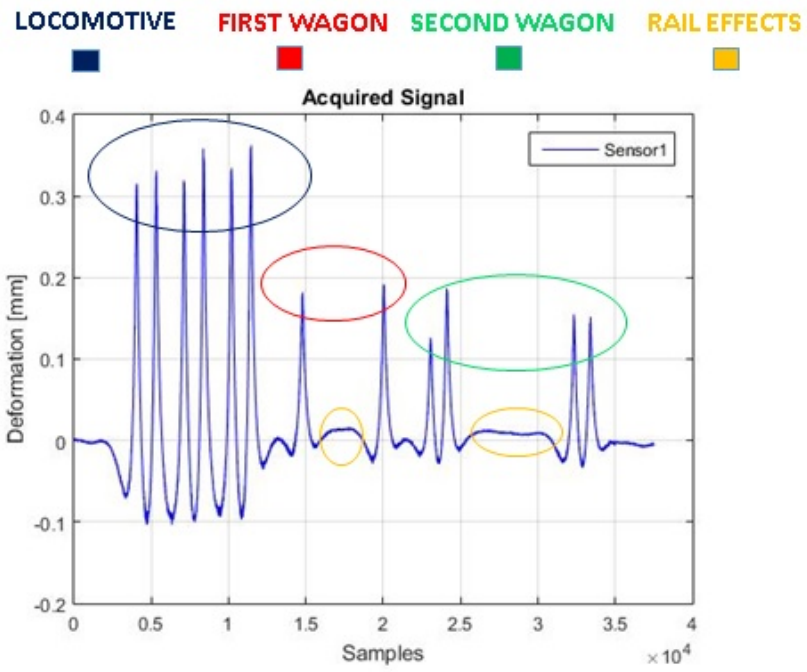

Figure 4.2: Experimental data of rail deformation due to the train axles: signal peaks correspond to the train axle and rail effects

4.1 Performance of the time domain approach (TDA)

Starting from the two measurements of rail deformation (see Fig. 4.3) the autocorrelation of the first one and its cross correlation with the second one is done (see Fig. 4.4).

Once the difference between the maximum values of the first and the second signals is computed, is possible to find the vehicle speed, as stated by Eq. 4.1.

$$V = D/(d12 * dt) * 3.6 = 15.36 km/h \tag{4.1}$$

where D (4.8 m) is the physical distance between the strain gauges, dt is the sampling time (0.0004 s) and $d12$(2814) is the difference between the samples corresponding with the maximum values of the autocorrelation of the first signal and its cross correlation with the second one. As regard the train detection functionality, as previously said, the application of the autocorrelation on signal composed by a high value of peaks may involve a very bigger number of autocorrelation ones (see Fig. 4.4 red line): for this reason the train detection can be done on sections of the original signal (see Fig. 4.5).

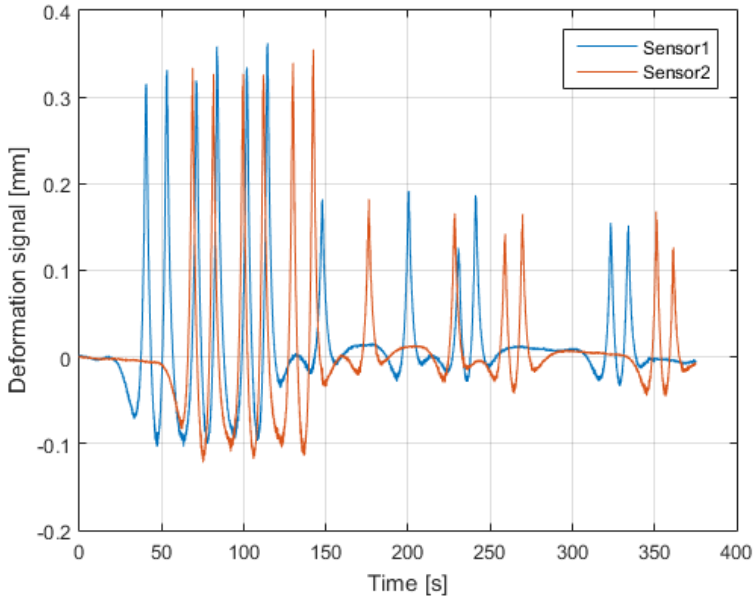

Figure 4.3: Deformation signals coming from the strain gauges described in Tab. 4.3

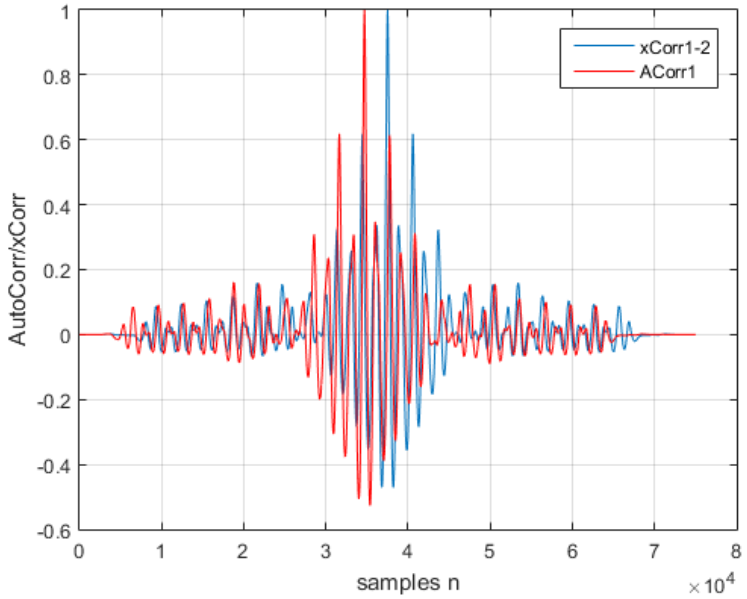

Figure 4.4: Autocorrelation of the first signal and its cross correlation with the second one

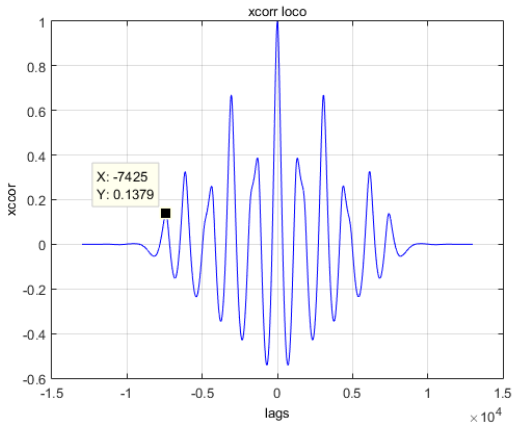

(a) Autocorrelation of the signal corresponding to the locomotive

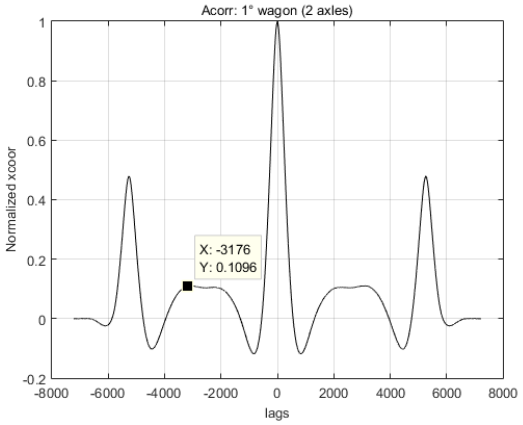

(b) Autocorrelation of the signal corresponding to the first wagon

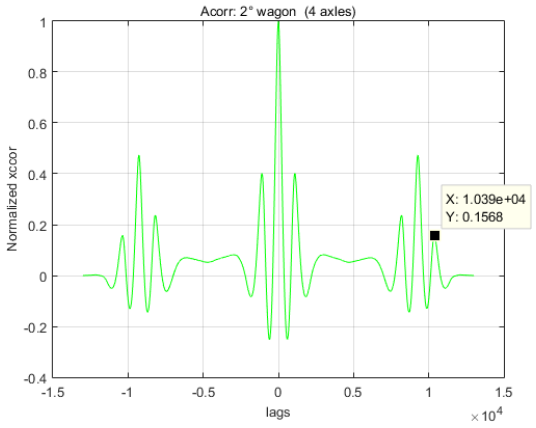

(c) Autocorrelation of the signal corresponding to the second wagon

Figure 4.5: Application of the autocorrelation on separated signals: locomotive + first and second wagons. The values useful to the train axles recognizing are in agree with the threshold established in the training phase

Fig. 4.5 also confirms the value of the threshold used to test the algorithm performance as train detector as indicated in Fig. 2.7. In particular Fig. 4.5b highlights that the threshold used in the training phase is useful to detect train axles and, at the same time, allows to not consider peaks due to rail effects in correspondence of the wheelbase of the two wagons(see Fig. 4.2).

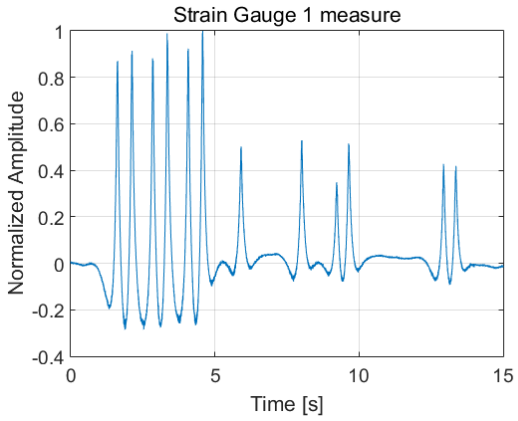

(a) Experimental deformation signal measured by a strain gauge

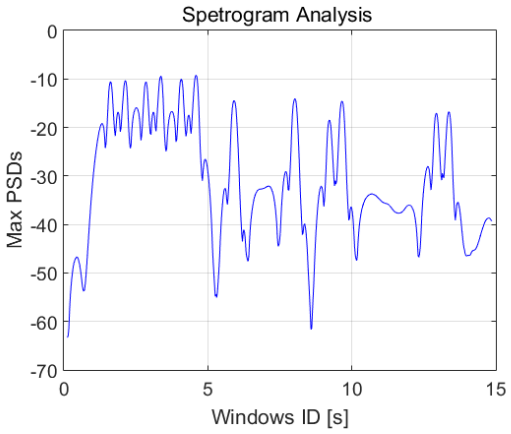

(b) PSD of the experimental signal

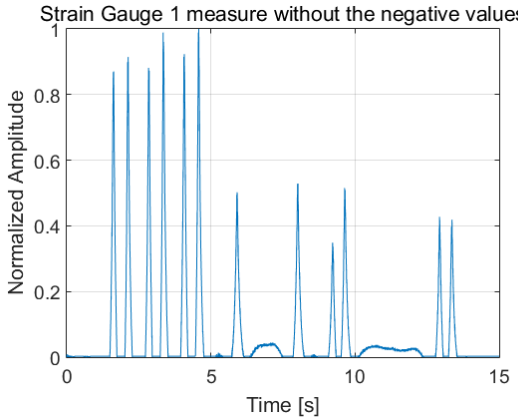

(c) Experimental deformation signal measured by a strain gauge with zero threshold cut-off

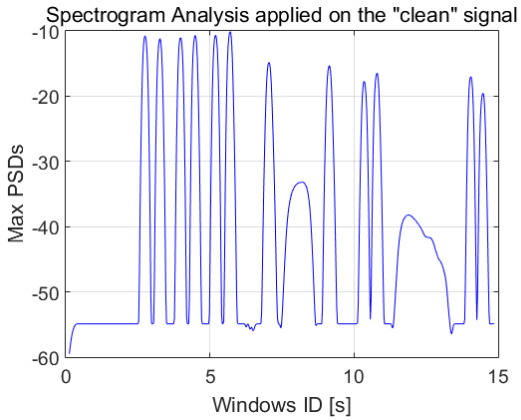

(d) PSD of the experimental signal

Figure 4.6: PSD of the experimental data: the threshold allows to cut undesired local peaks

4.2 Performance of the frequency domain approach (FDA)

The frequency domain approach has been applied to evaluate the train parameters on the experimental data coming from the strain gauges (see Fig. 4.3). The post processing of the signal is done (Fig. 4.7): starting from the experimental data also its positive values are considered to simplify the computing and not consider negative peaks caused but the rail extension (see Fig. 4.6 a-b). Then, once the spectrogram and each PSD maximum values are performed and plotted, the obtained signal is resampled. At

the end, just applying the cut off threshold of -24 dB (see Tab. 2.5), is possible to detect the train peaks (see Fig. 4.8).

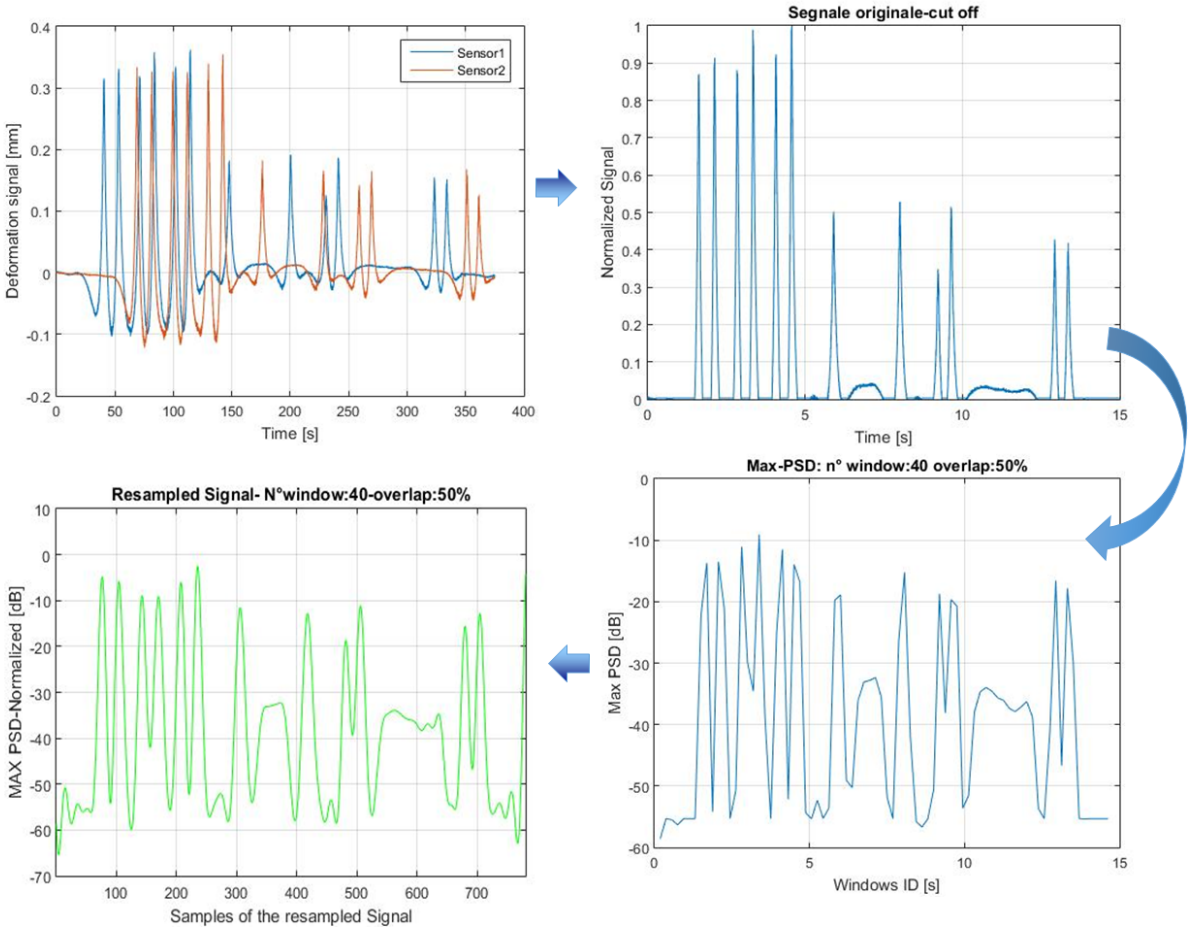

Figure 4.7: Post processing of the deformation signal: 1) signal amplitude normalization with also the cut-off of its the negative values 2) application of the spectrogram and plot of the signal composed by the maximum values of PSD for each window, 3) re-sampling of the obtained signal

Fig. 4.8 shows the results of the signal peaks detection process: using other thresholds is possible to detect peaks due to the locomotive axles from those provided by wagons. Furthermore, the performance of the algorithm as crossing times and speed estimator have been shown. As described in Par. 2.2 the estimation accuracy depends by the number of windows with which the spectrogram is applied. The final configuration used to estimate the vehicle speed and crossing times on measurement sleepers is a compromise between the computational time and the estimation accuracy.

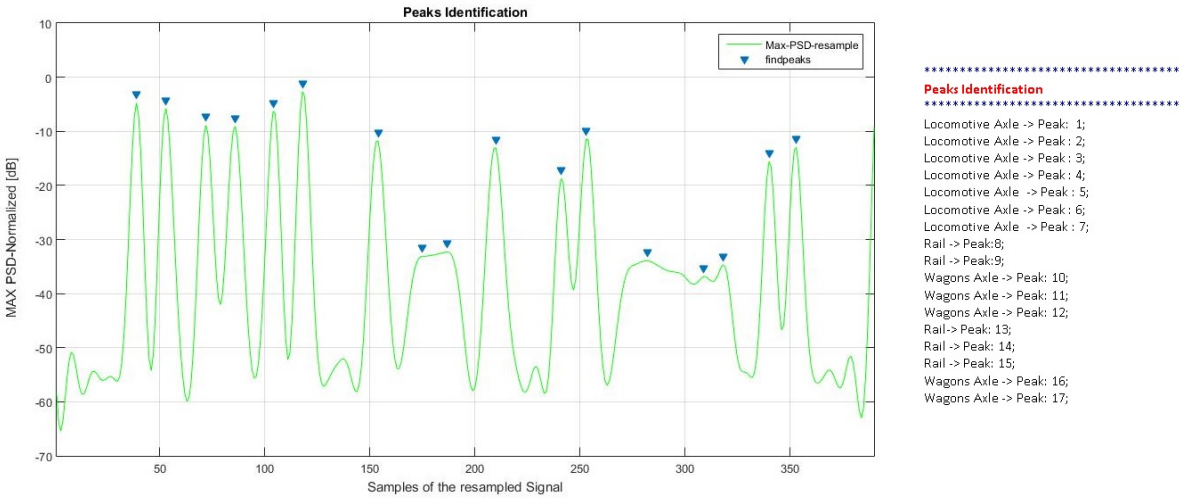

Figure 4.8: Peaks identification of the locomotive and wagons peaks by means of suitable cut-off thresholds

Table 4.4: Summarized results on crossing times and speed estimation

Strain Gauge	Locomotive						First Wagon		Second Wagon			
$SG1_{teo}$ [s]	1.6272	2.1312	2.8388	3.344	4.0784	4.580	5.9116	8.0076	9.2236	9.6396	12.9316	13.3636
$SG2_{teo}$ [s]	2.7636	3.2776s	3.9852	4.4904	5.2248s	5.7264	7.0580	9.1540s	10.3700	10.7860	14.0780	14.5100
Ti_{1est} [s]	1.613	2.1338	2.853	3.3738	4.0682	4.589	5.9034	8.0114	9.2266	9.6482	12.9218	13.3682
Ti_{2est} [s]	2.7538	3.2746s	3.9938	4.4898	5.1842s	5.705	7.0442	9.1522s	10.3426	10.789	14.0378	14.4842
Er_{1est} [%]	0.8727	-0.122	-0.5002	-0.8911	0.2501	-0.1965	0.1387	-0.0475	-0.0325	-0.08927	0.0758	-0.0344
Er_{2est} [%]	0.7139	0.0915	-0.2158	0.0134	0.7771	0.3737	0.1955	0.0197	0.2642	-0.0278	0.2856	0.1778
$V_{est}[\frac{m}{s}]$	4.2076	4.2076	4.2076	4.3011	4.3011	4.3011	4.2076	4.2076	4.3011	4.2076	4.3011	4.3011
Er_{Vest} [%]	0.7139	0.0915	-0.2158	0.0134	0.7771	0.3737	0.1955	0.0197	0.2642	-0.0278	0.2856	0.1778

In addition, the spectrogram configuration defined in Tab. 2.6 has been used to detect the crossing times on the two measurement points (see Tab. 4.3). Tab. 4.4 summarizes the theoretical, the estimated crossing times and their relative percentage errors.
Moreover, the estimated vehicle speed is computed for each detected axle (just dividing the physical distance between strain gauges with the difference between the axle crossing time on the two measurement points) and its mean value is equal to 0.17 % (see Fig. 4.9). Fig. 4.9 highlights how an increasing number of spectrogram windows may involve a better estimation accuracy but at the same time a higher computational cost. The chosen configuration (60 windows and 90% of overlap) allows to reduce the estimation percentage error (from 0.69% to 0.17%) with a computational time of a bit over 1 s.

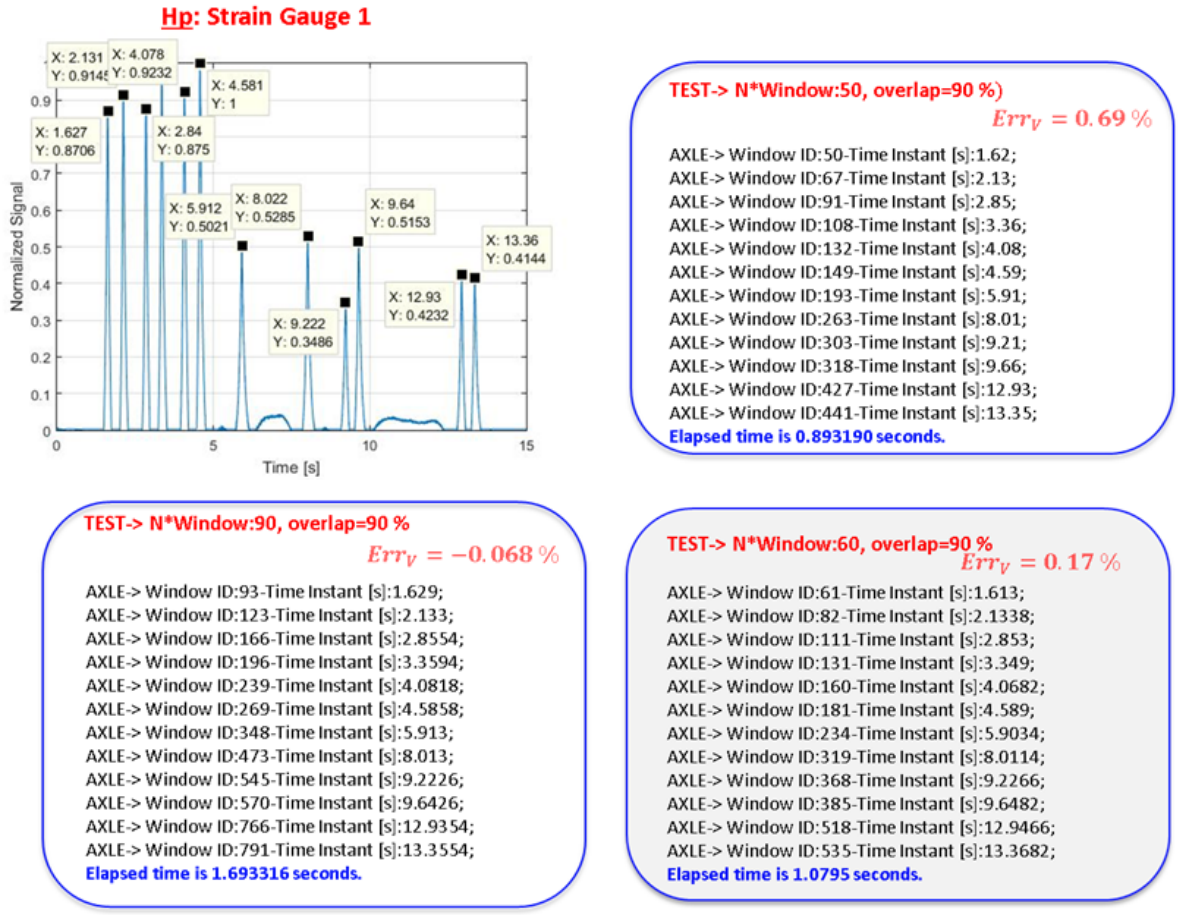

Figure 4.9: Comparison between the speed estimation accuracy and the required computational time, with an increasing number of spectrogram windows

In conclusion, the application of the approach to an experimental data has led several considerations on the algorithm robustness, concerning the spectrogram parameters and others regarding the approach. More focused, configurations of spectrograms aimed at estimating the number of crossing axles, crossing times on sensors and vehicle speed (see Tabs. 2.5, 2.6) have been validated. Furthermore, the value of the cut-off threshold (-24 dB) used to estimate the number of train axles during the training phase is also valid in the experimental test, despite the operating conditions (measurement layout, number and kind of sensing elements, mass and vehicle speed) are quite different. The approach allows also to avoid the detection of peaks different from train axle ones (see Fig. 4.8). The ending consideration concerns the noise affecting the input signal, that is several order smaller in the experimental test (see Fig. 4.3) than those set in the training campaign (see Fig. 2.7): this highlights how both of approaches have

been stressed, simulating operating conditions worse than the realistic ones.

4.3 Comparison between the TDA and FDA approaches on an experimental data

The above developed considerations on both the estimation approaches, once applied on an experimental data, confirm the drawbacks of the TDA and the benefits of the FDA approach. Indeed, Eq. 4.1 highlights the good operation of the correlation as speed estimator: the same cannot be said as axle counter detector due to the complexity of the autocorrelation signal, if applied on a composite input signal (see Fig. 4.4). As previously discussed, it is a weakness that it's no present with the approach making use of the spectrogram. The FDA approach also can detect the single wheel, involving functionalities of wheel detector, not only the train detector (guaranteed also by the TDA approach). In conclusion, the TDA approach is not enough flexible against a composite signal. The FDA approach is able to detect the crossing time of each train axles, information quite important for wheel detection purposes.

Chapter 5

WIM algorithm

Chapter Contents

In this chapter a WIM algorithm for the estimation of the vertical wheel loads is described (the weights of the wheelsets are included). The nominal values of the loads are taken from the model, in the simulated case, or are nominal train values in the experimental case. The WIM algorithm presented in this work is based on the vertical forces acting on the sleepers, acquired by means of dedicated force sensitive element placed over the sleepers in the section corresponding to the rail baseplate/pads (see Fig. 2.1). The WIM algorithm takes in input the estimated train parameters by the TDA/FDA approaches.

5.1 Architecture of the WIM algorithm

The general architecture of the algorithm is described in the diagram in Fig. 5.1.

The WIM algorithm is general purpose because it is able to manage different kinds of track measurements as input signals, such as rail deformations or forces acting on the sleepers and different measurement chains [52]. The WIM algorithm may

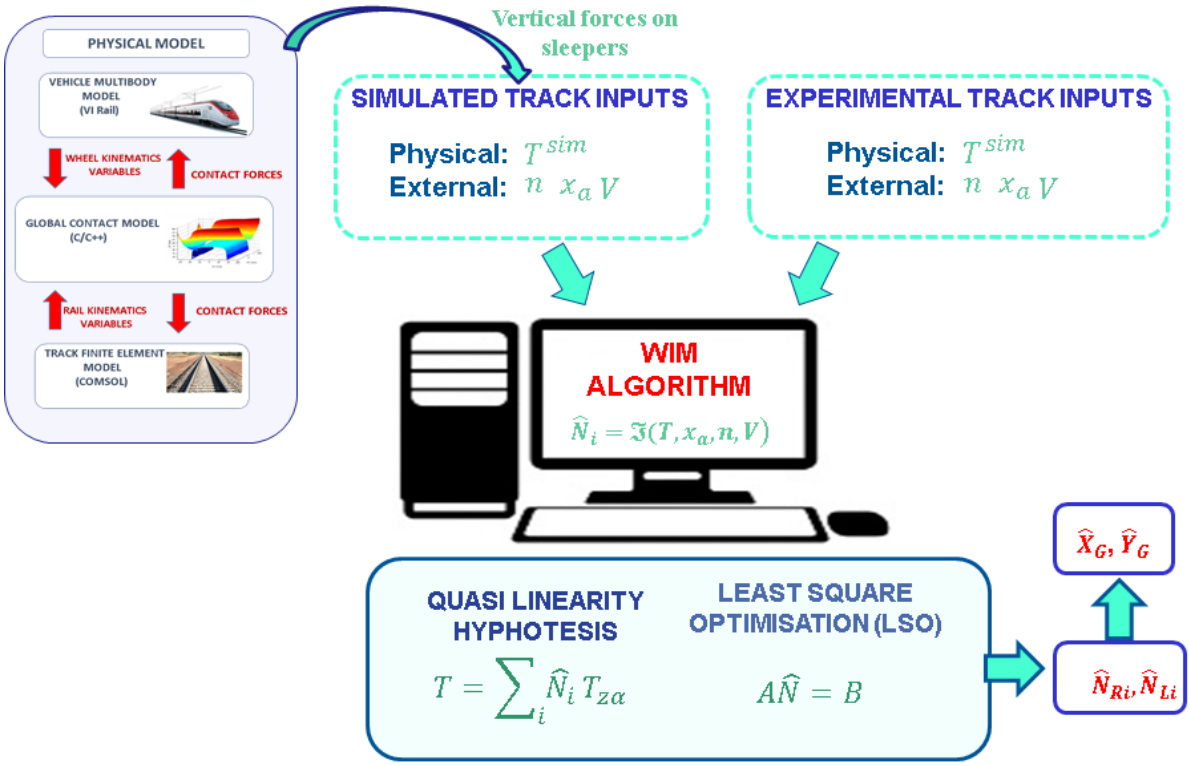

Figure 5.1: Operating of the WIM algorithm

operate both with simulated inputs ($\mathbf{T}_{rk}^{fn}$ and $\mathbf{T}_{lk}^{fn}$) provided by numerical models and with experimental data ($\mathbf{T}_{rk}^{sp}$ and $\mathbf{T}_{lk}^{sp}$) directly measured on the railway track. The developed WIM algorithm performs the estimation of the actual vertical right $\widehat{N}_{Ri}$ and left $\widehat{N}_{Li}$ wheel loads starting from the generic track measurements chosen as input signals $\mathbf{T}_{rk}$ and $\mathbf{T}_{lk}$ with $k = 1, .., N_m$ measured respectively at x_{rk} and x_{lk} (representing the abscissas of the right r and left l side of the $k-th$ measurement point). The WIM algorithm requires some additional information (external inputs) concerning the investigated vehicle. More specifically, vehicle speed V, the axle number n_{tot} and the axle positions inside the railway vehicle x_{ai} with $i = 1, .., n_{tot}$ must be known. These supplementary physical quantities may be identified by the approach previously discussed in Chapter 3 (the axle positions is guaranteed by the only FDA approach).
The main idea on which the new WIM algorithm is based arises from the quite intuitive hypothesis of supposing the system approximatively linear with respect to the vertical loads N_{Ri}, N_{Li} with $i = 1, ..., n_{tot}$ (the so-called *quasi-linearity hypothesis* (QLH)). In other words the effect of the generic load N_{Ri} and N_{Li} on the generic track measurement input $\mathbf{T}_{rk}$ and $\mathbf{T}_{lk}$ (in the present application the chosen track inputs are the simulated

vertical forces on the sleeper $\mathbf{F}^{fn}_{z\,rk}$ and $\mathbf{F}^{fn}_{z\,lk}$ or the measured ones $\mathbf{F}^{sp}_{z\,rk}$ and $\mathbf{F}^{sp}_{z\,lk}$) is assumed not to be affected by the presence of other loads (especially the contiguous ones). Evidently, in order to properly apply the superposition principle, the *quasi-linearity hypothesis* (QLH) must hold within the whole range of velocities V and cut frequencies f_n considered for the studied systems. Thanks to the previous assumption, the application of the superposition principle allows the calculation of the track inputs $\mathbf{T}_{rk}$ and $\mathbf{T}_{lk}$. More specifically, the track inputs $\mathbf{T}_{rk}$ and $\mathbf{T}_{lk}$ are respectively estimated through a linear combination of $2n_{tot}$ track fictitious input signals (namely the basis functions) produced by $2n_{tot}$ single fictitious loads N_f (one for each vehicle wheel) moving along the track and properly shifted in the time of a delay t_i. In order to find this basis, the algorithm makes use of the flexible multibody model of the track. In this case the linear combination coefficients are equal to $\widehat{N}_{Ri}/N_f$ and $\widehat{N}_{Li}/N_f$. Obviously, since the system can be assumed only approximately linear, a *Least Squares Optimization* (LQSO) is needed to minimize the approximation error and, at the same time, to optimize the values of $\widehat{N}_{Ri}$ and $\widehat{N}_{Li}$.

5.1.1 The quasi-linearity hypothesis

As previously stated, if the *quasi-linearity hypothesis* (QLH) holds, the application of the superposition effects allows to estimate the right $\mathbf{T}_{rk}$ and the left $\mathbf{T}_{lk}$ track inputs produced by the transit of the entire investigated vehicle through a linear combination of track responses (namely the basis functions) produced by single fictitious loads N_f. The presented WIM algorithm takes into account the coupling effect between the left and the right rail deformation caused by the dynamical behaviour of the sleeper-ballast ensemble. In the most general version of the WIM estimation procedure, the track basis functions due to the transit of both left and right fictitious loads are considered. More specifically, the quantities $\mathbf{B}^{rk}_{Ri}$ and $\mathbf{B}^{rk}_{Li}$ represent the chosen track fictitious response due to the transit of the $i-th$ fictitious load respectively on the right or on the left (denoted respectively with subscripts R and L) rail, measured at the right (r) side of the $k-th$ measurement point. Analogously, $\mathbf{B}^{lk}_{Ri}$ and $\mathbf{B}^{lk}_{Li}$ indicate the chosen track responses due to the transit of the $i-th$ fictitious load respectively on the right or on the left rail, measured at the left (l) side of the $k-th$ measurement station. All the $2n_{tot}$ right-side fictitious track inputs $\mathbf{B}^{rk}_{Ri}$ and $\mathbf{B}^{rk}_{Li}$ and the $2n_{tot}$ left-side fictitious track inputs $\mathbf{B}^{lk}_{Ri}$ and $\mathbf{B}^{lk}_{Li}$ with $i = 1, .., n_{tot}$ and $k = 1, .., N_m$ (in the present case the vertical

forces acting on the sleepers) produced by $2n_{tot}$ single fictitious loads N_f (with initial position x_{af}) can be easily assessed by introducing suitable time delays t_i:

$$t_i = \frac{x_{ai} - x_{af}}{V} \tag{5.1}$$

and by applying such delays to the track responses to the transit of a single fictitious load $B^{r/l}_{R/L\ k}(t)$ (i.e single wheel transit):

$$\mathbf{B}^{rk}_{Ri}(t) = \mathbf{B}^{rk}_{R}(t + t_i) \tag{5.2}$$

$$\mathbf{B}^{rk}_{Li}(t) = \mathbf{B}^{rk}_{L}(t + t_i) \tag{5.3}$$

$$\mathbf{B}^{lk}_{Ri}(t) = \mathbf{B}^{lk}_{R}(t + t_i) \tag{5.4}$$

$$\mathbf{B}^{lk}_{Li}(t) = \mathbf{B}^{lk}_{L}(t + t_i) \tag{5.5}$$

where $t \in [T_I, T_F - t_i]$.

At this point, thanks to the superposition principle, the track inputs $\mathbf{T}_{rk}$ $\mathbf{T}_{lk}$ produced by the transit of the entire train can be approximated according to the following expressions:

$$\mathbf{T}_{rk}(t) \approx \mathbf{T}_{rk\ app}(t) = \sum_{i=1}^{n_{tot}} \mathbf{B}^{rk}_{Ri}\alpha_{Ri} + \sum_{i=1}^{n_{tot}} \mathbf{B}^{rk}_{Li}\alpha_{Li} \tag{5.6}$$

$$\mathbf{T}_{lk}(t) \approx \mathbf{T}_{lk\ app}(t) = \sum_{i=1}^{n_{tot}} \mathbf{B}^{lk}_{Ri}\alpha_{Ri} + \sum_{i=1}^{n_{tot}} \mathbf{B}^{lk}_{Li}\alpha_{Li} \tag{5.7}$$

where the linear combination coefficients α_{Ri} α_{Li}, the estimated vertical loads $\widehat{N}_{Ri}$ $\widehat{N}_{Li}$ and the fictitious vertical load N_f are connected by the following expressions:

$$\alpha_{Ri} = \widehat{N}_{Ri}/N_{Rf}\alpha_{Li} = \widehat{N}_{Li}/N_{Lf}. \tag{5.8}$$

To simulate the sampling due to the measurement process, the time domain $t \in [T_I, T_F - t_i]$ has been discretized with a sample time Δt.
Re-arranging equations (5.6) and (5.7) in matrix form leads to the following equations:

$$\mathbf{T}_{rk} \approx B^{rk}_{R}\boldsymbol{\alpha}_R + B^{rk}_{L}\boldsymbol{\alpha}_L \tag{5.9}$$

$$\mathbf{T}_{lk} \approx B^{lk}_{R}\boldsymbol{\alpha}_R + B^{lk}_{L}\boldsymbol{\alpha}_L \tag{5.10}$$

where $k = 1, ..., N_m$, $\mathbf{T}_{rk}, \mathbf{T}_{lk} \in \mathbb{R}^{n_s \times 1}$, $B_R^{rk}, B_L^{rk}, B_R^{lk}, B_L^{lk} \in \mathbb{R}^{n_s \times n_{tot}}$ and $\boldsymbol{\alpha}_R, \boldsymbol{\alpha}_L \in \mathbb{R}^{n_{tot} \times 1}$. Considering the N_m measuring point a general expression can be written:

$$\mathbf{T}_r \approx B_R^r \boldsymbol{\alpha}_R + B_L^r \boldsymbol{\alpha}_L \tag{5.11}$$

$$\mathbf{T}_l \approx B_R^l \boldsymbol{\alpha}_R + B_L^l \boldsymbol{\alpha}_L \tag{5.12}$$

where $\mathbf{T}_r, \mathbf{T}_l \in \mathbb{R}^{n_s N_m \times 1}$, $B_R^r, B_L^r, B_R^l, B_L^l \in \mathbb{R}^{n_s N_m \times n_{tot}}$ and $\boldsymbol{\alpha}_R, \boldsymbol{\alpha}_L \in \mathbb{R}^{n_{tot} \times 1}$. Re-arranging equations (5.11) and (5.12) in a more compact matrix expression, Eq. 5.13 can be obtained:

$$\begin{bmatrix} \mathbf{T}_r \\ \mathbf{T}_l \end{bmatrix} = \begin{bmatrix} B_R^r B_L^r \\ B_R^l B_L^l \end{bmatrix} \begin{bmatrix} \boldsymbol{\alpha}_R \\ \boldsymbol{\alpha}_L \end{bmatrix}, \qquad \mathbf{T} = B\boldsymbol{\alpha} \tag{5.13}$$

where $\mathbf{T} \in \mathbb{R}^{2n_s N_m \times 1}$, $B \in \mathbb{R}^{2n_s N_m \times 2n_{tot}}$ and $\boldsymbol{\alpha} \in \mathbb{R}^{2n_{tot} \times 1}$.

5.1.2 Least squares estimation

Since the studied problem is only approximatively linear, a *Least Squares Optimization* (LSQO) is necessary to minimize the approximation error between $\mathbf{T}_{rk}$, $\mathbf{T}_{lk}$ and $\mathbf{T}_{rk\ app}$, $\mathbf{T}_{lk\ app}$ and, at the same time, to optimize the values of $\widehat{N}_{Ri}$, $\widehat{N}_{Li}$. In this specific case linear not-weighted least squares have been considered [53][54][55]. As previously said and shown in Fig. 1.1, the same inputs of TDA/FDA approaches and so the vertical forces acting on the sleepers (denoted with $\mathbf{F}_{z\ rk}^{fn}$ and $\mathbf{F}_{z\ lk}^{fn}$) have been adopted as track inputs, with a Hence, according to the adopted track inputs and taking into account the time sampling, equations (5.6) and (5.7) become:

$$\mathbf{F}_{z\ rk}^{fn}(t) \approx \sum_{i=1}^{n_{tot}} \alpha_{Ri}^{sim} \mathbf{B}_{Ri}^{rk}(t) + \sum_{i=1}^{n_{tot}} \alpha_{Li}^{sim} \mathbf{B}_{Li}^{rk}(t) \tag{5.14}$$

$$\mathbf{F}_{z\ lk}^{fn}(t) \approx \sum_{i=1}^{n_{tot}} \alpha_{Ri}^{sim} \mathbf{B}_{Ri}^{lk}(t) + \sum_{i=1}^{n_{tot}} \alpha_{Li}^{sim} \mathbf{B}_{Li}^{lk}(t) \tag{5.15}$$

with $h = 1, 2, \ldots, n_s$ and $k = 1, 2, \ldots, N_m$. Therefore, defining the $A \in \mathbb{R}^{2n_s N_m \times 2n_{tot}}$ matrix and vector $\mathbf{b}^{fn} \in \mathbb{R}^{2n_s N_m \times 1}$ as follows:

$$A = \left[\begin{array}{ccccccc|ccccc}
B^{r1}_{z\,R1} & \cdots & B^{r1}_{z\,Ri} & \cdots & B^{r1}_{z\,Rn_{tot}} & B^{r1}_{z\,S1} & \cdots & B^{r1}_{z\,Li} & \cdots & B^{r1}_{z\,Ln_{tot}} \\
\vdots & & \vdots & & \vdots & \vdots & & \vdots & & \vdots \\
B^{rk}_{z\,R1} & \cdots & B^{rk}_{z\,Ri} & \cdots & B^{rk}_{z\,Rn_{tot}} & B^{rk}_{z\,S1} & \cdots & B^{rk}_{z\,Li} & \cdots & B^{rk}_{z\,Ln_{tot}} \\
\vdots & & \vdots & & \vdots & \vdots & & \vdots & & \vdots \\
B^{rN_m}_{z\,R1} & \cdots & B^{rN_m}_{z\,Ri} & \cdots & B^{rN_m}_{z\,Rn_{tot}} & B^{rN_m}_{z\,L1} & \cdots & B^{rN_m}_{z\,Li} & \cdots & B^{rN_m}_{z\,Ln_{tot}} \\
\hline
B^{l1}_{z\,R1} & \cdots & B^{l1}_{z\,Ri} & \cdots & B^{l1}_{z\,Rn_{tot}} & B^{z\,l1}_{L1} & \cdots & B^{l1}_{z\,Li} & \cdots & B^{l1}_{z\,Ln_{tot}} \\
\vdots & & \vdots & & \vdots & \vdots & & \vdots & & \vdots \\
B^{lk}_{z\,R1} & \cdots & B^{lk}_{z\,Ri} & \cdots & B^{lk}_{z\,Rn_{tot}} & B^{z\,lk}_{L1} & \cdots & B^{lk}_{z\,Li} & \cdots & B^{lk}_{z\,Ln_{tot}} \\
\vdots & & \vdots & & \vdots & \vdots & & \vdots & & \vdots \\
B^{lN_m}_{z\,R1} & \cdots & B^{lN_m}_{z\,Ri} & \cdots & B^{lN_m}_{z\,Rn_{tot}} & B^{lN_m}_{z\,L1} & \cdots & B^{lN_m}_{z\,Li} & \cdots & B^{lN_m}_{z\,Ln_{tot}}
\end{array}\right] \tag{5.16}$$

$$(\mathbf{b}^{fn})^T = \left[\mathbf{F}^{fnT}_{z\,r1} \ldots \mathbf{F}^{fnT}_{z\,rk} \ldots \mathbf{F}^{fnT}_{z\,rN_m} \mathbf{F}^{fnT}_{z\,l1} \ldots \mathbf{F}^{fnT}_{z\,lk} \ldots \mathbf{F}^{fnT}_{z\,lN_m}\right]^T$$

the matrix form of (5.14) and (5.15) can be obtained:

$$\mathbf{b}^{fn} \simeq A\boldsymbol{\alpha}^{sim} \tag{5.17}$$

$$\boldsymbol{\alpha}^{sim} = \left[\alpha^{sim\,T}_R \alpha^{sim\,T}_L\right]^T \tag{5.18}$$

where

$$\boldsymbol{\alpha}^{sim}_R = \left[\alpha^{sim}_{R1}\alpha^{sim}_{R2}\alpha^{sim}_{R3}\alpha^{sim}_{R4}\right]^T \tag{5.19}$$

$$\boldsymbol{\alpha}^{sim}_L = \left[\alpha^{sim}_{L1}\alpha^{sim}_{L2}\alpha^{sim}_{L3}\alpha^{sim}_{L4}\right]^T. \tag{5.20}$$

By means of a *least squares optimization* (LQSO) (in this case linear and not-weighted), it is now possible to minimize the squared 2-norms $E^{fn2} = \left\|\mathbf{E}^{fn}\right\|^2_2$ of the approximation errors $\mathbf{E}^{fn} = A\boldsymbol{\alpha}^{sim} - \mathbf{b}^{fn}$ present in (5.17):

$$\boldsymbol{\alpha}^{sim} = \left(A^T A\right)^{-1} A^T \mathbf{b}^{fn} \tag{5.21}$$

where the matrix $A^T A$ is invertible if and only if the rank of A is maximum. Finally the values of the estimated vertical loads $\widehat{N}_{Ri}$, $\widehat{N}_{Li}$ can be computed starting from the knowledge of $\boldsymbol{\alpha}^{sim}$:

$$\boldsymbol{\alpha}^{sim} = \frac{N^{sim}}{N_f} = \left[\frac{\widehat{N}_{R1}}{N_{Rf}}\frac{\widehat{N}_{R2}}{N_{Rf}}\frac{\widehat{N}_{R3}}{N_{Rf}}\frac{\widehat{N}_{R4}}{N_{Rf}}\frac{\widehat{N}_{L1}}{N_{Lf}}\frac{\widehat{N}_{L2}}{N_{Lf}}\frac{\widehat{N}_{L3}}{N_{Lf}}\frac{\widehat{N}_{L4}}{N_{Lf}}\right]^T \tag{5.22}$$

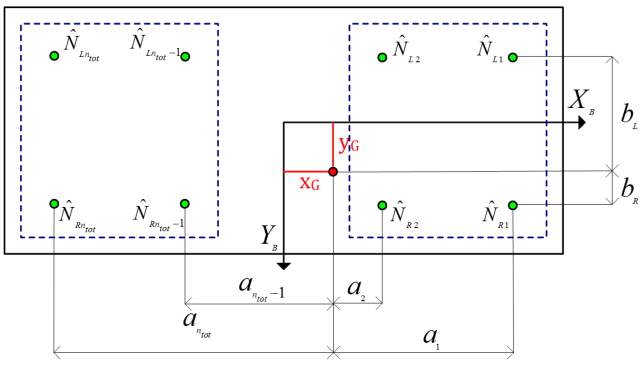

Figure 5.2: Evaluation of lateral Y_G and longitudinal X_G coordinates of the vehicle center of gravity.

where

$$\widehat{\mathbf{N}} = \left[\widehat{\mathbf{N}}_R^{sim^T} \widehat{\mathbf{N}}_L^{sim^T}\right]^T \tag{5.23}$$

with

$$\widehat{\mathbf{N}}_R = \left[\widehat{N}_{R1}\widehat{N}_{R2}\widehat{N}_{R3}\widehat{N}_{R4}\right]^T \tag{5.24}$$

$$\widehat{\mathbf{N}}_L = \left[\widehat{N}_{L1}\widehat{N}_{L2}\widehat{N}_{L3}\widehat{N}_{RL}\right]^T. \tag{5.25}$$

5.1.3 Center of gravity estimation

As previously stated, the innovative WIM algorithm, starting from the estimated wheel loads $\widehat{N}_{Ri}$ and $\widehat{N}_{Li}$, is able to evaluate the lateral Y_G and X_G longitudinal coordinates of the center of gravity. Considering the horizontal plane containing the center of gravity (COG) of the railway vehicle and introducing the reference system Oxy shown in Fig.5.2 where the origin O coincide with the geometric center of the carbody, the moment equilibrium around $X_B - axis$ and $Y_B - axis$ can be respectively expressed as:

$$\sum_{i=1}^{n_{tot}} (b_R \widehat{N}_{Ri} + b_L \widehat{N}_{Li}) = 0 \tag{5.26}$$

$$\sum_{i=1}^{n_{tot}} a_i (\widehat{N}_{Ri} + \widehat{N}_{Li}) = 0. \tag{5.27}$$

Taking into account the nominal values of the geometrical quantities of the vehicle such as the longitudinal position inside the train of each axle x_{ai} and the distance between the two nominal rolling radius s, the coefficients b_R, b_L, a_i can be re-written as function of the COG coordinates X_G, Y_G. More specifically, for the coefficients b_R, b_L the following expressions hold:

$$b_R = \frac{s}{2} - Y_G \tag{5.28}$$

$$b_L = -\frac{s}{2} - Y_G \tag{5.29}$$

whereas the coefficients a_i can be calculated as follows:

$$a_1 = -((x_{a1} - x_{a4})/2 + X_G = c1 + X_G \tag{5.30}$$

$$a_2 = -((x_{a2} - x_{a3})/2 + X_G = c2 + X_G \tag{5.31}$$

$$a_3 = ((x_{a2} - x_{a3})/2 + X_G = c3 + X_G \tag{5.32}$$

$$a_4 = -((x_{a1} - x_{a4})/2 + X_G = c4 + X_G. \tag{5.33}$$

At this point, the moment equilibrium equations can be re-written as:

$$C\widehat{\mathbf{G}} = \mathbf{d} \tag{5.34}$$

where $C \in \mathbb{R}^{2\times 2}$, $\widehat{G}, \mathbf{d} \in \mathbb{R}^2$ and

$$C = \begin{bmatrix} \sum_{i=1}^{n_{tot}} (\widehat{N}_{Ri} + \widehat{N}_{Li}) & 0 \\ 0 & \sum_{i=1}^{n_{tot}} (\widehat{N}_{Ri} + \widehat{N}_{Li}) \end{bmatrix} \tag{5.35}$$

$$\widehat{G} = \begin{bmatrix} \widehat{X}_G \\ \widehat{Y}_G \end{bmatrix} \tag{5.36}$$

$$\mathbf{d} = \begin{bmatrix} -\sum_{i=1}^{n_{tot}} (\widehat{N}_{Ri} + \widehat{N}_{Li}) c_i \\ \sum_{i=1}^{n_{tot}} (\widehat{N}_{Li} - \widehat{N}_{Ri}) \frac{s}{2} \end{bmatrix}. \tag{5.37}$$

Hence, the values of the estimated longitudinal $\widehat{X}_G$ and lateral $\widehat{Y}_G$ coordinates of the center of gravity G can be computed by inverting the C matrix according to the following expression:

$$\widehat{\mathbf{G}} = C^{-1}\mathbf{d} \tag{5.38}$$

Chapter 6

Performance of the WIM algorithm

Chapter Contents

The present section describes the performance of the WIM algorithm in estimating the vertical wheel loads $\widehat{N}_{Ri}$, $\widehat{N}_{Li}$ (with $i = 1, ..., n_{tot}$), starting from the knowledge of the vertical forces acting on the sleepers F_z. The WIM algorithm has been tested by means of two simulation campaigns, the first one is aimed at testing the accuracy in the vertical loads estimation, while the second one is focused on its performance to estimate the vehicle center of gravity. More particularly, simulation campaigns evaluate the performance of the WIM algorithm in terms of accuracy of the wheel load estimation and center of gravity, by varying different parameters of the vehicle and characteristics of the measurement system, such as the vehicle car body mass M, its speed V and the cut-off frequency f_n of the measurement chain. The basic procedure used to test the algorithm consists in comparing the nominal vertical wheel loads, N_{Ri} and N_{Li} (taken from the model, in the simulated case, or from nominal values in the experimental case) to the estimated loads $\widehat{N}_{Ri}$ and $\widehat{N}_{Li}$, computed by the WIM

estimation algorithm. This kind of comparison is really helpful to test the accuracy of the estimation algorithm model, when no experimental data are available.

6.1 Estimation of the vertical wheel loads $\widehat{N}_{Ri}$, $\widehat{N}_{Li}$

Initially, by way of example, the vertical forces on the sleepers $F^{fn}_{z\,rk}(t) = F^{fn}_{z\,rk}(x_{rk}, t)$ and $F^{fn}_{z\,lk}(t) = F^{fn}_{z\,lk}(x_{lk}, t)$ simulated through the physical model of the railway track (see Fig. 5.1) are compared with the vertical forces on the sleepers $F^{fn}_{z\,rk\,app}(t) = F^{fn}_{z\,rk\,app}(x_{rk}, t)$ and $F^{fn}_{z\,lk\,app}(t) = F^{fn}_{z\,lk\,app}(x_{lk}, t)$ estimated by means of the WIM algorithm. E.g the layout of the adopted measurement station consists in three measurement points ($N_m = 3$) on both rail sides ($x_{R1} = x_{L1} = 33$ m, $x_{R2} = x_{L2} = 34.2$ m and $x_{R3} = x_{L3} = 38.4$ m) (see Tab. 3.2, Fig. 6.1).

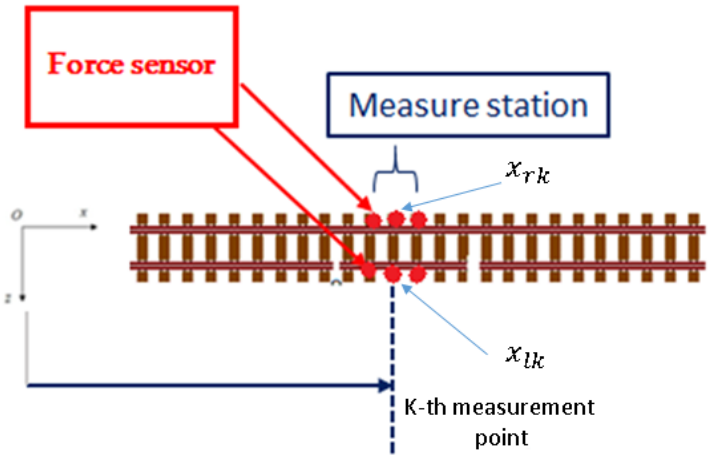

Figure 6.1: Reference measurement layout for the testing of the WIM algorithm

Fig. 6.2 illustrates both simulated $F^{fn}_{z\,r2}(t)$ $F^{fn}_{z\,l2}(t)$ and approximated $F^{fn}_{z\,r2\,app}(t)$ $F^{fn}_{z\,l2\,app}(t)$ (these simulations are shown as example) right and left vertical forces acting on the second measurement point on the right and left side of the sleeper ($x_{r2} = 34.2$ m) relative to a simulation performed at a speed value $V = 40$ m s^{-1} and a car body mass $M = 50$ t. The figure shows a good comparison between the simulated and estimated quantities hence confirming the accuracy of the *WIM* algorithm.

To compare the nominal N_{Ri}, N_{Li} and estimated $\hat{N}_{Ri}$, $\hat{N}_{Li}$ vertical loads on the wheels, an extensive simulations campaign has been carried out. In particular the dependence of the relative errors $e^{sim}_{Ri} = \frac{\widehat{N}^{sim}_{Ri} - N_{Ri}}{N_{Ri}}$ and $e^{sim}_{Li} = \frac{\widehat{N}^{sim}_{Li} - N_{Li}}{N_{Li}}$ on the vehicle speed V,

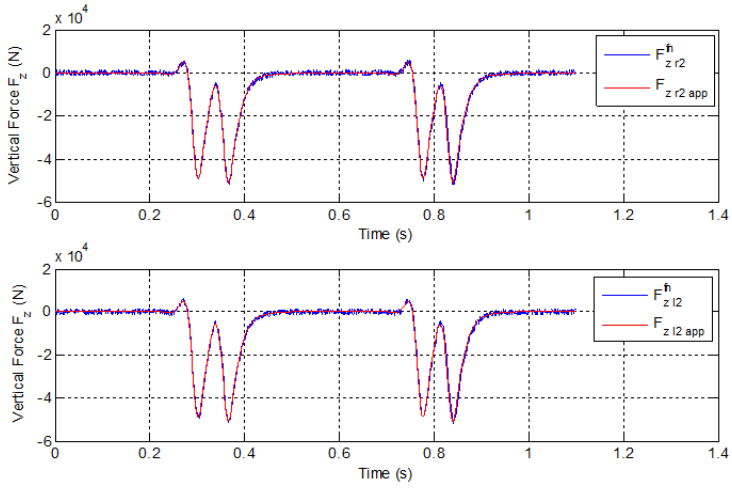

Figure 6.2: Vertical forces acting at $x_{r2} = 34.2$; comparison between the value resulting from the physical model $F^{fn}_{z\ r2}(t)$, $F^{fn}_{z\ l2}(t)$ and the one obtained according to the *quasi-linearity hypothesis* $F^{fn}_{z\ r2\ app}(t)$, $F^{fn}_{z\ l2\ app}(t)$

.

car-body mass M and the cut frequency f_n of the physical system is investigated. In Tab. 6.1 the considered variation ranges for the previous quantities are reported together with the resolutions adopted for the range discretization (ΔV, ΔM, Δf_n), where N_{sim} represent respectively the number of simulated values of V, M and f_n.

Table 6.1: Variation ranges of V, M and f_n adopted for the simulations campaign

Parameter	**Min.**	**Max.**	$\mathbf{N_{sim}}$	$\mathbf{\Delta}$
Velocity ($\mathrm{m\,s^{-1}}$)	10	40	4	$\Delta V = \frac{(V_{max}-V_{min})}{(N_v-1)}$
Car-body Mass (t)	20	50	4	$\Delta M = \frac{(M_{max}-M_{min})}{(N_M-1)}$
Frequency ($\mathrm{s^{-1}}$)	10	40	4	$\Delta f_n = \frac{(f_{n\ max}-f_{n\ min})}{(N_f-1)}$

The global performance of the *WIM* algorithm have been studied by considering the maximum relative error
$e^{sim}_{\max}(V, M, f_n)$:

$$e^{sim}_{\max} = \max_{1\le i\le n_{tot},} \left(max(|e^{sim}_{Ri}|, |e^{sim}_{Li}|)\right). \tag{6.1}$$

The values of the nominal N^{sim}_{Ri}, N^{sim}_{Li} and estimated $\widehat{N}^{sim}_{Ri}$, $\widehat{N}^{sim}_{Li}$ vertical loads acting on the vehicle wheels evaluated in a test performed with vehicle speed equal to V=40 $\mathrm{m\,s^{-1}}$, a car-body mass value $M = 50$ t and different values of f_n, are listed in Tab. 6.2. This case has been shown because it represents the worst case, in terms of error. The

good algorithm accuracy performance in estimating the vertical loads is mainly due to the capability of correctly describing the global shape of the solutions (both in space and in time) and not only the peaks, that are more affected by errors and noise. Tab. 6.2 shows a good accuracy of the *WIM* algorithm even for relatively low values of f_n. The maximum resulting error among the simulation campaign is equal to 1.9 $\%$ and it is relative to a simulation performed considering the following values: V=40 m s^{-1}, M=50 t and $f_n = 10$ s^{-1}.

Table 6.2: Estimated vertical loads on the vehicle wheels, $\widehat{N}_{Ri}^{sim}$, $\widehat{N}_{Li}^{sim}$: V=40 m s^{-1}, M=50 t, with different values of f_n.

Cut frequency f_n	Parameter	Value	Parameter	Value
Hz		kN		$\%$
10	$\widehat{N}_{R1}^{sim}$	75.4	e_{R1}^{sim}	1.4%
20		76.4		0.3%
30		76.4		0.3%
40		76.8		0.2%
10	$\widehat{N}_{L1}^{sim}$	75.4	e_{L1}^{sim}	1.7%
20		76.5		0.2%
30		76.6		0.01%
40		76.7		0.03%
10	$\widehat{N}_{R2}^{sim}$	75.9	e_{R2}^{sim}	0.7%
20		76.6		0.05%
30		76.6		0.1%
40		76.7		0.2%
10	$\widehat{N}_{L2}^{sim}$	76.2	e_{L2}^{sim}	0.4%
20		76.2		0.4%
30		76.4		0.17%
40		76.1		0.5%
10	$\widehat{N}_{R3}^{sim}$	75.2	e_{R3}^{sim}	1.7%
20		76.2		0.5%
30		76.4		0.19%
40		76.4		0.2%
10	$\widehat{N}_{L3}^{sim}$	75.1	e_{L3}^{sim}	1.9%
20		76.2		0.4%
30		76.2		0.01%
40		76.5		0.4%
10	$\widehat{N}_{R4}^{sim}$	75.3	e_{R4}^{sim}	1.7%
20		76.2		0.6%
30		76.9		0.3%
40		76.8		0.1%
10	$\widehat{N}_{L4}^{sim}$	75.7	e_{L4}^{sim}	1.3%
20		76.6		0.1%
30		76.7		0.06%
40		76.7		0.06%

Fig. 6.3 shows a comparison between the maximum relative percentage errors $e^{sim}_{\max}(V, M, f_n)$ and their behaviour as a function of speed V and cut-off frequencies f_n; each graph is relative to a different value of the vehicle car body mass M.

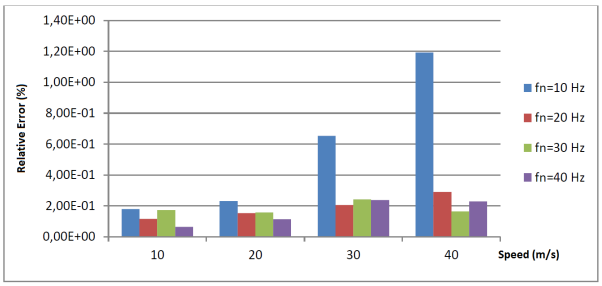

(a) M=20 t

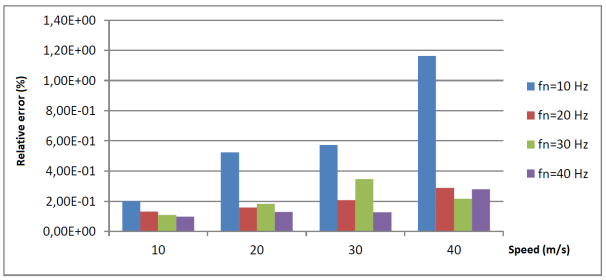

(b) M=30 t

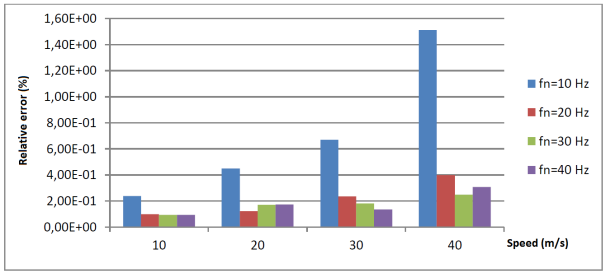

(c) M=40 t

Figure 6.3: Behaviour of the percentage $e^{sim}_{\max}(V, M, f_n)$ relative error as a function of speed V, car body mass M and cut-off frequency f_n

Although the good algorithm performance, these results show how the estimation of vertical loads becomes more difficult, in front of an increase of the travel speed V and low values of the cut-off frequency f_n, because the quasi-linearity hypothesis begins to be a critically condition if these quantities become too high.

6.1.1 Estimation of the vertical wheel loads $\widehat{N}_{Ri}$, $\widehat{N}_{Li}$ with different measurement layouts

In this section, the performance of algorithm in estimating of the vertical wheel load are estimated in several working conditions concerning the measurement layout. Figs. 6.4-6.7 show the trend of the maximum value of the relative estimation error computed between the right and left loads and among all the sleepers that equip the measurement layouts (see Tab. 3.2). The simulation parameters are those indicated in Tab. 6.1 with a cut-off frequency f_n of 20 Hz. Fig. 6.4 highlights how layouts equipped with consecutive sleepers involve bigger errors and their trends are not constant with the increasing of the vehicle speed: better trend are obtained with a space between the two sensing elements. Similar considerations can be done for the other test case.
Results highlight the good operation of the estimation algorithm on vertical loads against measurement layouts that differ for the number and spacing among the sensing elements: in particular, the increasing of the number of force sensors involves lower estimation errors but also a bigger number of sensing elements, maintenance time and installation cost. A good compromise between installation maintenance and cost and the estimation accuracy can be provided by measurement layouts equipped of three sensor spaced of 1.8 m, which involves estimation errors below the 0.5 % (Layout 7).

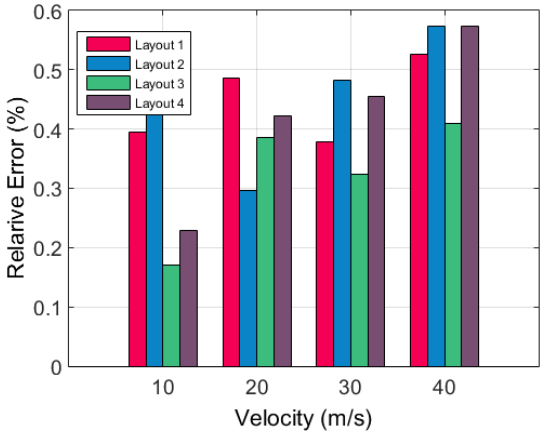

(a) M=20 t

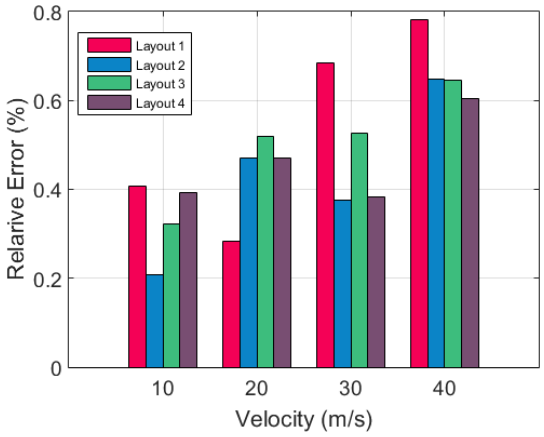

(b) M=30 t

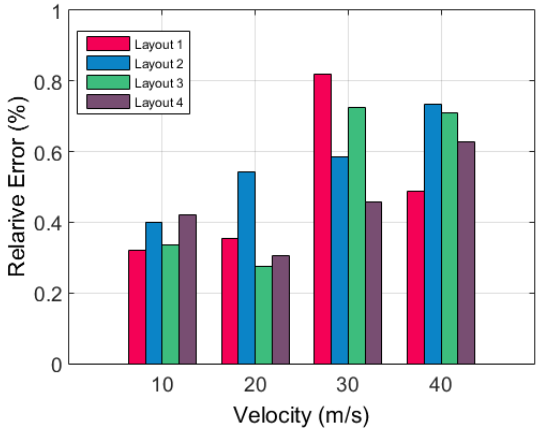

(c) M=40 t

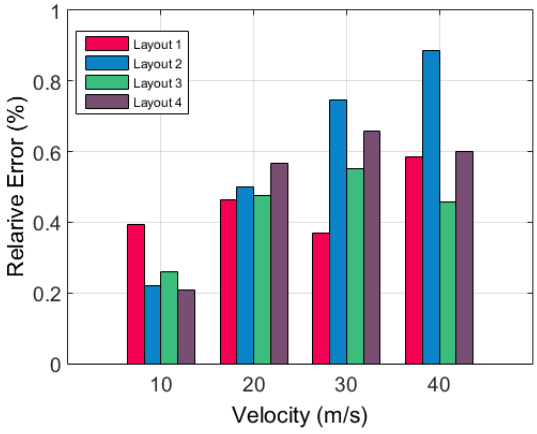

(d) M=50 t

Figure 6.4: Behaviour of the percentage $e^{sim}_{\max}(V, M, f_n)$ relative as a function of the measurement layout equipped of two sleepers: errors are below the 1 %

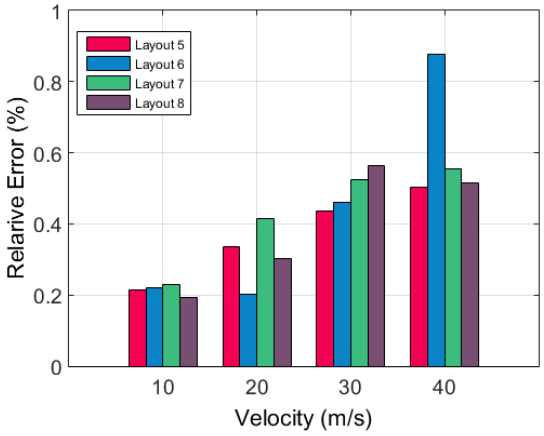

(a) M=20 t

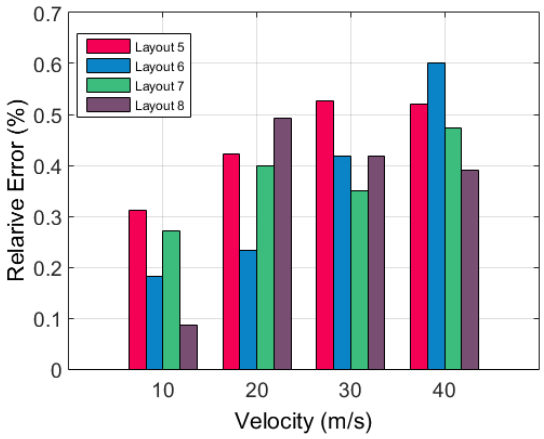

(b) M=30 t

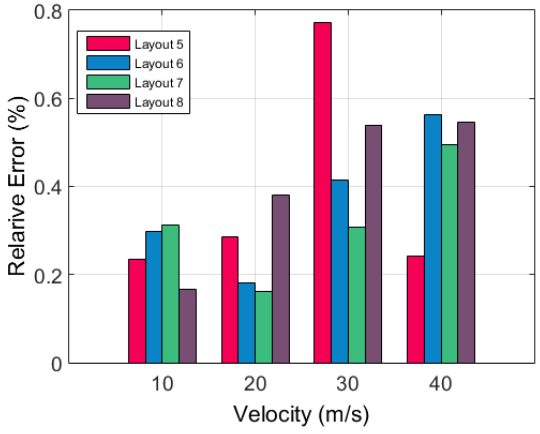

(c) M=40 t

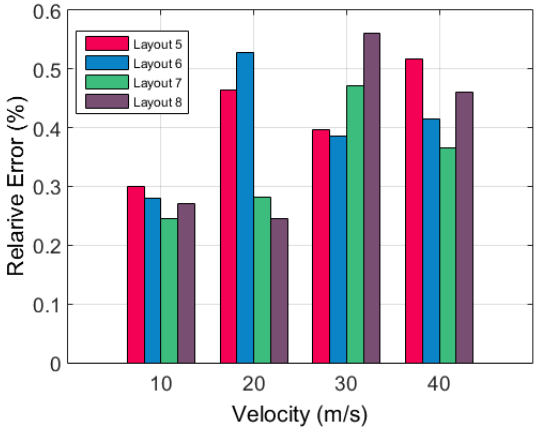

(d) M=50 t

Figure 6.5: Behaviour of the percentage $e^{sim}_{\max}(V, M, f_n)$ relative as a function of the measurement layout equipped of three sleepers: errors are below the 0.9 %

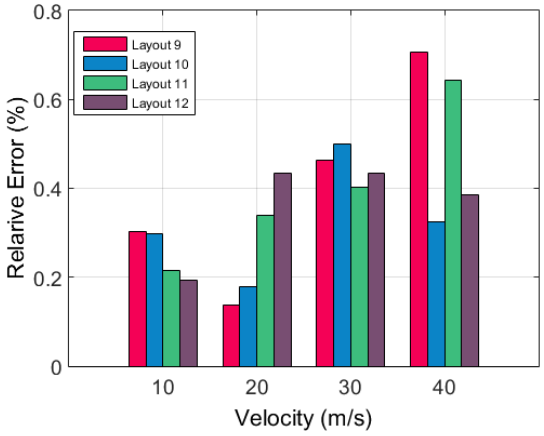

(a) M=20 t

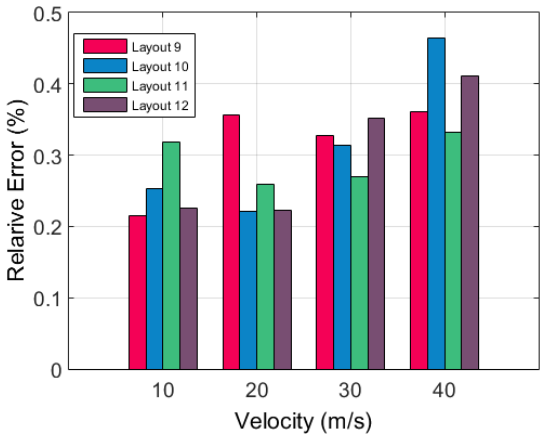

(b) M=30 t

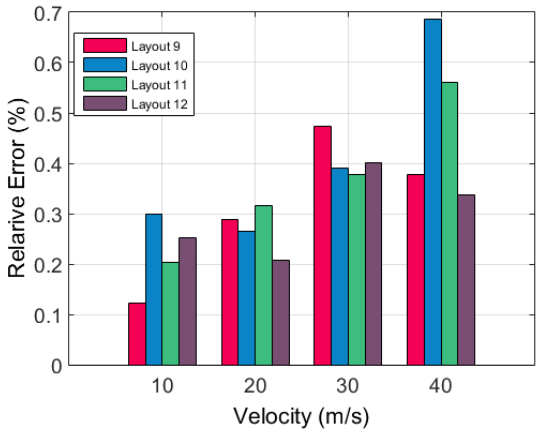

(c) M=40 t

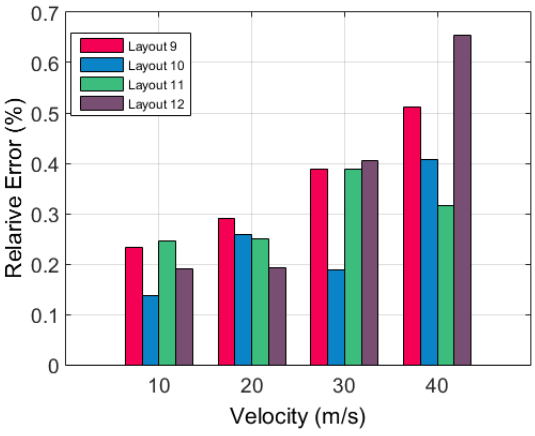

(d) M=50 t

Figure 6.6: Behaviour of the percentage $e^{sim}_{\max}(V, M, f_n)$ relative as a function of the measurement layout equipped of four sleepers: errors are below the 0.7 %

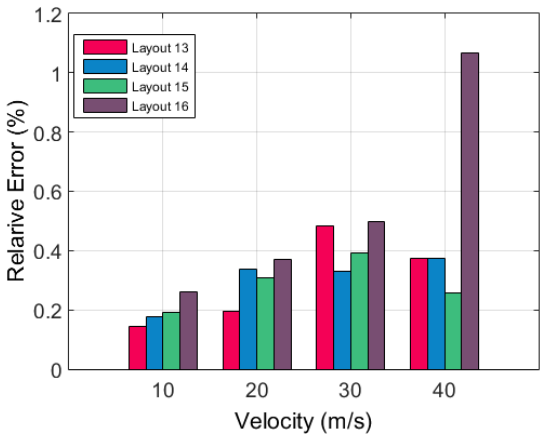

(a) M=20 t

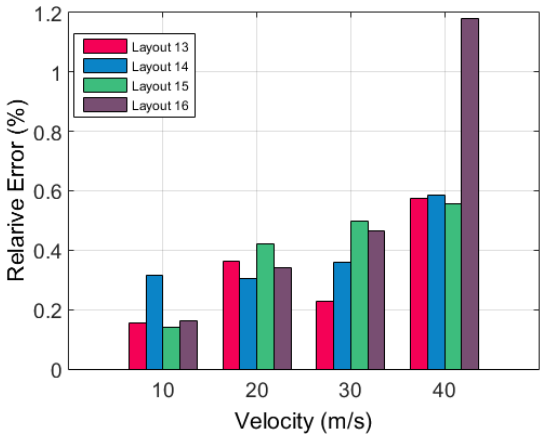

(b) M=30 t

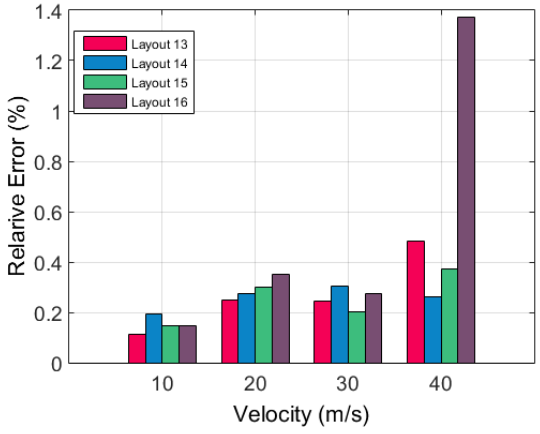

(c) M=40 t

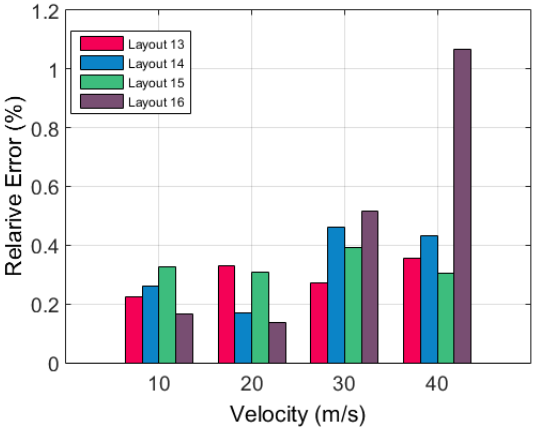

(d) M=50 t

Figure 6.7: Behaviour of the percentage $e^{sim}_{\max}(V, M, f_n)$ relative as a function of the measurement layout equipped of five sleepers: errors are below the 0.6 %

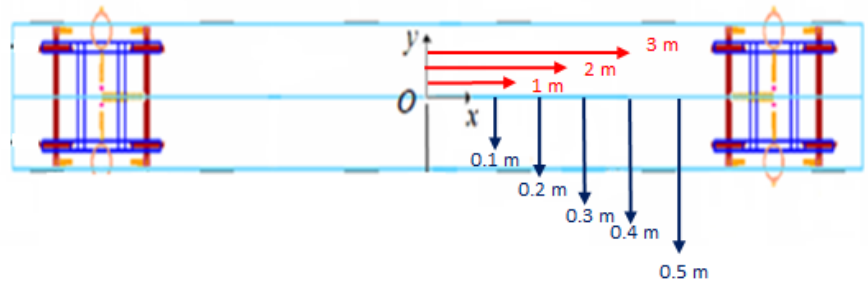

Figure 6.8: Positions of $G_b(x_b, y_b)$ used to modify $G(x, y)$

6.2 Estimation of the longitudinal X_G and lateral Y_G coordinates of the center of gravity G

The good accuracy properties exhibited by the WIM algorithm in estimating vertical loads acting on the wheels make the algorithm suitable for the estimation of the longitudinal X_G and lateral Y_G position of the vehicle center of mass G, to avoid possible imbalances. To test the performance of the WIM algorithm in the estimation of the longitudinal X_G and lateral Y_G coordinates of the center of gravity G, two dedicated simulation campaign have been performed. Firstly the actual longitudinal X_G, and then the lateral Y_G position of the center of mass G of the train have been varied by changing the position of the center of mass of the carbody G_B in the physical model of the train according to the values shown in Fig. 6.8 and indicated in Tab. 6.3.

Table 6.3: Positions of the center of mass of the car-body G_b expressed in longitudinal X_b and lateral Y_b coordinates

X_b	Y_b
$X_b = 0.0$ m	$Y_b = 0.0$ m
$X_b = 1.0$ m	$Y_b = 0.1$ m
$X_b = 2.0$ m	$Y_b = 0.2$ m
$X_b = 3.0$ m	$Y_b = 0.3$ m
	$Y_b = 0.4$ m
	$Y_b = 0.5$ m

Fig. 6.9 shows the comparison among the estimated loads $\hat{N}_R$, $\hat{N}_L$ with different value of the longitudinal displacement X_b performed with a vehicle speed $V = 10$ m s^{-1}: it

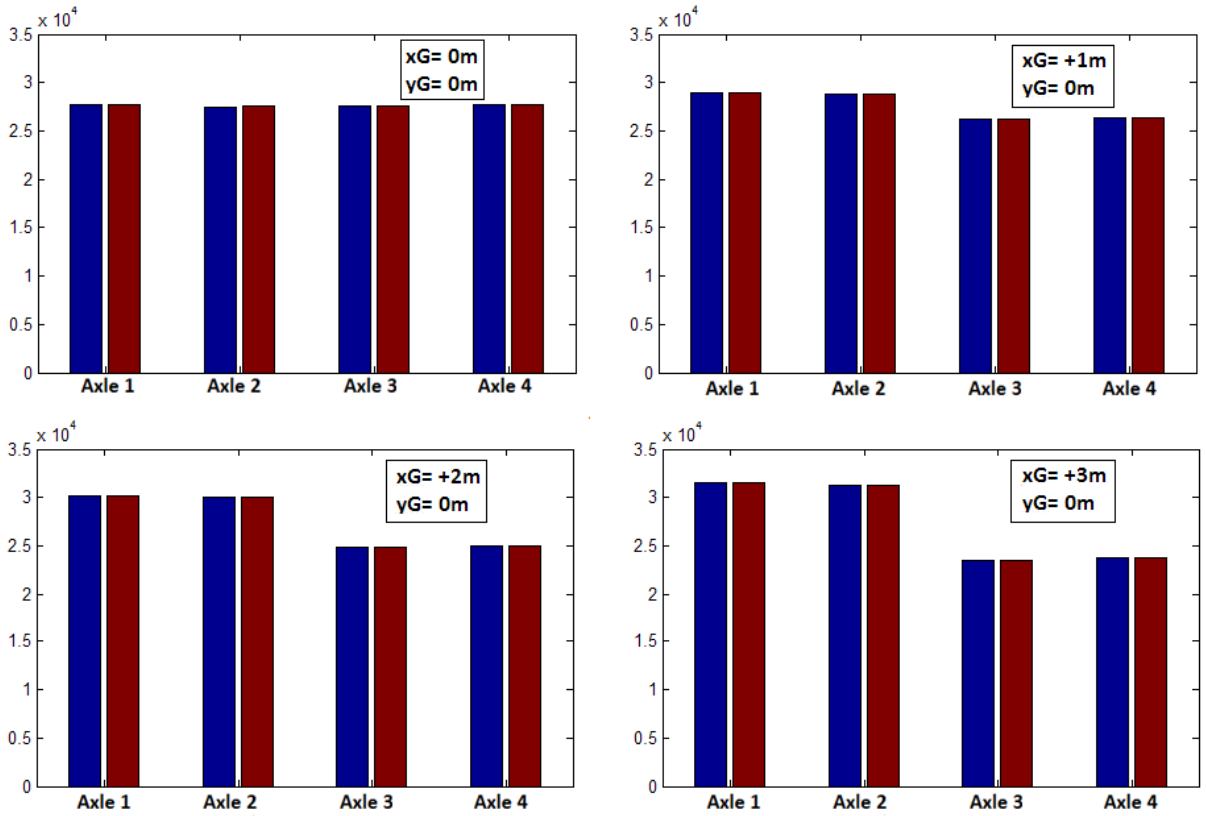

Figure 6.9: Comparison between estimated loads $\hat{N}_R$, $\hat{N}_L$ with different value of longitudinal displacement X_b of the centre of mass, performed with a vehicle speed $V = 10$ m s^{-1}. Blue bar: load on the left wheel - Red bar: load on the right wheel

can be seen that loads are perfectly symmetrical with respect to a longitudinal plane, being the center of gravity G placed along the longitudinal axis of the vehicle (the vehicle is not unbalanced along the lateral axis). The position of the car body center of gravity G_b is translated longitudinally toward the head of the train, with a consequent increase of the loads acting on the wheels of the frontal bogie ($\widehat{N}_{R_1}$, $\widehat{N}_{L_1}$, $\widehat{N}_{R_2}$, $\widehat{N}_{L_2}$) and a decrease ones of the rear bogie ($\widehat{N}_{R_3}$, $\widehat{N}_{L_3}$, $\widehat{N}_{R_4}$, $\widehat{N}_{L_4}$).

The test campaign has been performed considering a car-body mass value $M = 10$ t, a cut-off frequency $f_n = 20$ s^{-1} and four different values of the vehicle velocity ($V = 10, 20, 30, 40$ m s^{-1}). Tab. 6.4 summarizes the maximum percentage relative error on estimated loads as a function of the vehicle speed V and longitudinal displacement X_b of center of gravity G_b, performed with a car-body mass $M = 10$ t and a cut-off frequency $f_n = 20$ s^{-1}.

The second simulation campaign is focused on the lateral displacement Y_G of the

Table 6.4: Percentage relative error on estimation loads with different speed and longitudinal displacement position of car body center of gravity X_b, performed with a car body mass M=10 t and a cut-off frequency f_n=20 s^{-1}

Position m	Par.	**Speed** 10 m s^{-1}	**Speed** 20 m s^{-1}	**Speed** 30 m s^{-1}	**Speed** 40 m s^{-1}
$X_b = 0$		0.10 %	0.16 %	0.26 %	0.26 %
$X_b = +1$	$e^{sim}_{\max}$	0.19 %	0.16 %	0.20 %	0.42 %
$X_b = +2$		0.19 %	0.24 %	0.25 %	0.33 %
$X_b = +3$		0.17 %	0.29 %	0.19 %	0.37 %

Table 6.5: Percentage relative error on estimation loads with different speed and lateral displacement position of car body center of gravity Y_b, performed with a car body mass M=10 t and a cut-off frequency f_n=20 s^{-1}

Position m	**Speed** 10 m s^{-1}	**Speed** 20 m s^{-1}	**Speed** 30 m s^{-1}	**Speed** 40 m s^{-1}
$Y_b = 0$ (m)	0.13 %	0.14 %	0.20 %	0.27 %
$Y_b = +0.1$ (m)	0.15 %	0.15 %	0.251 %	0.278 %
$Y_b = +0.2$ (m)	0.19 %	0.24 %	0.28 %	0.213 %
$Y_b = +0.3$ (m)	0.17 %	0.29 %	0.19 %	0.22 %
$Y_b = +0.4$ (m)	0.17 %	0.29 %	0.19 %	0.22 %

vehicle center of gravity for different values of speed V, according to the real dimensions of the car. Fig. 6.10 shows the trends of the estimated loads in according with the displacement of the center of mass in the lateral direction. Table. 6.5 indicates the behaviour of the errors as a function of speed, performed with a car body mass M=10 t and a cut-off frequency f_n=20 s^{-1}: a weak increase of the errors with the speed is present. These results confirm the good performance of the proposed WIM algorithm in estimating unbalance loads consequently it can be used to compute the vehicle centre of gravity $\widehat{G}$, starting from the values of vertical estimated loads on the wheel.

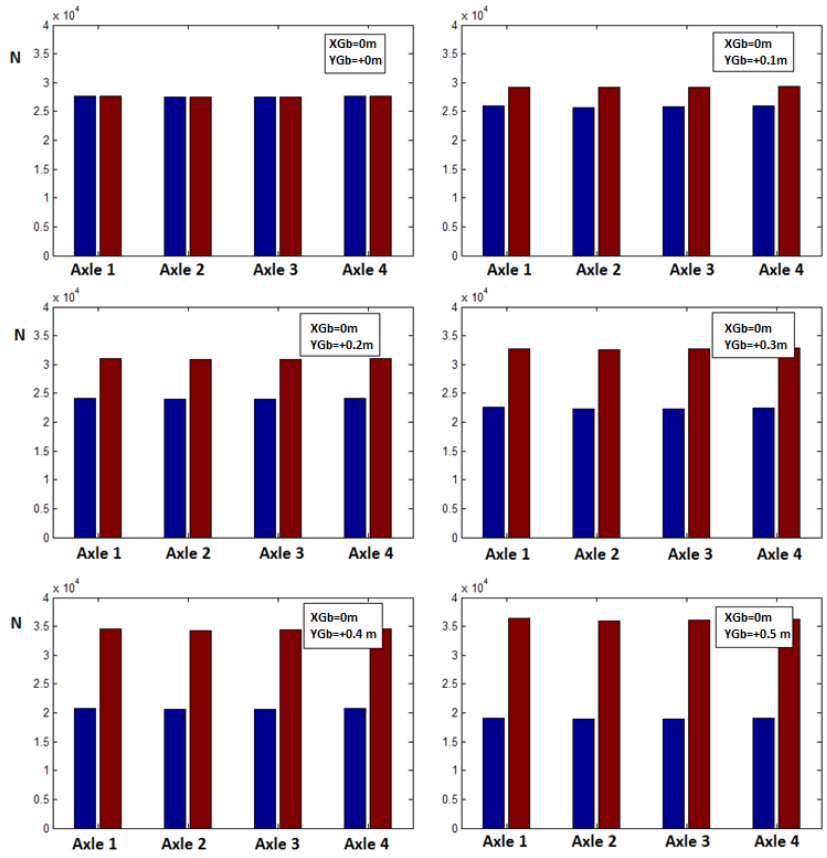

Figure 6.10: Comparison between estimated loads $\hat{N}_R$, $\hat{N}_L$ with different value of lateral displacement Y_b of the centre of mass, performed with a vehicle speed $V = 10$ m s^{-1} . Blue bar: load on the left wheel - Red bar: load on the right wheel

6.2.1 Estimation of the longitudinal X_G and lateral Y_G coordinates of the center of gravity G with different measurement layouts

The performance of the estimation on the center of mass have been verified with different measurement layouts as done for the estimation of the vertical load, carrying out estimation errors below the 0.1%: there is no a relevant dependence between the estimation accuracy and the measurement layouts. E.g the results in estimating the center of mass with a longitudinal displacement of 1 m and lateral one of 0.2 m are shown for the measurement layouts equipped of three sensing elements (see Figs. 6.11-6.12).

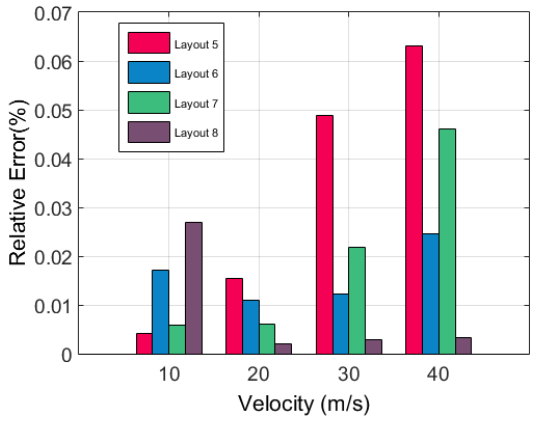

(a) M=20 t

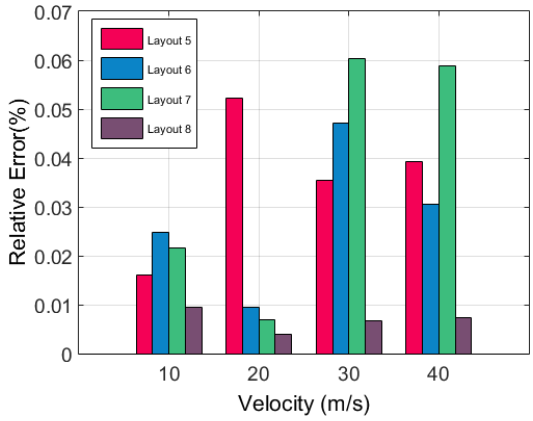

(b) M=30 t

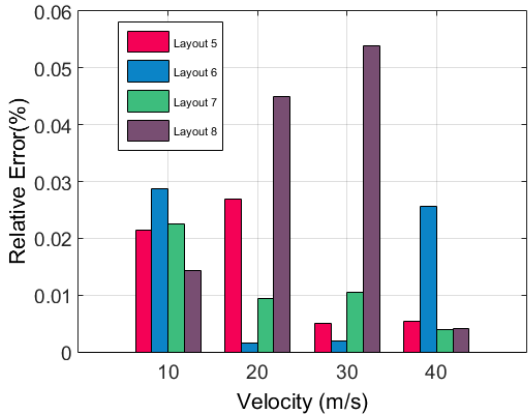

(c) M=40 t

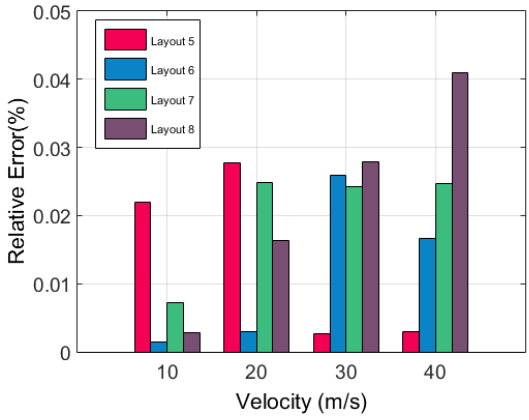

(d) M=50 t

Figure 6.11: Estimation errors of the centre of mass with a longitudinal displacement of 1 mand measurement layouts equipped of 3 sensing elements

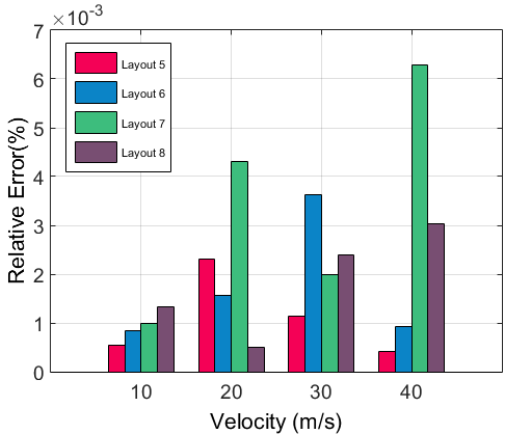

(a) M=20 t

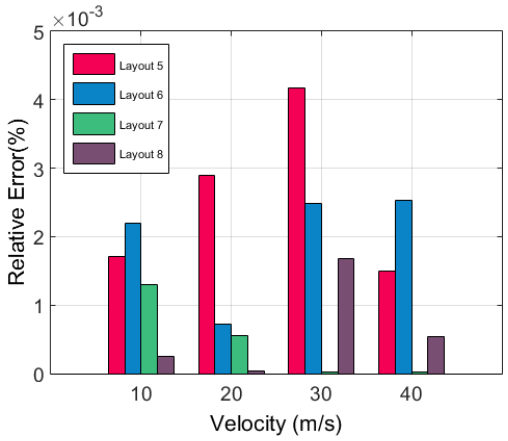

(b) M=30 t

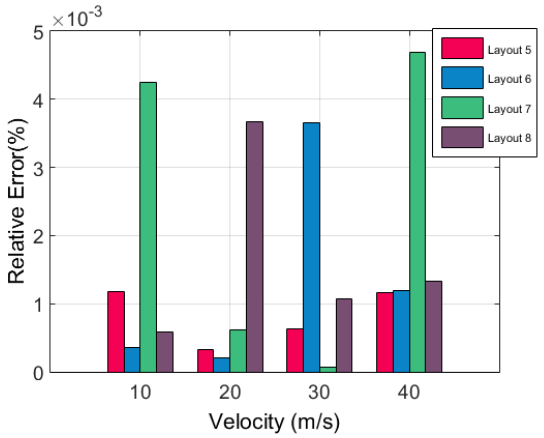

(c) M=40 t

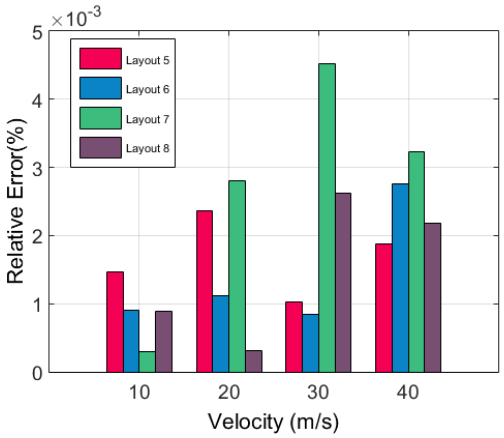

(d) M=50 t

Figure 6.12: Estimation errors of the centre of mass with a lateral displacement of 0.2 mand measurement layouts equipped of 3 sensing elements

Chapter 7

Conclusion, final remarks and future developments

This work has led the development of several estimation algorithms of train parameters, towards aims of train detection and monitoring of the railway traffic on the rail for vehicle maintenance and diagnostic purposes. Two estimation approaches (TDA/FDA) have been formulated to carry out functionalities of train detection: moreover a WIM (Weigh in Motion) algorithm has been studied which, taking in input several train parameters estimated by the TDA/FDA approaches, is able to do accurate estimations of vertical wheel loads and the vehicle center of gravity.
The estimation approaches are able to manage both the experimental data or, in absence of them, simulated track inputs provided by a physical model of vehicle, track and a global contact model that manages the interaction between them. The benchmark vehicle is the Manchester wagon. The developed approaches can manage different kind of input signals, in the proposed work vertical forces on measurement sleepers are considered.
The physical model has been also used to test the global performance in a wide range of operating conditions concerning the vehicle (mass and speed) and the measurement chain, in terms of number of sensing elements and their displacement.
A comparison between the TDA and FDA approaches have been done, both on their estimations accuracy, functionalities and required computational times.
There is no a relevant difference between the estimation errors, but the FDA algorithm has shown a better flexibility towards the performance of the measurement chain, vehicle parameters and, in addition, provides more data on train, thanks to the

detection of each train axles: these information may be useful for the train geometry recognition and the wheel detection, no possible with the TDA approach. As a consequence, the FDA is more powerful than the TDA, because is able to estimate train parameters and define also the vehicle geometry. The performance of the approaches have been also verified simulating performance of the measurement chain worse than that of a real scenario, in terms of noise affecting the measure: results highlight a major robustness of the FDA rather than that of the TDA, entailing low estimation errors, despite the high noise level applied on the input signal (SNR: 4dB). The only weakness of the FDA approach lies in its computational times, especially in the speed computing, if are compared with those required by the TDA algorithm, but this can be a good compromise, considering its capability to detect each train axles. A study on the optimal configuration of the measurement chain has been done, as a compromise among maintenance and installation cost and the estimation accuracy of the TDA/FDA approaches: to this end, the chosen measurement layout is equipped of two sensing elements spaced of 1.8 m. In this scenario both approaches (TDA/FDA) have led estimation errors of the vehicle speed below the 1% in the [2-80]m s^{-1} speed range and [10-50]t mass range. The FDA approach entails errors of train detection only for vehicle speeds bigger than 70 m s^{-1} (no errors are committed with layouts equipped of a bigger number of sensing elements) and the TDA no commits errors until 60 m s^{-1}. The approaches optimized in the training phase have been validated on an experimental data, showing the major robustness of the FDA algorithm towards signals corresponding to a train composition.

In conclusion, the FDA is the better estimation approach proposed in this work, able to compute train parameters like the crossing times, speed and axles recognition, entailing very low errors and showing flexibility towards different kind of input signal and measurement layout and provides robustness against possible high white noise level on the measured input signal. The TDA approach requires less computational times, especially in the speed computation, but is not flexible and robust in the same way as shown by the FDA approach. Moreover, a WIM algorithm has been developed, aimed at estimating the vertical wheel loads and the vehicle center of gravity, whose estimation accuracies has a big relevance to face problems concerning possible unbalances: the approach has been tested in the [20-50]m s^{-1} speed range and [10-40]t mass range and the estimation errors are always below the 1% in all the measurement layouts. A good compromise between installation maintenance/cost and the estimation accuracy, can be offered by measurement layouts equipped of three

sensors spaced of 1.8 m, which involve estimation errors below the 0.5%.
The proposed approaches have a great impact especially in the state of art of this topic, due to the absence of studies that develop algorithms to estimate several train parameters, in different working conditions about the measurement layout, sensors and train composition. The studied solutions are able to do estimation of different train parameters, starting from the same sensors and using the same approach(Auto/Cross Correlation (TDA), Spectrogram(FDA)). Moreover, another aspect of novelty of this study (if compared with those present in literature) lies in the training of the algorithms with a wide simulation campaign in order to verify their operation also in worse working condition than those of a real measurement scenario. At the end, efforts have been done to drive the development towards efficient solutions efficient, able to meet realistic requirements, concerning their performance (estimation accuracy, computational times) and the measurement station properties (number of sensors and maintenance times). Future developments regard the integration of the proposed estimation approaches in electronic boards in order to perform a wide experimental campaign, aimed at testing their good operation shown by this study.

Appendix A

Appendix-TDA

The global performance of the TDA approach have been evaluated in all the measurement layouts. Following, the trend of the estimation accuracy on the vehicle speed obtained with the Monte Carlo analysis are shown for different measurement layouts in order to evaluate the performance of the approach against the noise level inserted in the estimation process. Results are comfortable due to the reaching of the Monte Carlo convergence in each operating condition, concerning the vehicle (mass, speed) and the layouts (number and spacing among sensing elements).

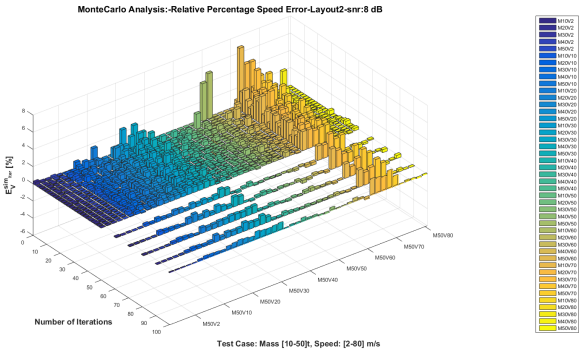

(a) $E_v^{sim_{iter}}$ trend in the full speed range (2-80) $\mathrm{m\,s^{-1}}$ and mass one (10-50) t

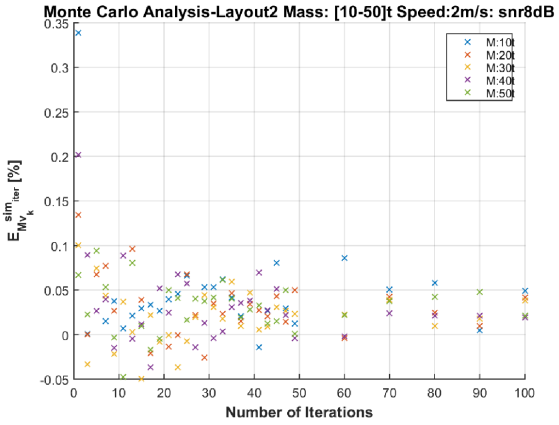

(b) $E_{Mv_k}^{sim_{iter}}$ with k=2 $\mathrm{m\,s^{-1}}$ trend for each Monte Carlo iteration

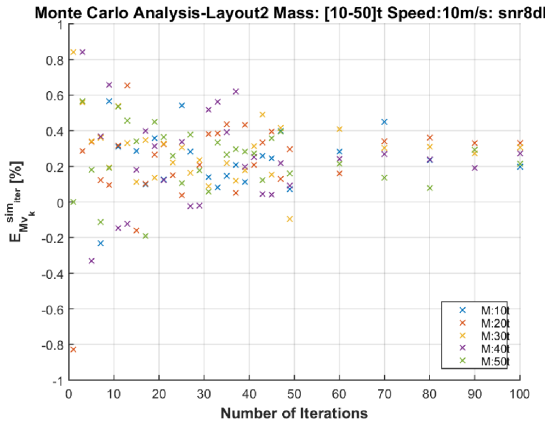

(c) $E_{Mv_k}^{sim_{iter}}$ with k=10 $\mathrm{m\,s^{-1}}$ trend for each Monte Carlo iteration

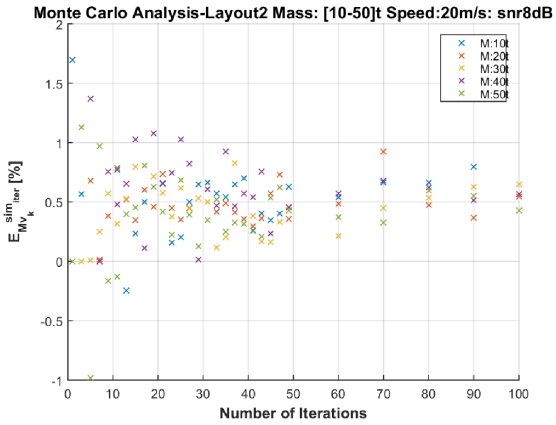

(d) $E_{Mv_k}^{sim_{iter}}$ with k=20 $\mathrm{m\,s^{-1}}$ trend for each Monte Carlo iteration

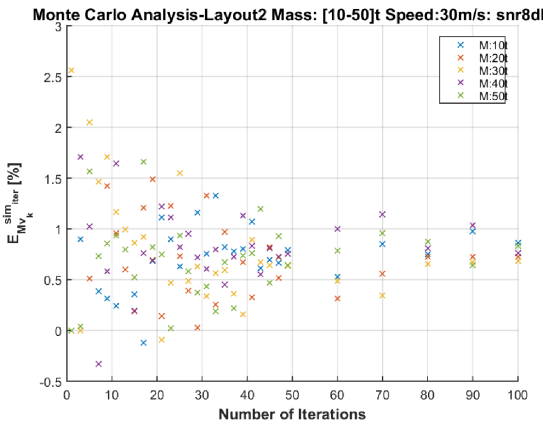

(e) $E_{Mv_k}^{sim_{iter}}$ with k=30 $\mathrm{m\,s^{-1}}$ trend for each Monte Carlo iteration

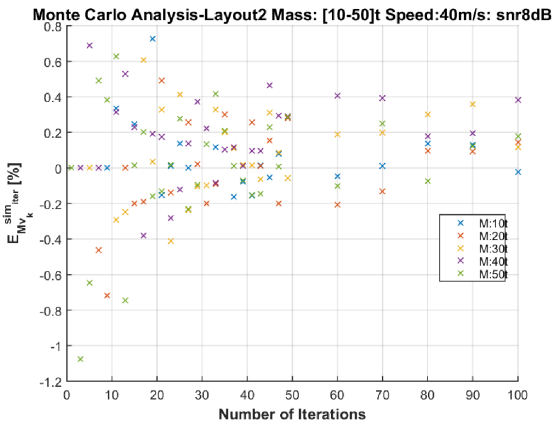

(f) $E_{Mv_k}^{sim_{iter}}$ with k=40 $\mathrm{m\,s^{-1}}$ trend for each Monte Carlo iteration

Figure A.1: Layout2: (a) $E_v^{sim_{iter}}[\%]$ convergence with the Monte Carlo Analysis in all vehicle mass and speed. Focus on $E_{Mv_k}^{sim}$ with k=(2-80) $\mathrm{m\,s^{-1}}$ (b-f)

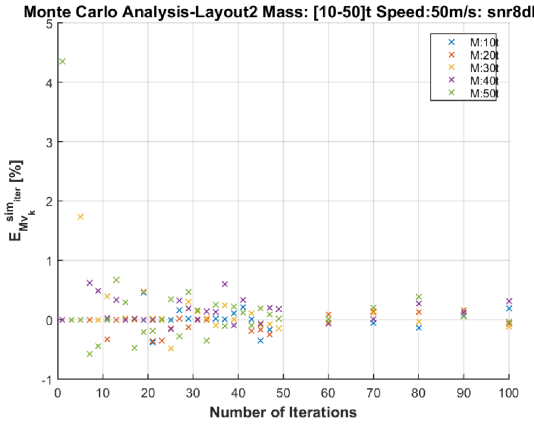

(a) $E_{M}{}_{v_k}^{sim_{iter}}$ with k=50 $\mathrm{m\,s^{-1}}$ trend for each Monte Carlo iteration

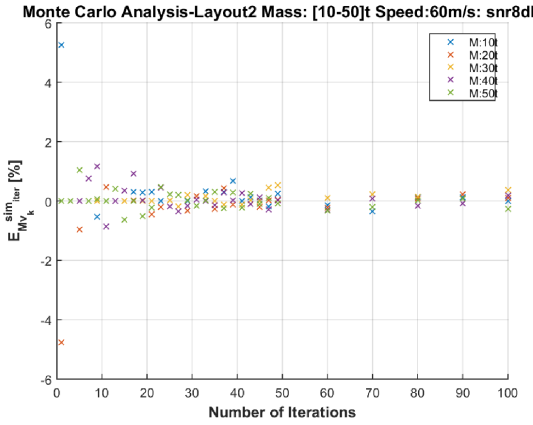

(b) $E_{M}{}_{v_k}^{sim_{iter}}$ with k=60 $\mathrm{m\,s^{-1}}$ trend for each Monte Carlo iteration

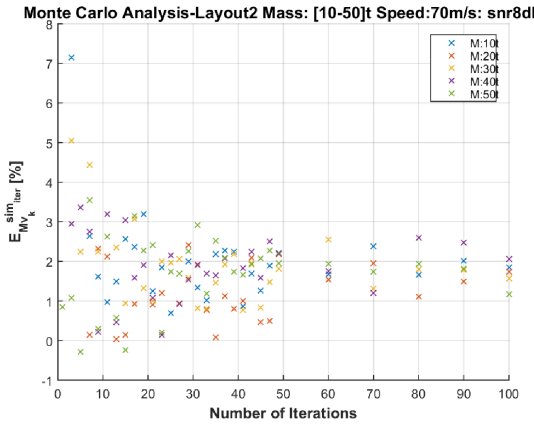

(c) $E_{M}{}_{v_k}^{sim_{iter}}$ with k=70 $\mathrm{m\,s^{-1}}$ trend for each Monte Carlo iteration

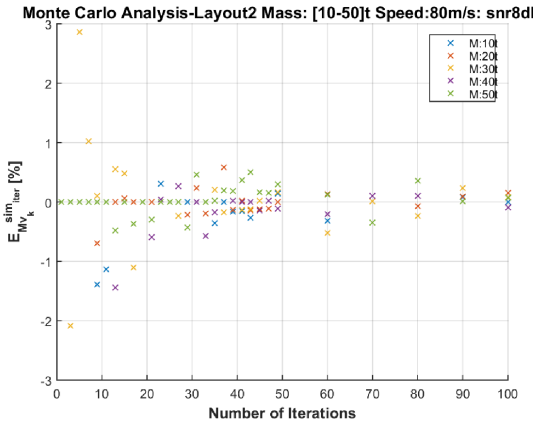

(d) $E_{M}{}_{v_k}^{sim_{iter}}$ with k=80 $\mathrm{m\,s^{-1}}$ trend for each Monte Carlo iteration

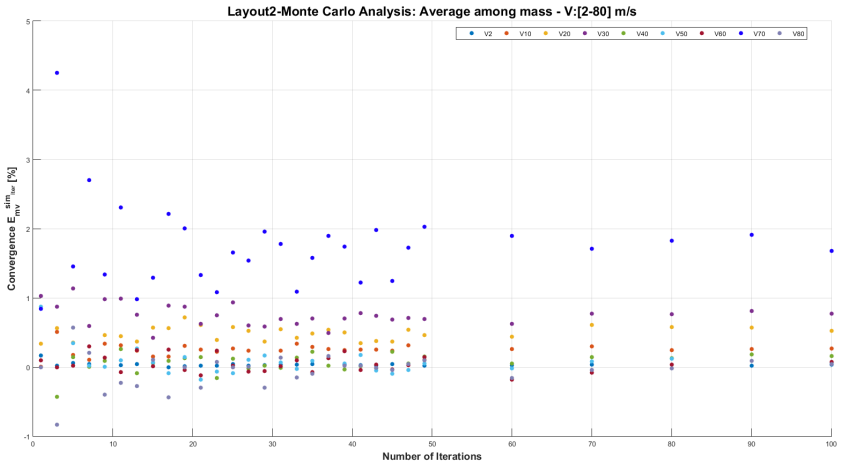

(e) Percentage relative errors on the vehicle speed $\mathbf{Em}_{v_k}^{sim_{iter}}$ with k=(2-80)$\mathrm{m\,s^{-1}}$

Figure A.2: Layout2: Focus on $E_{M}{}_{v_k}^{sim_{iter}}$ trends for each mass and vehicle speed (a-d) and $\mathbf{Em}_{v_k}^{sim_{iter}}[\%]$ trend for each speed(e): the convergence is reached for about 40 algorithm iterations

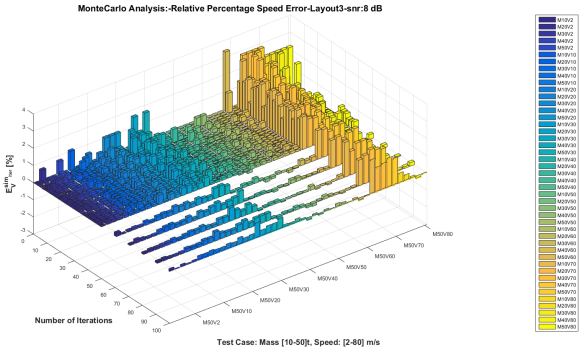

(a) $E_v^{sim_{iter}}$ trend in the full speed range (2-80) $\mathrm{m\,s^{-1}}$ and mass one (10-50) t

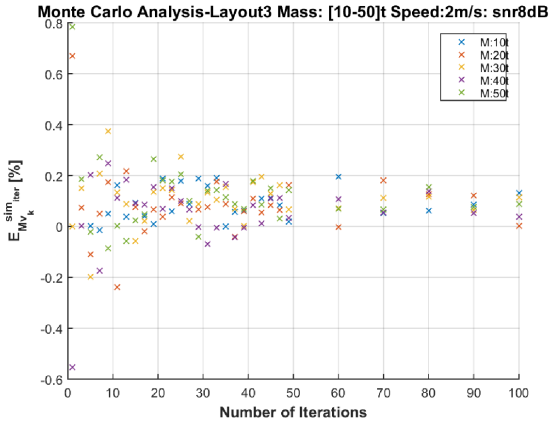

(b) $E_{Mv_k}^{sim_{iter}}$ with k=2 $\mathrm{m\,s^{-1}}$ trend for each Monte Carlo iteration

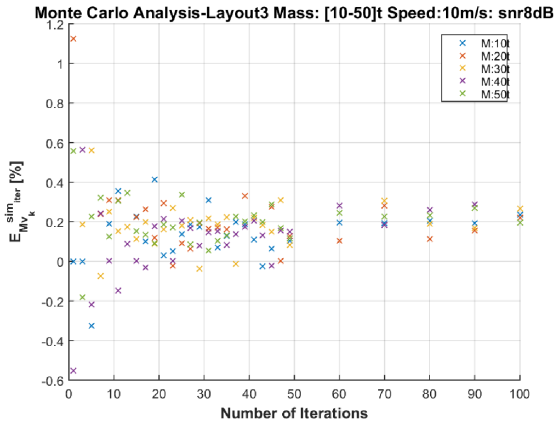

(c) $E_{Mv_k}^{sim_{iter}}$ with k=10 $\mathrm{m\,s^{-1}}$ trend for each Monte Carlo iteration

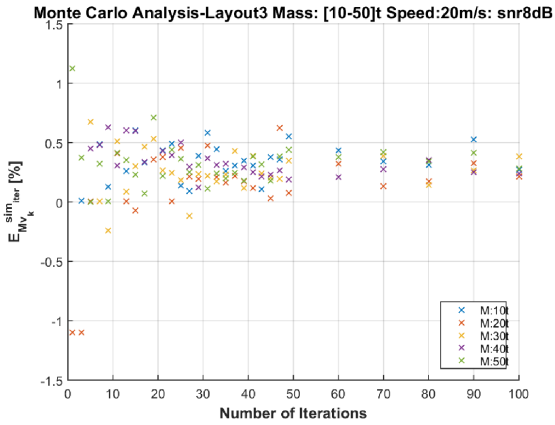

(d) $E_{Mv_k}^{sim_{iter}}$ with k=20 $\mathrm{m\,s^{-1}}$ trend for each Monte Carlo iteration

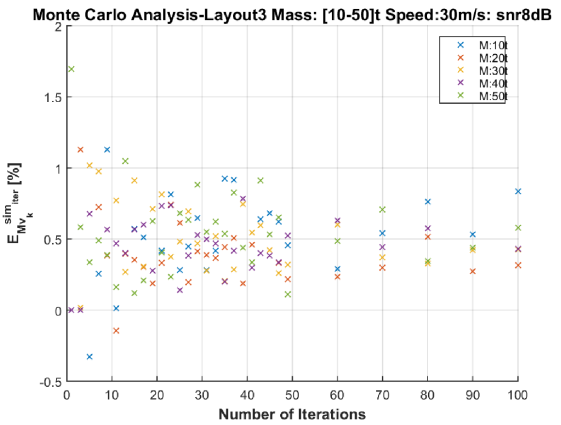

(e) $E_{Mv_k}^{sim_{iter}}$ with k=30 $\mathrm{m\,s^{-1}}$ trend for each Monte Carlo iteration

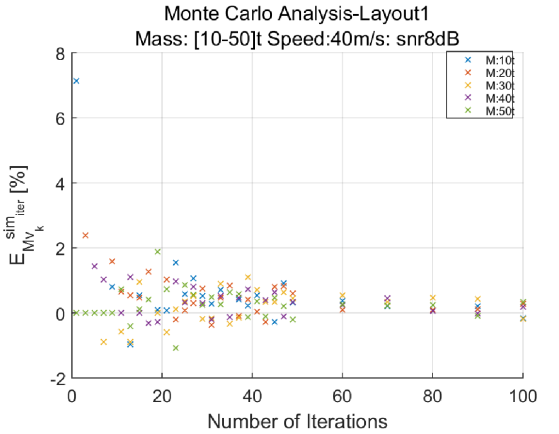

(f) $E_{Mv_k}^{sim_{iter}}$ with k=40 $\mathrm{m\,s^{-1}}$ trend for each Monte Carlo iteration

Figure A.3: Layout3: (a) $E_v^{sim_{iter}}[\%]$ convergence with the Monte Carlo Analysis in all vehicle mass and speed. Focus on $E_{Mv_k}^{sim_{iter}}$ with k=(2-80) $\mathrm{m\,s^{-1}}$ (b-f)

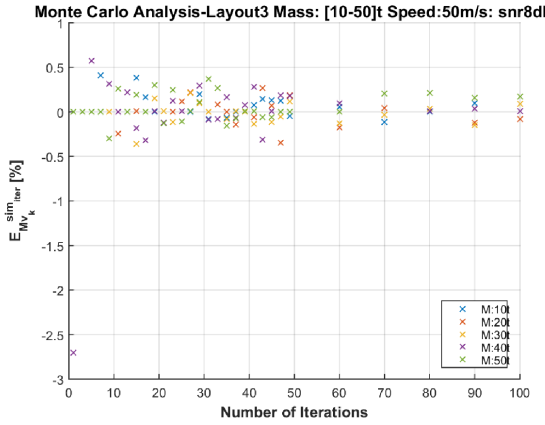

(a) $E_{M}{}_{v_k}^{sim_{iter}}$ with k=50 $\mathrm{m\,s^{-1}}$ trend for each Monte Carlo iteration

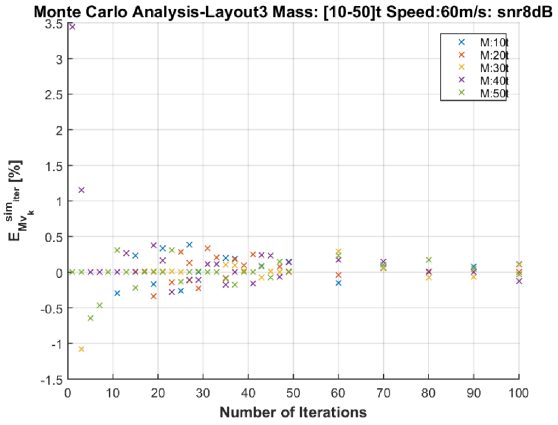

(b) $E_{M}{}_{v_k}^{sim_{iter}}$ with k=60 $\mathrm{m\,s^{-1}}$ trend for each Monte Carlo iteration

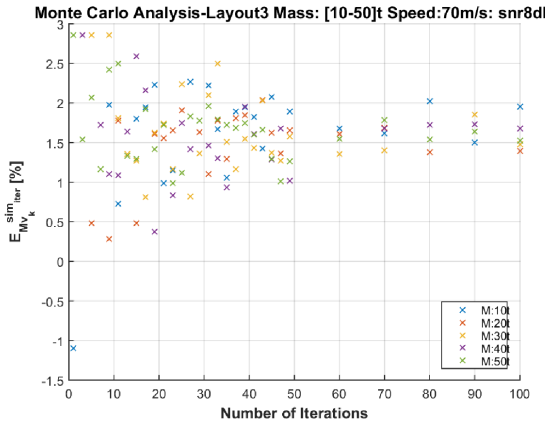

(c) $E_{M}{}_{v_k}^{sim_{iter}}$ with k=70 $\mathrm{m\,s^{-1}}$ trend for each Monte Carlo iteration

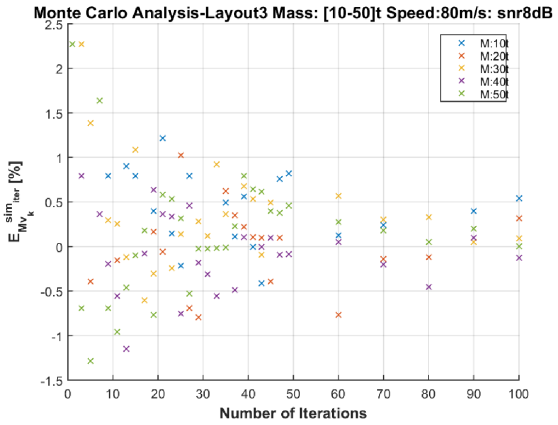

(d) $E_{M}{}_{v_k}^{sim_{iter}}$ with k=80 $\mathrm{m\,s^{-1}}$ trend for each Monte Carlo iteration

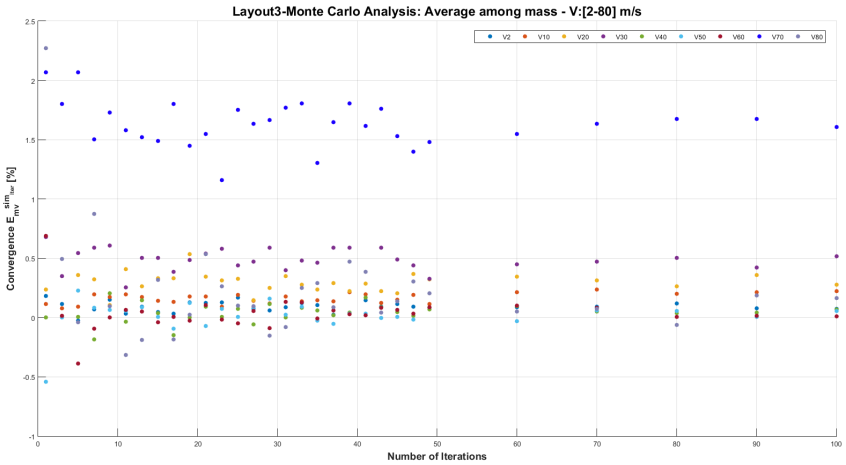

(e) Percentage relative errors on the vehicle speed $\mathbf{Em}_{v_k}^{sim_{iter}}$ with k=(2-80)$\mathrm{m\,s^{-1}}$

Figure A.4: Layout3: Focus on $E_{M}{}_{v_k}^{sim_{iter}}$ trends for each mass and vehicle speed (a-d) and $\mathbf{Em}_{v_k}^{sim_{iter}}[\%]$ trend for each speed(e): the convergence is reached for about 40 algorithm iterations

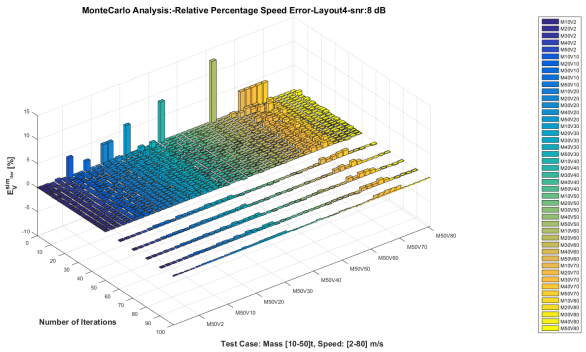

(a) $E_v^{sim_{iter}}$ trend in the full speed range (2-80) $\mathrm{m\,s^{-1}}$ and mass one (10-50) t

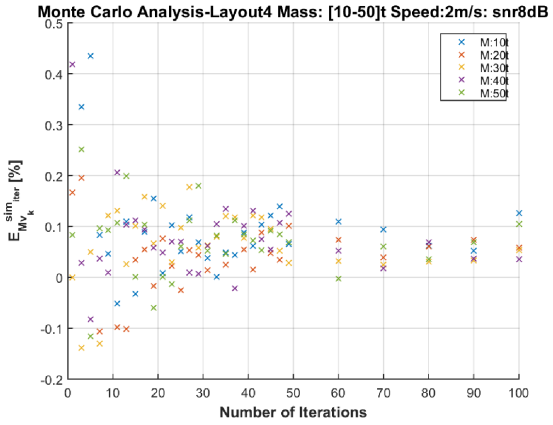

(b) $E_{Mv_k}^{sim_{iter}}$ with k=2 $\mathrm{m\,s^{-1}}$ trend for each Monte Carlo iteration

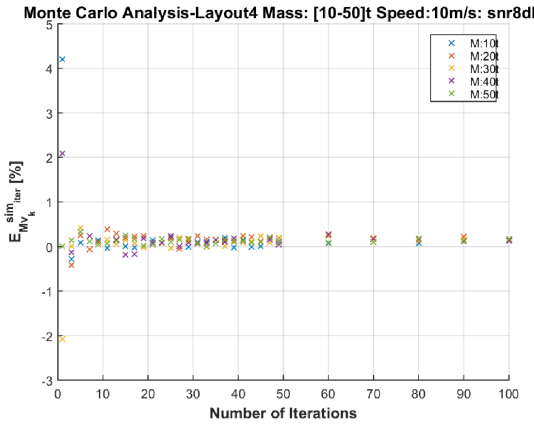

(c) $E_{Mv_k}^{sim_{iter}}$ with k=10 $\mathrm{m\,s^{-1}}$ trend for each Monte Carlo iteration

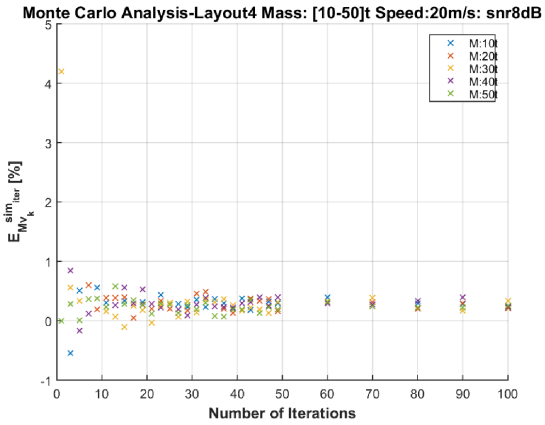

(d) $E_{Mv_k}^{sim_{iter}}$ with k=20 $\mathrm{m\,s^{-1}}$ trend for each Monte Carlo iteration

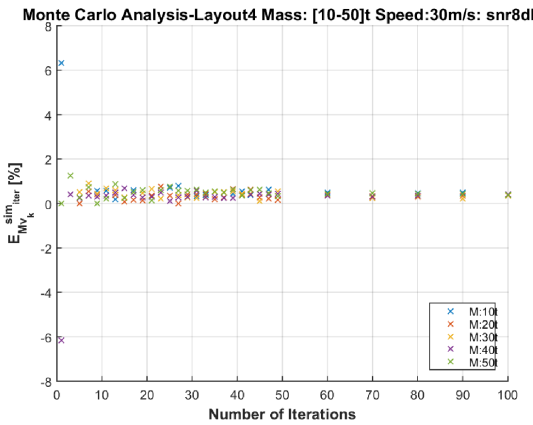

(e) $E_{Mv_k}^{sim_{iter}}$ with k=30 $\mathrm{m\,s^{-1}}$ trend for each Monte Carlo iteration

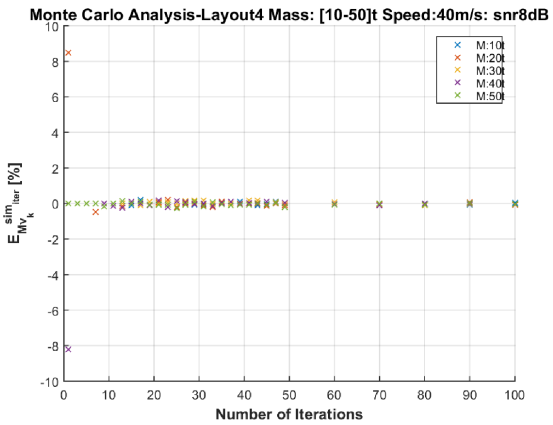

(f) $E_{Mv_k}^{sim_{iter}}$ with k=40 $\mathrm{m\,s^{-1}}$ trend for each Monte Carlo iteration

Figure A.5: Layout4: (a) $E_v^{sim_{iter}}[\%]$ convergence with the Monte Carlo Analysis in all vehicle mass and speed. Focus on $E_{Mv_k}^{sim_{iter}}$ with k=(2-80) $\mathrm{m\,s^{-1}}$ (b-f)

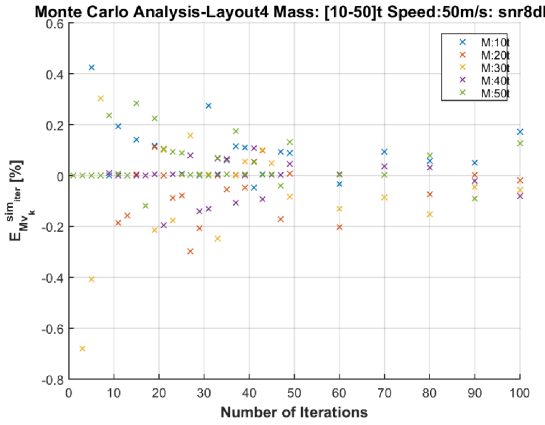

(a) $E_{M}{}_{v_k}^{sim_{iter}}$ with k=50 $\mathrm{m\,s^{-1}}$ trend for each Monte Carlo iteration

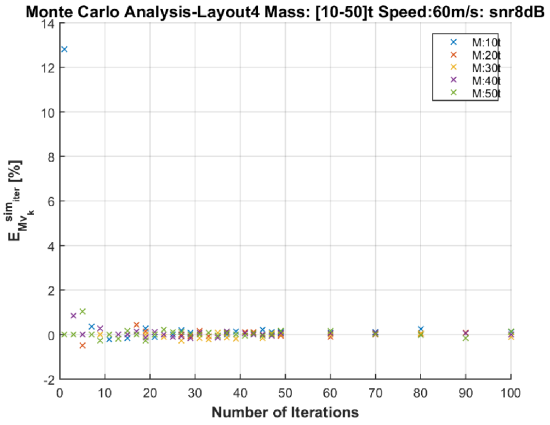

(b) $E_{M}{}_{v_k}^{sim_{iter}}$ with k=60 $\mathrm{m\,s^{-1}}$ trend for each Monte Carlo iteration

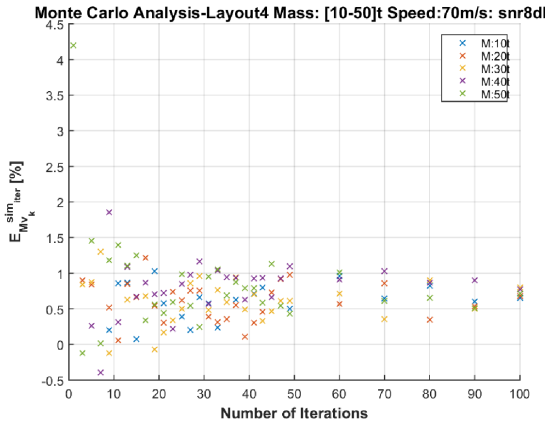

(c) $E_{M}{}_{v_k}^{sim_{iter}}$ with k=70 $\mathrm{m\,s^{-1}}$ trend for each Monte Carlo iteration

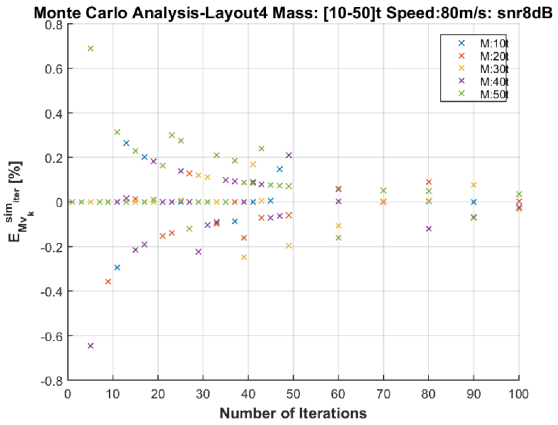

(d) $E_{M}{}_{v_k}^{sim_{iter}}$ with k=80 $\mathrm{m\,s^{-1}}$ trend for each Monte Carlo iteration

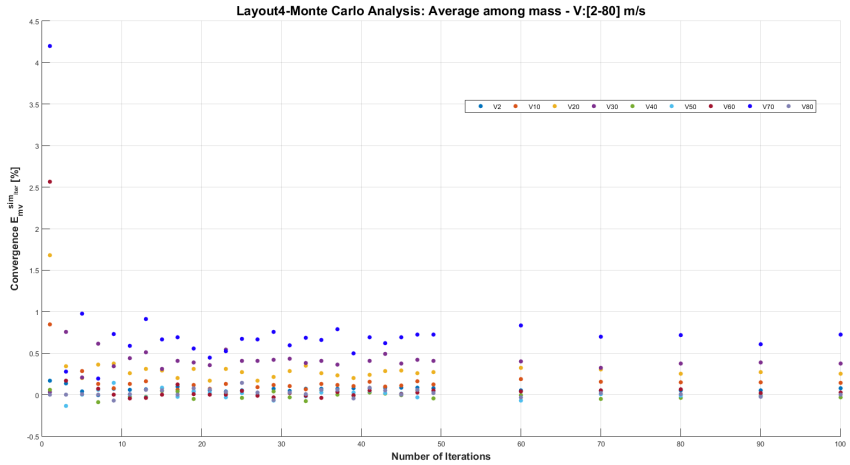

(e) Percentage relative errors on the vehicle speed $\mathbf{Em}_{v_k}^{sim_{iter}}$ with k=(2-80)$\mathrm{m\,s^{-1}}$

Figure A.6: Layout4: Focus on $E_{M}{}_{v_k}^{sim_{iter}}$ trends for each mass and vehicle speed (a-d) and $\mathbf{Em}_{v_k}^{sim_{iter}}[\%]$ trend for each speed(e): the convergence is reached for about 40 algorithm iterations

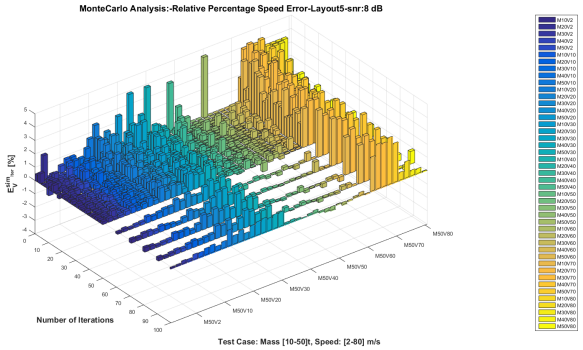

(a) $E_v^{sim_{iter}}$ trend in the full speed range (2-80) $\mathrm{m\,s^{-1}}$ and mass one (10-50) t

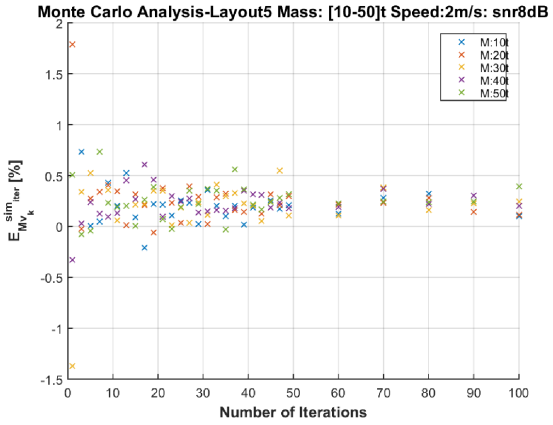

(b) $E_{M\,v_k}^{sim_{iter}}$ with k=2 $\mathrm{m\,s^{-1}}$ trend for each Monte Carlo iteration

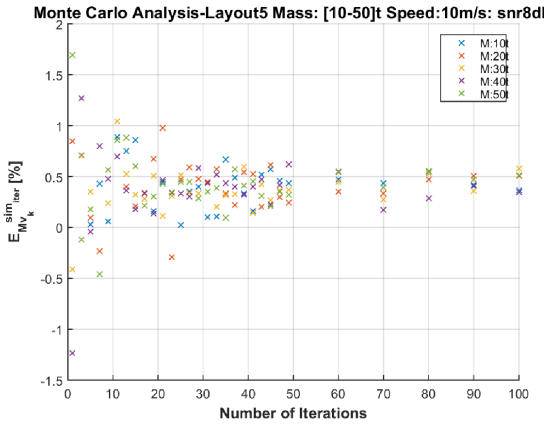

(c) $E_{M\,v_k}^{sim_{iter}}$ with k=10 $\mathrm{m\,s^{-1}}$ trend for each Monte Carlo iteration

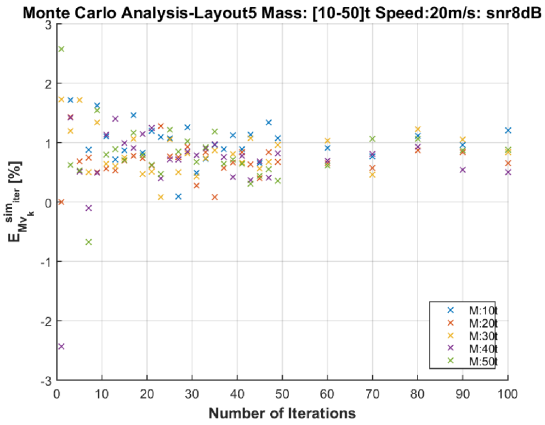

(d) $E_{M\,v_k}^{sim_{iter}}$ with k=20 $\mathrm{m\,s^{-1}}$ trend for each Monte Carlo iteration

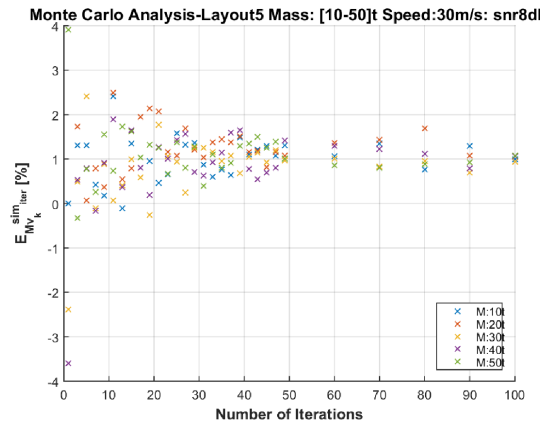

(e) $E_{M\,v_k}^{sim_{iter}}$ with k=30 $\mathrm{m\,s^{-1}}$ trend for each Monte Carlo iteration

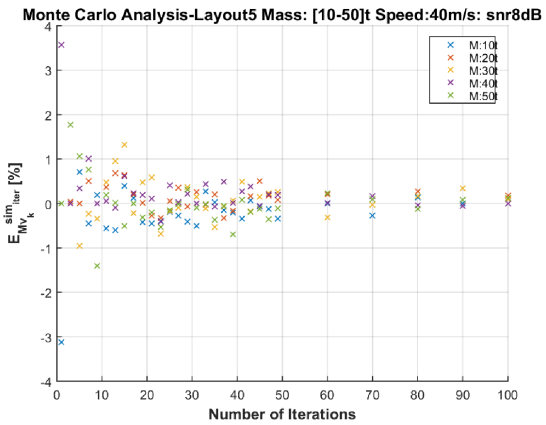

(f) $E_{M\,v_k}^{sim_{iter}}$ with k=40 $\mathrm{m\,s^{-1}}$ trend for each Monte Carlo iteration

Figure A.7: Layout5: (a) $E_v^{sim_{iter}}[\%]$ convergence with the Monte Carlo Analysis in all vehicle mass and speed. Focus on $E_{M\,v_k}^{sim_{iter}}$ with k=(2-80) $\mathrm{m\,s^{-1}}$ (b-f)

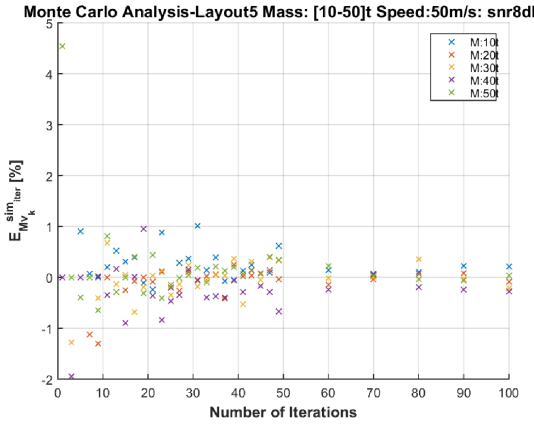

(a) $E_{M}{}_{v_k}^{sim_{iter}}$ with k=50 $\mathrm{m\,s^{-1}}$ trend for each Monte Carlo iteration

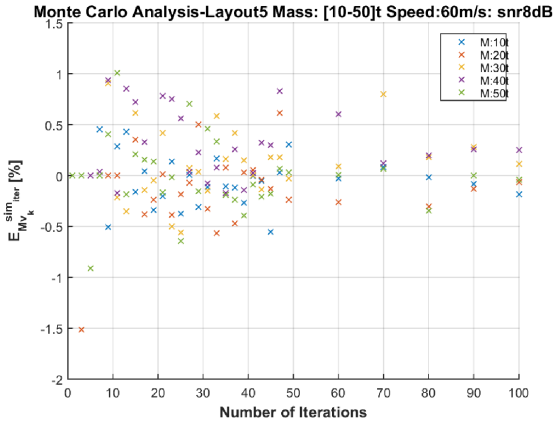

(b) $E_{M}{}_{v_k}^{sim_{iter}}$ with k=60 $\mathrm{m\,s^{-1}}$ trend for each Monte Carlo iteration

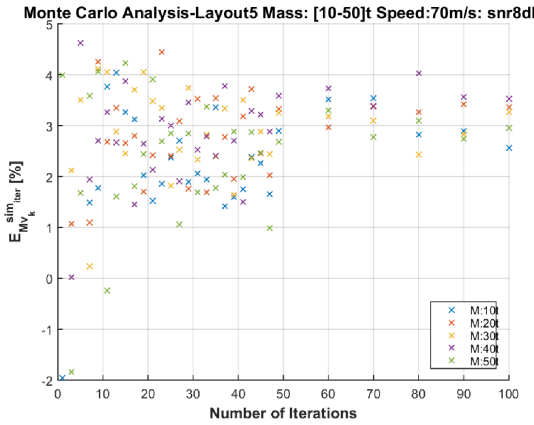

(c) $E_{M}{}_{v_k}^{sim_{iter}}$ with k=70 $\mathrm{m\,s^{-1}}$ trend for each Monte Carlo iteration

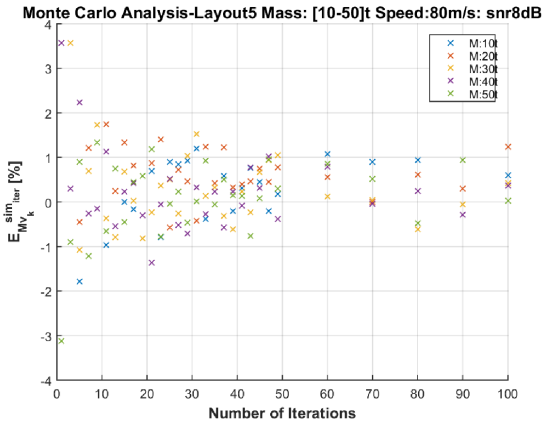

(d) $E_{M}{}_{v_k}^{sim_{iter}}$ with k=80 $\mathrm{m\,s^{-1}}$ trend for each Monte Carlo iteration

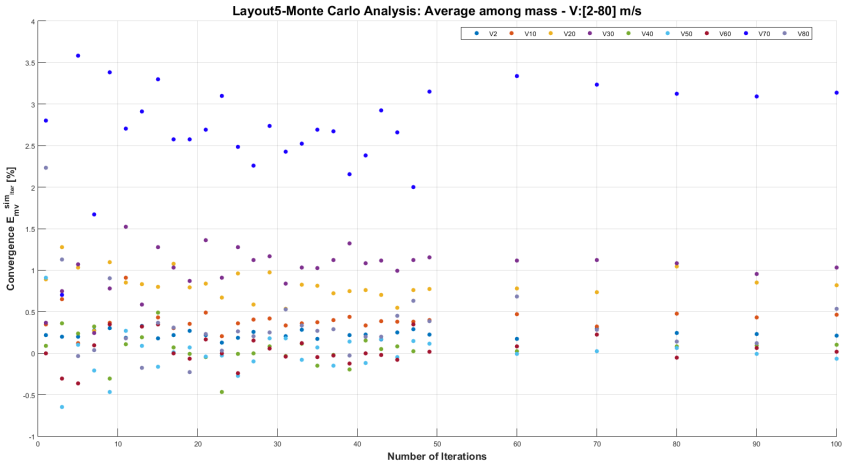

(e) Percentage relative errors on the vehicle speed $\mathbf{Em}_{v_k}^{sim_{iter}}$ with k=(2-80)$\mathrm{m\,s^{-1}}$

Figure A.8: Layout5: Focus on $E_{M}{}_{v_k}^{sim_{iter}}$ trends for each mass and vehicle speed (a-d) and $\mathbf{Em}_{v_k}^{sim_{iter}}[\%]$ trend for each speed(e): the convergence is reached for about 40 algorithm iterations

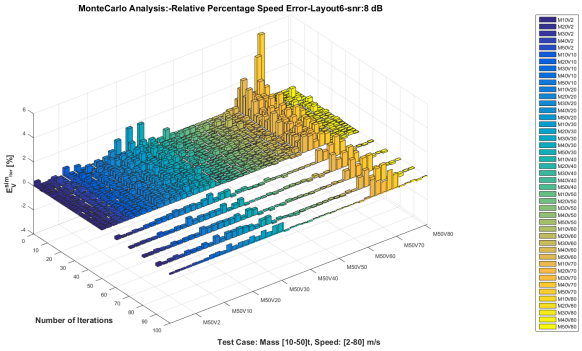

(a) $E_v^{sim_{iter}}$ trend in the full speed range (2-80) $\mathrm{m\,s^{-1}}$ and mass one (10-50) t

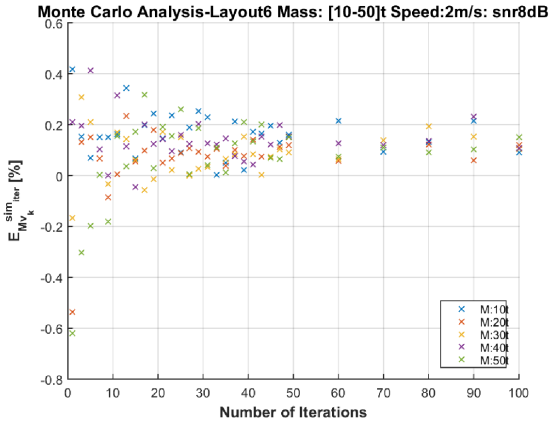

(b) $E_{M\,v_k}^{sim_{iter}}$ with k=2 $\mathrm{m\,s^{-1}}$ trend for each Monte Carlo iteration

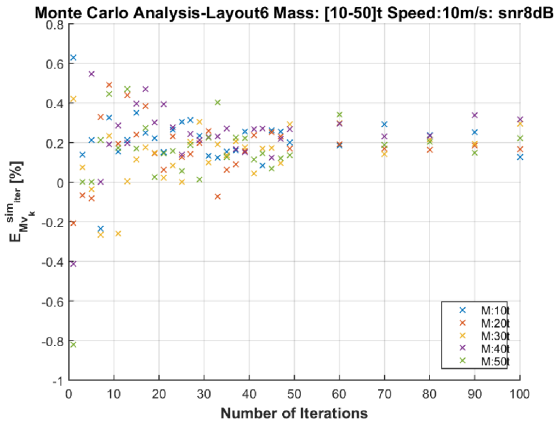

(c) $E_{M\,v_k}^{sim_{iter}}$ with k=10 $\mathrm{m\,s^{-1}}$ trend for each Monte Carlo iteration

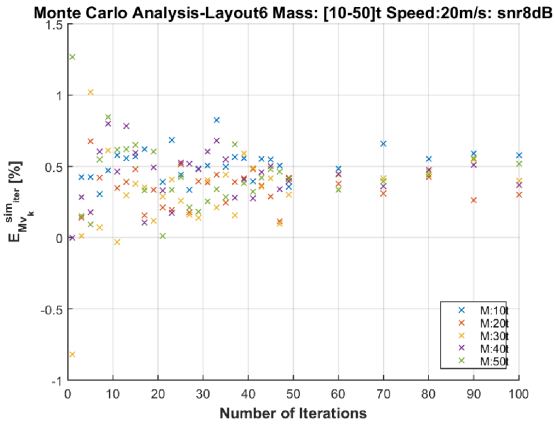

(d) $E_{M\,v_k}^{sim_{iter}}$ with k=20 $\mathrm{m\,s^{-1}}$ trend for each Monte Carlo iteration

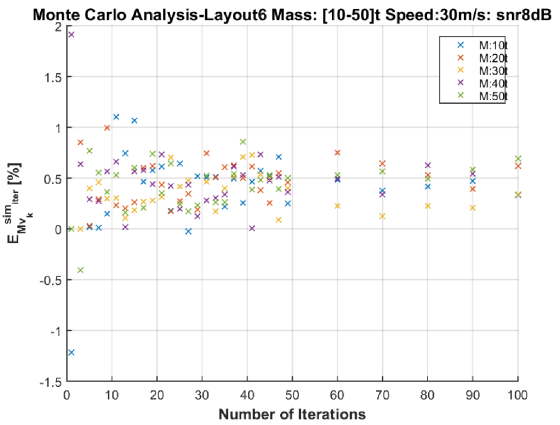

(e) $E_{M\,v_k}^{sim_{iter}}$ with k=30 $\mathrm{m\,s^{-1}}$ trend for each Monte Carlo iteration

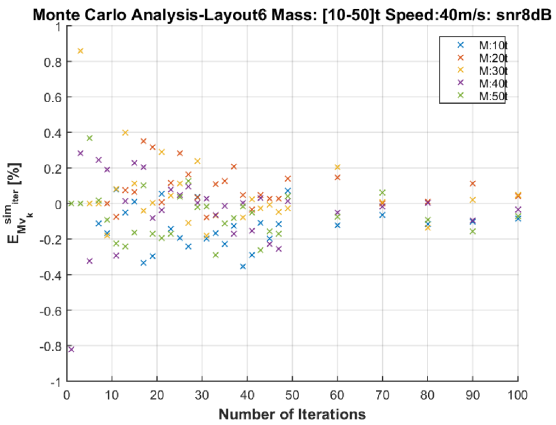

(f) $E_{M\,v_k}^{sim_{iter}}$ with k=40 $\mathrm{m\,s^{-1}}$ trend for each Monte Carlo iteration

Figure A.9: Layout6: (a) $E_v^{sim_{iter}}[\%]$ convergence with the Monte Carlo Analysis in all vehicle mass and speed. Focus on $E_{M\,v_k}^{sim_{iter}}$ with k=(2-80) $\mathrm{m\,s^{-1}}$ (b-f)

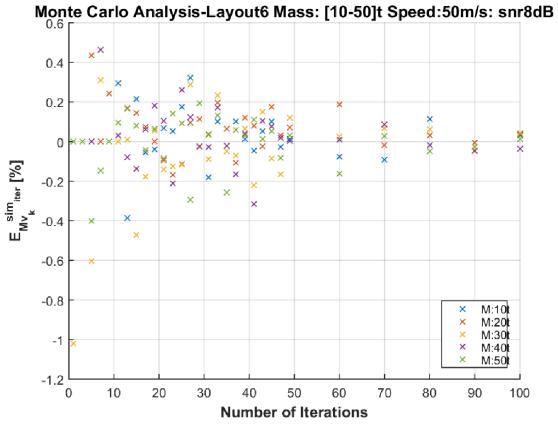

(a) $E_{M}{}_{v_k}^{sim_{iter}}$ with k=50 $\mathrm{m\,s^{-1}}$ trend for each Monte Carlo iteration

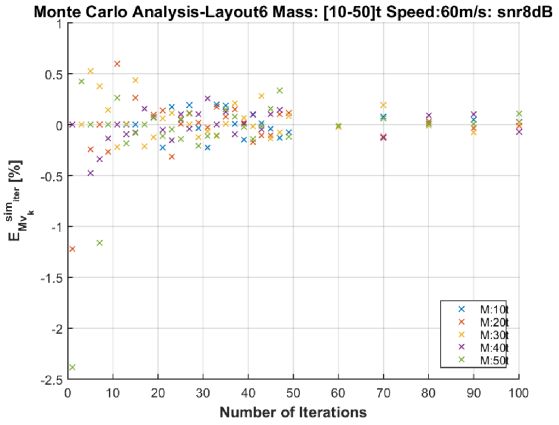

(b) $E_{M}{}_{v_k}^{sim_{iter}}$ with k=60 $\mathrm{m\,s^{-1}}$ trend for each Monte Carlo iteration

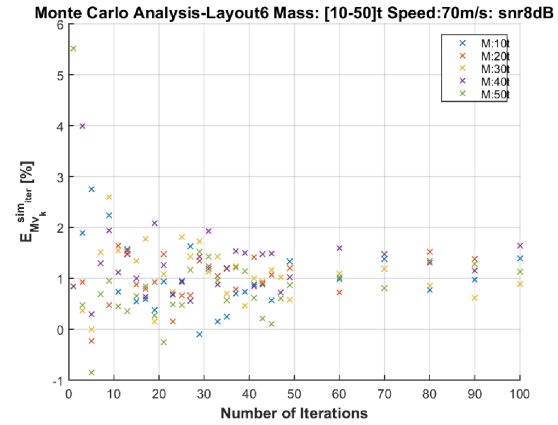

(c) $E_{M}{}_{v_k}^{sim_{iter}}$ with k=70 $\mathrm{m\,s^{-1}}$ trend for each Monte Carlo iteration

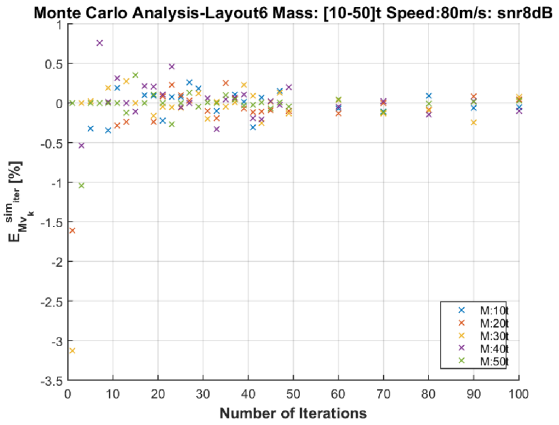

(d) $E_{M}{}_{v_k}^{sim_{iter}}$ with k=80 $\mathrm{m\,s^{-1}}$ trend for each Monte Carlo iteration

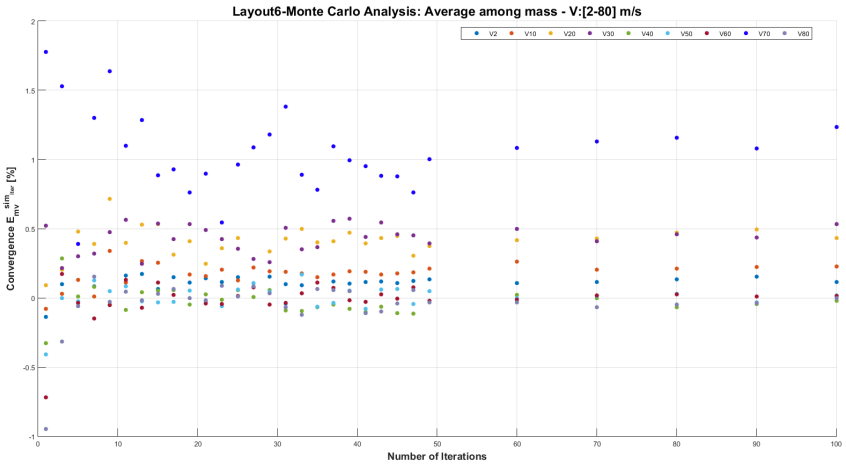

(e) Percentage relative errors on the vehicle speed $\mathbf{Em}_{v_k}^{sim_{iter}}$ with k=(2-80)$\mathrm{m\,s^{-1}}$

Figure A.10: Layout6: Focus on $E_{M}{}_{v_k}^{sim_{iter}}$ trends for each mass and vehicle speed (a-d) and $\mathbf{Em}_{v_k}^{sim_{iter}}[\%]$ trend for each speed(e): the convergence is reached for about 40 algorithm iterations

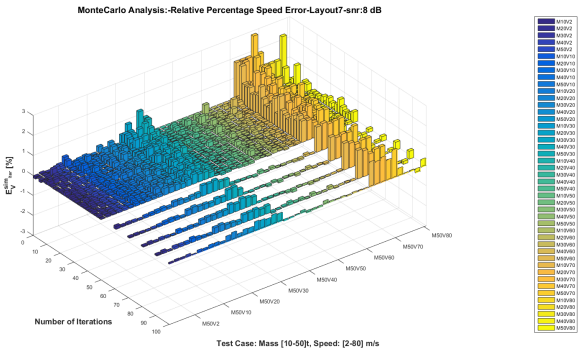

(a) $E_v^{sim_{iter}}$ trend in the full speed range (2-80) $\mathrm{m\,s^{-1}}$ and mass one (10-50) t

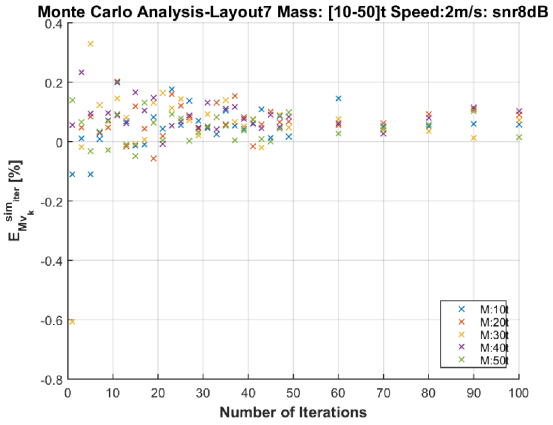

(b) $E_{M\,v_k}^{sim_{iter}}$ with k=2 $\mathrm{m\,s^{-1}}$ trend for each Monte Carlo iteration

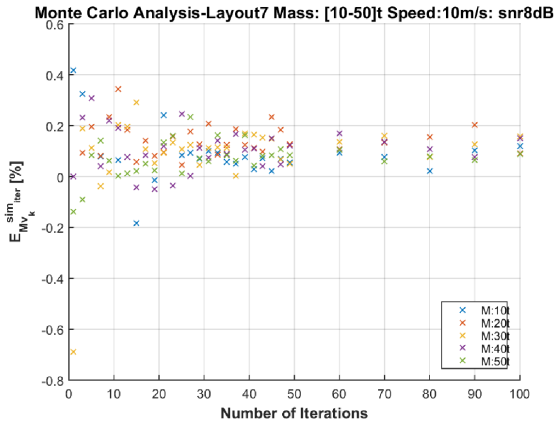

(c) $E_{M\,v_k}^{sim_{iter}}$ with k=10 $\mathrm{m\,s^{-1}}$ trend for each Monte Carlo iteration

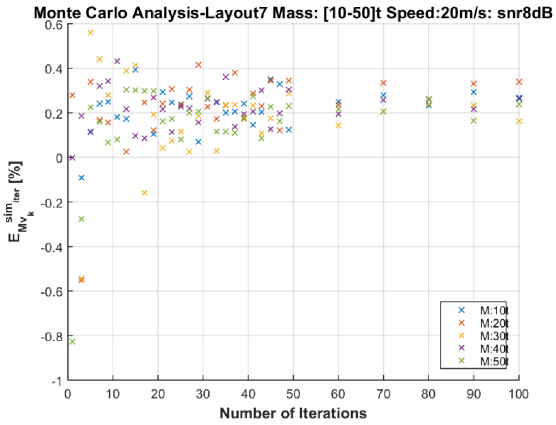

(d) $E_{M\,v_k}^{sim_{iter}}$ with k=20 $\mathrm{m\,s^{-1}}$ trend for each Monte Carlo iteration

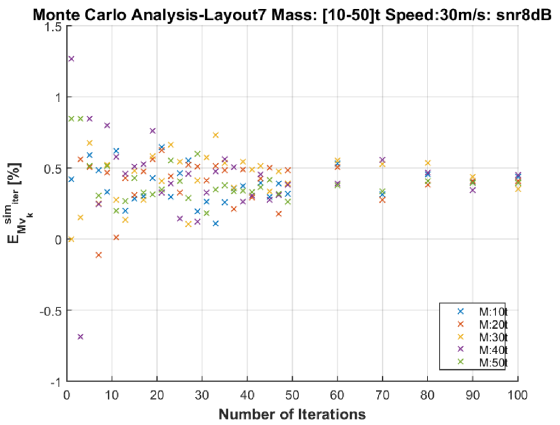

(e) $E_{M\,v_k}^{sim_{iter}}$ with k=30 $\mathrm{m\,s^{-1}}$ trend for each Monte Carlo iteration

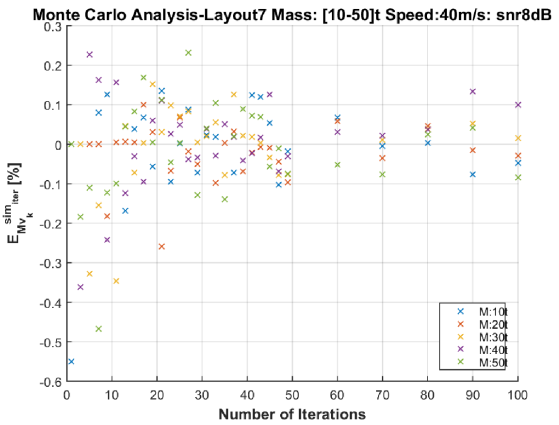

(f) $E_{M\,v_k}^{sim_{iter}}$ with k=40 $\mathrm{m\,s^{-1}}$ trend for each Monte Carlo iteration

Figure A.11: Layout7: (a) $E_v^{sim_{iter}}[\%]$ convergence with the Monte Carlo Analysis in all vehicle mass and speed. Focus on $E_{M\,v_k}^{sim_{iter}}$ with k=(2-80) $\mathrm{m\,s^{-1}}$ (b-f)

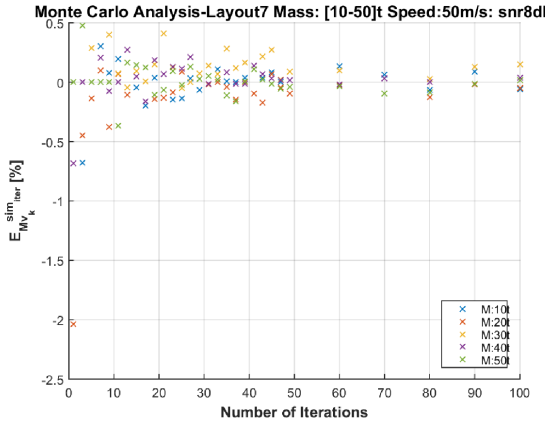

(a) $E_{M}{}_{v_k}^{sim_{iter}}$ with k=50 $\mathrm{m\,s^{-1}}$ trend for each Monte Carlo iteration

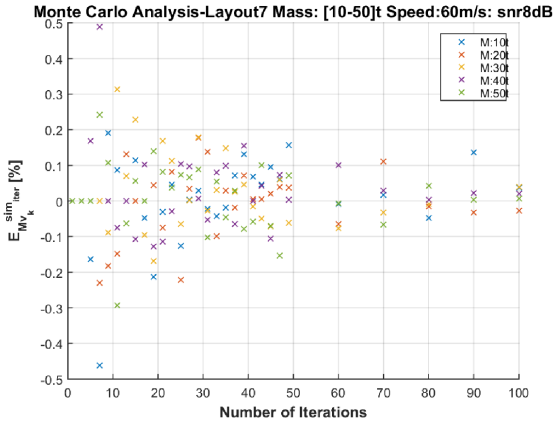

(b) $E_{M}{}_{v_k}^{sim_{iter}}$ with k=60 $\mathrm{m\,s^{-1}}$ trend for each Monte Carlo iteration

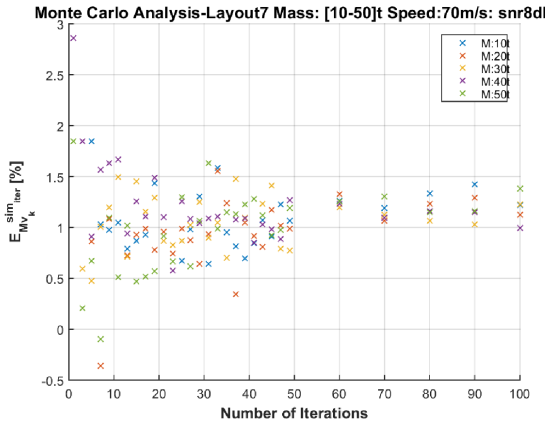

(c) $E_{M}{}_{v_k}^{sim_{iter}}$ with k=70 $\mathrm{m\,s^{-1}}$ trend for each Monte Carlo iteration

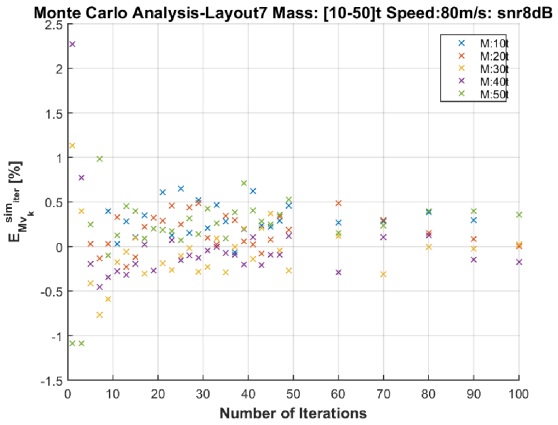

(d) $E_{M}{}_{v_k}^{sim_{iter}}$ with k=80 $\mathrm{m\,s^{-1}}$ trend for each Monte Carlo iteration

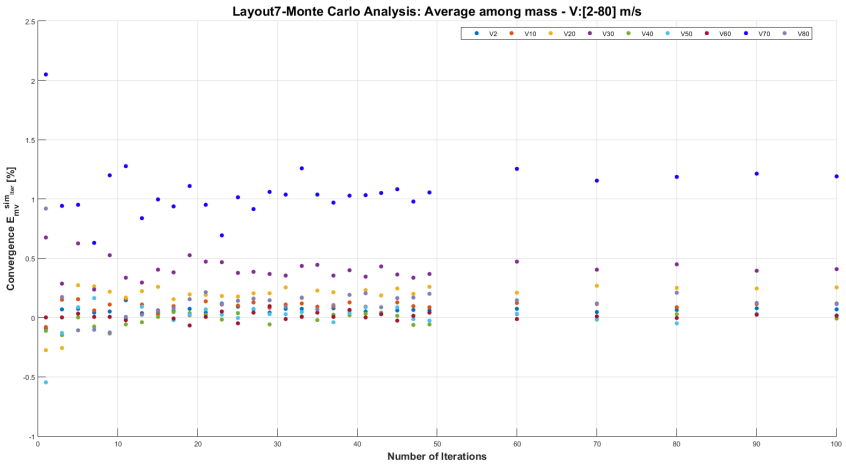

(e) Percentage relative errors on the vehicle speed $\mathbf{Em}_{v_k}^{sim_{iter}}$ with k=(2-80)$\mathrm{m\,s^{-1}}$

Figure A.12: Layout7: Focus on $E_{M}{}_{v_k}^{sim_{iter}}$ trends for each mass and vehicle speed (a-d) and $\mathbf{Em}_{v_k}^{sim_{iter}}[\%]$ trend for each speed(e): the convergence is reached for about 40 algorithm iterations

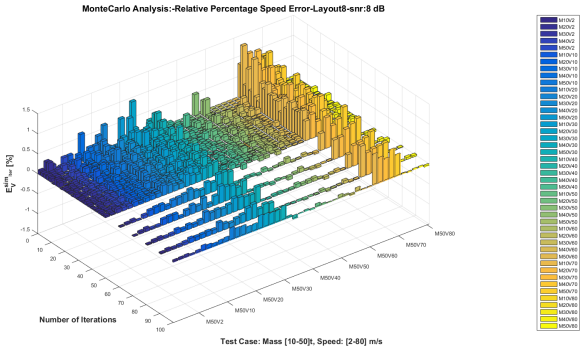

(a) $E_v^{sim_{iter}}$ trend in the full speed range (2-80) $\mathrm{m\,s^{-1}}$ and mass one (10-50) t

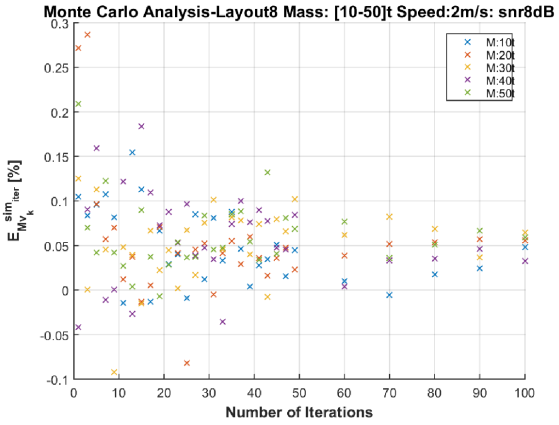

(b) $E_{Mv_k}^{sim_{iter}}$ with k=2 $\mathrm{m\,s^{-1}}$ trend for each Monte Carlo iteration

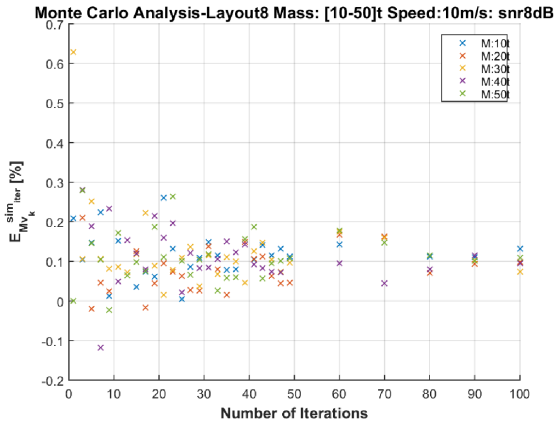

(c) $E_{Mv_k}^{sim_{iter}}$ with k=10 $\mathrm{m\,s^{-1}}$ trend for each Monte Carlo iteration

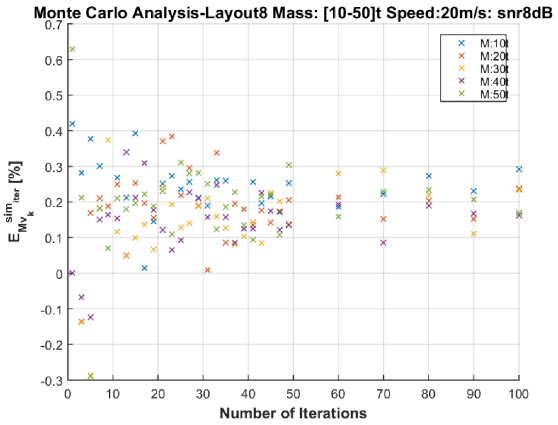

(d) $E_{Mv_k}^{sim_{iter}}$ with k=20 $\mathrm{m\,s^{-1}}$ trend for each Monte Carlo iteration

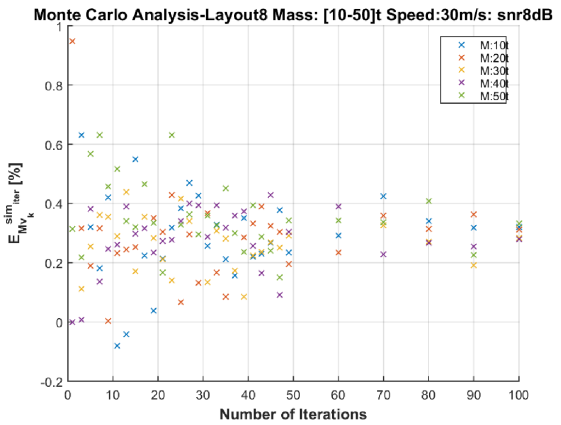

(e) $E_{Mv_k}^{sim_{iter}}$ with k=30 $\mathrm{m\,s^{-1}}$ trend for each Monte Carlo iteration

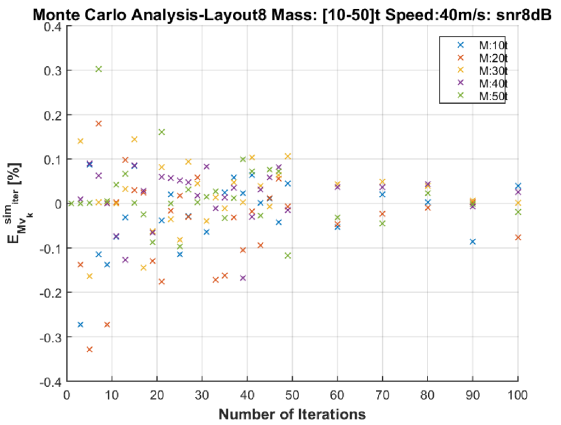

(f) $E_{Mv_k}^{sim_{iter}}$ with k=40 $\mathrm{m\,s^{-1}}$ trend for each Monte Carlo iteration

Figure A.13: Layout8: (a) $E_v^{sim_{iter}}[\%]$ convergence with the Monte Carlo Analysis in all vehicle mass and speed. Focus on $E_{Mv_k}^{sim_{iter}}$ with k=(2-80) $\mathrm{m\,s^{-1}}$ (b-f)

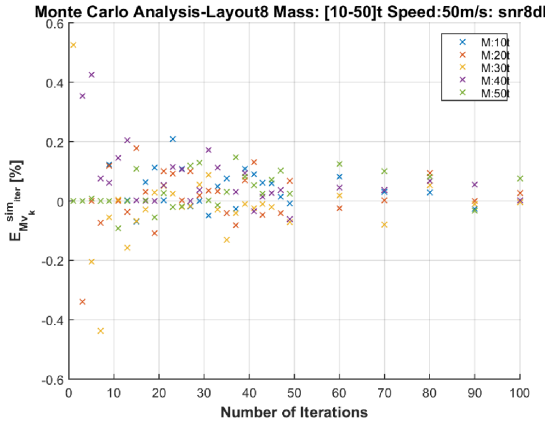

(a) $E_{M}{}_{v_k}^{sim_{iter}}$ with k=50 $\mathrm{m\,s^{-1}}$ trend for each Monte Carlo iteration

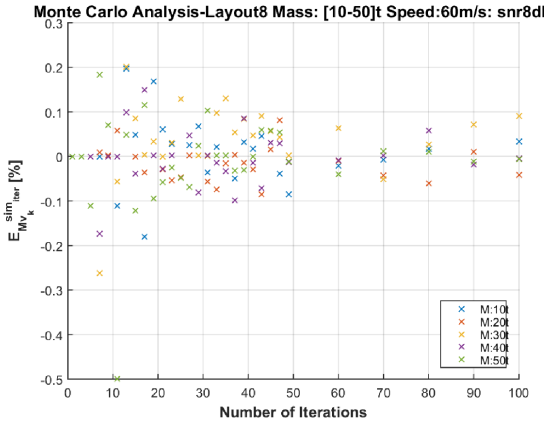

(b) $E_{M}{}_{v_k}^{sim_{iter}}$ with k=60 $\mathrm{m\,s^{-1}}$ trend for each Monte Carlo iteration

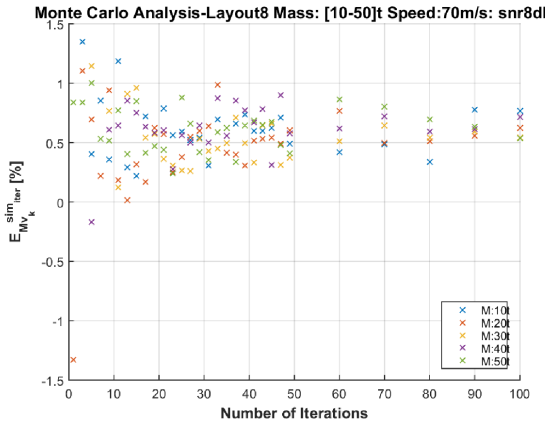

(c) $E_{M}{}_{v_k}^{sim_{iter}}$ with k=70 $\mathrm{m\,s^{-1}}$ trend for each Monte Carlo iteration

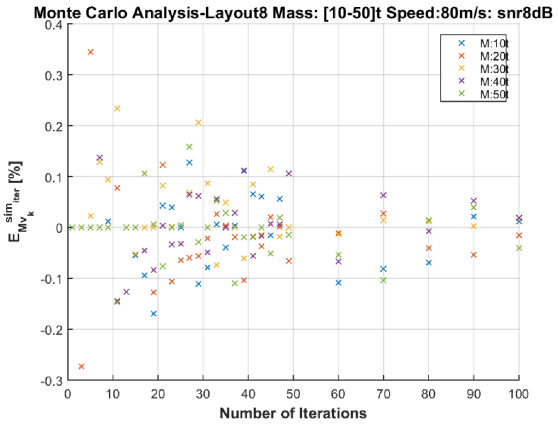

(d) $E_{M}{}_{v_k}^{sim_{iter}}$ with k=80 $\mathrm{m\,s^{-1}}$ trend for each Monte Carlo iteration

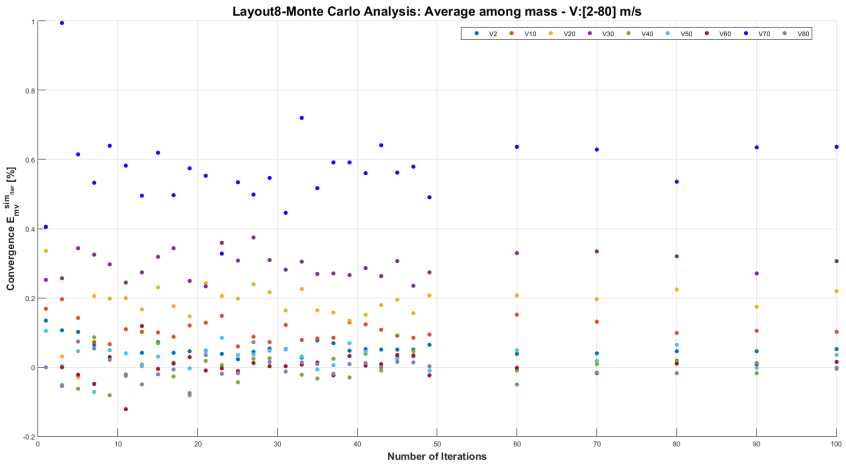

(e) Percentage relative errors on the vehicle speed $\mathbf{Em}_{v_k}^{sim_{iter}}$ with k=(2-80)$\mathrm{m\,s^{-1}}$

Figure A.14: Layout8: Focus on $E_{M}{}_{v_k}^{sim_{iter}}$ trends for each mass and vehicle speed (a-d) and $\mathbf{Em}_{v_k}^{sim_{iter}}[\%]$ trend for each speed(e): the convergence is reached for about 40 algorithm iterations

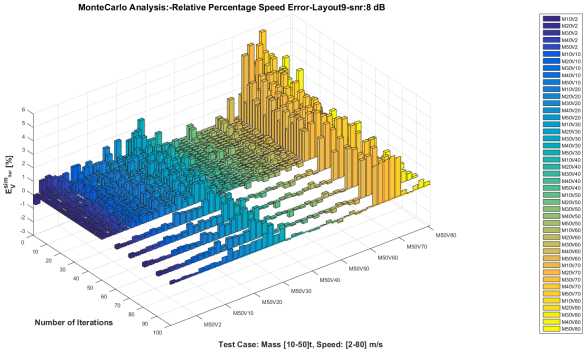

(a) $E_v^{sim_{iter}}$ trend in the full speed range (2-80) $\mathrm{m\,s^{-1}}$ and mass one (10-50) t

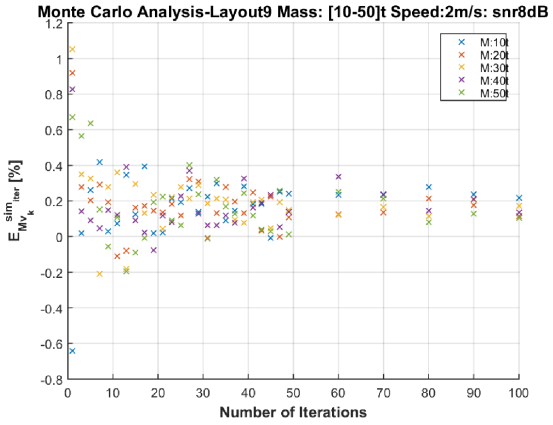

(b) $E_{M\,v_k}^{sim_{iter}}$ with k=2 $\mathrm{m\,s^{-1}}$ trend for each Monte Carlo iteration

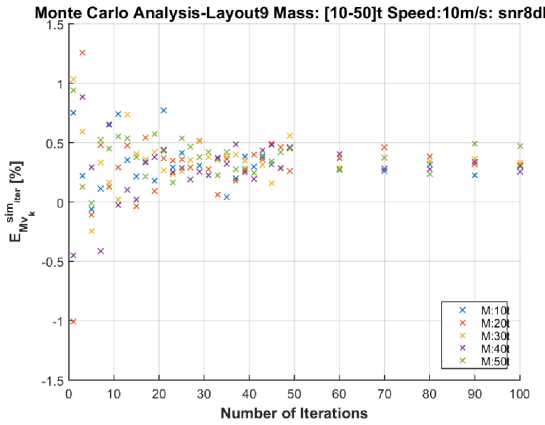

(c) $E_{M\,v_k}^{sim_{iter}}$ with k=10 $\mathrm{m\,s^{-1}}$ trend for each Monte Carlo iteration

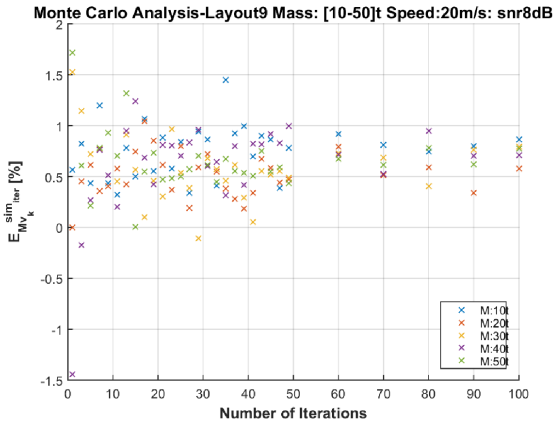

(d) $E_{M\,v_k}^{sim_{iter}}$ with k=20 $\mathrm{m\,s^{-1}}$ trend for each Monte Carlo iteration

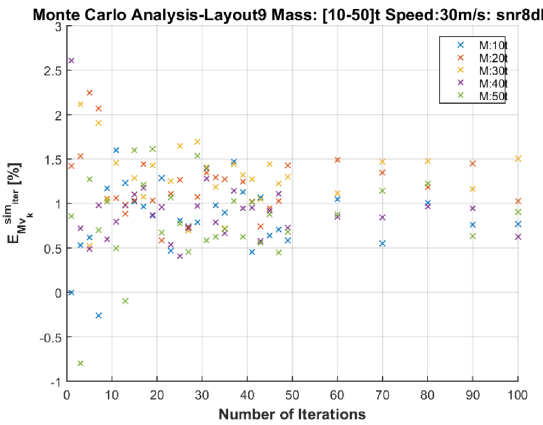

(e) $E_{M\,v_k}^{sim_{iter}}$ with k=30 $\mathrm{m\,s^{-1}}$ trend for each Monte Carlo iteration

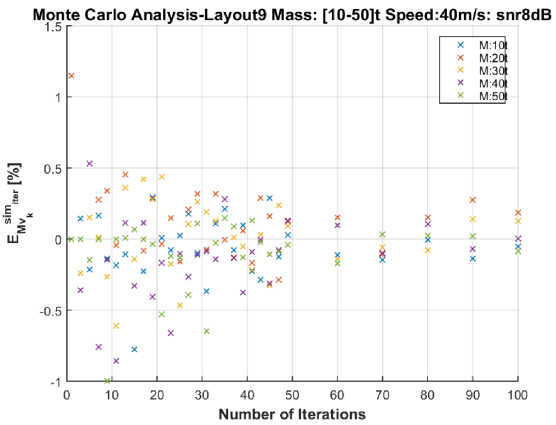

(f) $E_{M\,v_k}^{sim_{iter}}$ with k=40 $\mathrm{m\,s^{-1}}$ trend for each Monte Carlo iteration

Figure A.15: Layout9: (a) $E_v^{sim_{iter}}[\%]$ convergence with the Monte Carlo Analysis in all vehicle mass and speed. Focus on $E_{M\,v_k}^{sim_{iter}}$ with k=(2-80) $\mathrm{m\,s^{-1}}$ (b-f)

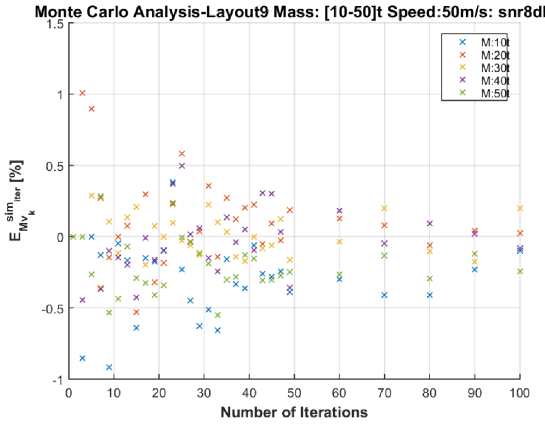

(a) $E_{M}{}_{v_k}^{sim_{iter}}$ with k=50 $\mathrm{m\,s^{-1}}$ trend for each Monte Carlo iteration

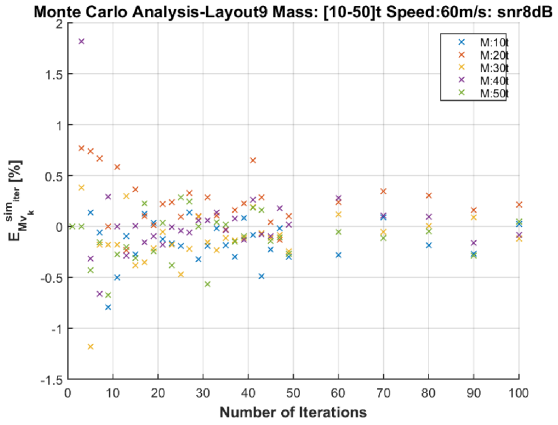

(b) $E_{M}{}_{v_k}^{sim_{iter}}$ with k=60 $\mathrm{m\,s^{-1}}$ trend for each Monte Carlo iteration

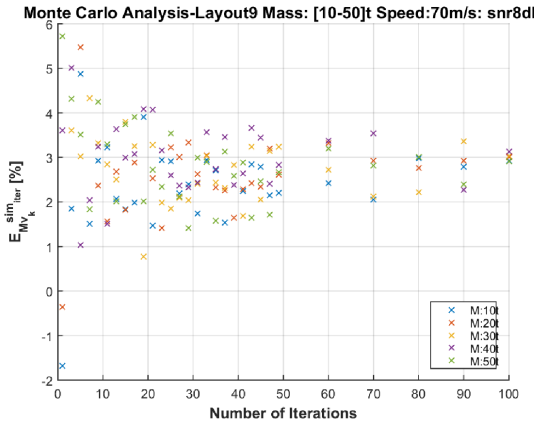

(c) $E_{M}{}_{v_k}^{sim_{iter}}$ with k=70 $\mathrm{m\,s^{-1}}$ trend for each Monte Carlo iteration

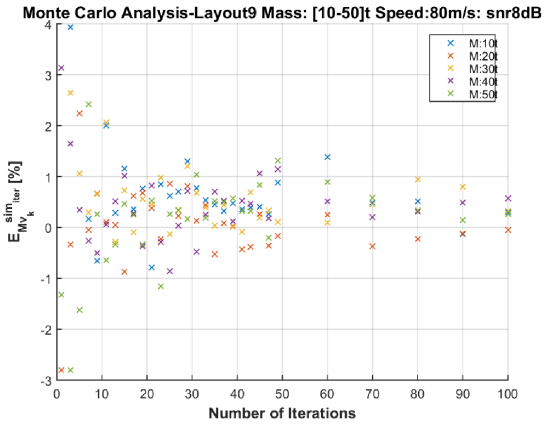

(d) $E_{M}{}_{v_k}^{sim_{iter}}$ with k=80 $\mathrm{m\,s^{-1}}$ trend for each Monte Carlo iteration

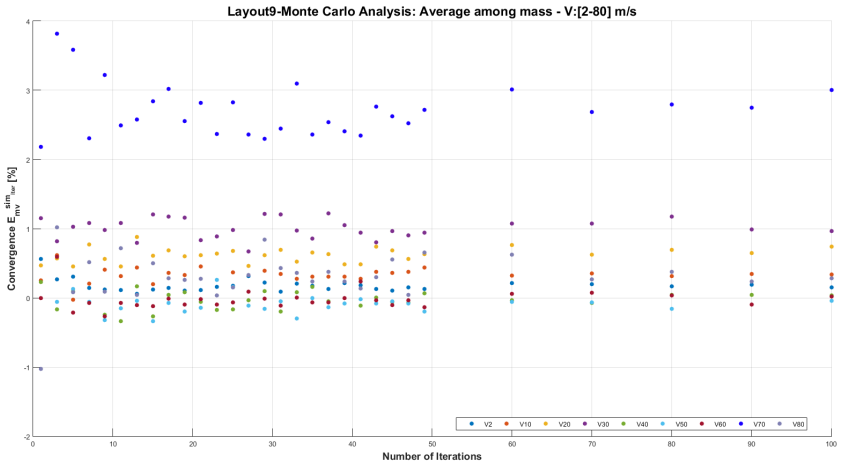

(e) Percentage relative errors on the vehicle speed $\mathbf{Em}_{v_k}^{sim_{iter}}$ with k=(2-80)$\mathrm{m\,s^{-1}}$

Figure A.16: Layout9: Focus on $E_{M}{}_{v_k}^{sim_{iter}}$ trends for each mass and vehicle speed (a-d) and $\mathbf{Em}_{v_k}^{sim_{iter}}[\%]$ trend for each speed(e): the convergence is reached for about 40 algorithm iterations

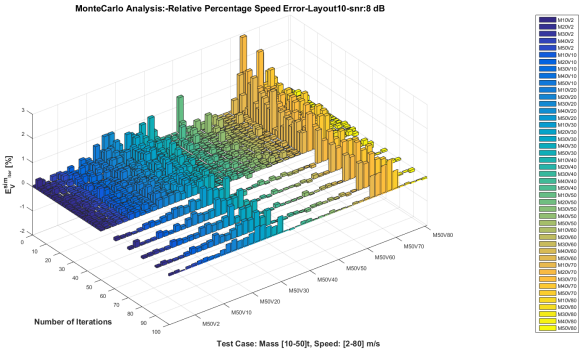

(a) $E_v^{sim_{iter}}$ trend in the full speed range (2-80) $\mathrm{m\,s^{-1}}$ and mass one (10-50) t

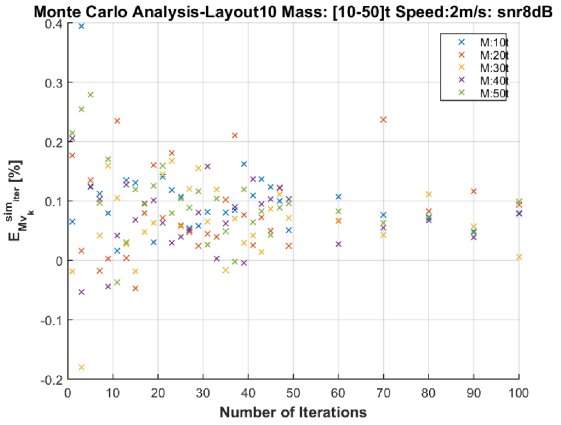

(b) $E_{M\,v_k}^{sim_{iter}}$ with k=2 $\mathrm{m\,s^{-1}}$ trend for each Monte Carlo iteration

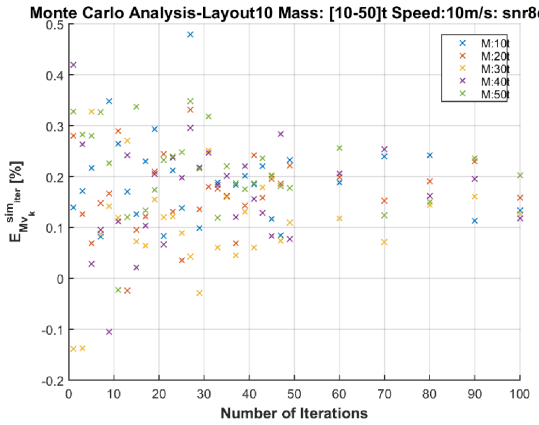

(c) $E_{M\,v_k}^{sim_{iter}}$ with k=10 $\mathrm{m\,s^{-1}}$ trend for each Monte Carlo iteration

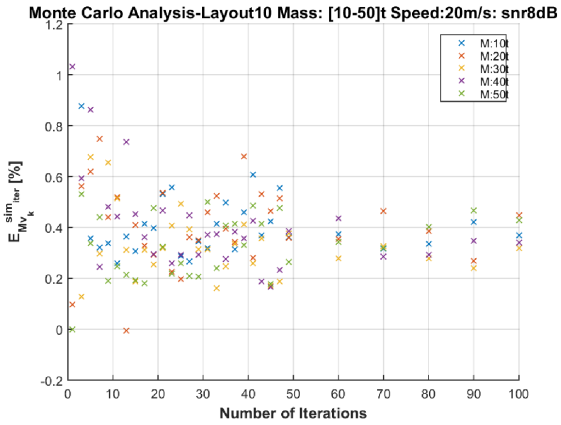

(d) $E_{M\,v_k}^{sim_{iter}}$ with k=20 $\mathrm{m\,s^{-1}}$ trend for each Monte Carlo iteration

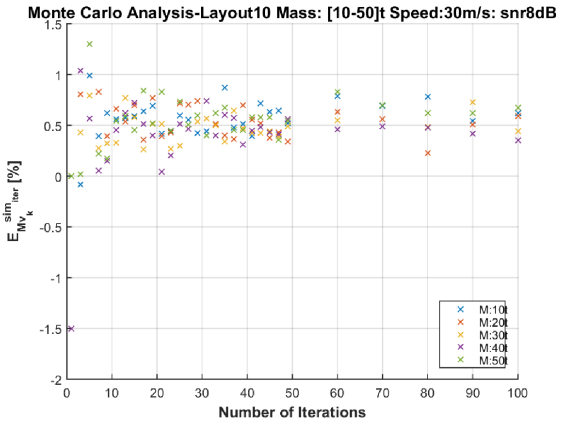

(e) $E_{M\,v_k}^{sim_{iter}}$ with k=30 $\mathrm{m\,s^{-1}}$ trend for each Monte Carlo iteration

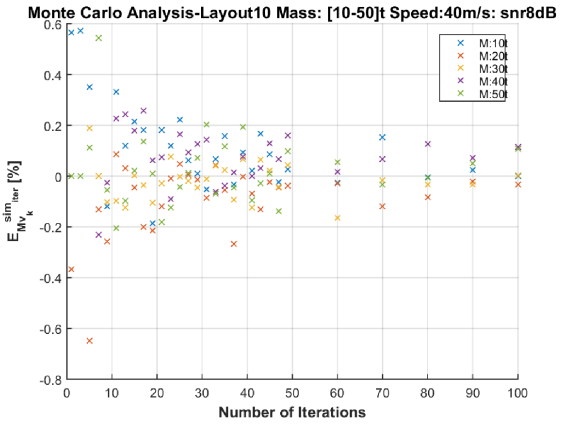

(f) $E_{M\,v_k}^{sim_{iter}}$ with k=40 $\mathrm{m\,s^{-1}}$ trend for each Monte Carlo iteration

Figure A.17: Layout10: (a) $E_v^{sim_{iter}}[\%]$ convergence with the Monte Carlo Analysis in all vehicle mass and speed. Focus on $E_{M\,v_k}^{sim_{iter}}$ with k=(2-80) $\mathrm{m\,s^{-1}}$ (b-f)

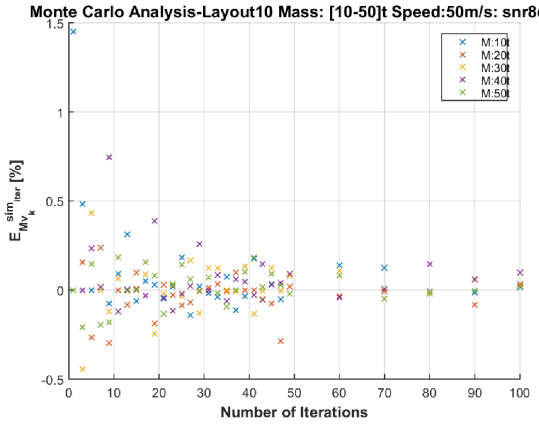

(a) $E_{M}{}_{v_k}^{sim_{iter}}$ with k=50 $\mathrm{m\,s^{-1}}$ trend for each Monte Carlo iteration

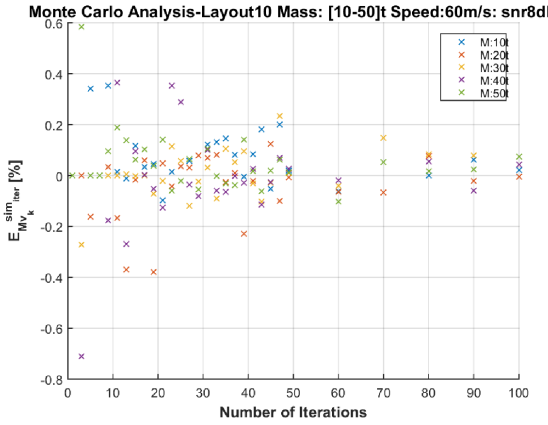

(b) $E_{M}{}_{v_k}^{sim_{iter}}$ with k=60 $\mathrm{m\,s^{-1}}$ trend for each Monte Carlo iteration

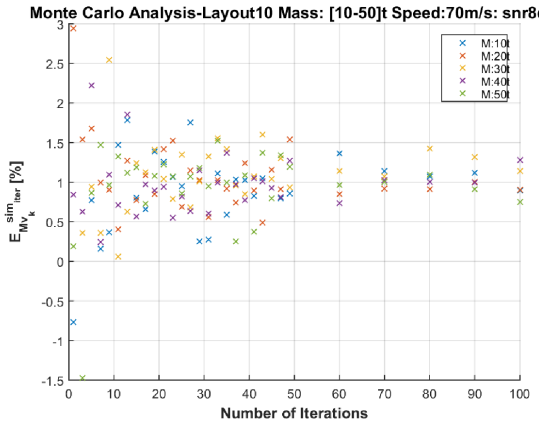

(c) $E_{M}{}_{v_k}^{sim_{iter}}$ with k=70 $\mathrm{m\,s^{-1}}$ trend for each Monte Carlo iteration

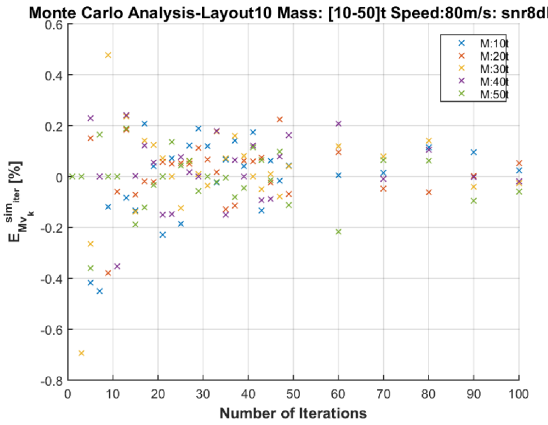

(d) $E_{M}{}_{v_k}^{sim_{iter}}$ with k=80 $\mathrm{m\,s^{-1}}$ trend for each Monte Carlo iteration

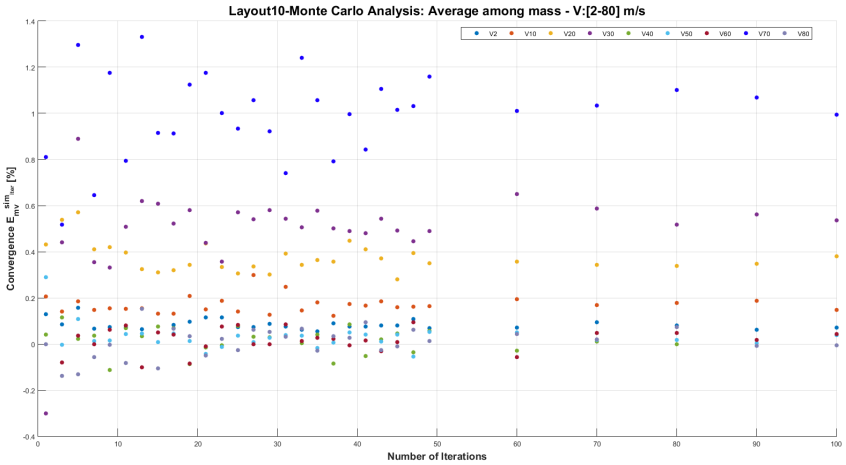

(e) Percentage relative errors on the vehicle speed $\mathbf{Em}_{v_k}^{sim_{iter}}$ with k=(2-80)$\mathrm{m\,s^{-1}}$

Figure A.18: Layout10: Focus on $E_{M}{}_{v_k}^{sim_{iter}}$ trends for each mass and vehicle speed (a-d) and $\mathbf{Em}_{v_k}^{sim_{iter}}[\%]$ trend for each speed(e): the convergence is reached for about 40 algorithm iterations

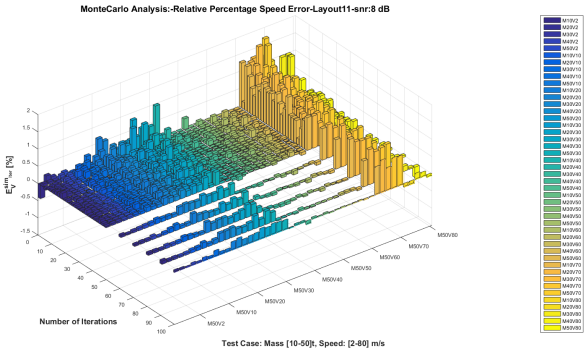

(a) $E_v^{sim_{iter}}$ trend in the full speed range (2-80) $\mathrm{m\,s^{-1}}$ and mass one (10-50) t

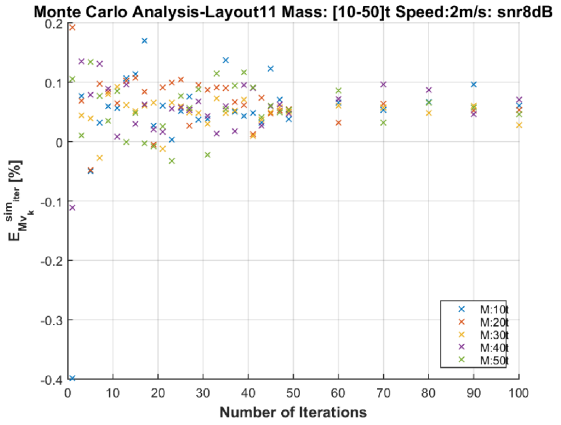

(b) $E_{M_{v_k}}^{sim_{iter}}$ with k=2 $\mathrm{m\,s^{-1}}$ trend for each Monte Carlo iteration

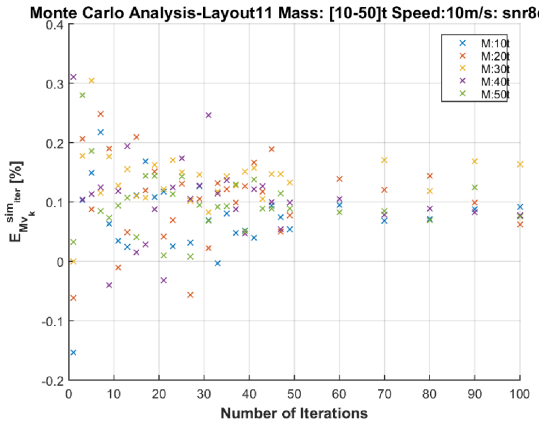

(c) $E_{M_{v_k}}^{sim_{iter}}$ with k=10 $\mathrm{m\,s^{-1}}$ trend for each Monte Carlo iteration

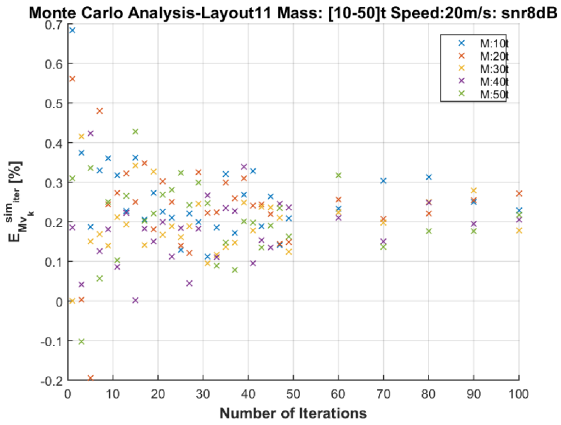

(d) $E_{M_{v_k}}^{sim_{iter}}$ with k=20 $\mathrm{m\,s^{-1}}$ trend for each Monte Carlo iteration

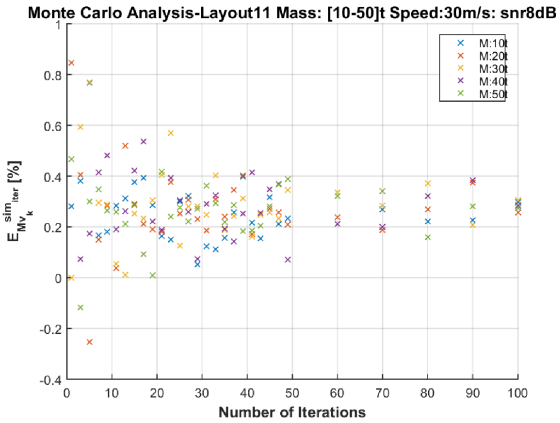

(e) $E_{M_{v_k}}^{sim_{iter}}$ with k=30 $\mathrm{m\,s^{-1}}$ trend for each Monte Carlo iteration

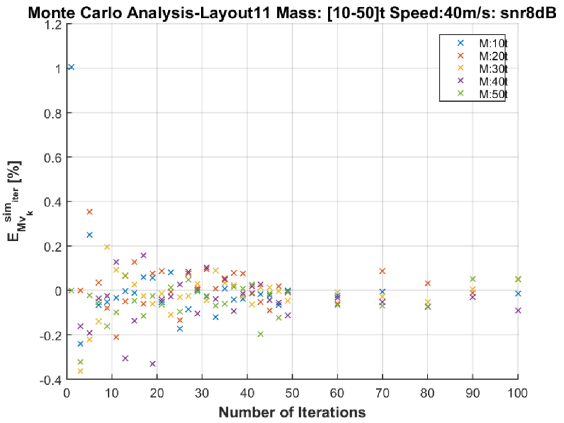

(f) $E_{M_{v_k}}^{sim_{iter}}$ with k=40 $\mathrm{m\,s^{-1}}$ trend for each Monte Carlo iteration

Figure A.19: Layout11: (a) $E_v^{sim_{iter}}[\%]$ convergence with the Monte Carlo Analysis in all vehicle mass and speed. Focus on $E_{M_{v_k}}^{sim_{iter}}$ with k=(2-80) $\mathrm{m\,s^{-1}}$ (b-f)

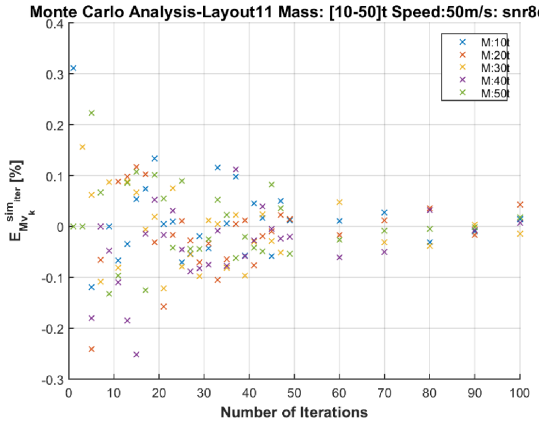

(a) $E_{M}{}_{v_k}^{sim_{iter}}$ with k=50 $\mathrm{m\,s^{-1}}$ trend for each Monte Carlo iteration

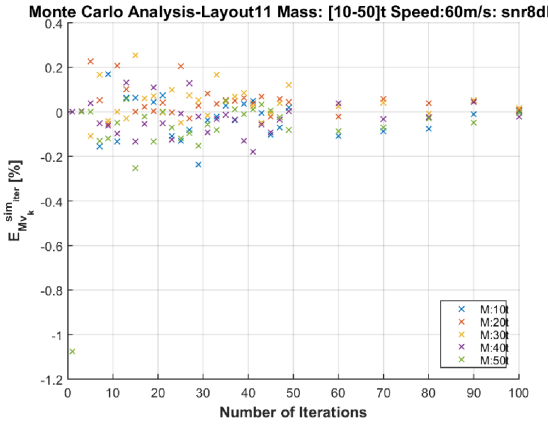

(b) $E_{M}{}_{v_k}^{sim_{iter}}$ with k=60 $\mathrm{m\,s^{-1}}$ trend for each Monte Carlo iteration

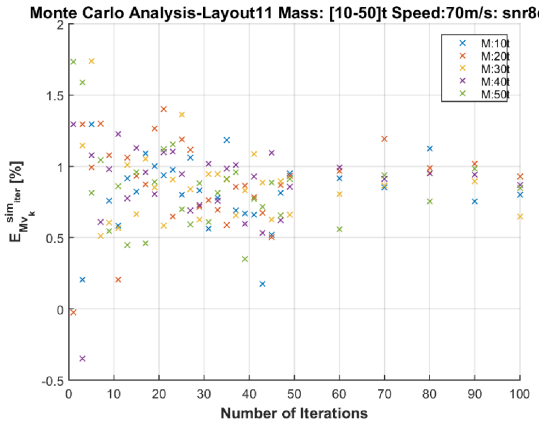

(c) $E_{M}{}_{v_k}^{sim_{iter}}$ with k=70 $\mathrm{m\,s^{-1}}$ trend for each Monte Carlo iteration

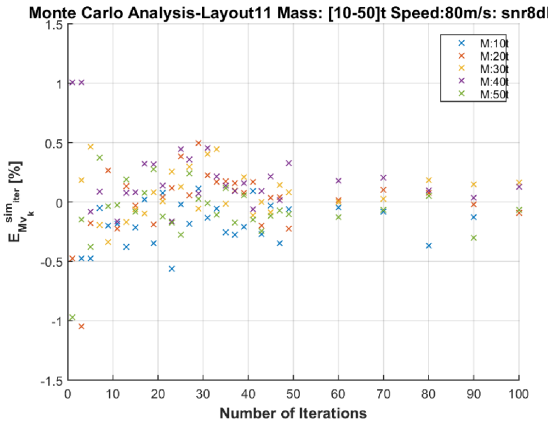

(d) $E_{M}{}_{v_k}^{sim_{iter}}$ with k=80 $\mathrm{m\,s^{-1}}$ trend for each Monte Carlo iteration

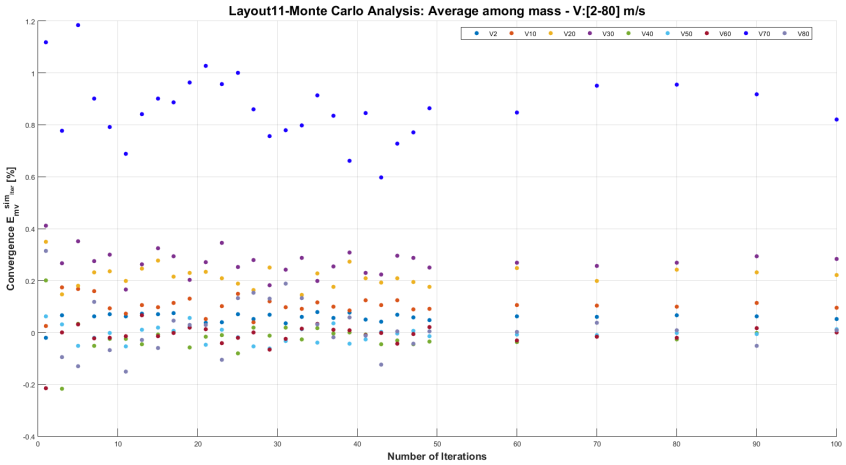

(e) Percentage relative errors on the vehicle speed $\mathbf{Em}_{v_k}^{sim_{iter}}$ with k=(2-80)$\mathrm{m\,s^{-1}}$

Figure A.20: Layout11: Focus on $E_{M}{}_{v_k}^{sim_{iter}}$ trends for each mass and vehicle speed (a-d) and $\mathbf{Em}_{v_k}^{sim_{iter}}[\%]$ trend for each speed(e): the convergence is reached for about 40 algorithm iterations

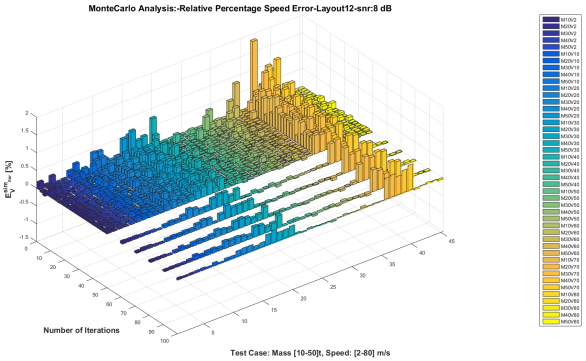

(a) $E_v^{sim_{iter}}$ trend in the full speed range (2-80) $\mathrm{m\,s^{-1}}$ and mass one (10-50) t

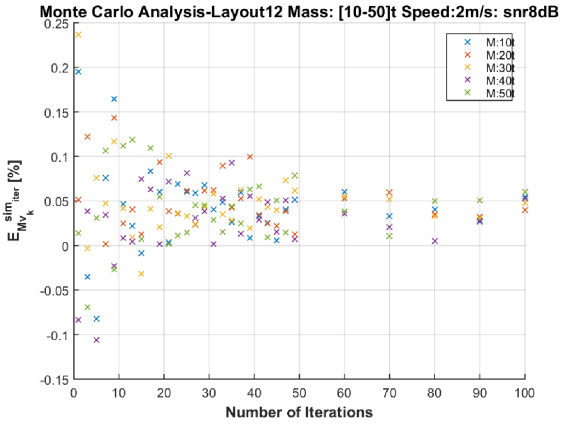

(b) $E_{M\,v_k}^{sim_{iter}}$ with k=2 $\mathrm{m\,s^{-1}}$ trend for each Monte Carlo iteration

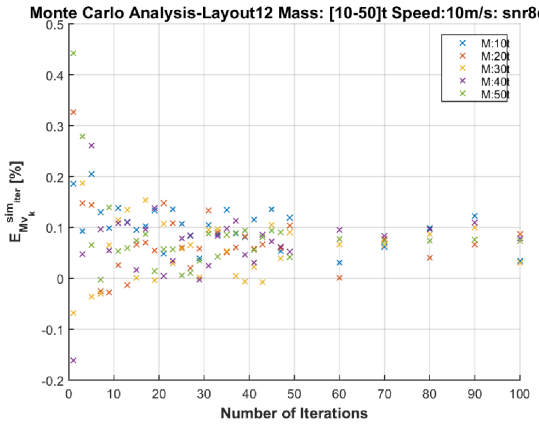

(c) $E_{M\,v_k}^{sim_{iter}}$ with k=10 $\mathrm{m\,s^{-1}}$ trend for each Monte Carlo iteration

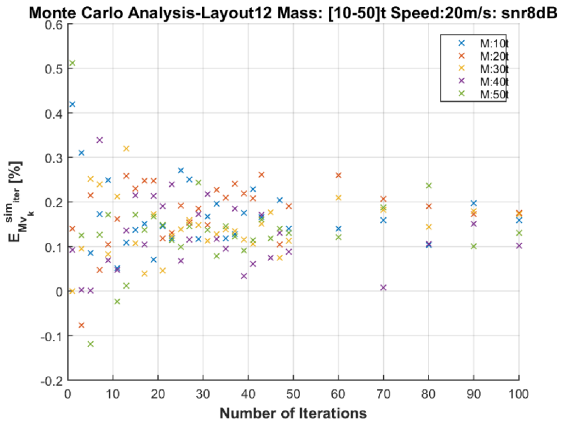

(d) $E_{M\,v_k}^{sim_{iter}}$ with k=20 $\mathrm{m\,s^{-1}}$ trend for each Monte Carlo iteration

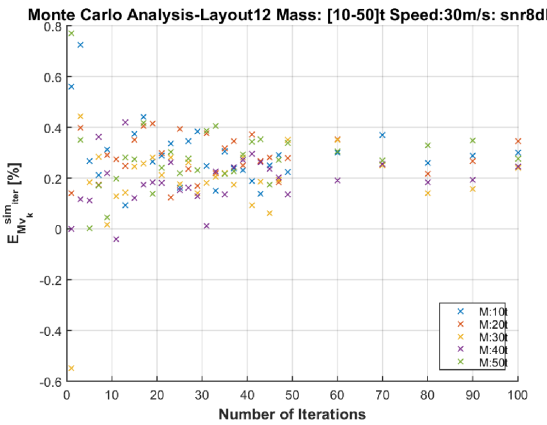

(e) $E_{M\,v_k}^{sim_{iter}}$ with k=30 $\mathrm{m\,s^{-1}}$ trend for each Monte Carlo iteration

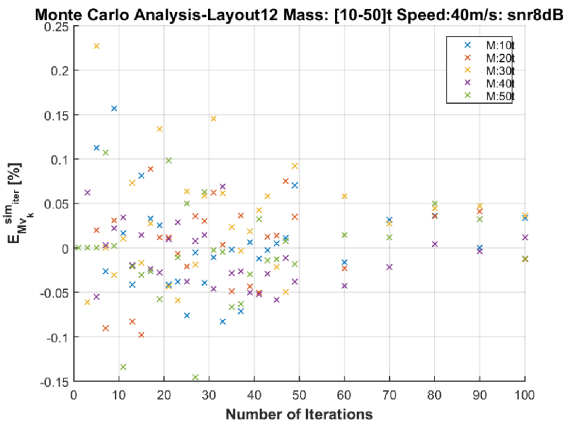

(f) $E_{M\,v_k}^{sim_{iter}}$ with k=40 $\mathrm{m\,s^{-1}}$ trend for each Monte Carlo iteration

Figure A.21: Layout12: (a) $E_v^{sim_{iter}}[\%]$ convergence with the Monte Carlo Analysis in all vehicle mass and speed. Focus on $E_{M\,v_k}^{sim_{iter}}$ with k=(2-80) $\mathrm{m\,s^{-1}}$ (b-f)

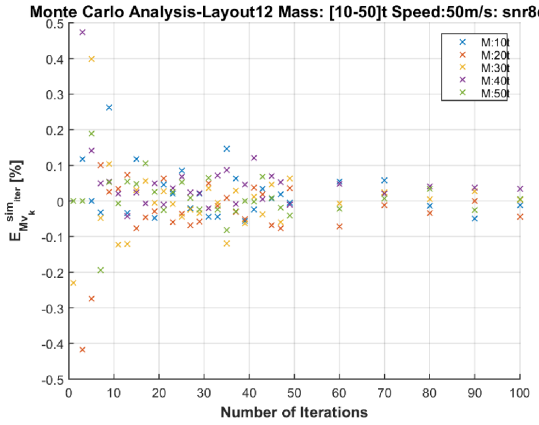

(a) $E_{M}{}_{v_k}^{sim_{iter}}$ with k=50 $\mathrm{m\,s^{-1}}$ trend for each Monte Carlo iteration

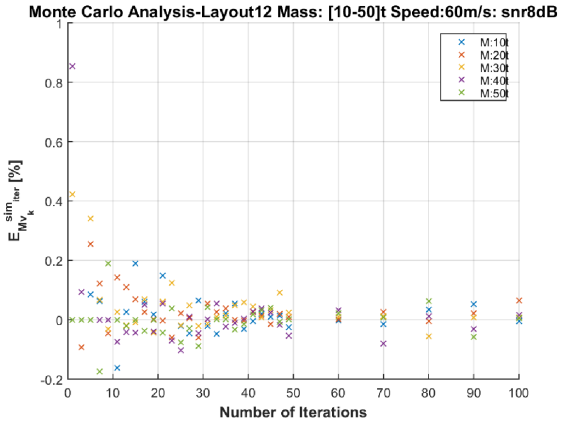

(b) $E_{M}{}_{v_k}^{sim_{iter}}$ with k=60 $\mathrm{m\,s^{-1}}$ trend for each Monte Carlo iteration

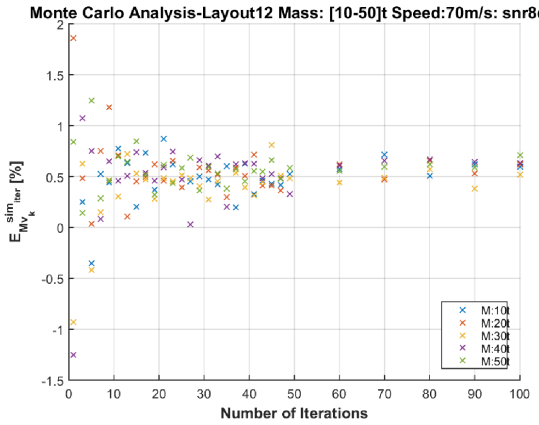

(c) $E_{M}{}_{v_k}^{sim_{iter}}$ with k=70 $\mathrm{m\,s^{-1}}$ trend for each Monte Carlo iteration

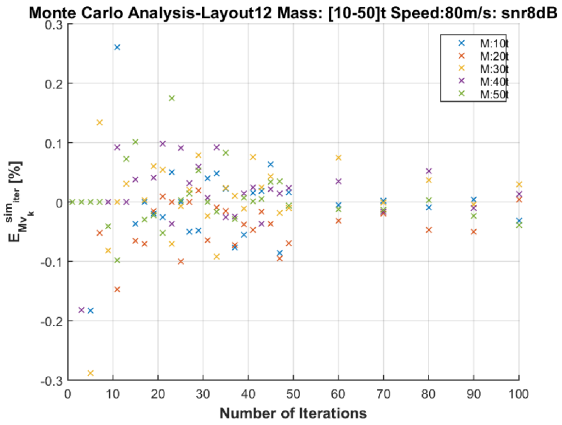

(d) $E_{M}{}_{v_k}^{sim_{iter}}$ with k=80 $\mathrm{m\,s^{-1}}$ trend for each Monte Carlo iteration

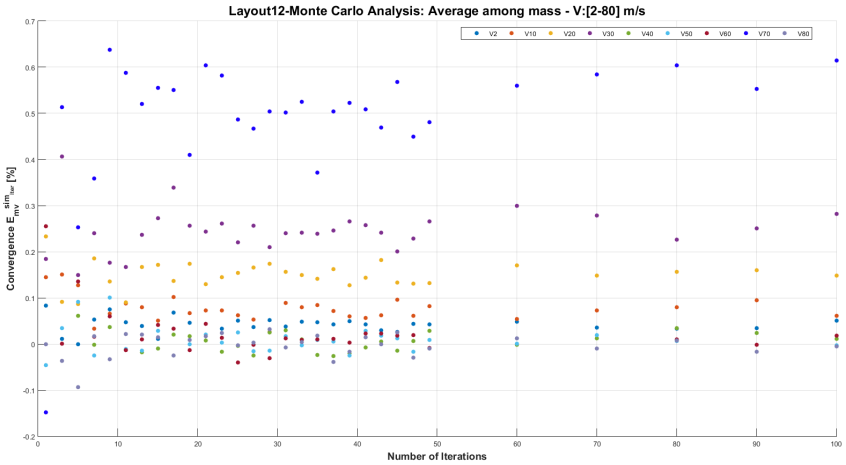

(e) Percentage relative errors on the vehicle speed $\mathbf{Em}_{v_k}^{sim_{iter}}$ with k=(2-80)$\mathrm{m\,s^{-1}}$

Figure A.22: Layout12: Focus on $E_{M}{}_{v_k}^{sim_{iter}}$ trends for each mass and vehicle speed (a-d) and $\mathbf{Em}_{v_k}^{sim_{iter}}[\%]$ trend for each speed(e): the convergence is reached for about 40 algorithm iterations

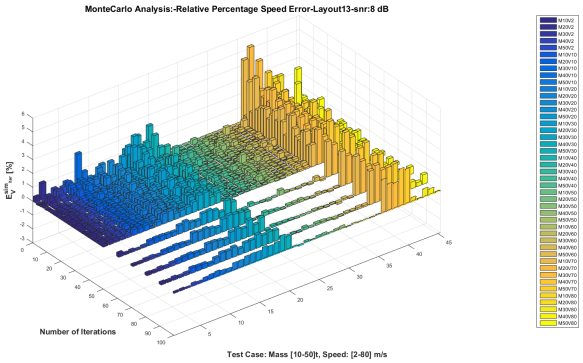

(a) $E_v^{sim_{iter}}$ trend in the full speed range (2-80) $\mathrm{m\,s^{-1}}$ and mass one (10-50) t

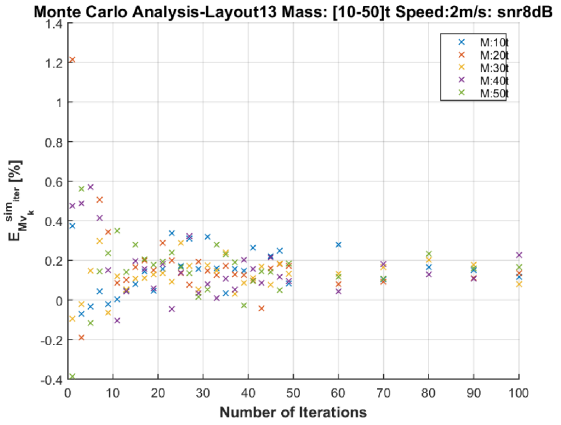

(b) $E_{M\,v_k}^{sim_{iter}}$ with k=2 $\mathrm{m\,s^{-1}}$ trend for each Monte Carlo iteration

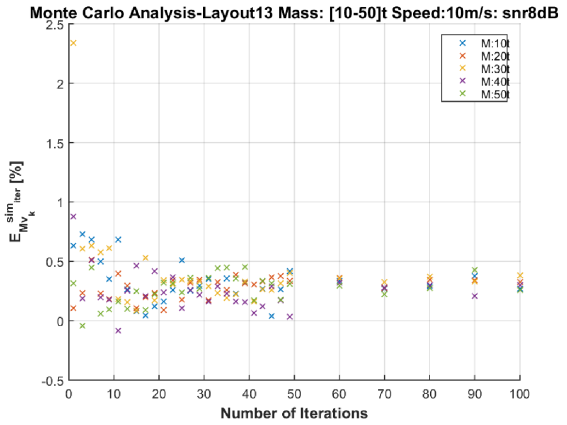

(c) $E_{M\,v_k}^{sim_{iter}}$ with k=10 $\mathrm{m\,s^{-1}}$ trend for each Monte Carlo iteration

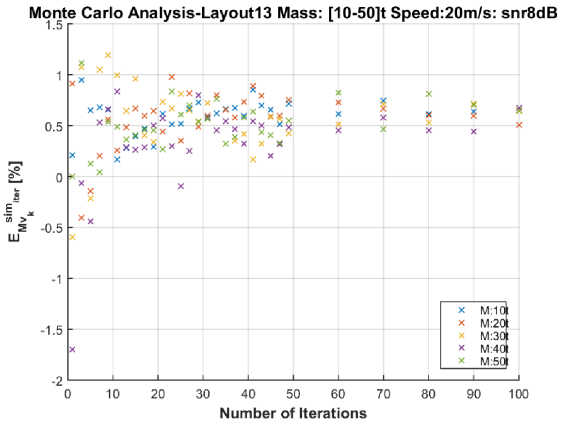

(d) $E_{M\,v_k}^{sim_{iter}}$ with k=20 $\mathrm{m\,s^{-1}}$ trend for each Monte Carlo iteration

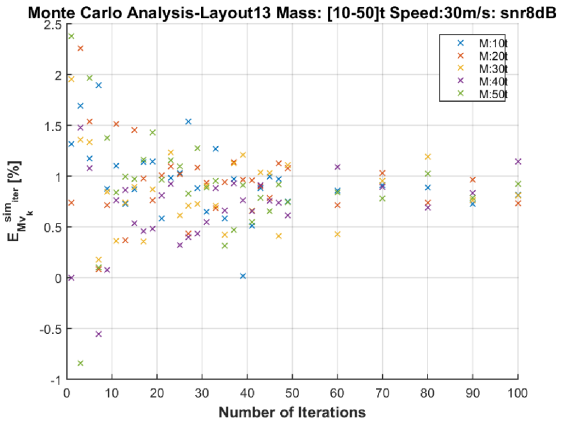

(e) $E_{M\,v_k}^{sim_{iter}}$ with k=30 $\mathrm{m\,s^{-1}}$ trend for each Monte Carlo iteration

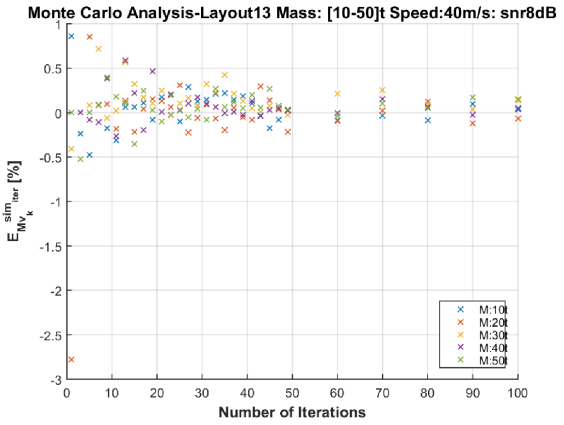

(f) $E_{M\,v_k}^{sim_{iter}}$ with k=40 $\mathrm{m\,s^{-1}}$ trend for each Monte Carlo iteration

Figure A.23: Layout13: (a) $E_v^{sim_{iter}}[\%]$ convergence with the Monte Carlo Analysis in all vehicle mass and speed. Focus on $E_{M\,v_k}^{sim_{iter}}$ with k=(2-80) $\mathrm{m\,s^{-1}}$ (b-f)

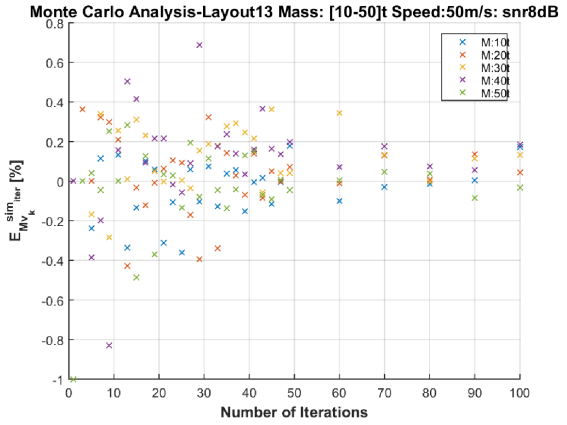

(a) $E_{M}{}_{v_k}^{sim_{iter}}$ with k=50 $\mathrm{m\,s^{-1}}$ trend for each Monte Carlo iteration

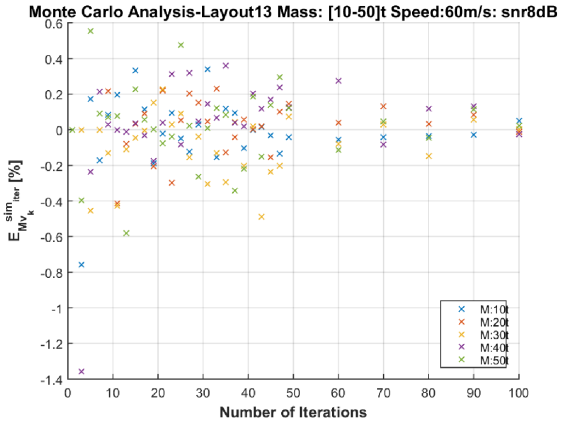

(b) $E_{M}{}_{v_k}^{sim_{iter}}$ with k=60 $\mathrm{m\,s^{-1}}$ trend for each Monte Carlo iteration

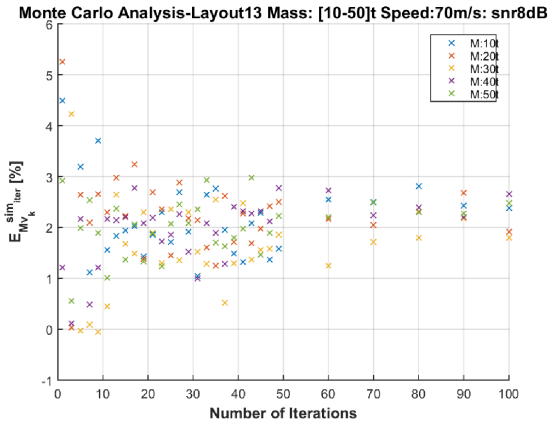

(c) $E_{M}{}_{v_k}^{sim_{iter}}$ with k=70 $\mathrm{m\,s^{-1}}$ trend for each Monte Carlo iteration

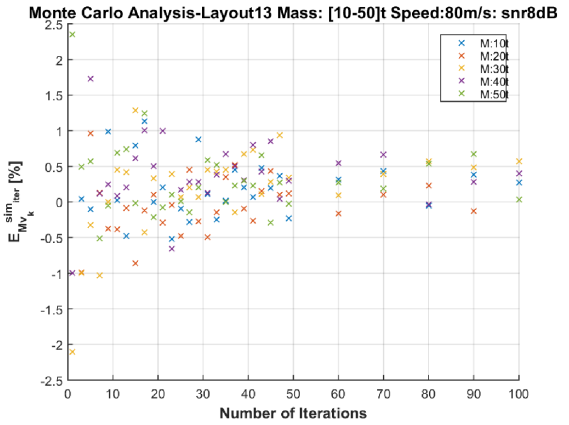

(d) $E_{M}{}_{v_k}^{sim_{iter}}$ with k=80 $\mathrm{m\,s^{-1}}$ trend for each Monte Carlo iteration

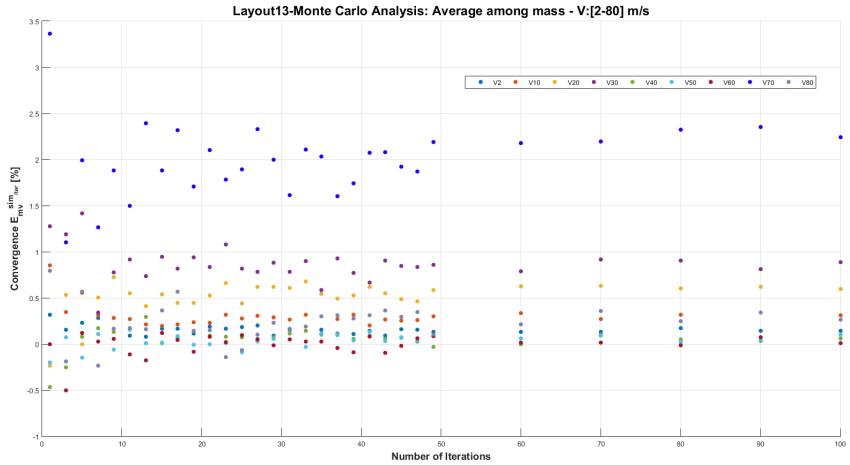

(e) Percentage relative errors on the vehicle speed $\mathbf{Em}_{v_k}^{sim_{iter}}$ with k=(2-80)$\mathrm{m\,s^{-1}}$

Figure A.24: Layout13: Focus on $E_{M}{}_{v_k}^{sim_{iter}}$ trends for each mass and vehicle speed (a-d) and $\mathbf{Em}_{v_k}^{sim_{iter}}[\%]$ trend for each speed(e): the convergence is reached for about 40 algorithm iterations

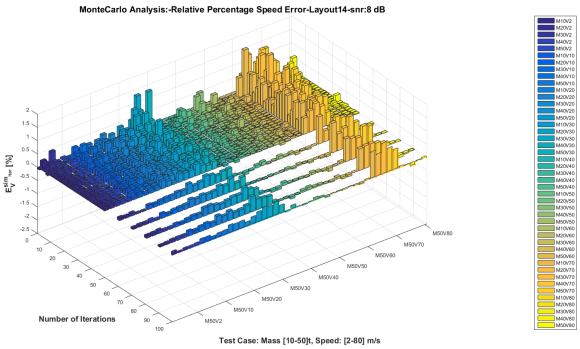

(a) $E_v^{sim_{iter}}$ trend in the full speed range (2-80) $\mathrm{m\,s^{-1}}$ and mass one (10-50) t

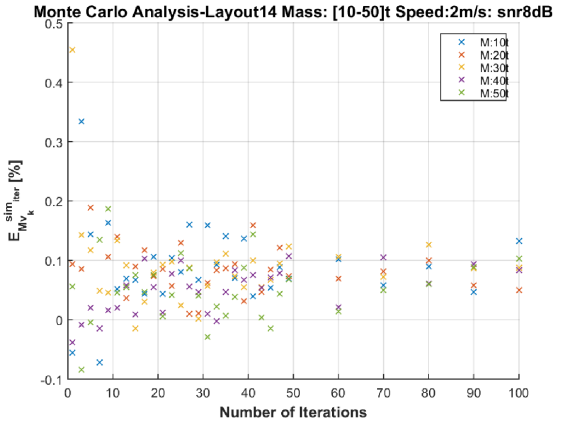

(b) $E_{M\,v_k}^{sim_{iter}}$ with k=2 $\mathrm{m\,s^{-1}}$ trend for each Monte Carlo iteration

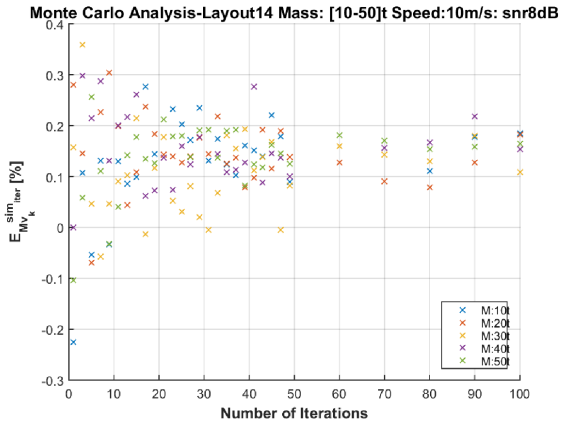

(c) $E_{M\,v_k}^{sim_{iter}}$ with k=10 $\mathrm{m\,s^{-1}}$ trend for each Monte Carlo iteration

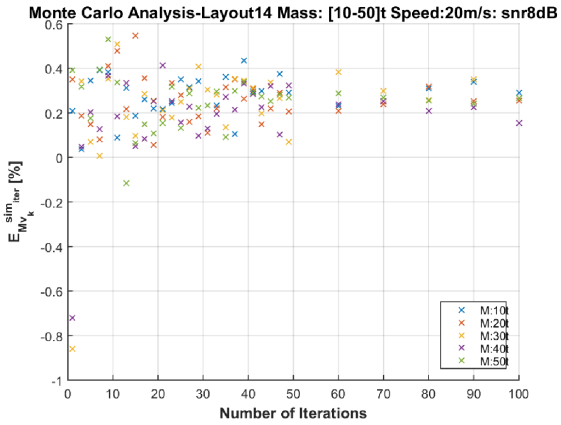

(d) $E_{M\,v_k}^{sim_{iter}}$ with k=20 $\mathrm{m\,s^{-1}}$ trend for each Monte Carlo iteration

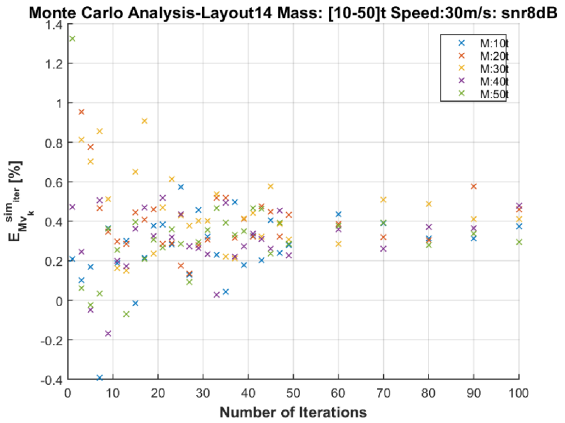

(e) $E_{M\,v_k}^{sim_{iter}}$ with k=30 $\mathrm{m\,s^{-1}}$ trend for each Monte Carlo iteration

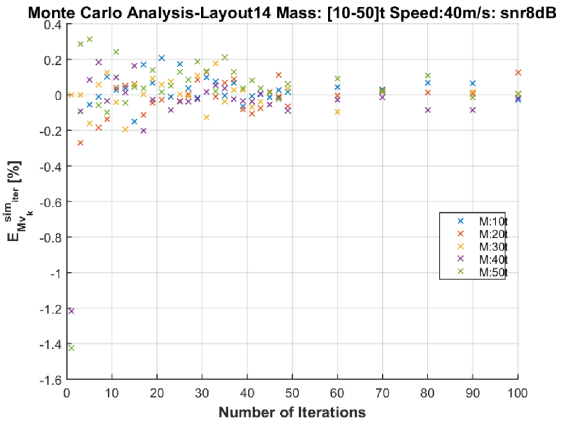

(f) $E_{M\,v_k}^{sim_{iter}}$ with k=40 $\mathrm{m\,s^{-1}}$ trend for each Monte Carlo iteration

Figure A.25: Layout14: (a) $E_v^{sim_{iter}}[\%]$ convergence with the Monte Carlo Analysis in all vehicle mass and speed. Focus on $E_{M\,v_k}^{sim_{iter}}$ with k=(2-80) $\mathrm{m\,s^{-1}}$ (b-f)

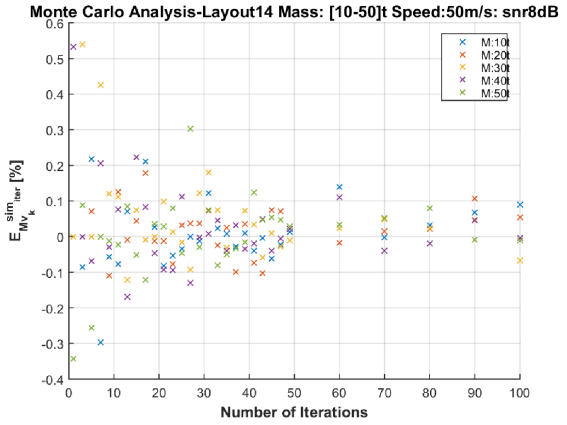

(a) $E_{M}{}_{v_k}^{sim_{iter}}$ with k=50 $\mathrm{m\,s^{-1}}$ trend for each Monte Carlo iteration

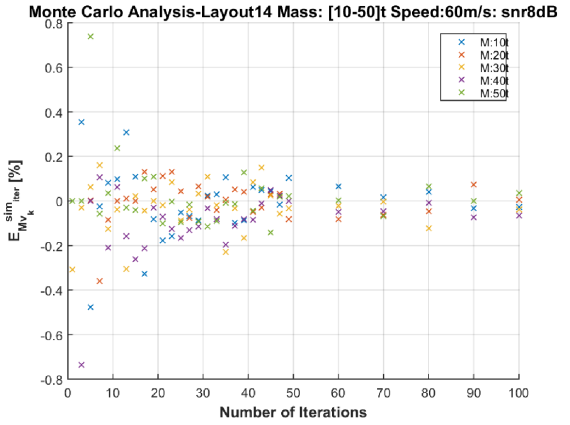

(b) $E_{M}{}_{v_k}^{sim_{iter}}$ with k=60 $\mathrm{m\,s^{-1}}$ trend for each Monte Carlo iteration

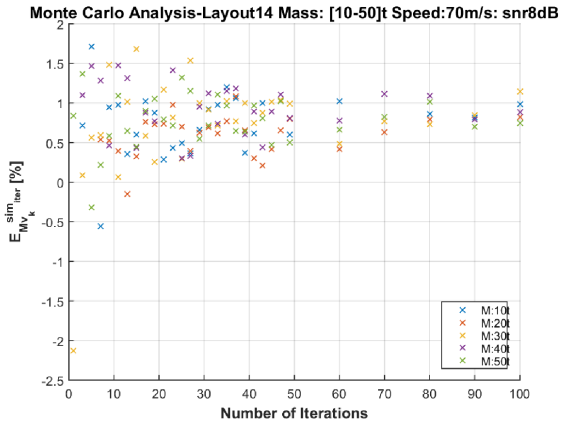

(c) $E_{M}{}_{v_k}^{sim_{iter}}$ with k=70 $\mathrm{m\,s^{-1}}$ trend for each Monte Carlo iteration

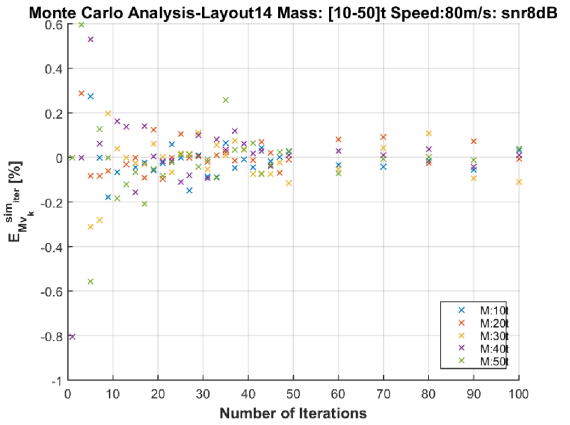

(d) $E_{M}{}_{v_k}^{sim_{iter}}$ with k=80 $\mathrm{m\,s^{-1}}$ trend for each Monte Carlo iteration

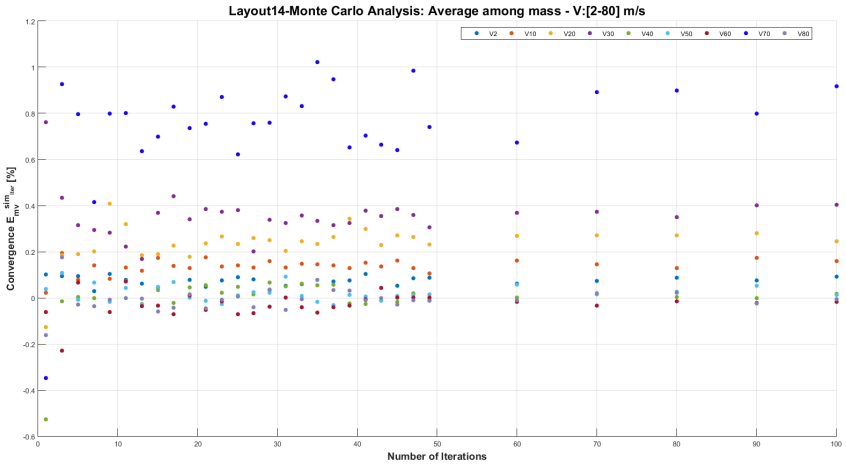

(e) Percentage relative errors on the vehicle speed $\mathbf{Em}_{v_k}^{sim_{iter}}$ with k=(2-80)$\mathrm{m\,s^{-1}}$

Figure A.26: Layout14: Focus on $E_{M}{}_{v_k}^{sim_{iter}}$ trends for each mass and vehicle speed (a-d) and $\mathbf{Em}_{v_k}^{sim_{iter}}[\%]$ trend for each speed(e): the convergence is reached for about 40 algorithm iterations

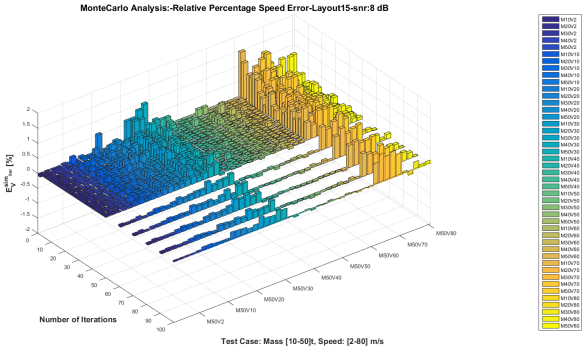

(a) $E_v^{sim_{iter}}$ trend in the full speed range (2-80) $\mathrm{m\,s^{-1}}$ and mass one (10-50) t

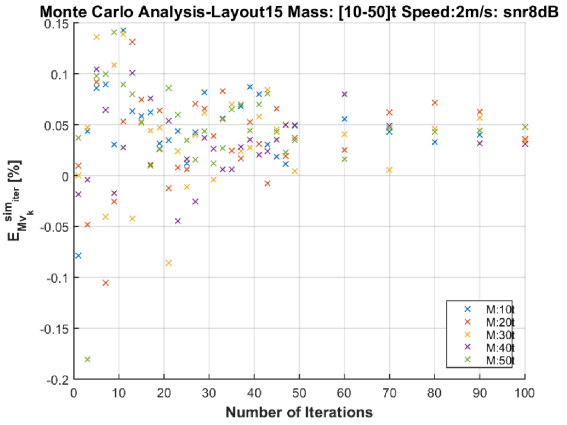

(b) $E_{M\,v_k}^{sim_{iter}}$ with k=2 $\mathrm{m\,s^{-1}}$ trend for each Monte Carlo iteration

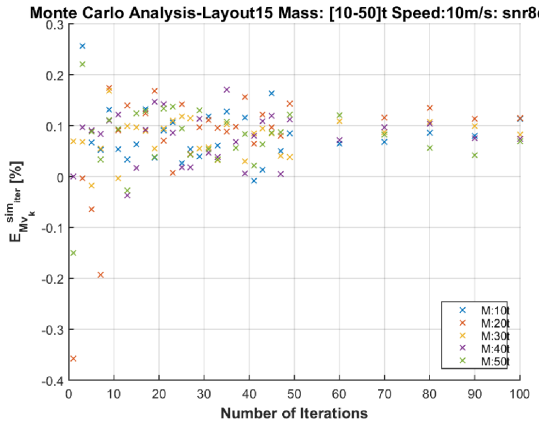

(c) $E_{M\,v_k}^{sim_{iter}}$ with k=10 $\mathrm{m\,s^{-1}}$ trend for each Monte Carlo iteration

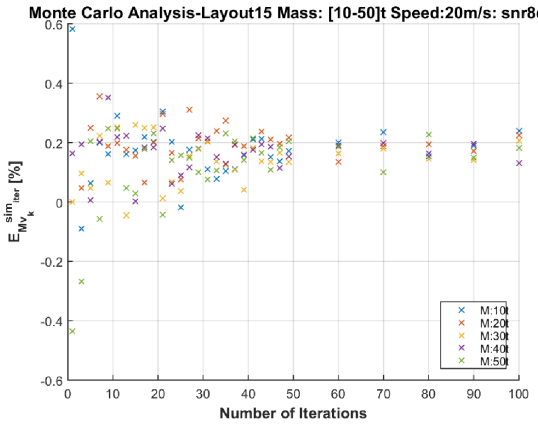

(d) $E_{M\,v_k}^{sim_{iter}}$ with k=20 $\mathrm{m\,s^{-1}}$ trend for each Monte Carlo iteration

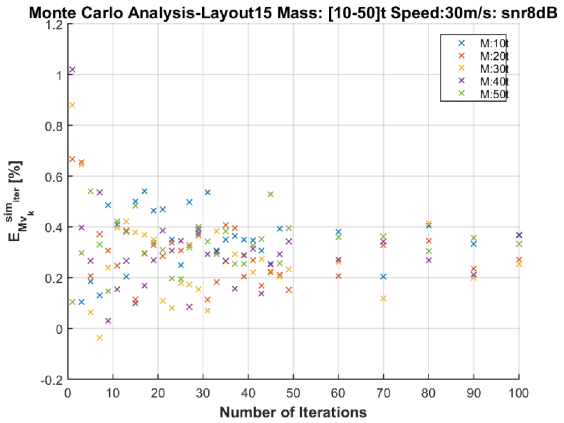

(e) $E_{M\,v_k}^{sim_{iter}}$ with k=30 $\mathrm{m\,s^{-1}}$ trend for each Monte Carlo iteration

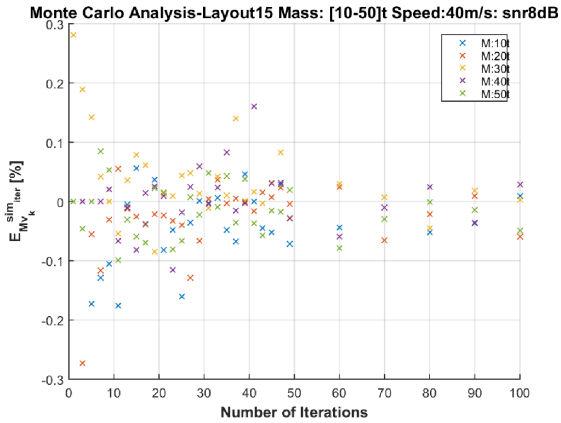

(f) $E_{M\,v_k}^{sim_{iter}}$ with k=40 $\mathrm{m\,s^{-1}}$ trend for each Monte Carlo iteration

Figure A.27: Layout15: (a) $E_v^{sim_{iter}}[\%]$ convergence with the Monte Carlo Analysis in all vehicle mass and speed. Focus on $E_{M\,v_k}^{sim_{iter}}$ with k=(2-80) $\mathrm{m\,s^{-1}}$ (b-f)

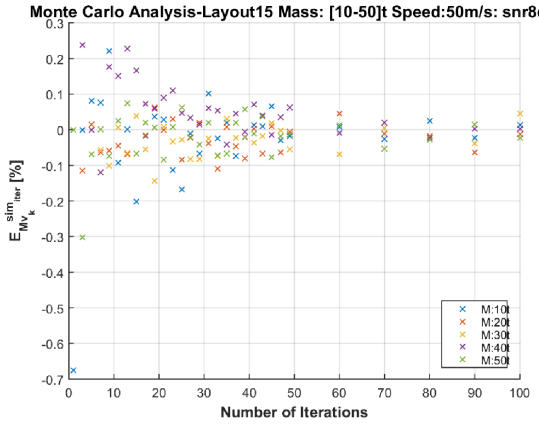

(a) $E_{M}{}_{v_k}^{sim_{iter}}$ with k=50 $\mathrm{m\,s^{-1}}$ trend for each Monte Carlo iteration

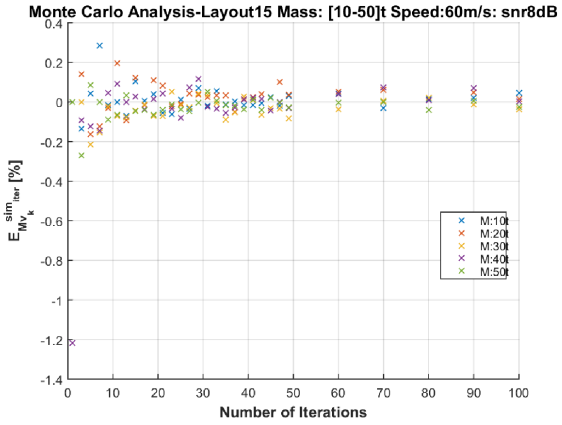

(b) $E_{M}{}_{v_k}^{sim_{iter}}$ with k=60 $\mathrm{m\,s^{-1}}$ trend for each Monte Carlo iteration

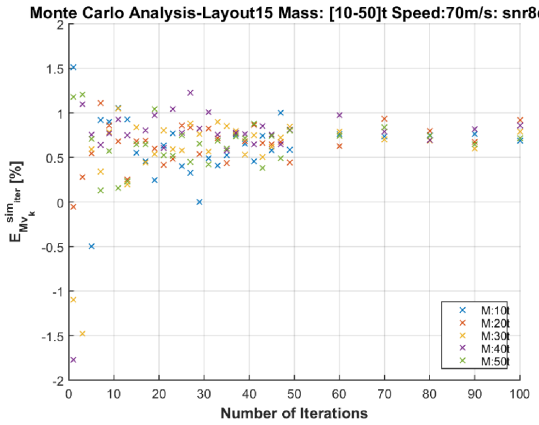

(c) $E_{M}{}_{v_k}^{sim_{iter}}$ with k=70 $\mathrm{m\,s^{-1}}$ trend for each Monte Carlo iteration

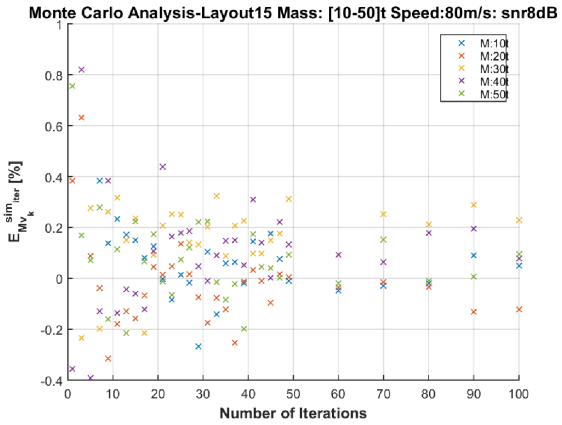

(d) $E_{M}{}_{v_k}^{sim_{iter}}$ with k=80 $\mathrm{m\,s^{-1}}$ trend for each Monte Carlo iteration

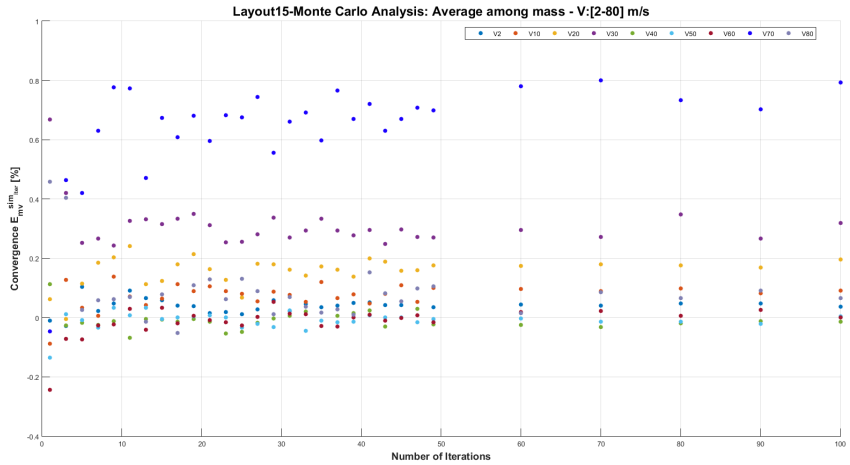

(e) Percentage relative errors on the vehicle speed $\mathbf{Em}_{v_k}^{sim_{iter}}$ with k=(2-80)$\mathrm{m\,s^{-1}}$

Figure A.28: Layout15: Focus on $E_{M}{}_{v_k}^{sim_{iter}}$ trends for each mass and vehicle speed (a-d) and $\mathbf{Em}_{v_k}^{sim_{iter}}[\%]$ trend for each speed(e): the convergence is reached for about 40 algorithm iterations

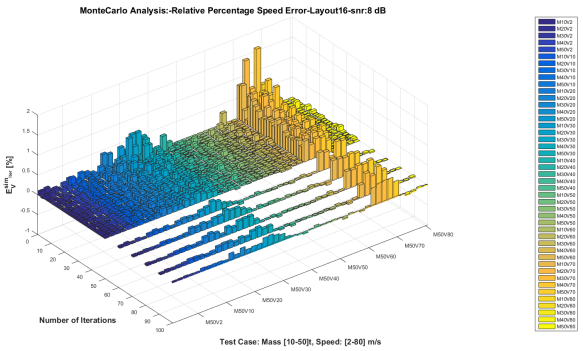

(a) $E_v^{sim_{iter}}$ trend in the full speed range (2-80) $\mathrm{m\,s^{-1}}$ and mass one (10-50) t

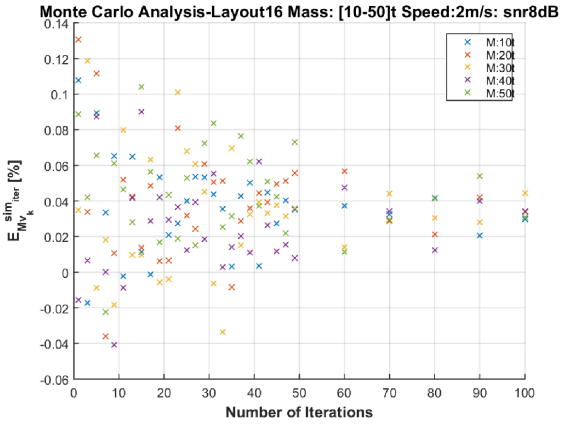

(b) $E_{Mv_k}^{sim_{iter}}$ with k=2 $\mathrm{m\,s^{-1}}$ trend for each Monte Carlo iteration

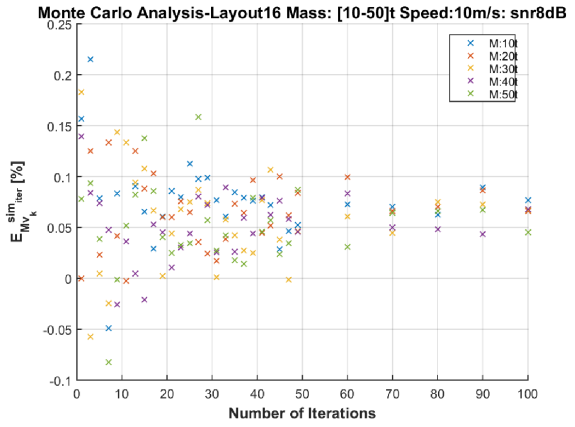

(c) $E_{Mv_k}^{sim_{iter}}$ with k=10 $\mathrm{m\,s^{-1}}$ trend for each Monte Carlo iteration

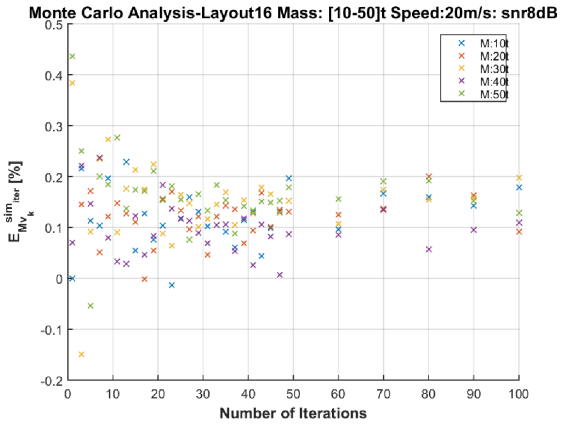

(d) $E_{Mv_k}^{sim_{iter}}$ with k=20 $\mathrm{m\,s^{-1}}$ trend for each Monte Carlo iteration

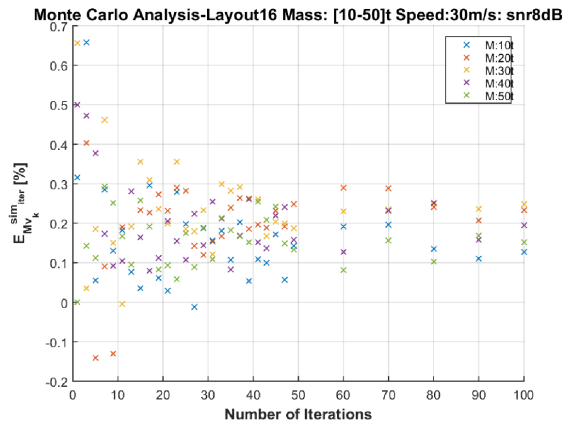

(e) $E_{Mv_k}^{sim_{iter}}$ with k=30 $\mathrm{m\,s^{-1}}$ trend for each Monte Carlo iteration

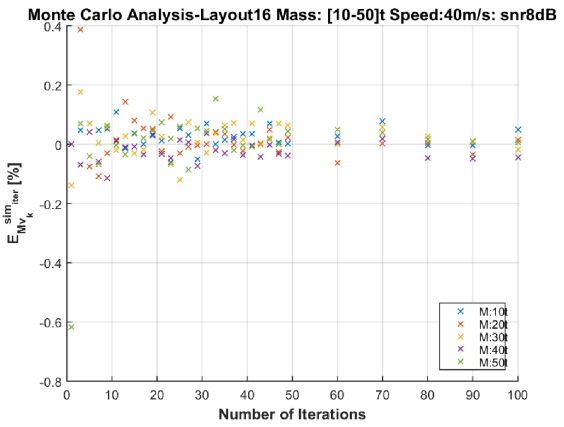

(f) $E_{Mv_k}^{sim_{iter}}$ with k=40 $\mathrm{m\,s^{-1}}$ trend for each Monte Carlo iteration

Figure A.29: Layout16: (a) $E_v^{sim_{iter}}[\%]$ convergence with the Monte Carlo Analysis in all vehicle mass and speed. Focus on $E_{Mv_k}^{sim_{iter}}$ with k=(2-80) $\mathrm{m\,s^{-1}}$ (b-f)

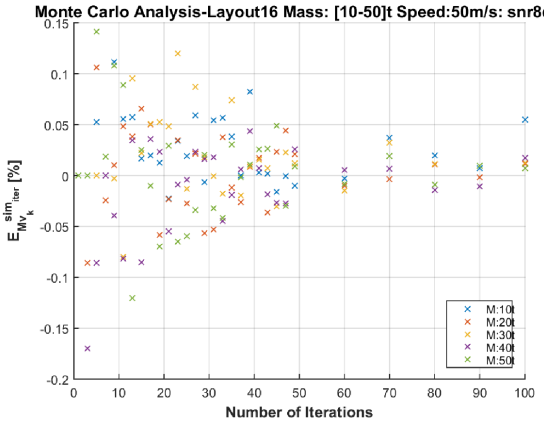

(a) $E_M{}_{v_k}^{sim_{iter}}$ with k=50 $\mathrm{m\,s^{-1}}$ trend for each Monte Carlo iteration

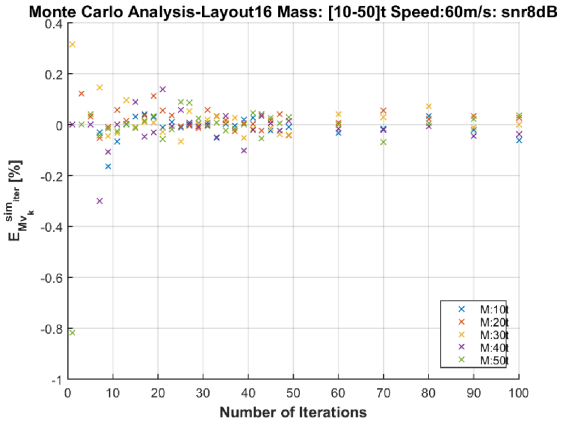

(b) $E_M{}_{v_k}^{sim_{iter}}$ with k=60 $\mathrm{m\,s^{-1}}$ trend for each Monte Carlo iteration

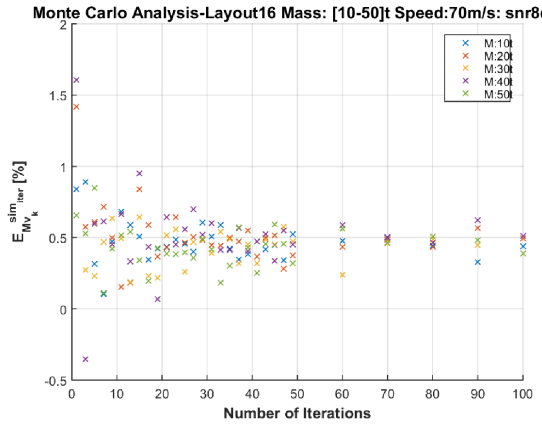

(c) $E_M{}_{v_k}^{sim_{iter}}$ with k=70 $\mathrm{m\,s^{-1}}$ trend for each Monte Carlo iteration

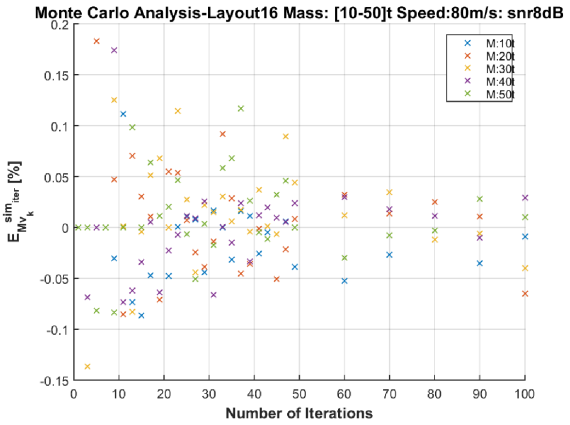

(d) $E_M{}_{v_k}^{sim_{iter}}$ with k=80 $\mathrm{m\,s^{-1}}$ trend for each Monte Carlo iteration

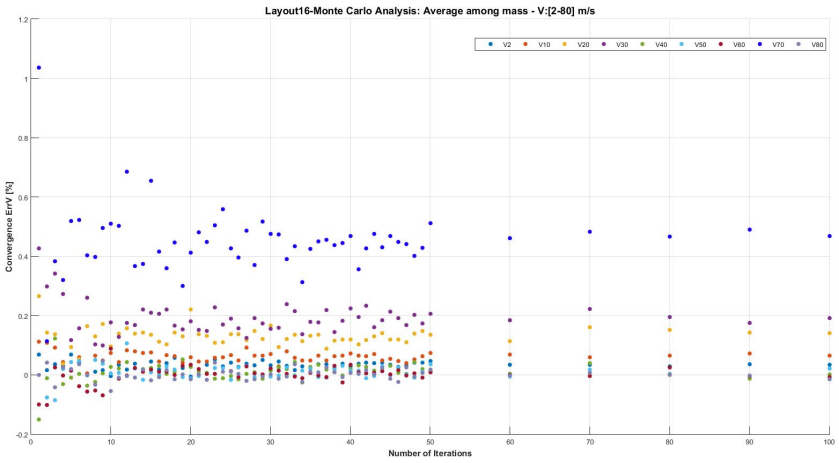

(e) Percentage relative errors on the vehicle speed $\mathbf{Em}_{v_k}^{sim_{iter}}$ with k=(2-80)$\mathrm{m\,s^{-1}}$

Figure A.30: Layout16: Focus on $E_M{}_{v_k}^{sim_{iter}}$ trends for each mass and vehicle speed (a-d) and $\mathbf{Em}_{v_k}^{sim_{iter}}[\%]$ trend for each speed(e): the convergence is reached for about 40 algorithm iterations

Appendix B

Appendix-FDA

The global performance of the FDA approach has been evaluated in all the measurement layouts. Following, the error trends on the train axles crossing times and the vehicle speed, analysed with the Monte Carlo approach, have been summarized, showing good results as indicated and discussed in Chapter 3. More focused, the trend of the estimation errors with the Monte Carlo analysis about the vehicle speed in the full speed and mass range is shown, for each measurement layout. The Monte Carlo convergence is shown both with the process aimed at estimating the vehicle speed both with the procedure to estimate the axles crossing times.

Layout3

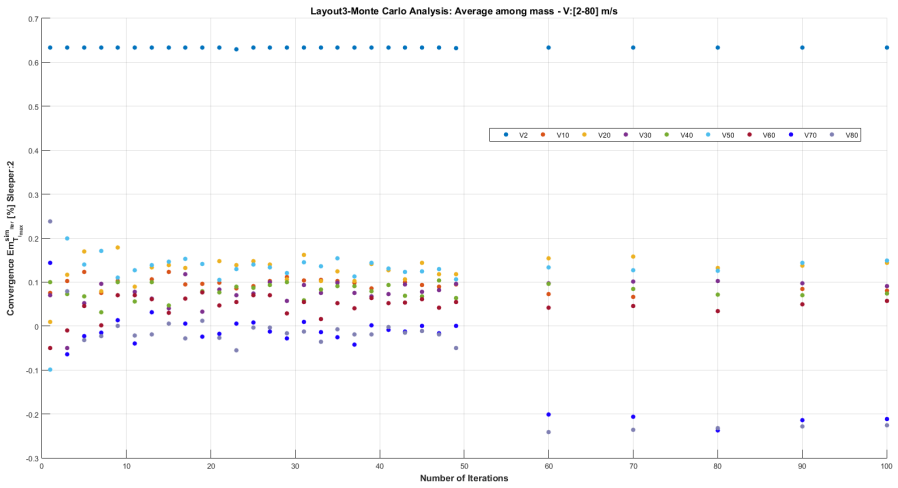

Figure B.1: Layout3: Monte Carlo analysis on the $Em_{T_{imax}}^{sim_{iter}}$: results show as after 30 iterations the convergence is reached

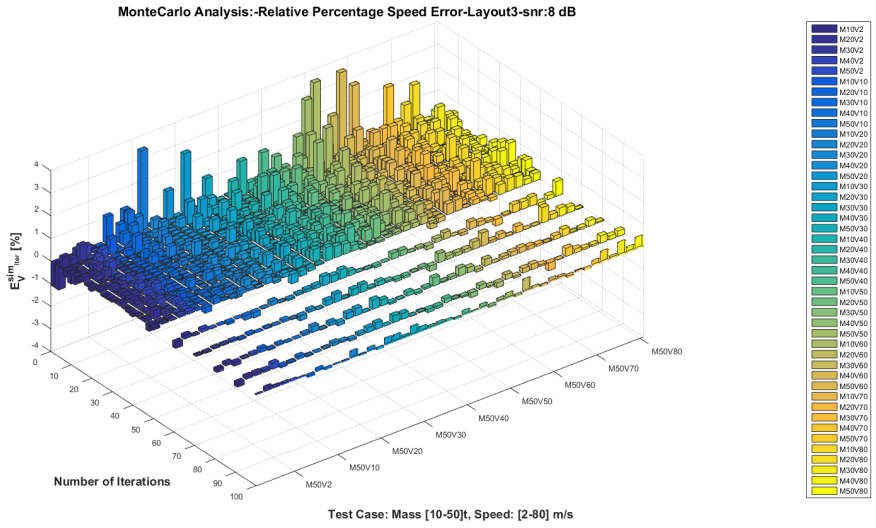

Figure B.2: Layout3: Percentage $E_V^{sim_{iter}}$ trend in all speed and mass range: results highlight how, for each speed, the value of mass vehicle not involves a relevant effect on the errors

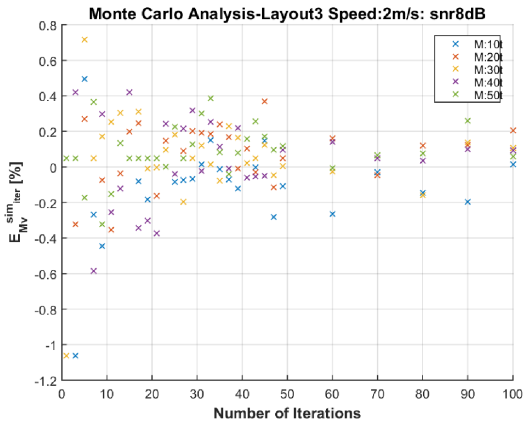

(a) Percentage $E_M{}_{v_k}^{sim_{iter}}$ (with k=2 m s^{-1})

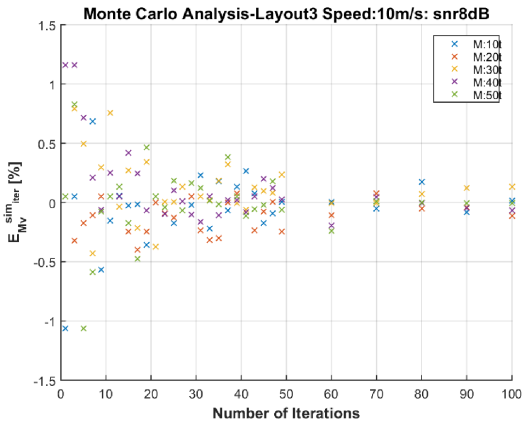

(b) Percentage $E_M{}_{v_k}^{sim_{iter}}$ (with k=10 m s^{-1})

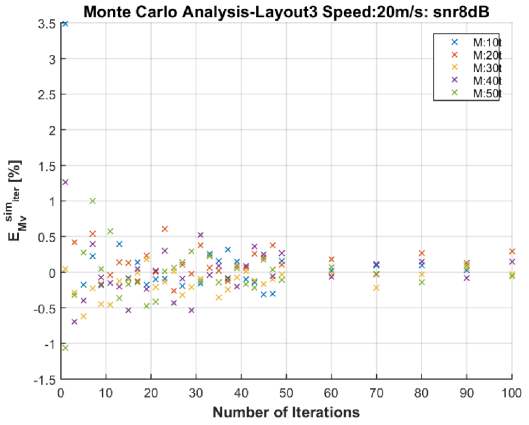

(c) Percentage $E_M{}_{v_k}^{sim_{iter}}$ (with k=20 m s^{-1})

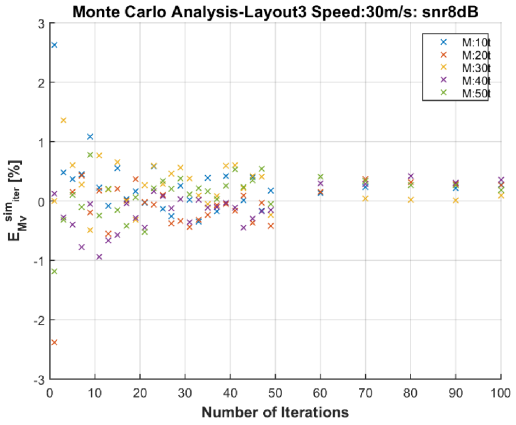

(d) Percentage $E_M{}_{v_k}^{sim_{iter}}$ (with k=30 m s^{-1})

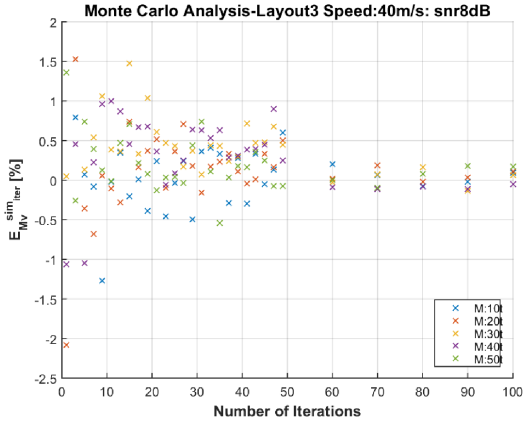

(e) Percentage $E_M{}_{v_k}^{sim_{iter}}$ (with k=40 m s^{-1})

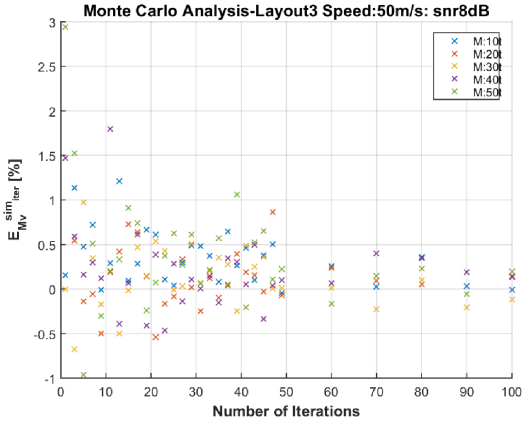

(f) Percentage $E_M{}_{v_k}^{sim_{iter}}$ (with k=50 m s^{-1})

Figure B.3: Layout3: Speed Estimation-Monte Carlo Analysis with k=(2-50) m s^{-1}

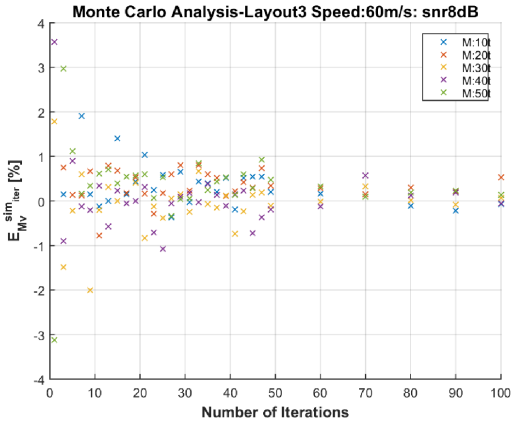

(a) Percentage $E_M{}_{v_k}^{sim_{iter}}$ (with k=60 m s^{-1})

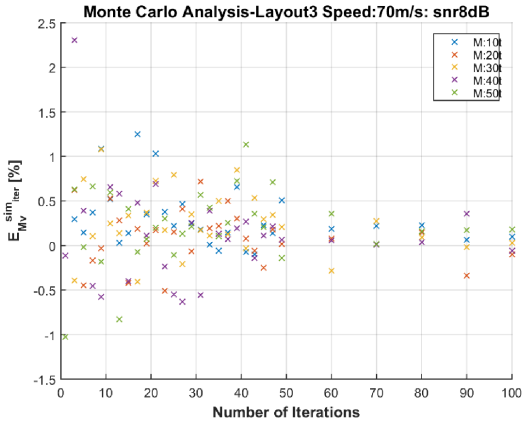

(b) Percentage $E_M{}_{v_k}^{sim_{iter}}$ (with k=70 m s^{-1})

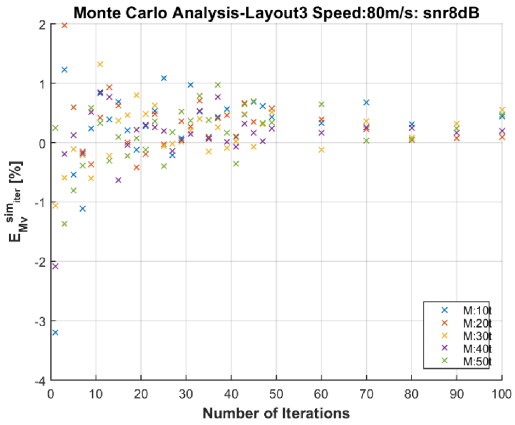

(c) Percentage $E_M{}_{v_k}^{sim_{iter}}$ (with k=80 m s^{-1})

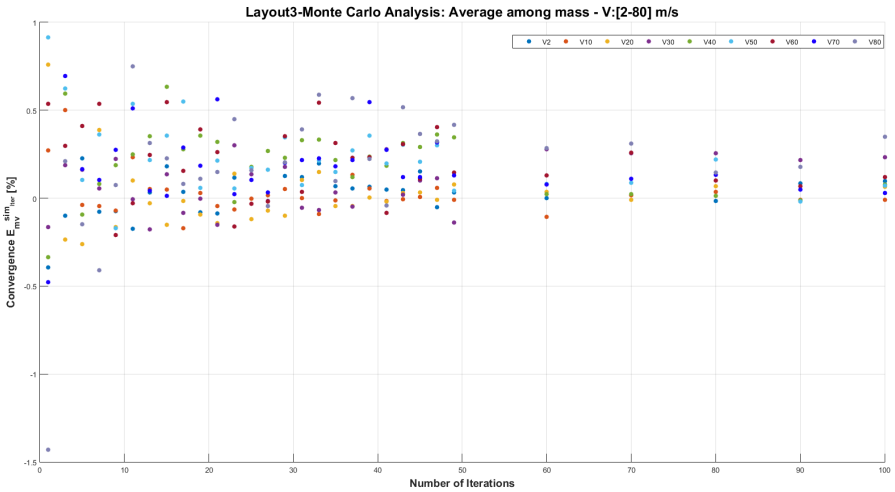

(d) Monte Carlo convergence of $\mathbf{Em}_{v_k}^{sim_{iter}}$ reached at about 30 iteration

Figure B.4: Layout3: Speed Estimation-Monte Carlo Analysis with k=(60-80) m s^{-1} and (d) Monte Carlo convergence

Layout4

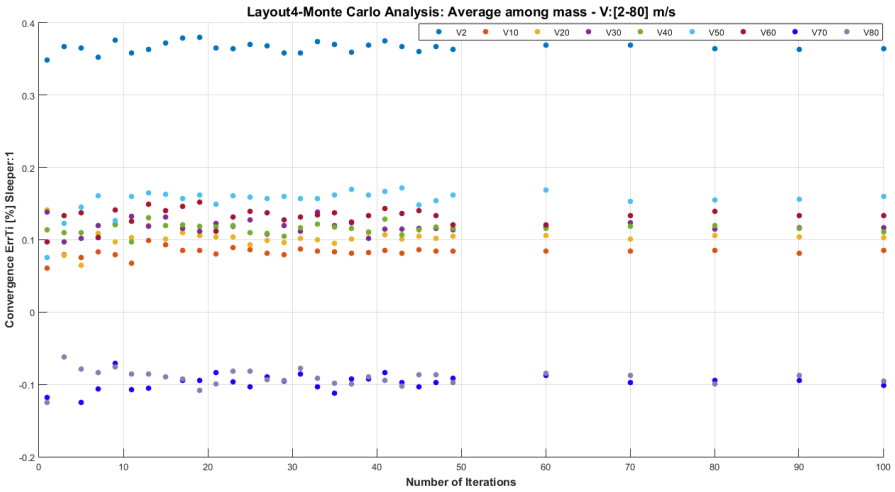

Figure B.5: Layout4: Monte Carlo analysis on the $Em_{T_{imax}}^{sim_{iter}}$: results show as after 30 iterations the convergence is reached

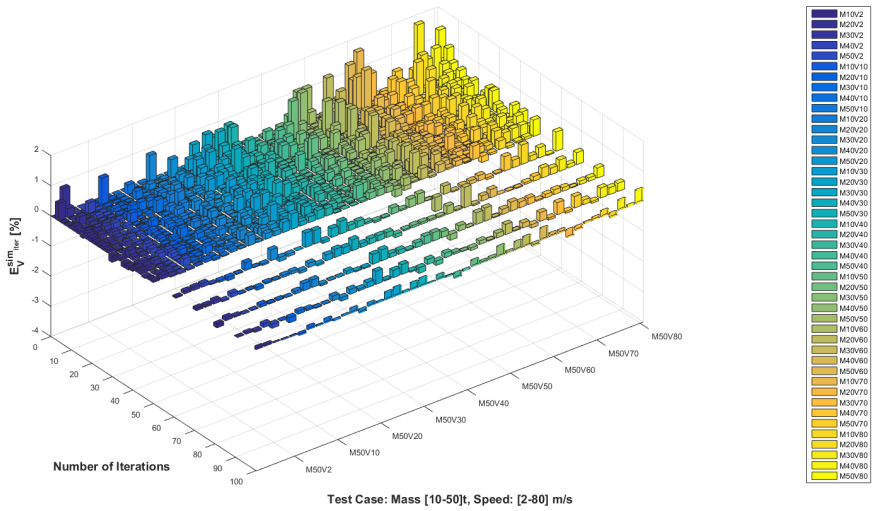

Figure B.6: Layout4: Percentage $E_V^{sim_{iter}}$ trend in all speed and mass range: results highlight how, for each speed, the value of mass vehicle not involves a relevant effect on the errors

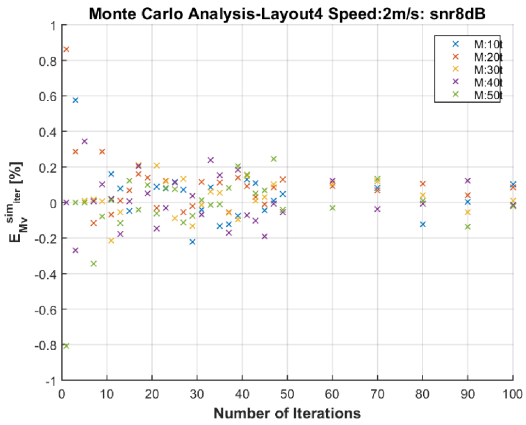

(a) Percentage $E_{M}{}_{v_k}^{sim_{iter}}$ (with k=2 m s^{-1})

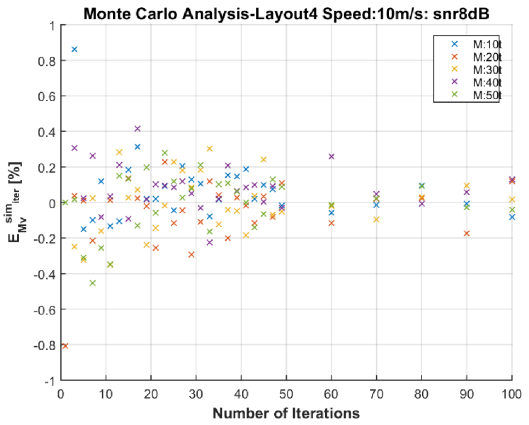

(b) Percentage $E_{M}{}_{v_k}^{sim_{iter}}$ (with k=10 m s^{-1})

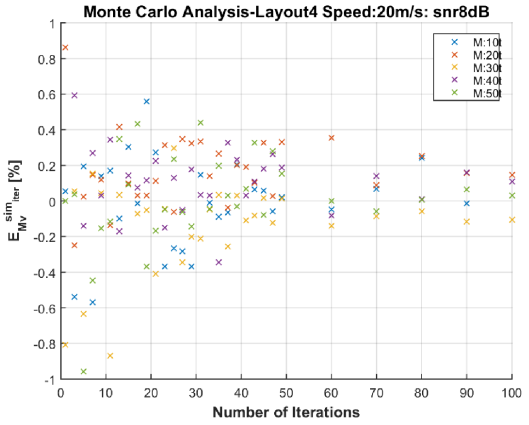

(c) Percentage $E_{M}{}_{v_k}^{sim_{iter}}$ (with k=20 m s^{-1})

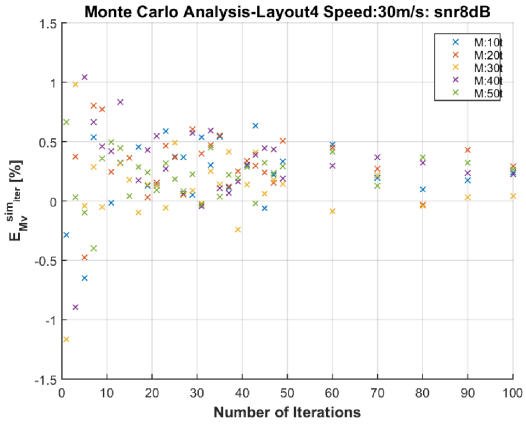

(d) Percentage $E_{M}{}_{v_k}^{sim_{iter}}$ (with k=30 m s^{-1})

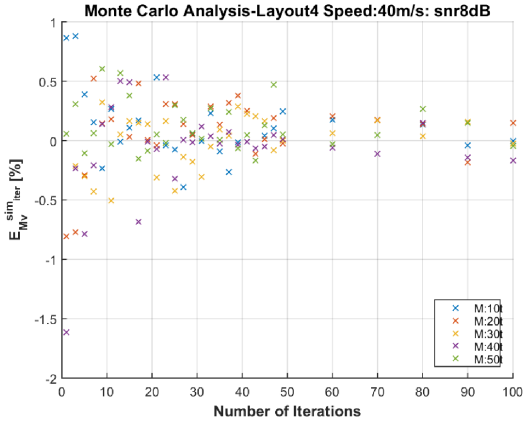

(e) Percentage $E_{M}{}_{v_k}^{sim_{iter}}$ (with k=40 m s^{-1})

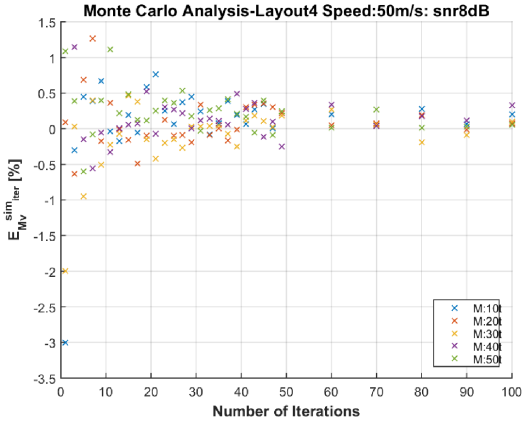

(f) Percentage $E_{M}{}_{v_k}^{sim_{iter}}$ (with k=50 m s^{-1})

Figure B.7: Layout4: Speed Estimation-Monte Carlo Analysis with k=(2-50) m s^{-1}

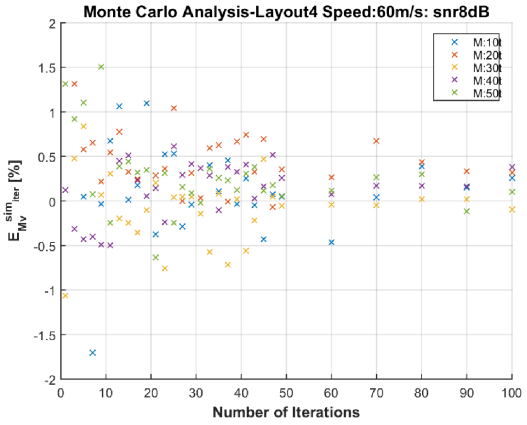

(a) Percentage $E_M{}_{v_k}^{sim_{iter}}$ (with k=60 m s^{-1})

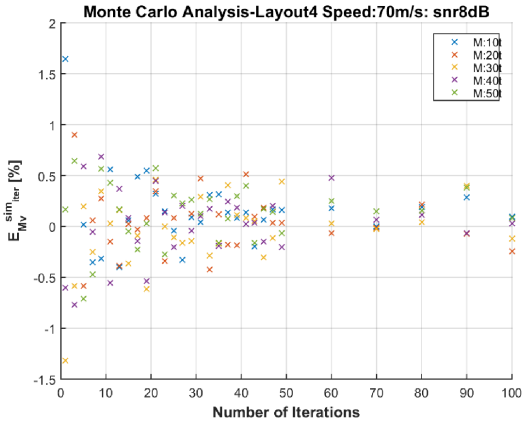

(b) Percentage $E_M{}_{v_k}^{sim_{iter}}$ (with k=70 m s^{-1})

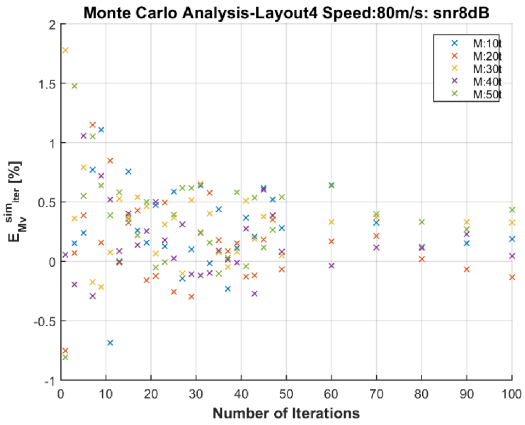

(c) Percentage $E_M{}_{v_k}^{sim_{iter}}$ (with k=80 m s^{-1})

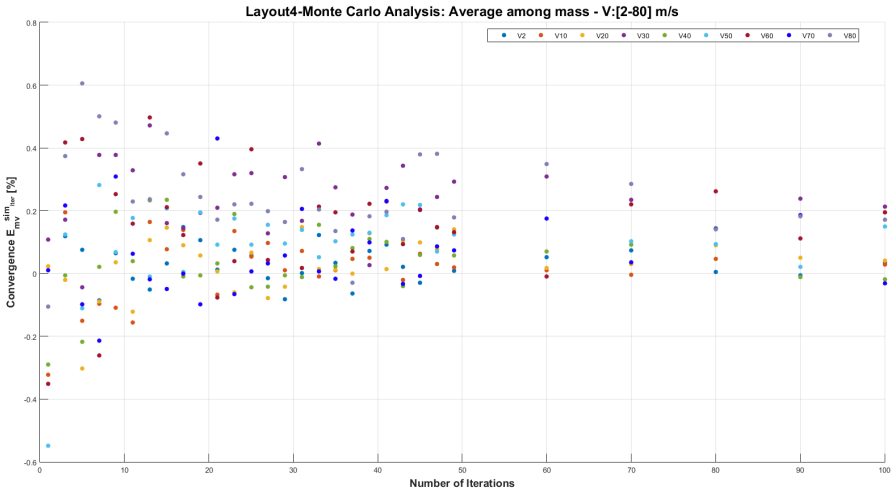

(d) Monte Carlo convergence of $\mathbf{Em}_{v_k}^{sim_{iter}}$ reached at about 30 iteration

Figure B.8: Layout4: Speed Estimation-Monte Carlo Analysis with k=(60-80) m s^{-1} and (d) Monte Carlo convergence

Layout5

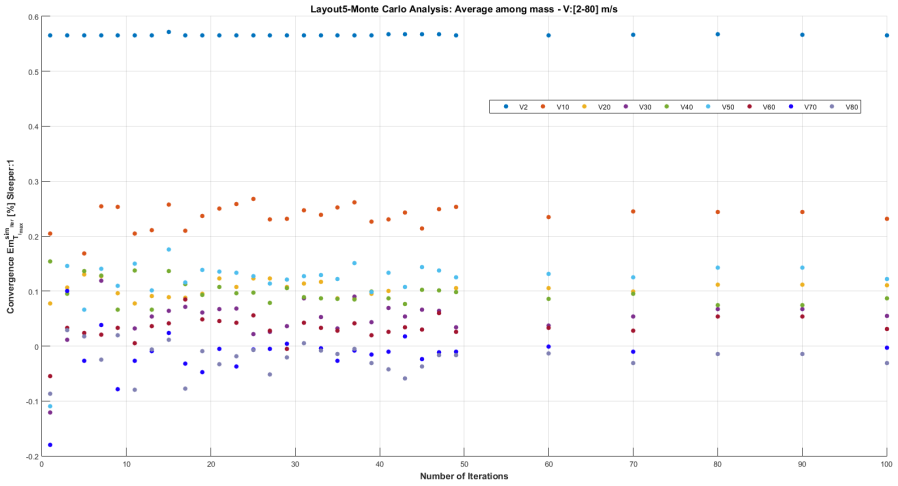

Figure B.9: Layout5: Monte Carlo analysis on the $Em_{T_{imax}}^{sim_{iter}}$: results show as after 49 iterations the convergence is reached

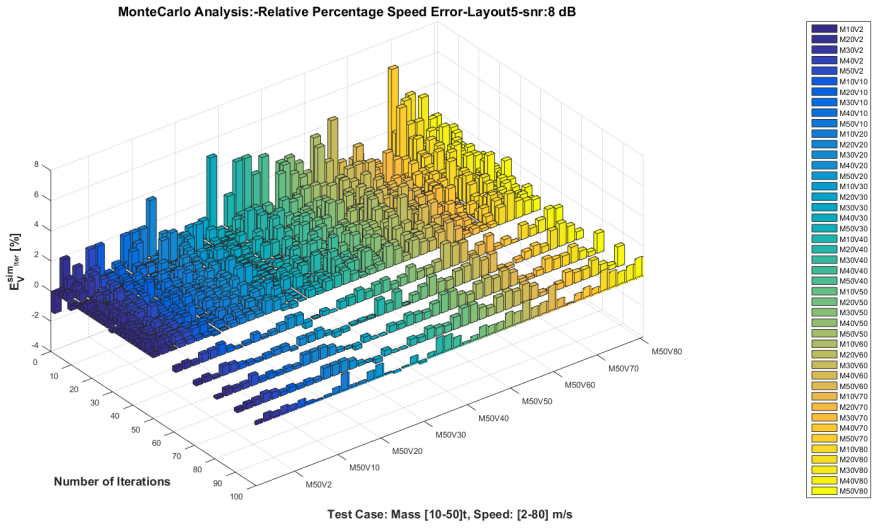

Figure B.10: Layout5: Percentage $E_V^{sim_{iter}}$ trend in all speed and mass range: results highlight how, for each speed, the value of mass vehicle not involves a relevant effect on the errors

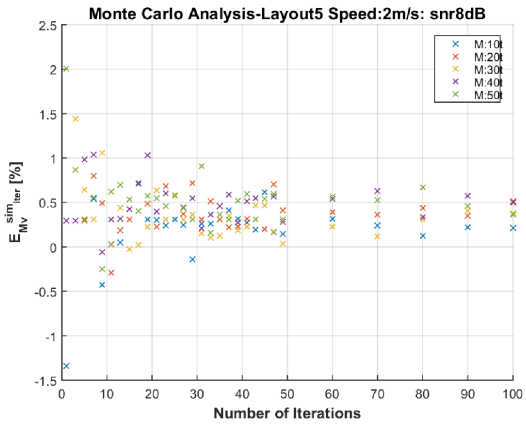

(a) Percentage $E_M{}_{v_k}^{sim_{iter}}$ (with k=2 m s^{-1})

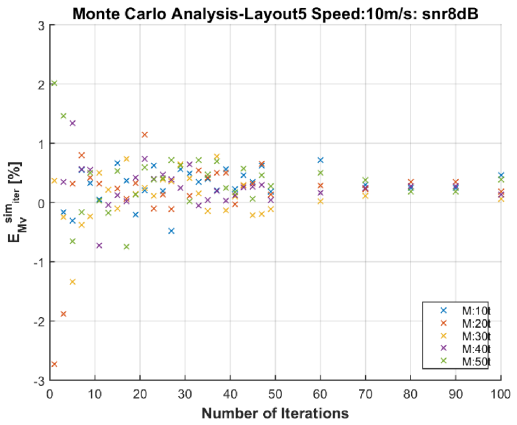

(b) Percentage $E_M{}_{v_k}^{sim_{iter}}$ (with k=10 m s^{-1})

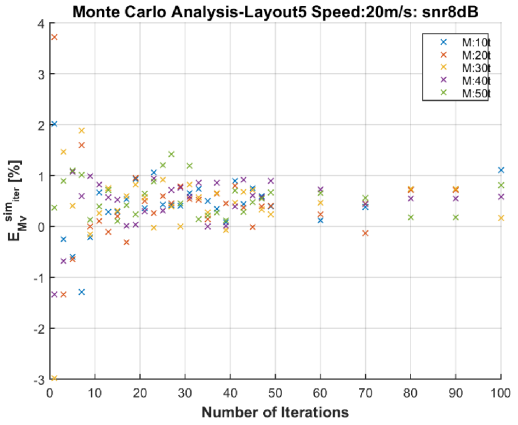

(c) Percentage $E_M{}_{v_k}^{sim_{iter}}$ (with k=20 m s^{-1})

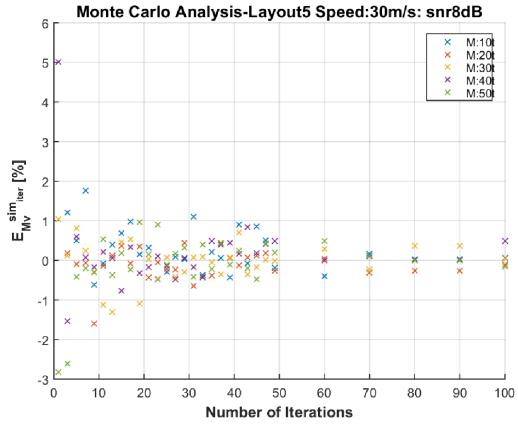

(d) Percentage $E_M{}_{v_k}^{sim_{iter}}$ (with k=30 m s^{-1})

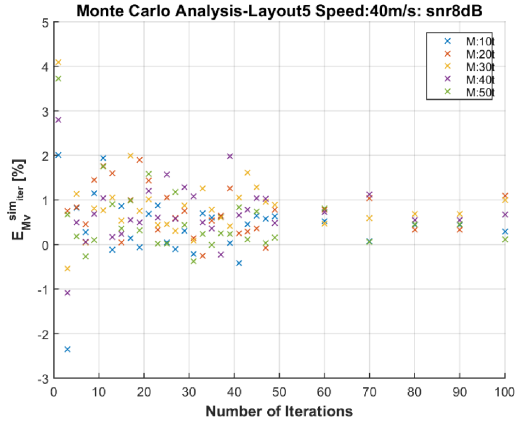

(e) Percentage $E_M{}_{v_k}^{sim_{iter}}$ (with k=40 m s^{-1})

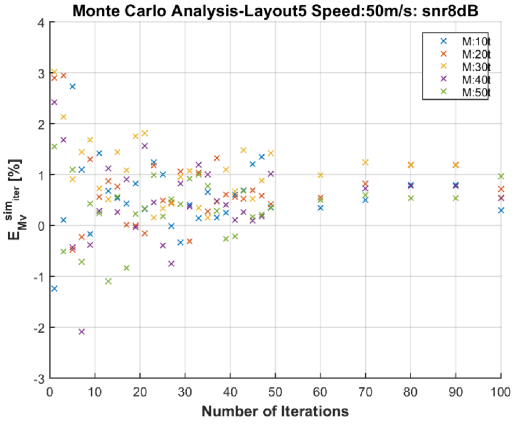

(f) Percentage $E_M{}_{v_k}^{sim_{iter}}$ (with k=50 m s^{-1})

Figure B.11: Layout5: Speed Estimation-Monte Carlo Analysis with k=(2-50) m s^{-1}

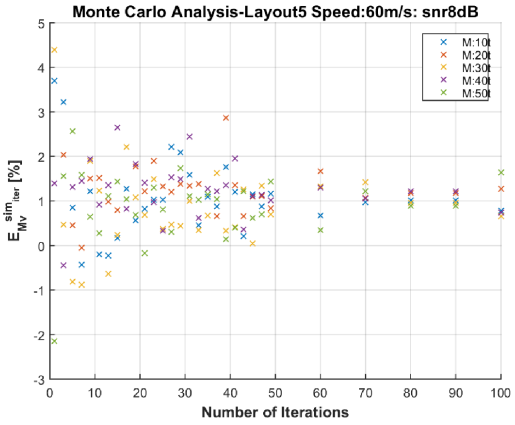

(a) Percentage $E_M{}_{v_k}^{sim_{iter}}$ (with k=60 m s^{-1})

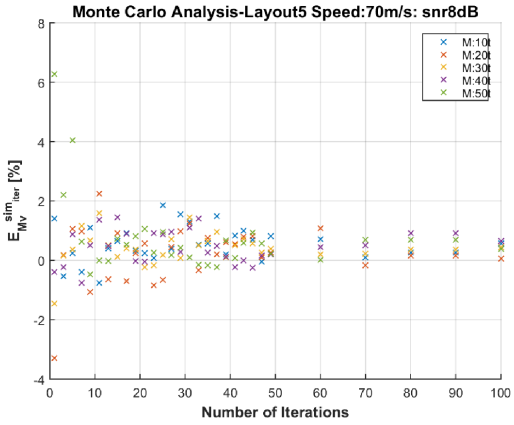

(b) Percentage $E_M{}_{v_k}^{sim_{iter}}$ (with k=70 m s^{-1})

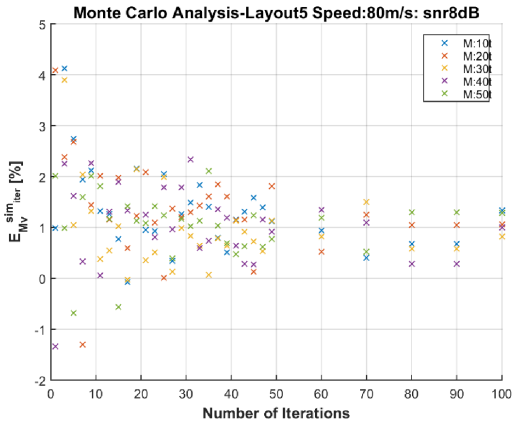

(c) Percentage $E_M{}_{v_k}^{sim_{iter}}$ (with k=80 m s^{-1})

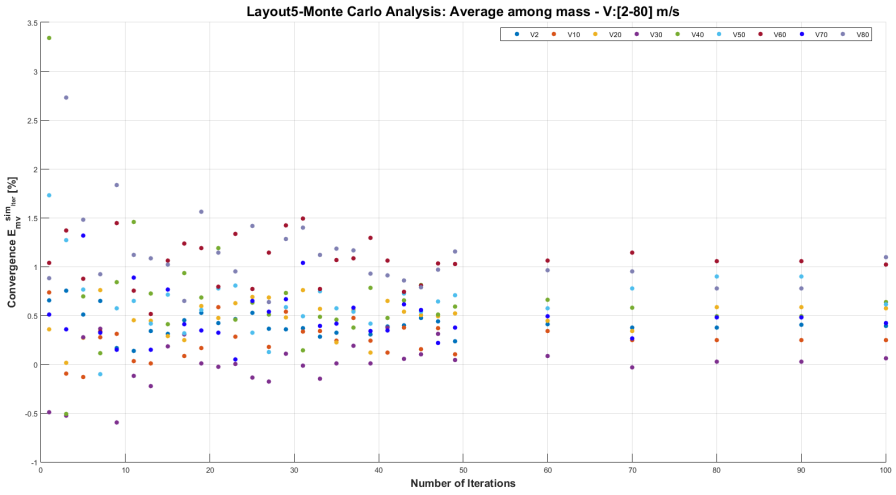

(d) Monte Carlo convergence of $\mathbf{Em}_{v_k}^{sim_{iter}}$ reached at about 30 iteration

Figure B.12: Layout5: Speed Estimation-Monte Carlo Analysis with k=(60-80) m s^{-1} and (d) Monte Carlo convergence

Layout6

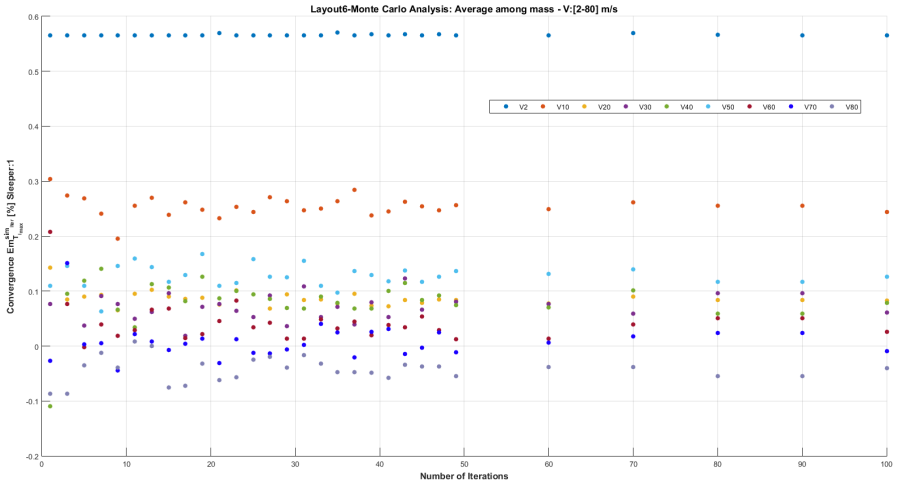

Figure B.13: Layout6: Monte Carlo analysis on the $Em_{T_{imax}}^{sim_{iter}}$: results show as after 49 iterations the convergence is reached

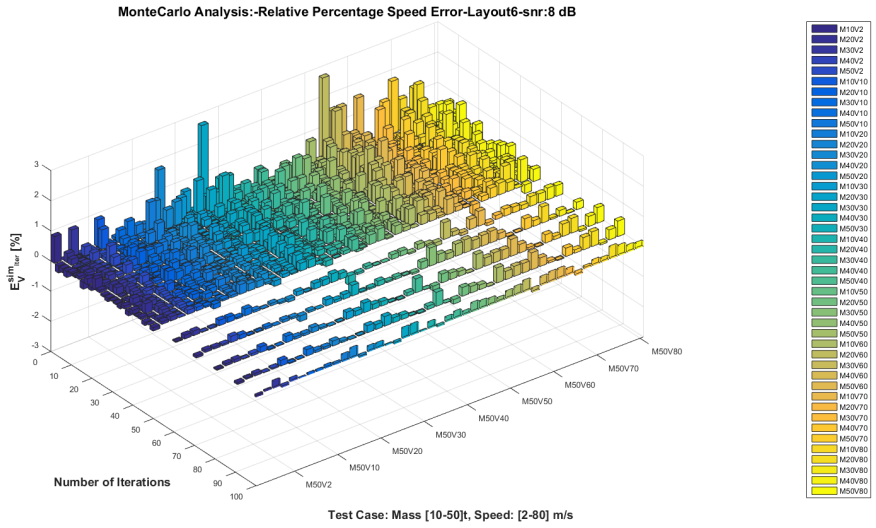

Figure B.14: Layout6: Percentage $E_V^{sim_{iter}}$ trend in all speed and mass range: results highlight how, for each speed, the value of mass vehicle not involves a relevant effect on the errors

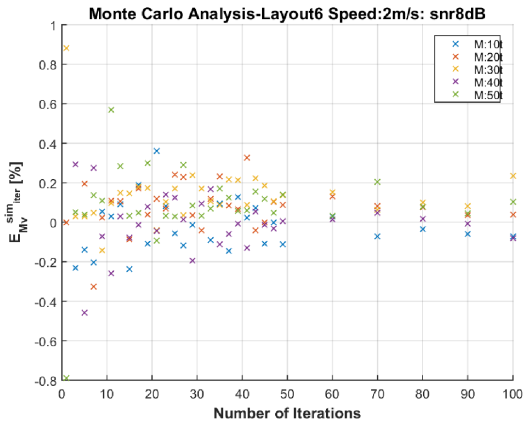

(a) Percentage $E_M{}_{v_k}^{sim_{iter}}$ (with k=2 m s^{-1})

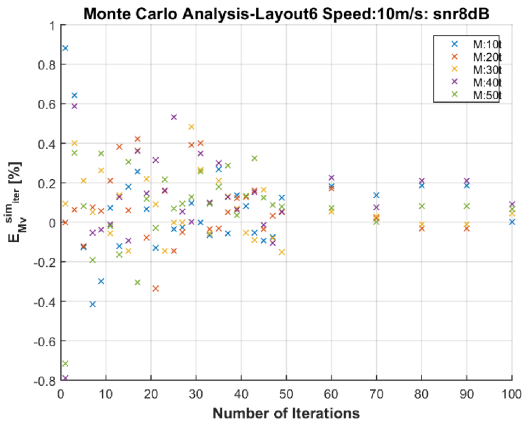

(b) Percentage $E_M{}_{v_k}^{sim_{iter}}$ (with k=10 m s^{-1})

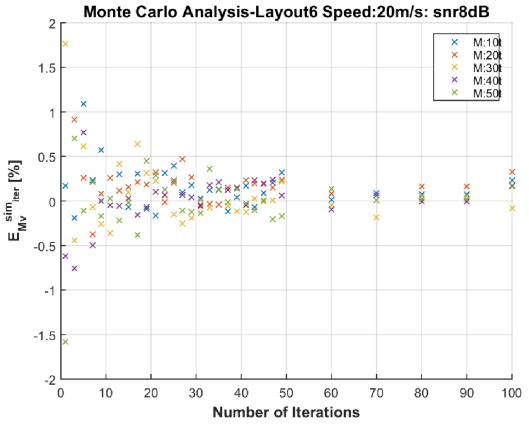

(c) Percentage $E_M{}_{v_k}^{sim_{iter}}$ (with k=20 m s^{-1})

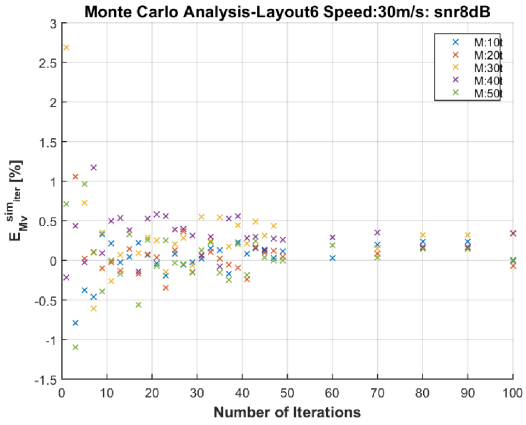

(d) Percentage $E_M{}_{v_k}^{sim_{iter}}$ (with k=30 m s^{-1})

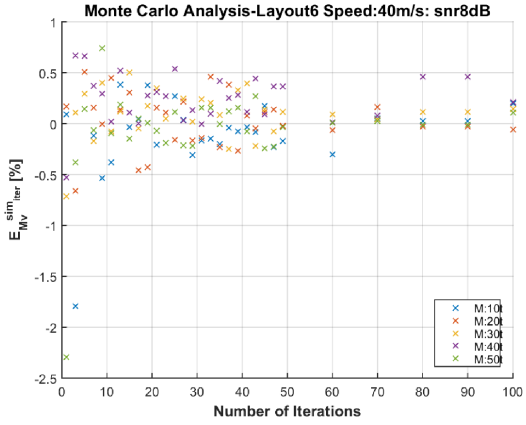

(e) Percentage $E_M{}_{v_k}^{sim_{iter}}$ (with k=40 m s^{-1})

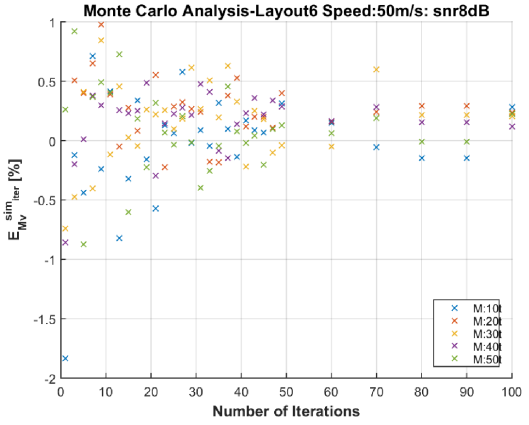

(f) Percentage $E_M{}_{v_k}^{sim_{iter}}$ (with k=50 m s^{-1})

Figure B.15: Layout6: Speed Estimation-Monte Carlo Analysis with k=(2-50) m s^{-1}

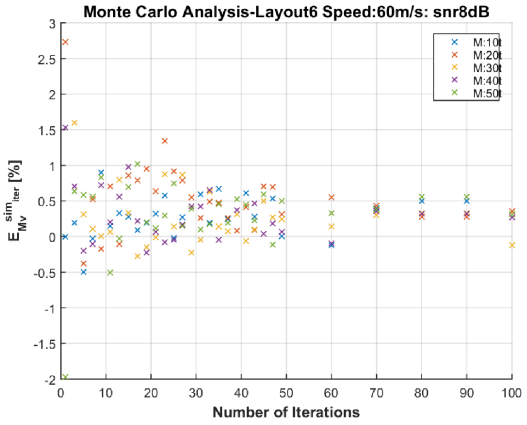

(a) Percentage $E_M{}_{v_k}^{sim_{iter}}$ (with k=60 m s^{-1})

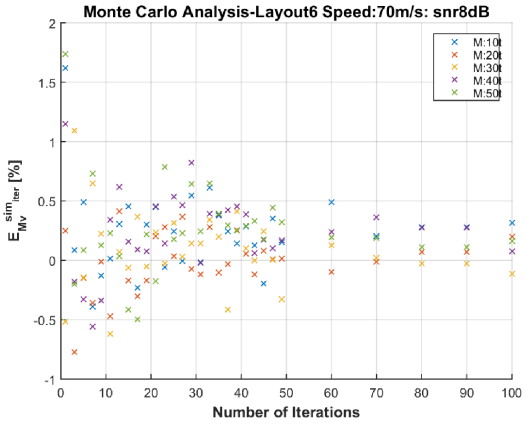

(b) Percentage $E_M{}_{v_k}^{sim_{iter}}$ (with k=70 m s^{-1})

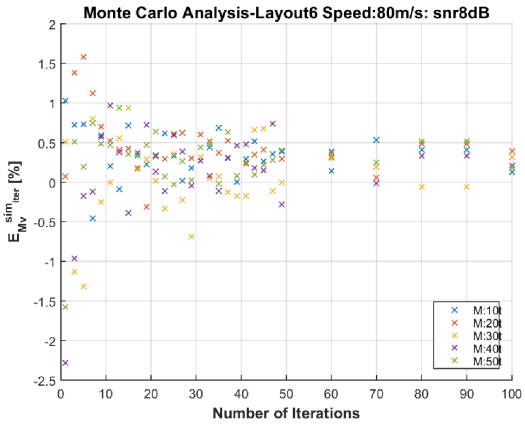

(c) Percentage $E_M{}_{v_k}^{sim_{iter}}$ (with k=80 m s^{-1})

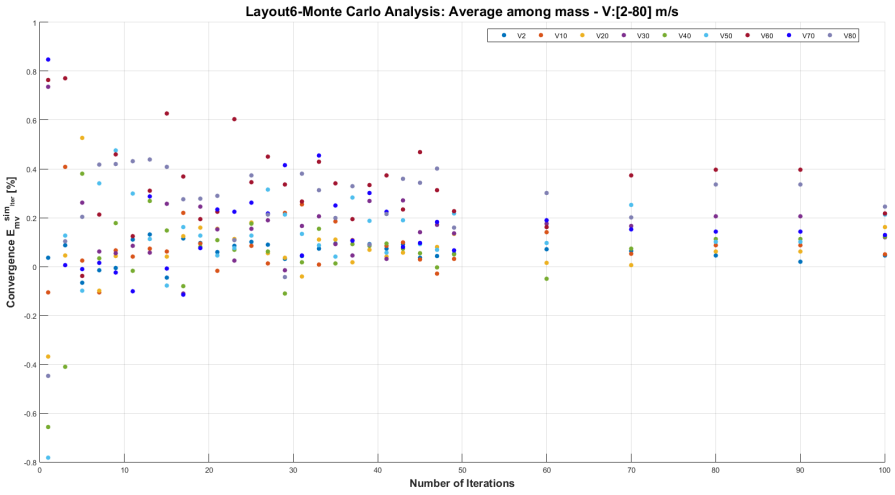

(d) Monte Carlo convergence of $\mathbf{Em}_{v_k}^{sim_{iter}}$ reached at about 30 iteration

Figure B.16: Layout6: Speed Estimation-Monte Carlo Analysis with k=(60-80) m s^{-1} and (d) Monte Carlo convergence

Layout7

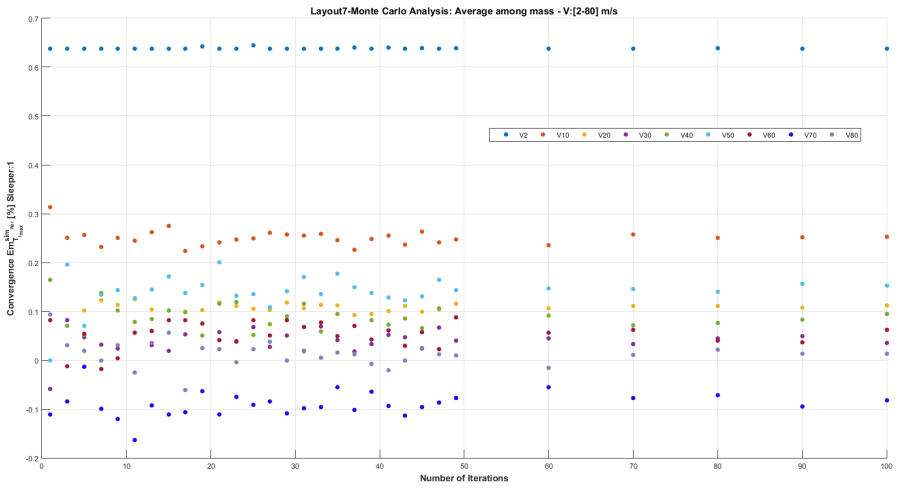

Figure B.17: Layout7: Monte Carlo analysis on the $Em_{T_{imax}}^{sim_{iter}}$: results show as after 49 iterations the convergence is reached

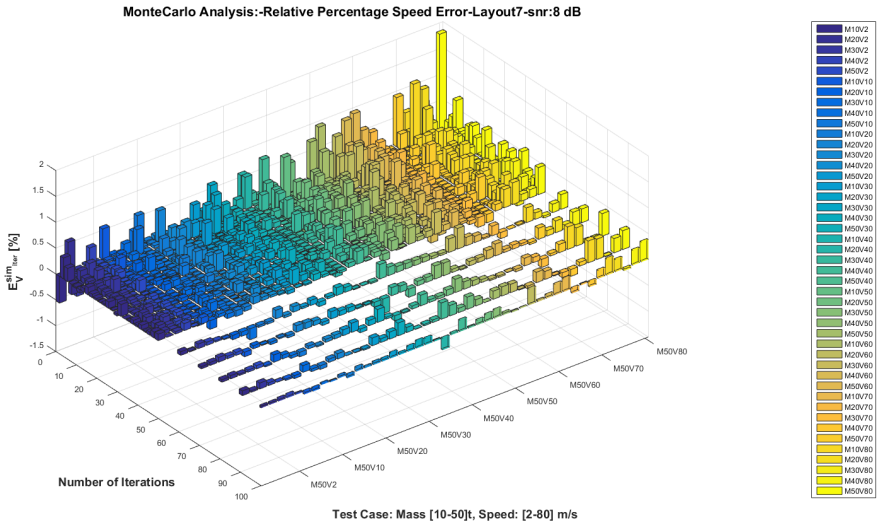

Figure B.18: Layout7: Percentage $E_V^{sim_{iter}}$ trend in all speed and mass range: results highlight how, for each speed, the value of mass vehicle not involves a relevant effect on the errors

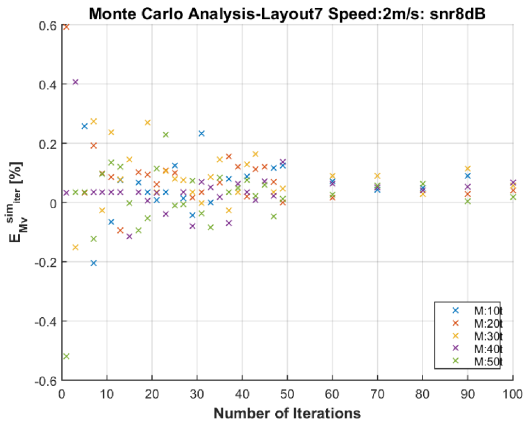

(a) Percentage $E_M{}_{v_k}^{sim_{iter}}$ (with k=2 m s^{-1})

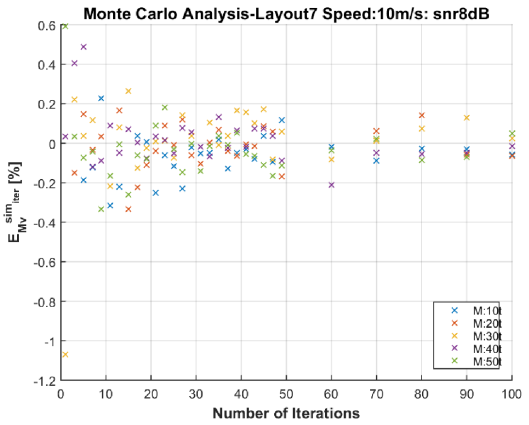

(b) Percentage $E_M{}_{v_k}^{sim_{iter}}$ (with k=10 m s^{-1})

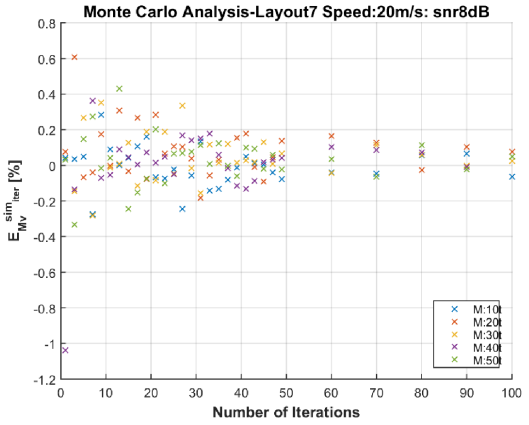

(c) Percentage $E_M{}_{v_k}^{sim_{iter}}$ (with k=20 m s^{-1})

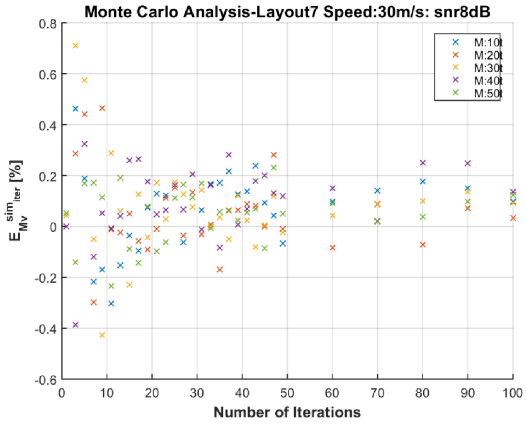

(d) Percentage $E_M{}_{v_k}^{sim_{iter}}$ (with k=30 m s^{-1})

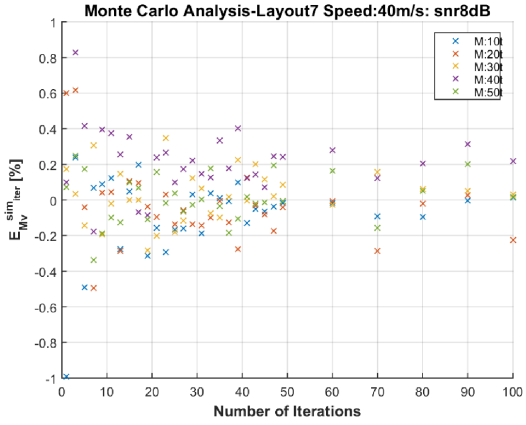

(e) Percentage $E_M{}_{v_k}^{sim_{iter}}$ (with k=40 m s^{-1})

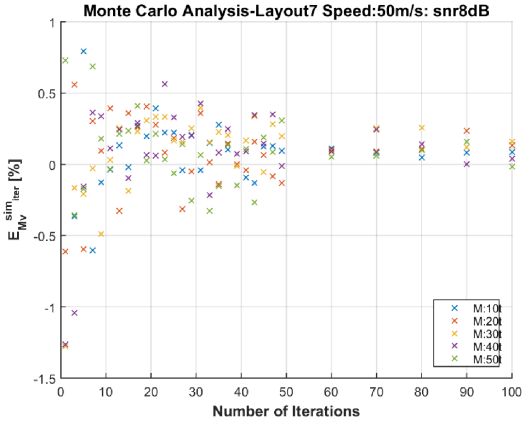

(f) Percentage $E_M{}_{v_k}^{sim_{iter}}$ (with k=50 m s^{-1})

Figure B.19: Layout7: Speed Estimation-Monte Carlo Analysis with k=(2-50) m s^{-1}

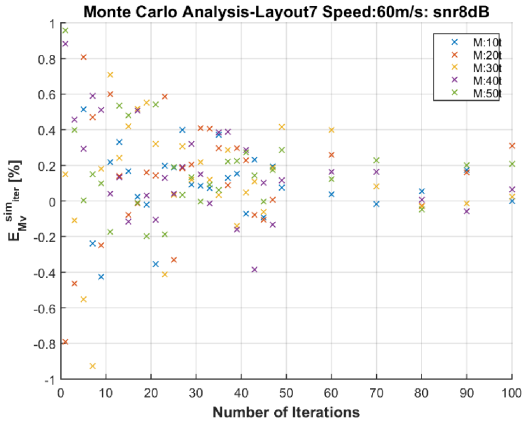

(a) Percentage $E_M{}_{v_k}^{sim_{iter}}$ (with k=60 m s^{-1})

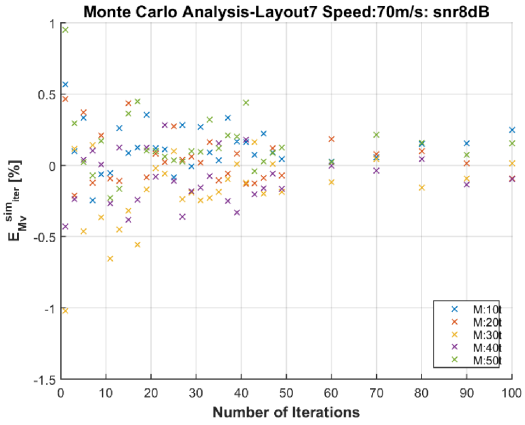

(b) Percentage $E_M{}_{v_k}^{sim_{iter}}$ (with k=70 m s^{-1})

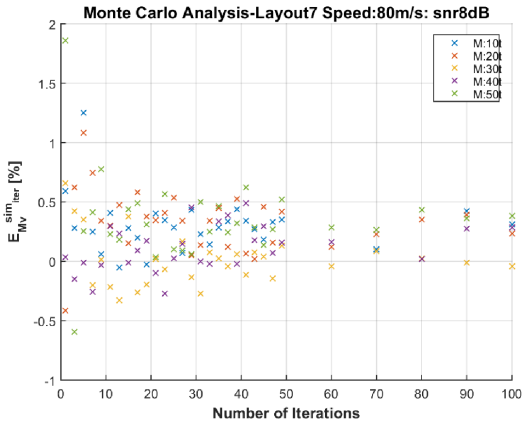

(c) Percentage $E_M{}_{v_k}^{sim_{iter}}$ (with k=80 m s^{-1})

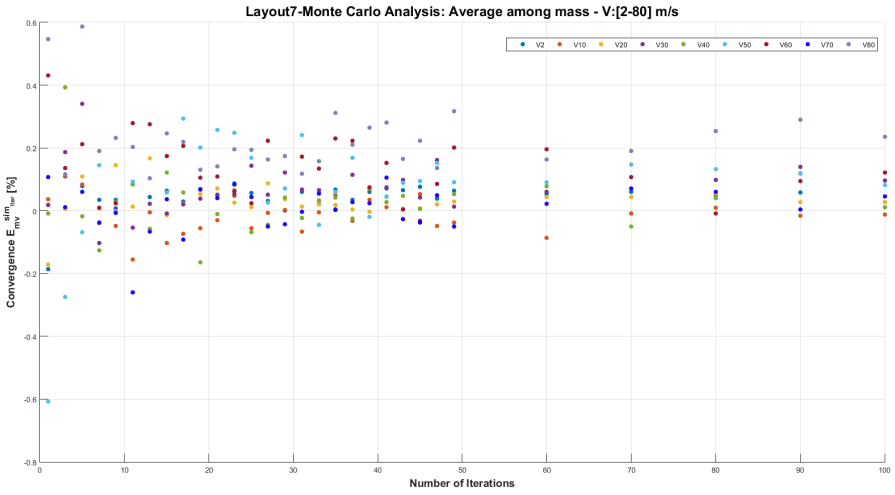

(d) Monte Carlo convergence of $\mathbf{Em}_{v_k}^{sim_{iter}}$ reached at about 30 iteration

Figure B.20: Layout7: Speed Estimation-Monte Carlo Analysis with k=(60-80) m s^{-1} and (d) Monte Carlo convergence

Layout8

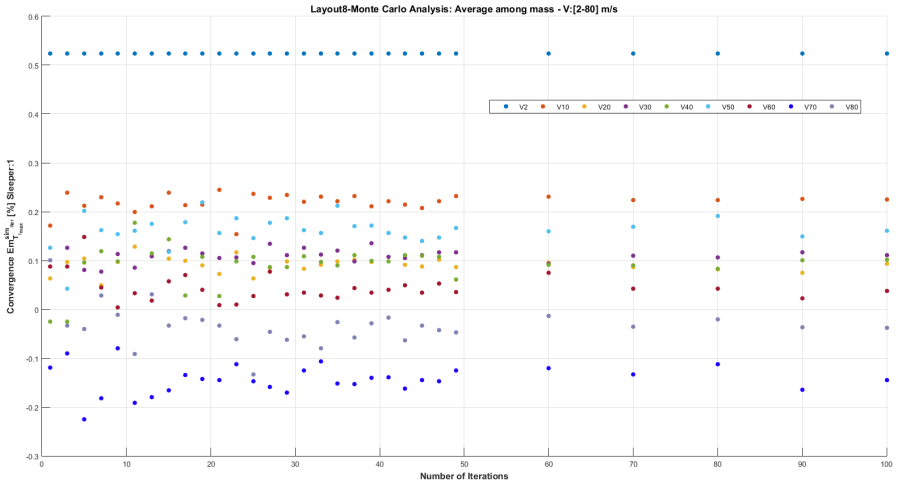

Figure B.21: Layout8: Monte Carlo analysis on the $Em_{T_{imax}}^{sim_{iter}}$: results show as after 30 iterations the convergence is reached

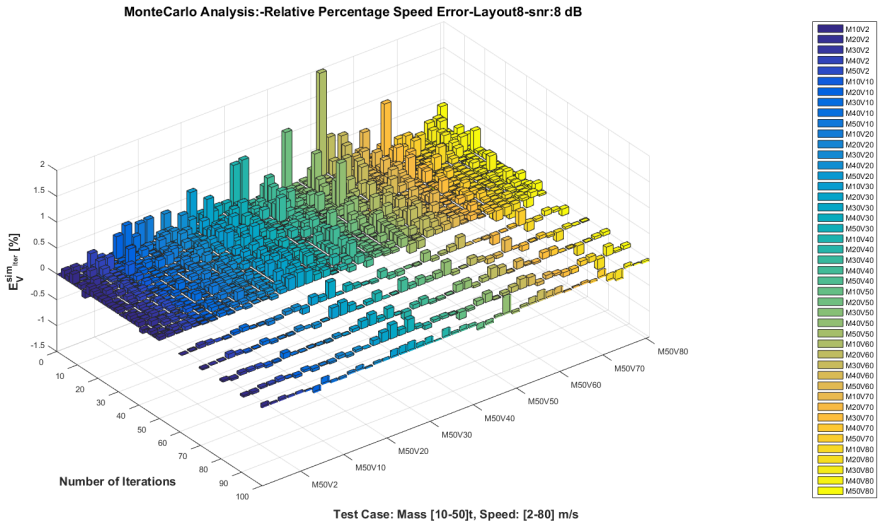

Figure B.22: Layout8: Percentage $E_V^{sim_{iter}}$ trend in all speed and mass range: results highlight how, for each speed, the value of mass vehicle not involves a relevant effect on the errors

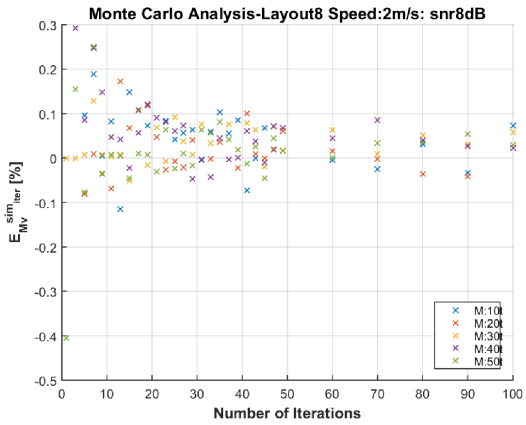

(a) Percentage $E_M{}_{v_k}^{sim_{iter}}$ (with k=2 m s^{-1})

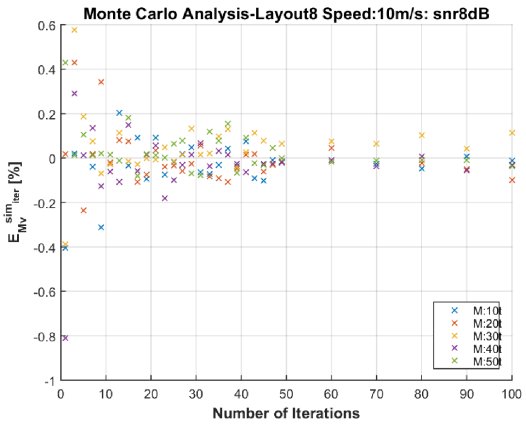

(b) Percentage $E_M{}_{v_k}^{sim_{iter}}$ (with k=10 m s^{-1})

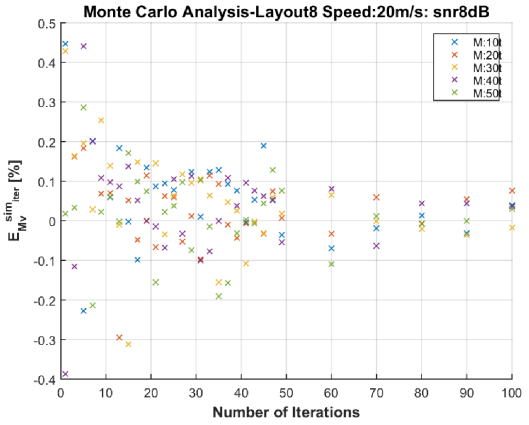

(c) Percentage $E_M{}_{v_k}^{sim_{iter}}$ (with k=20 m s^{-1})

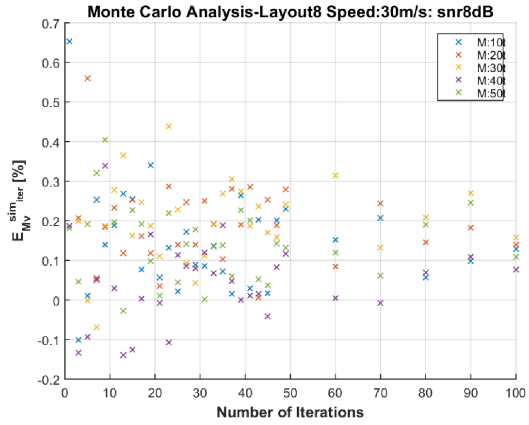

(d) Percentage $E_M{}_{v_k}^{sim_{iter}}$ (with k=30 m s^{-1})

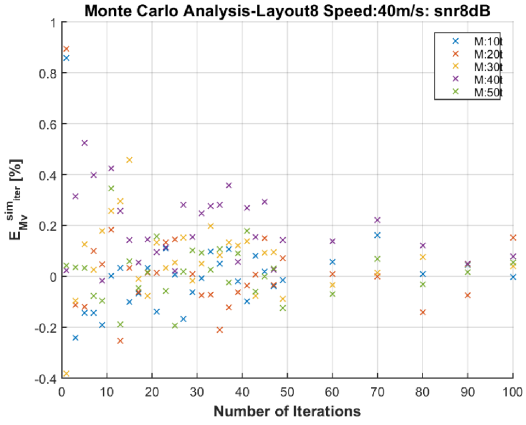

(e) Percentage $E_M{}_{v_k}^{sim_{iter}}$ (with k=40 m s^{-1})

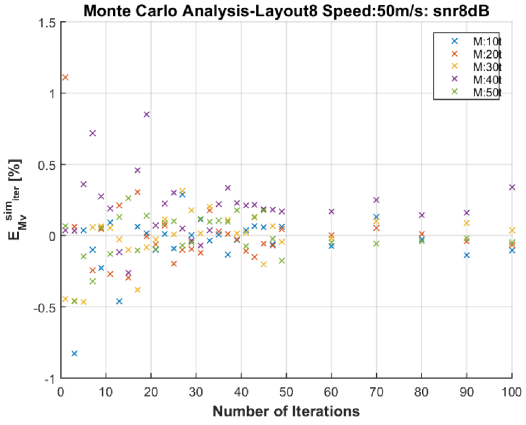

(f) Percentage $E_M{}_{v_k}^{sim_{iter}}$ (with k=50 m s^{-1})

Figure B.23: Layout8: Speed Estimation-Monte Carlo Analysis with k=(2-50) m s^{-1}

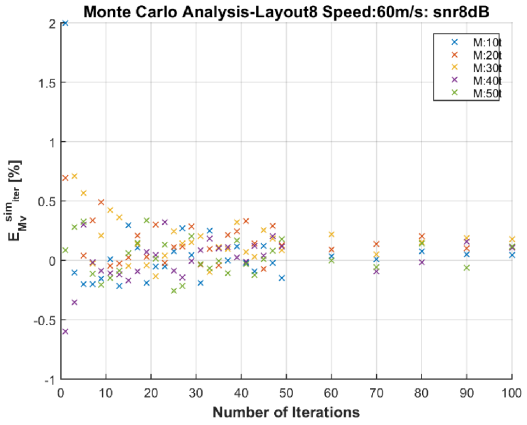

(a) Percentage $E_M{}_{v_k}^{sim_{iter}}$ (with k=60 m s^{-1})

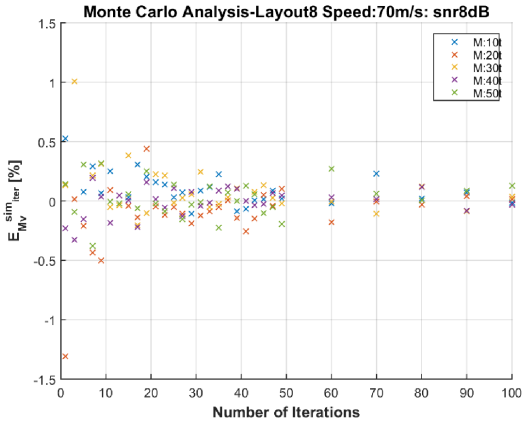

(b) Percentage $E_M{}_{v_k}^{sim_{iter}}$ (with k=70 m s^{-1})

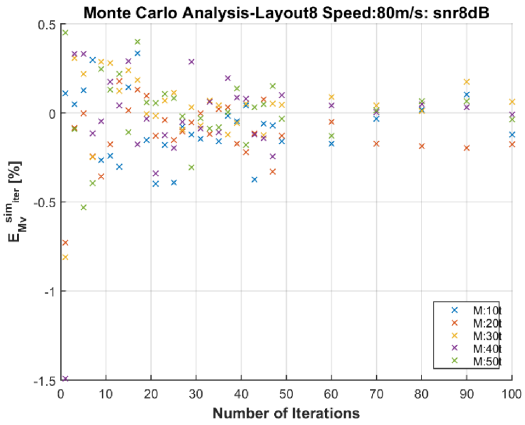

(c) Percentage $E_M{}_{v_k}^{sim_{iter}}$ (with k=80 m s^{-1})

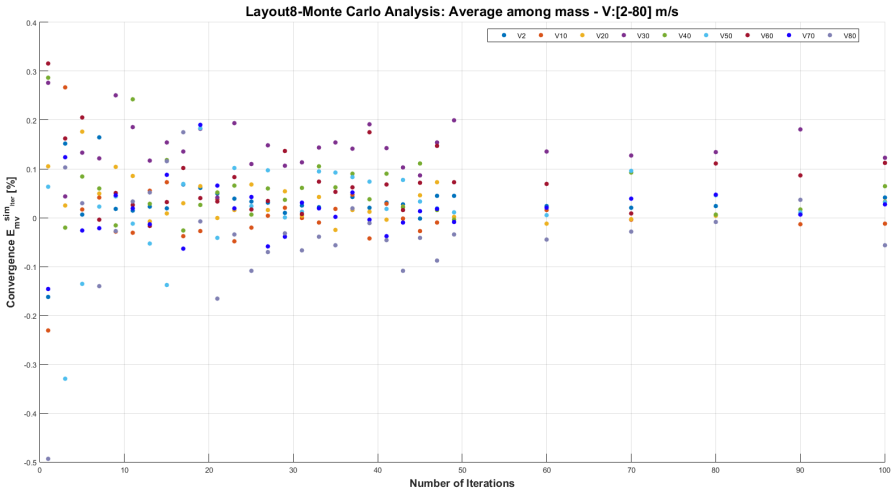

(d) Monte Carlo convergence of $\mathbf{Em}_{v_k}^{sim_{iter}}$ reached at about 49 iteration

Figure B.24: Layout8: Speed Estimation-Monte Carlo Analysis with k=(60-80) m s^{-1} and (d) Monte Carlo convergence

Layout9

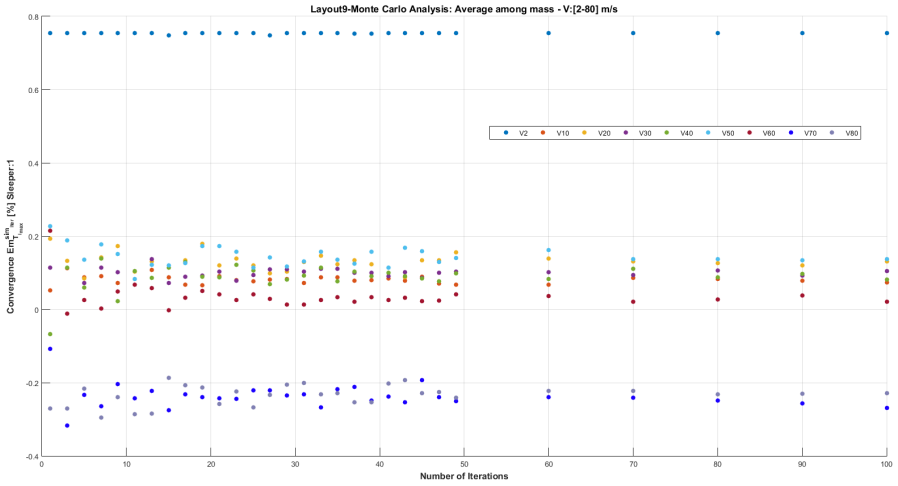

Figure B.25: Layout9: Monte Carlo analysis on the $Em_{T_{imax}}^{sim_{iter}}$: results show as after 49 iterations the convergence is reached

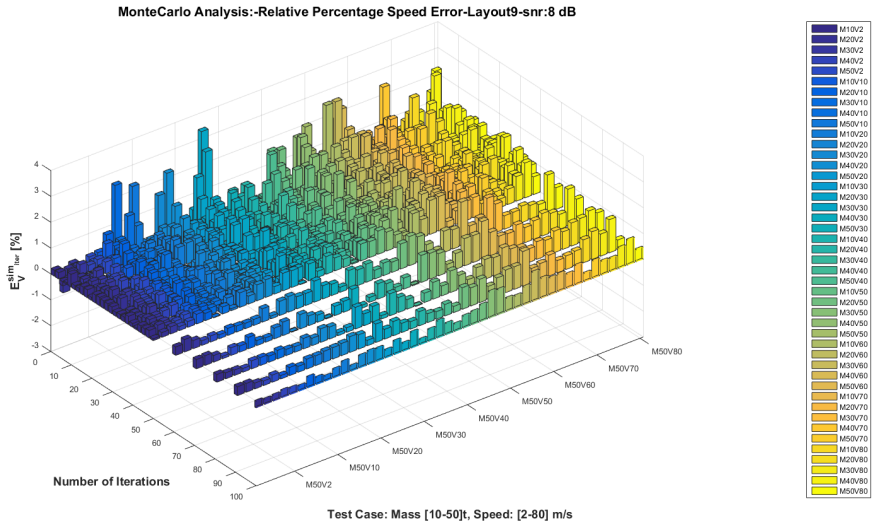

Figure B.26: Layout9: Percentage $E_V^{sim_{iter}}$ trend in all speed and mass range: results highlight how, for each speed, the value of mass vehicle not involves a relevant effect on the errors

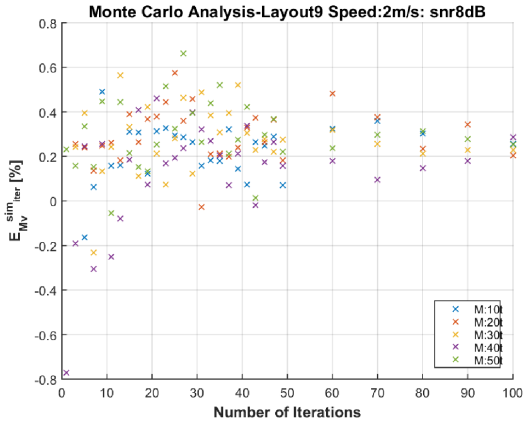

(a) Percentage $E_{M_{v_k}}^{sim_{iter}}$ (with k=2 m s^{-1})

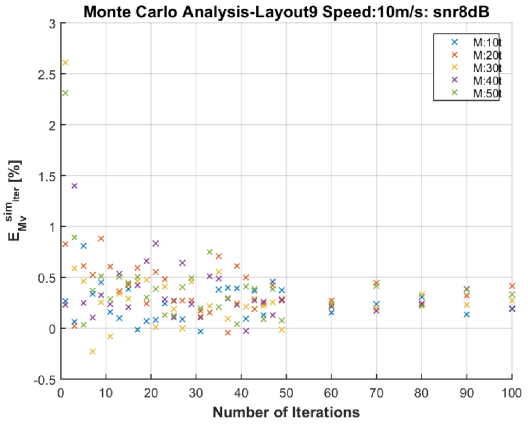

(b) Percentage $E_{M_{v_k}}^{sim_{iter}}$ (with k=10 m s^{-1})

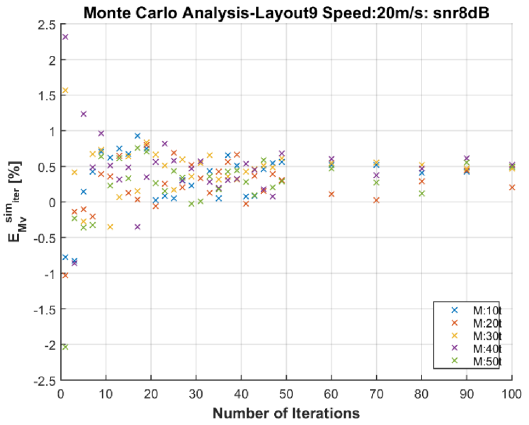

(c) Percentage $E_{M_{v_k}}^{sim_{iter}}$ (with k=20 m s^{-1})

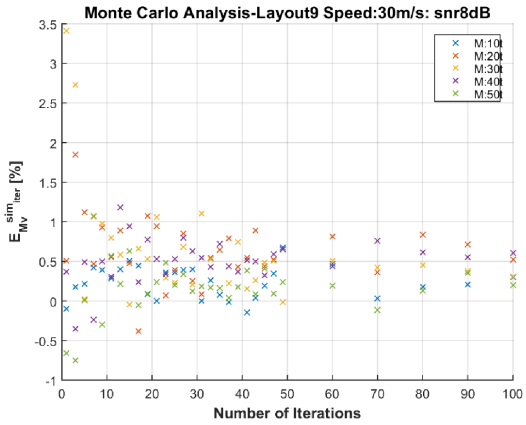

(d) Percentage $E_{M_{v_k}}^{sim_{iter}}$ (with k=30 m s^{-1})

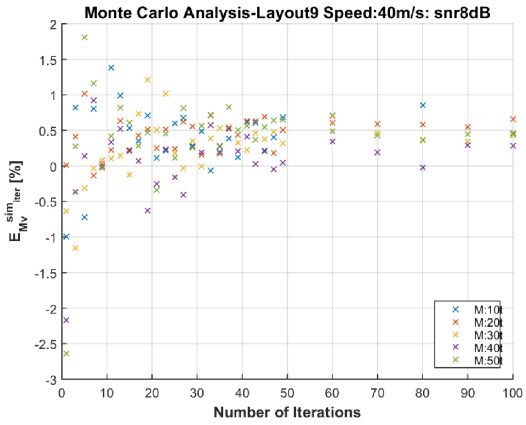

(e) Percentage $E_{M_{v_k}}^{sim_{iter}}$ (with k=40 m s^{-1})

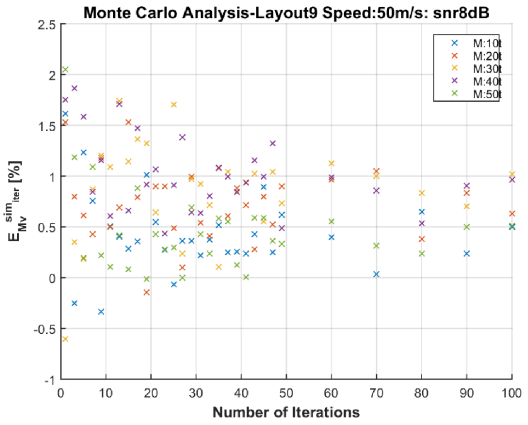

(f) Percentage $E_{M_{v_k}}^{sim_{iter}}$ (with k=50 m s^{-1})

Figure B.27: Layout9: Speed Estimation-Monte Carlo Analysis with k=(2-50) m s^{-1}

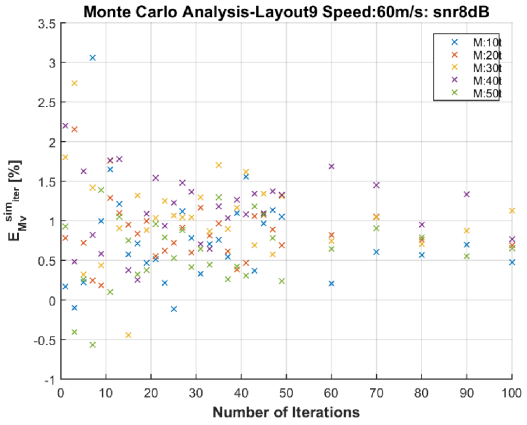

(a) Percentage $E_M{}_{v_k}^{sim_{iter}}$ (with k=60 m s^{-1})

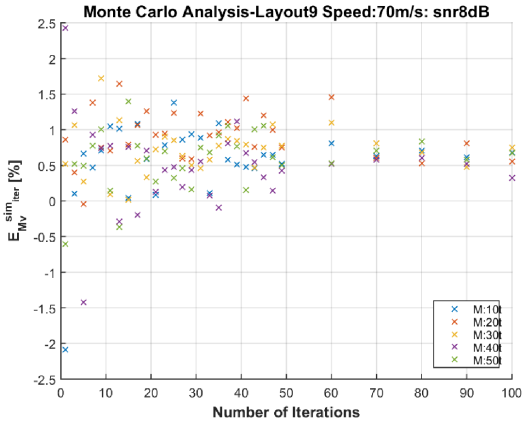

(b) Percentage $E_M{}_{v_k}^{sim_{iter}}$ (with k=70 m s^{-1})

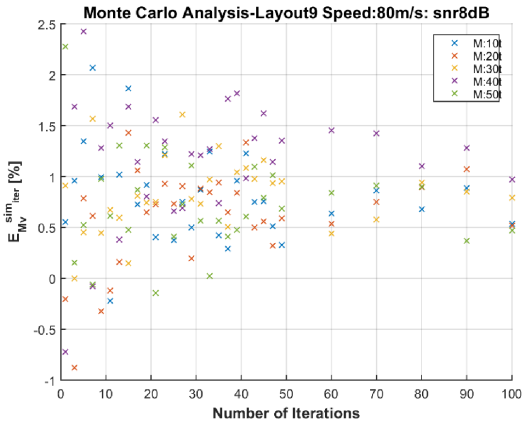

(c) Percentage $E_M{}_{v_k}^{sim_{iter}}$ (with k=80 m s^{-1})

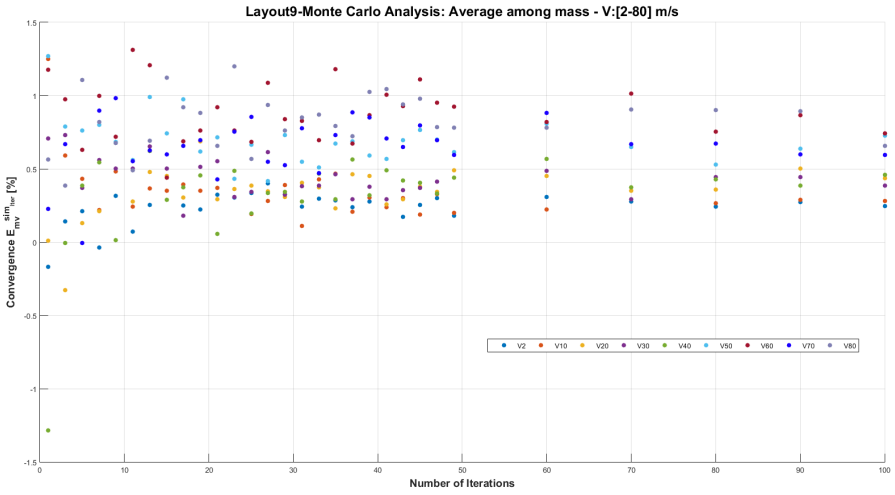

(d) Monte Carlo convergence of $\mathbf{Em}_{v_k}^{sim_{iter}}$ reached at about 30 iteration

Figure B.28: Layout9: Speed Estimation-Monte Carlo Analysis with k=(60-80) m s^{-1} and (d) Monte Carlo convergence

Layout10

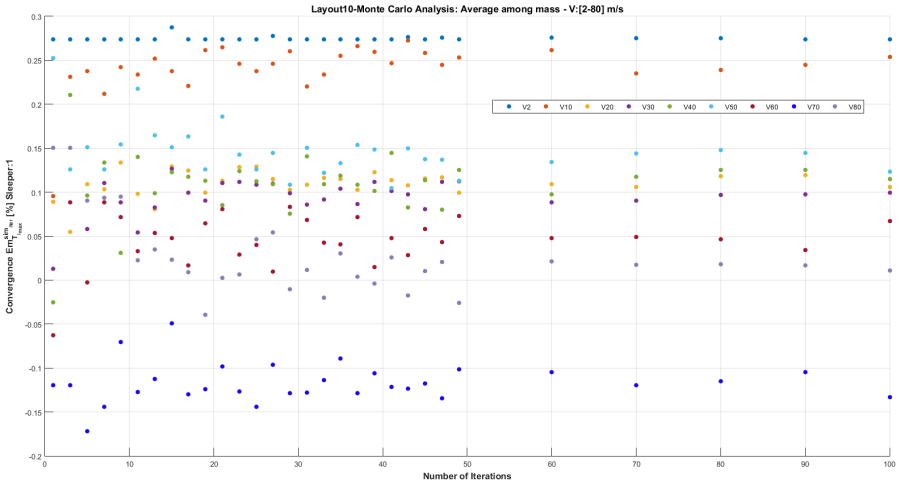

Figure B.29: Layout10: Monte Carlo analysis on the $Em_{T_{i_{max}}}^{sim_{iter}}$: results show as after 49 iterations the convergence is reached

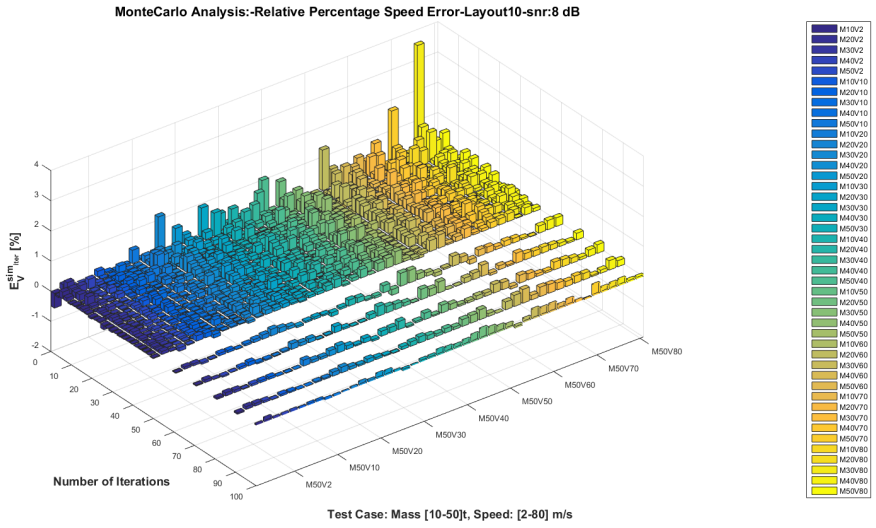

Figure B.30: Layout10: Percentage $E_V^{sim_{iter}}$ trend in all speed and mass range: results highlight how, for each speed, the value of mass vehicle not involves a relevant effect on the errors

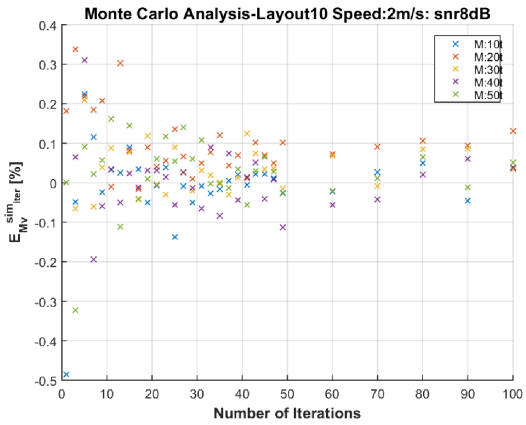

(a) Percentage $E_M{}_{v_k}^{sim_{iter}}$ (with k=2 m s^{-1})

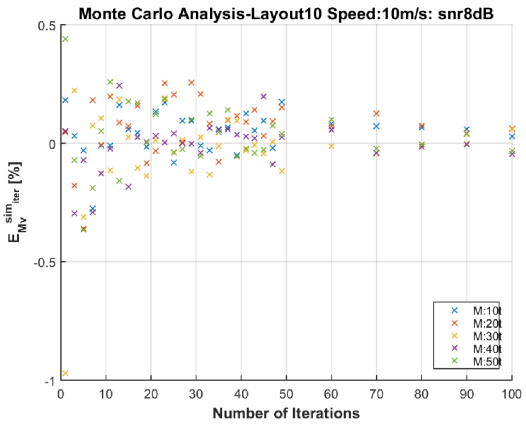

(b) Percentage $E_M{}_{v_k}^{sim_{iter}}$ (with k=10 m s^{-1})

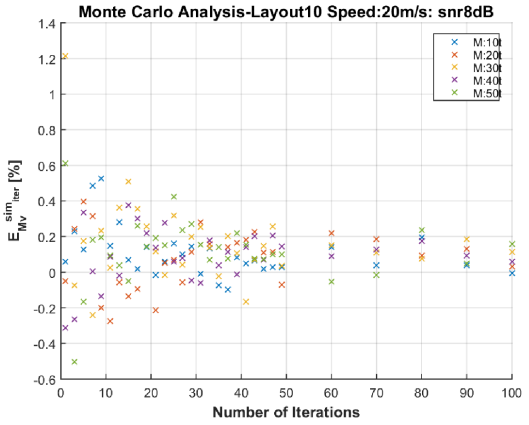

(c) Percentage $E_M{}_{v_k}^{sim_{iter}}$ (with k=20 m s^{-1})

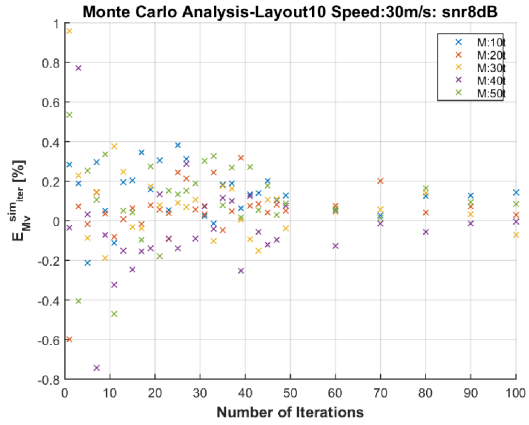

(d) Percentage $E_M{}_{v_k}^{sim_{iter}}$ (with k=30 m s^{-1})

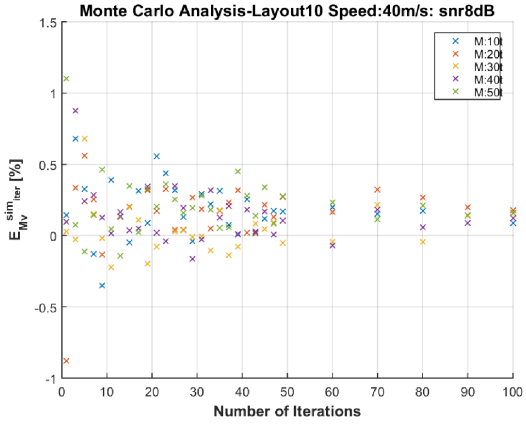

(e) Percentage $E_M{}_{v_k}^{sim_{iter}}$ (with k=40 m s^{-1})

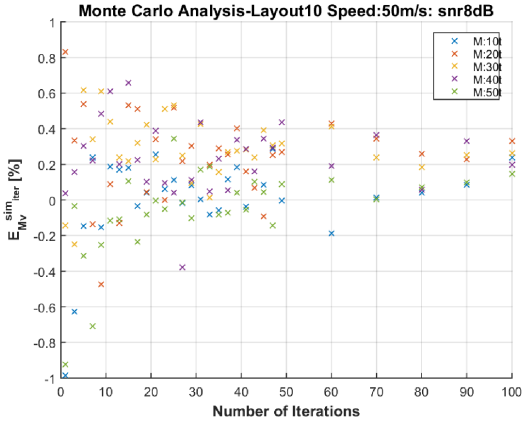

(f) Percentage $E_M{}_{v_k}^{sim_{iter}}$ (with k=50 m s^{-1})

Figure B.31: Layout10: Speed Estimation-Monte Carlo Analysis with k=(2-50) m s^{-1}

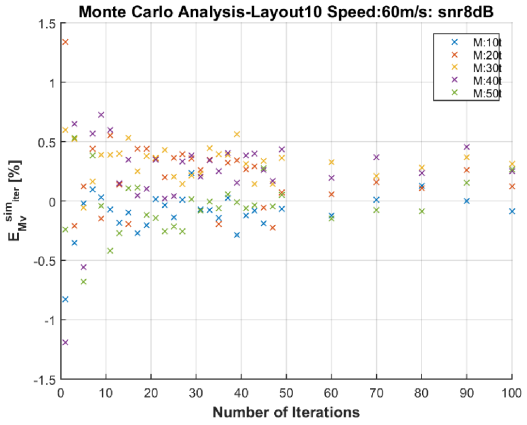

(a) Percentage $E_M{}_{v_k}^{sim_{iter}}$ (with k=60 m s^{-1})

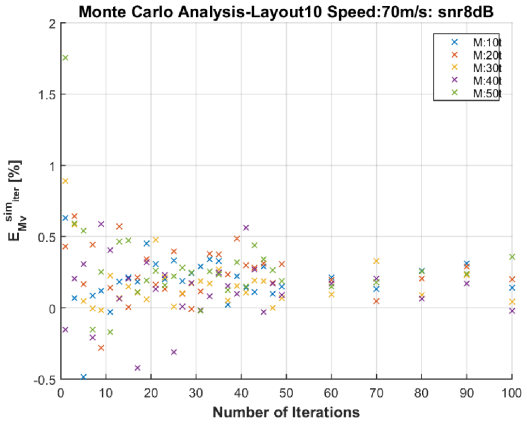

(b) Percentage $E_M{}_{v_k}^{sim_{iter}}$ (with k=70 m s^{-1})

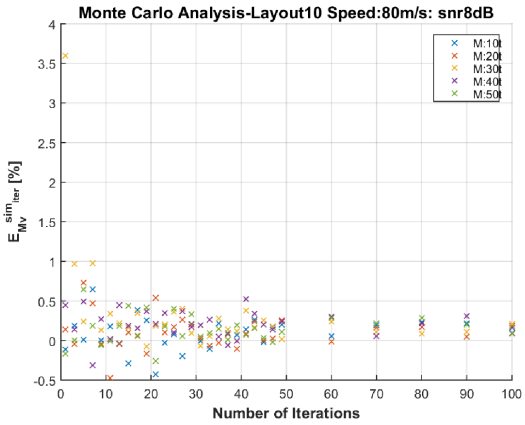

(c) Percentage $E_M{}_{v_k}^{sim_{iter}}$ (with k=80 m s^{-1})

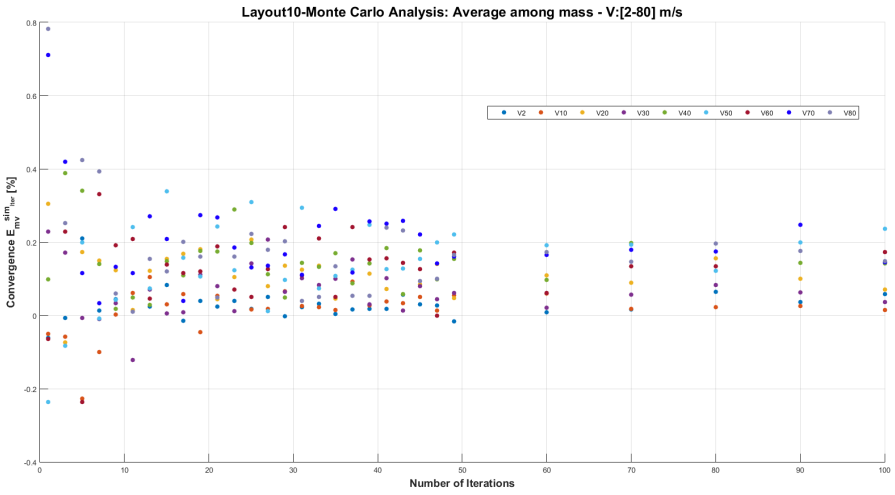

(d) Monte Carlo convergence of $\mathbf{Em}_{v_k}^{sim_{iter}}$ reached at about 30 iteration

Figure B.32: Layout10: Speed Estimation-Monte Carlo Analysis with k=(60-80) m s^{-1} and (d) Monte Carlo convergence

Layout11

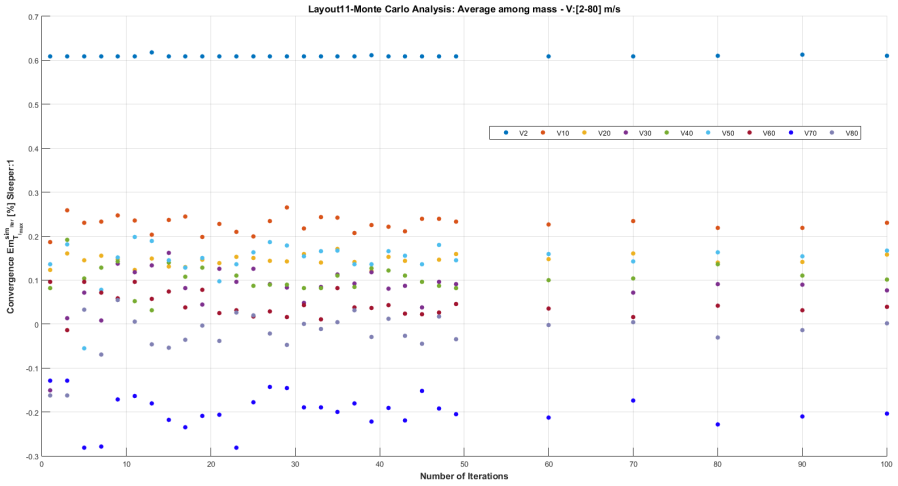

Figure B.33: Layout11: Monte Carlo analysis on the $Em_{T_{i_{max}}}^{sim_{iter}}$: results show as after 49 iterations the convergence is reached

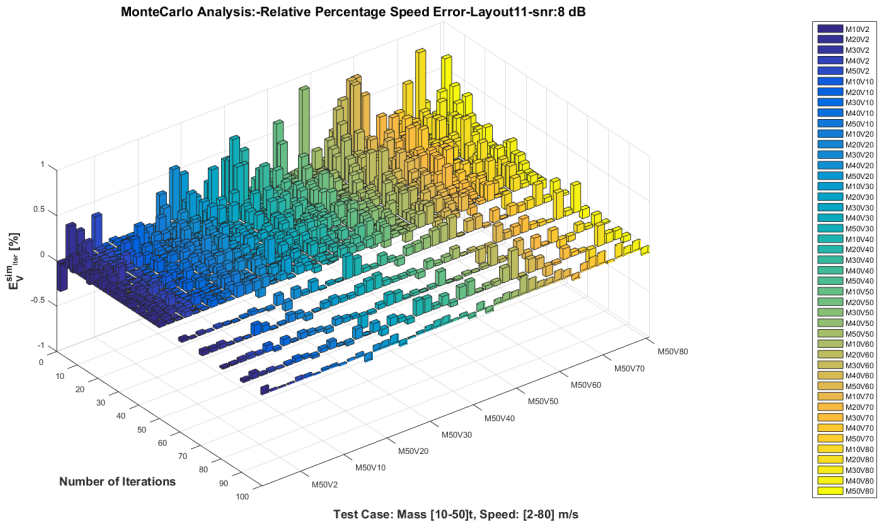

Figure B.34: Layout11: Percentage $E_V^{sim_{iter}}$ trend in all speed and mass range: results highlight how, for each speed, the value of mass vehicle not involves a relevant effect on the errors

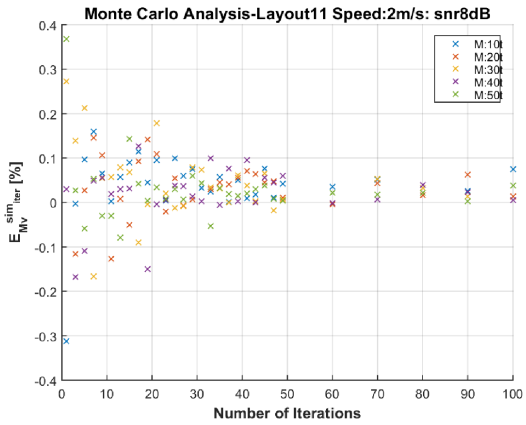

(a) Percentage $E_M{}_{v_k}^{sim_{iter}}$ (with k=2 m s^{-1})

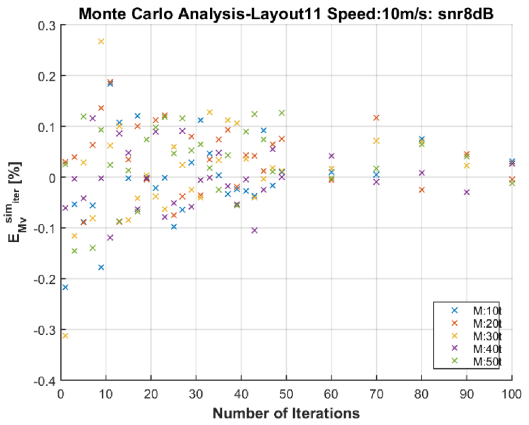

(b) Percentage $E_M{}_{v_k}^{sim_{iter}}$ (with k=10 m s^{-1})

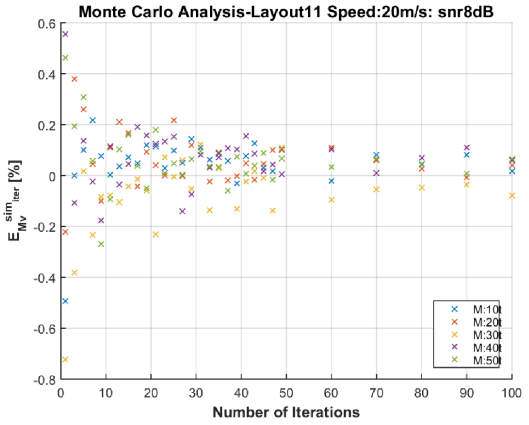

(c) Percentage $E_M{}_{v_k}^{sim_{iter}}$ (with k=20 m s^{-1})

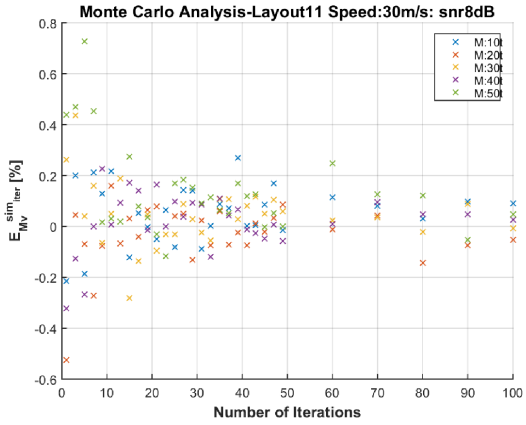

(d) Percentage $E_M{}_{v_k}^{sim_{iter}}$ (with k=30 m s^{-1})

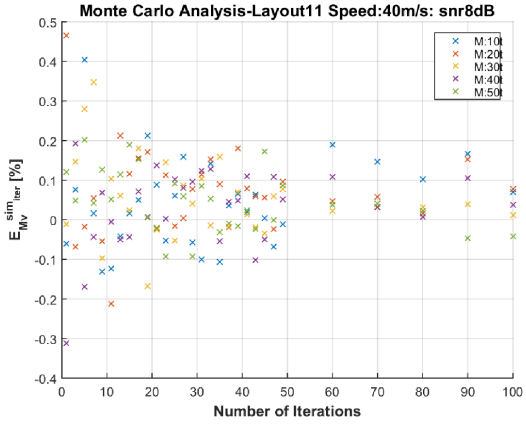

(e) Percentage $E_M{}_{v_k}^{sim_{iter}}$ (with k=40 m s^{-1})

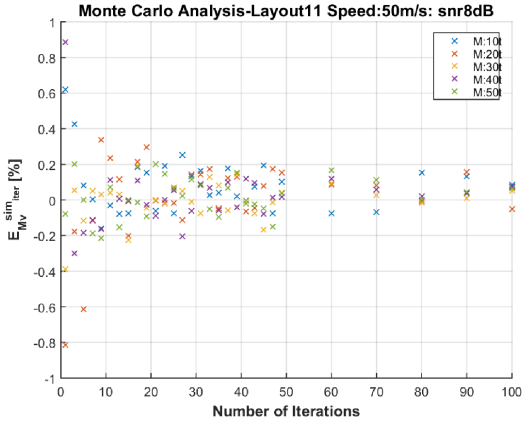

(f) Percentage $E_M{}_{v_k}^{sim_{iter}}$ (with k=50 m s^{-1})

Figure B.35: Layout11: Speed Estimation-Monte Carlo Analysis with k=(2-50) m s^{-1}

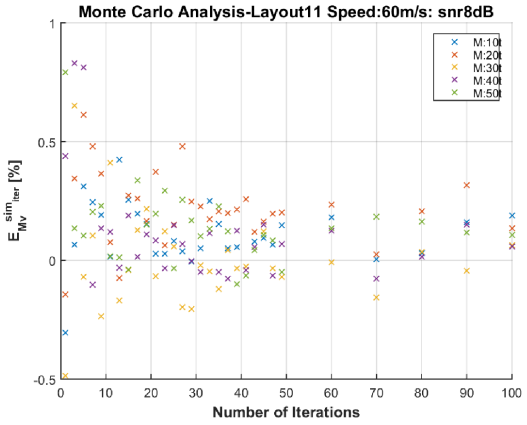

(a) Percentage $E_M{}_{v_k}^{sim_{iter}}$ (with k=60 m s^{-1})

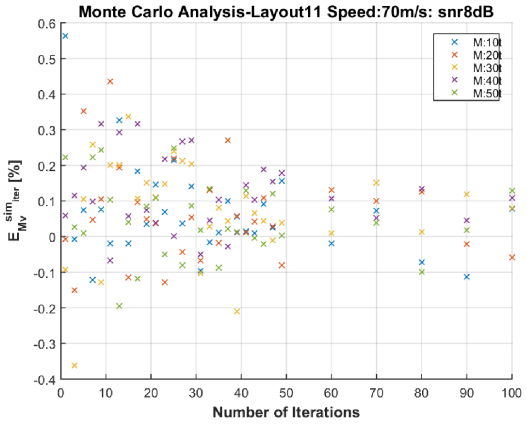

(b) Percentage $E_M{}_{v_k}^{sim_{iter}}$ (with k=70 m s^{-1})

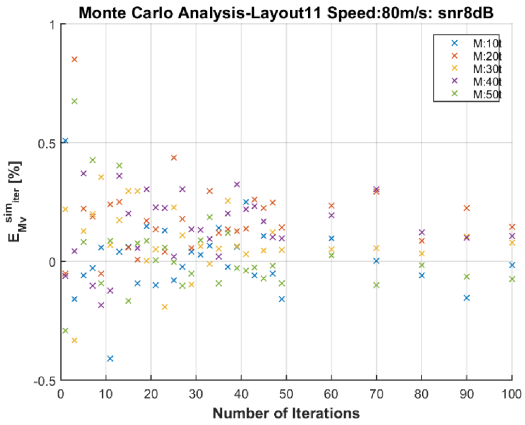

(c) Percentage $E_M{}_{v_k}^{sim_{iter}}$ (with k=80 m s^{-1})

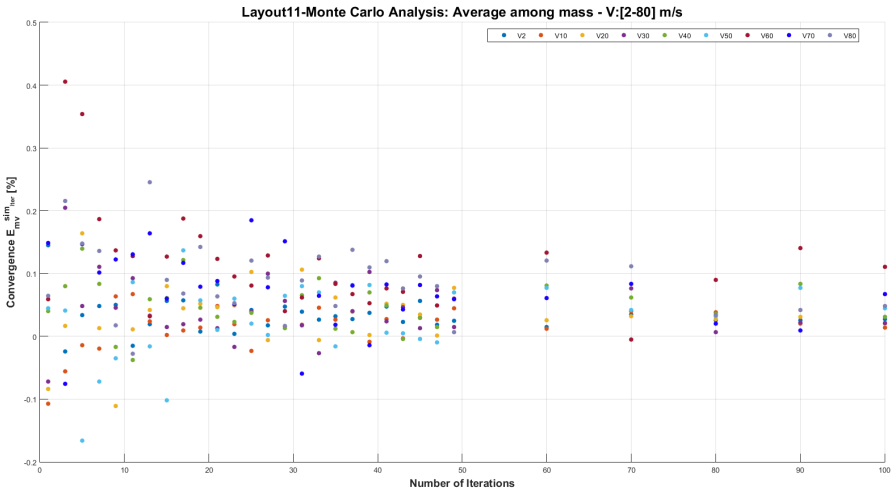

(d) Monte Carlo convergence of $\mathbf{Em}_{v_k}^{sim_{iter}}$ reached at about 30 iteration

Figure B.36: Layout11: Speed Estimation-Monte Carlo Analysis with k=(60-80) m s^{-1} and (d) Monte Carlo convergence

Layout12

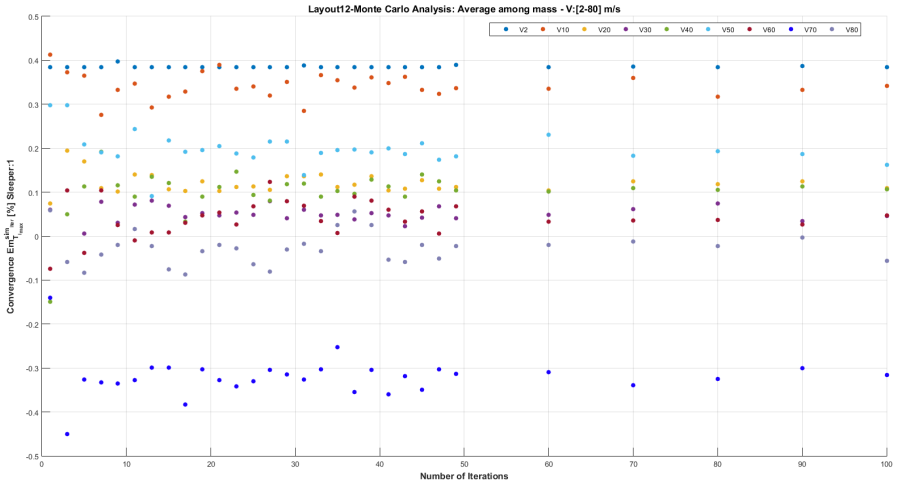

Figure B.37: Layout12: Monte Carlo analysis on the $Em_{Ti_{max}}^{sim_{iter}}$: results show as after 49 iterations the convergence is reached

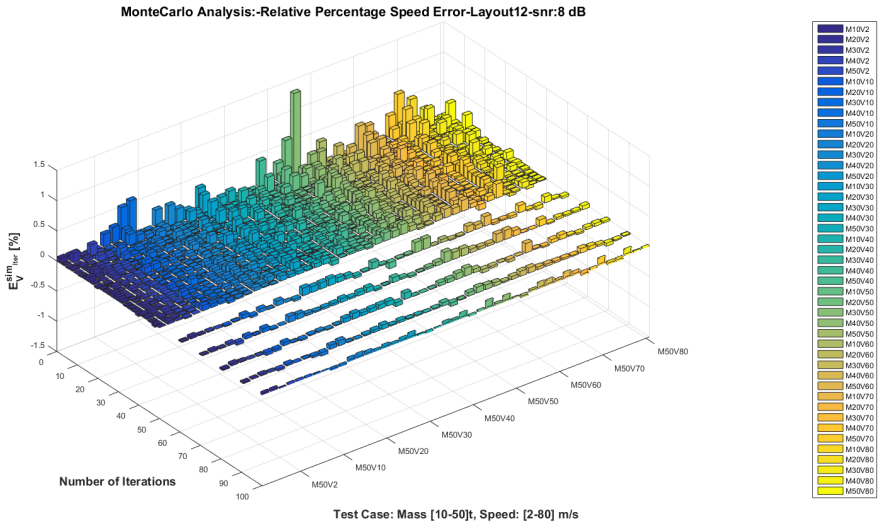

Figure B.38: Layout12: Percentage $E_V^{sim_{iter}}$ trend in all speed and mass range: results highlight how, for each speed, the value of mass vehicle not involves a relevant effect on the errors

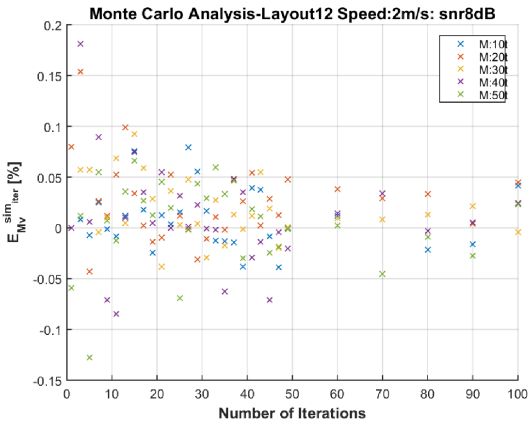

(a) Percentage $E_M{}_{v_k}^{sim_{iter}}$ (with k=2 m s^{-1})

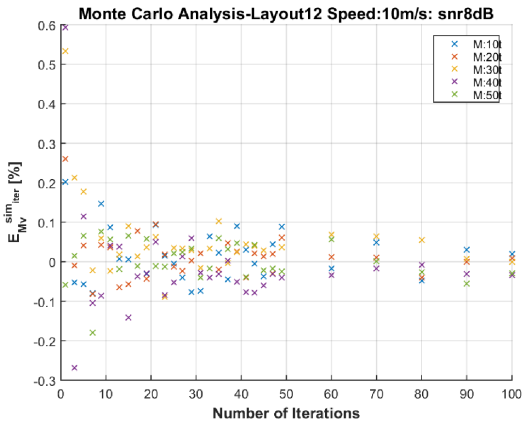

(b) Percentage $E_M{}_{v_k}^{sim_{iter}}$ (with k=10 m s^{-1})

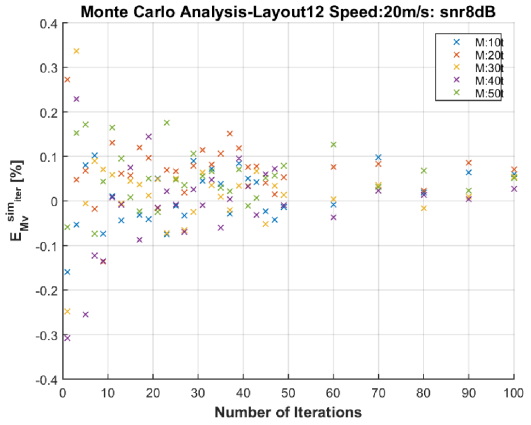

(c) Percentage $E_M{}_{v_k}^{sim_{iter}}$ (with k=20 m s^{-1})

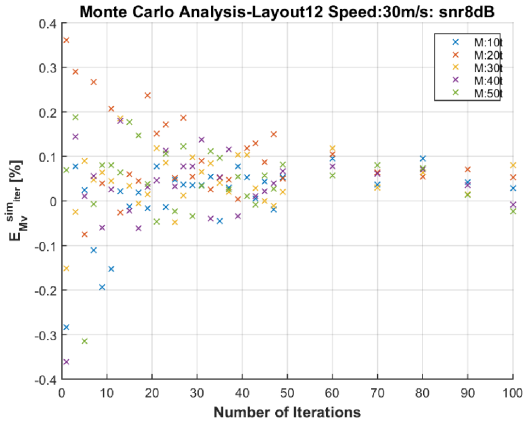

(d) Percentage $E_M{}_{v_k}^{sim_{iter}}$ (with k=30 m s^{-1})

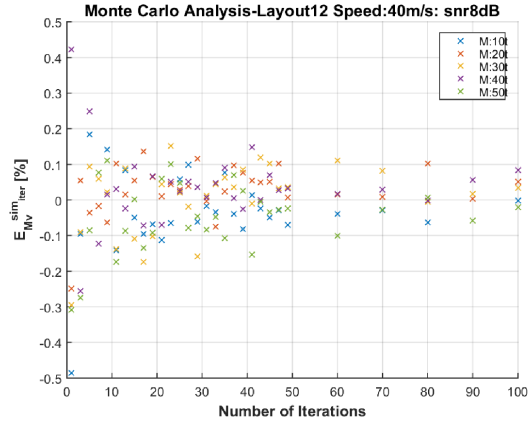

(e) Percentage $E_M{}_{v_k}^{sim_{iter}}$ (with k=40 m s^{-1})

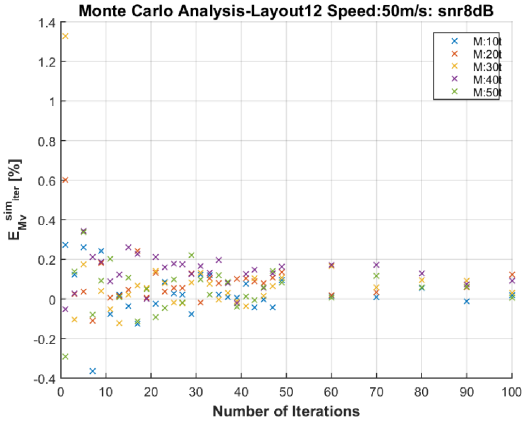

(f) Percentage $E_M{}_{v_k}^{sim_{iter}}$ (with k=50 m s^{-1})

Figure B.39: Layout12: Speed Estimation-Monte Carlo Analysis with k=(2-50) m s^{-1}

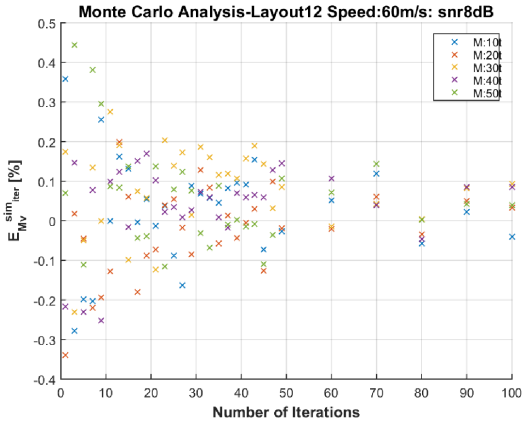

(a) Percentage $E_M{}_{v_k}^{sim_{iter}}$ (with k=60 m s^{-1})

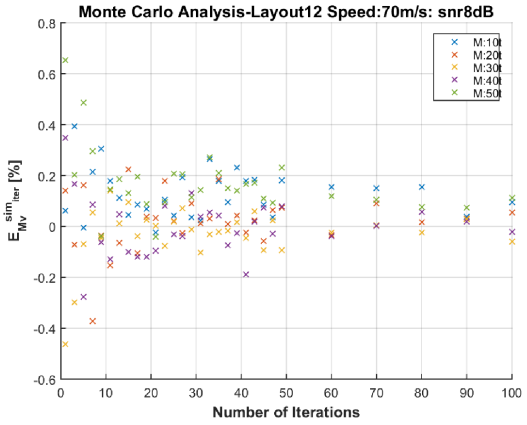

(b) Percentage $E_M{}_{v_k}^{sim_{iter}}$ (with k=70 m s^{-1})

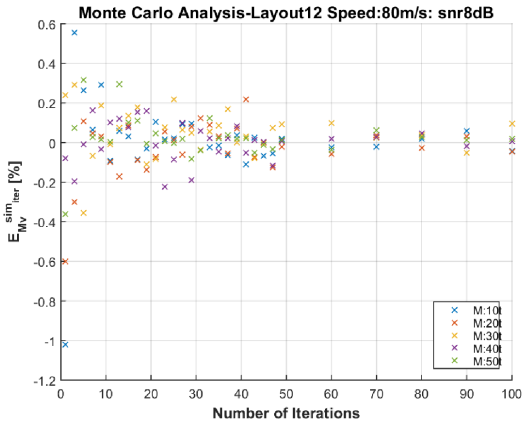

(c) Percentage $E_M{}_{v_k}^{sim_{iter}}$ (with k=80 m s^{-1})

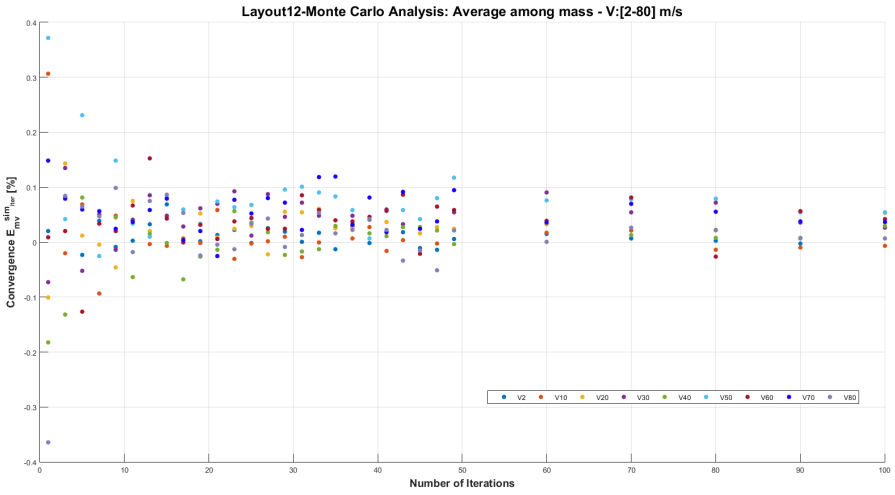

(d) Monte Carlo convergence of $\mathbf{Em}_{v_k}^{sim_{iter}}$ reached at about 49 iteration

Figure B.40: Layout12: Speed Estimation-Monte Carlo Analysis with k=(60-80) m s^{-1} and (d) Monte Carlo convergence

Layout13

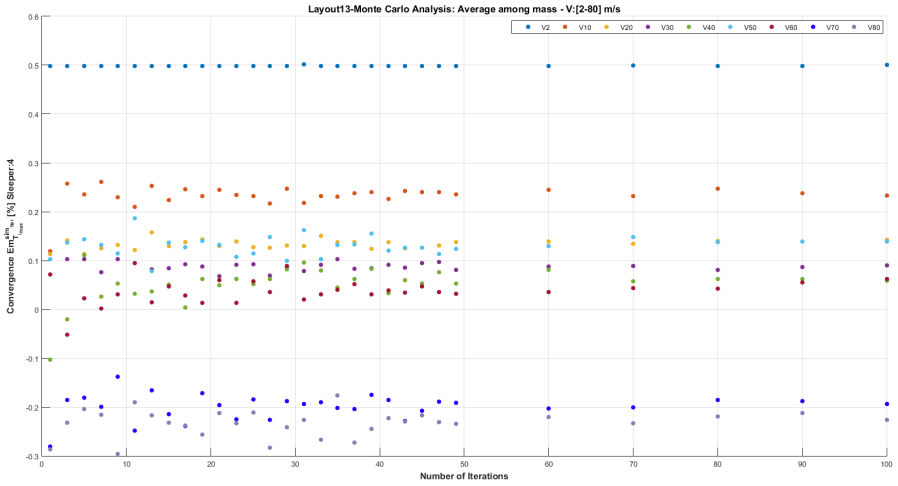

Figure B.41: Layout13: Monte Carlo analysis on the $Em_{Ti_{max}}^{sim_{iter}}$: results show as after 49 iterations the convergence is reached

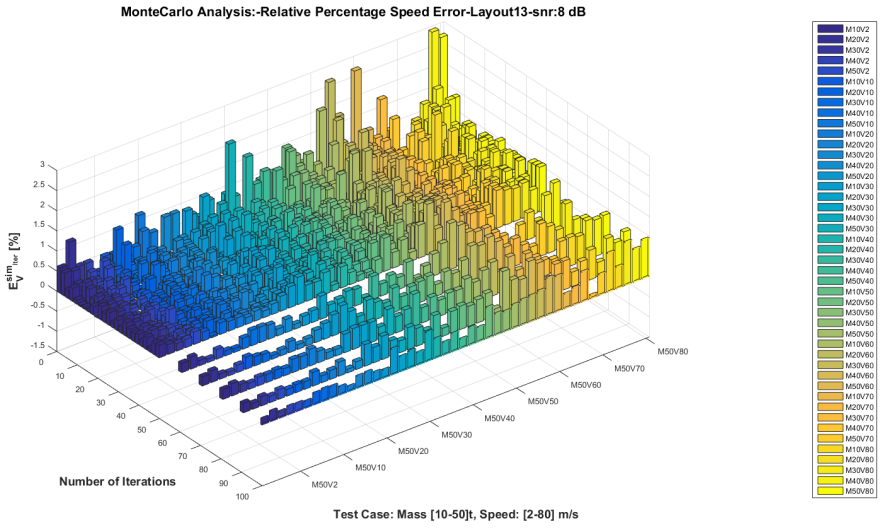

Figure B.42: Layout13: Percentage $E_V^{sim_{iter}}$ trend in all speed and mass range: results highlight how, for each speed, the value of mass vehicle not involves a relevant effect on the errors

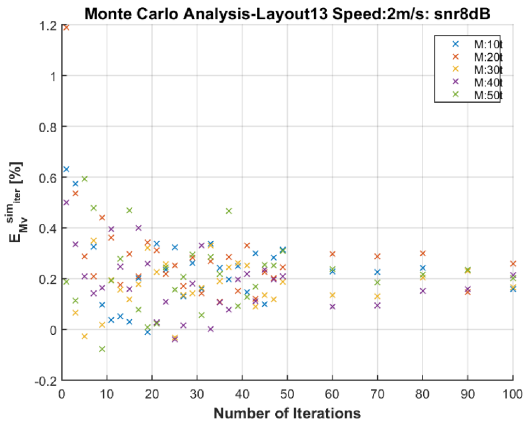

(a) Percentage $E_M{}_{v_k}^{sim_{iter}}$ (with k=2 m s^{-1})

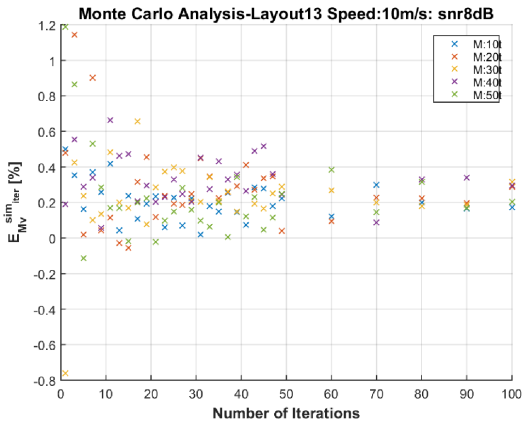

(b) Percentage $E_M{}_{v_k}^{sim_{iter}}$ (with k=10 m s^{-1})

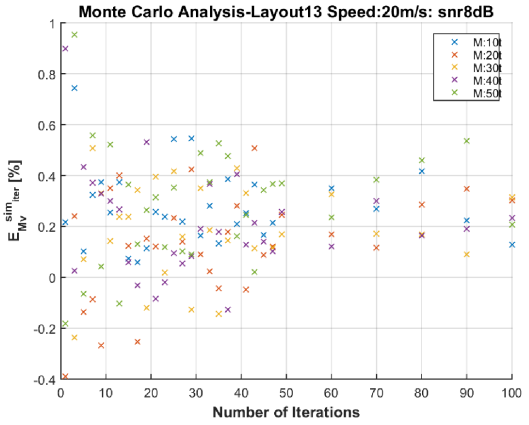

(c) Percentage $E_M{}_{v_k}^{sim_{iter}}$ (with k=20 m s^{-1})

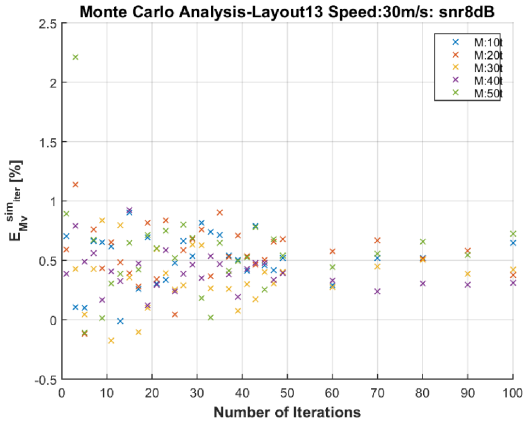

(d) Percentage $E_M{}_{v_k}^{sim_{iter}}$ (with k=30 m s^{-1})

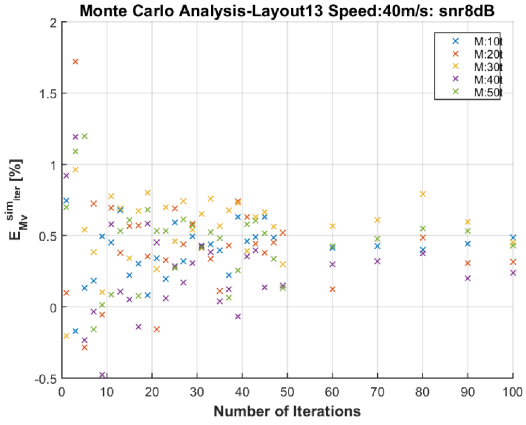

(e) Percentage $E_M{}_{v_k}^{sim_{iter}}$ (with k=40 m s^{-1})

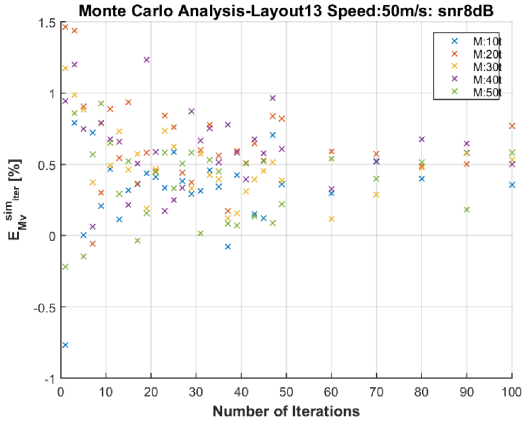

(f) Percentage $E_M{}_{v_k}^{sim_{iter}}$ (with k=50 m s^{-1})

Figure B.43: Layout13: Speed Estimation-Monte Carlo Analysis with k=(2-50) m s^{-1}

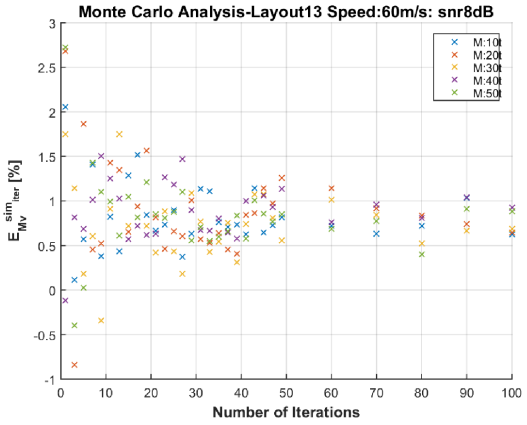

(a) Percentage $E_M{}_{v_k}^{sim_{iter}}$ (with k=60 m s^{-1})

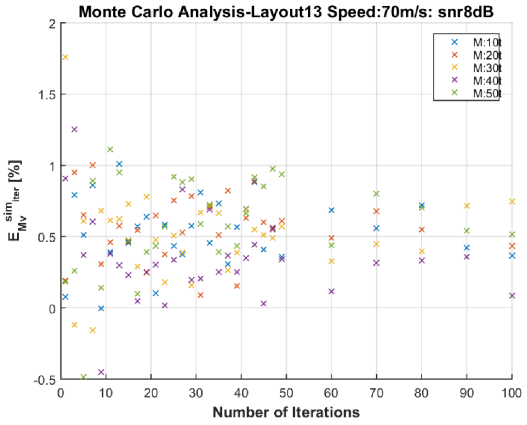

(b) Percentage $E_M{}_{v_k}^{sim_{iter}}$ (with k=70 m s^{-1})

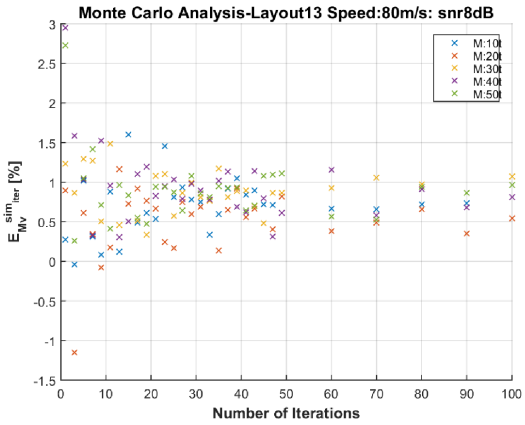

(c) Percentage $E_M{}_{v_k}^{sim_{iter}}$ (with k=80 m s^{-1})

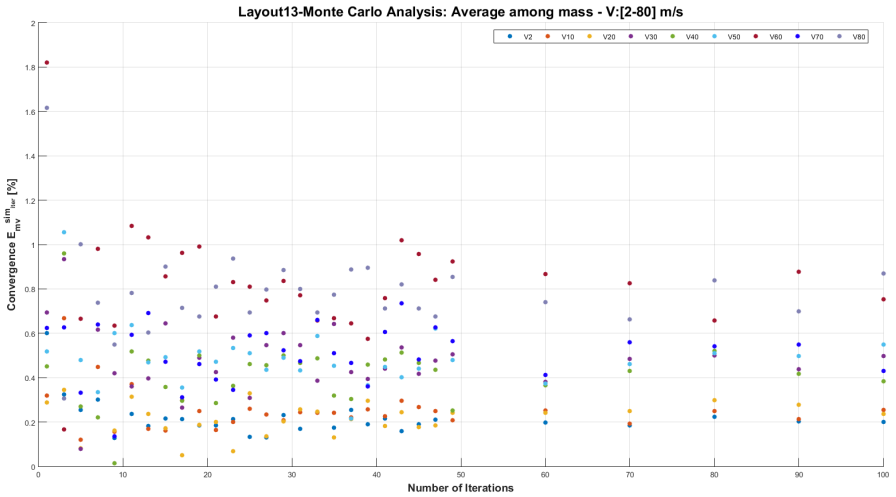

(d) Monte Carlo convergence of $\mathbf{Em}_{v_k}^{sim_{iter}}$ reached at about 30 iteration

Figure B.44: Layout13: Speed Estimation-Monte Carlo Analysis with k=(60-80) m s^{-1} and (d) Monte Carlo convergence

Layout14

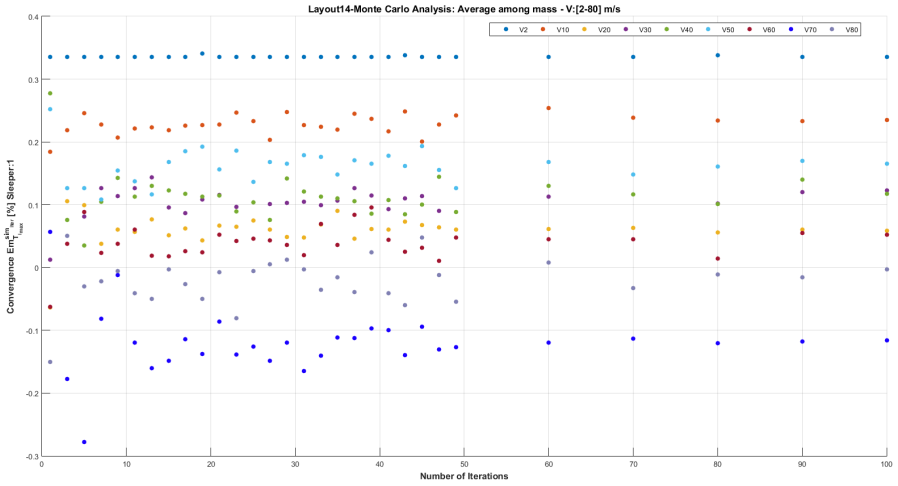

Figure B.45: Layout14: Monte Carlo analysis on the $Em_{T_{i_{max}}}^{sim_{iter}}$: results show as after 49 iterations the convergence is reached

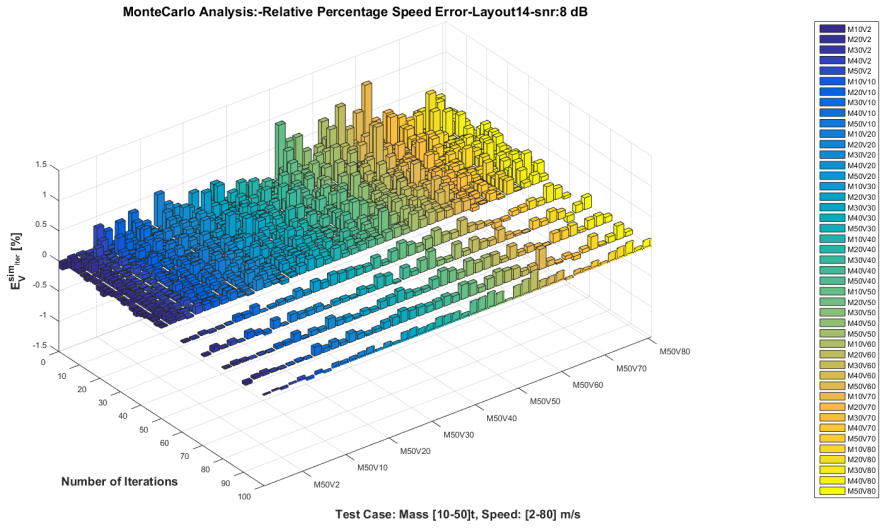

Figure B.46: Layout14: Percentage $E_V^{sim_{iter}}$ trend in all speed and mass range: results highlight how, for each speed, the value of mass vehicle not involves a relevant effect on the errors

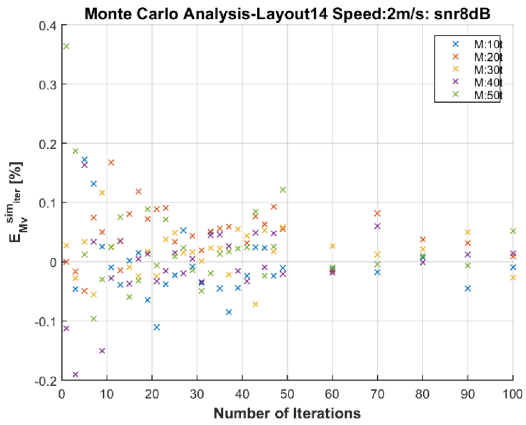

(a) Percentage $E_{v_k}^{sim_{iter}}$ (with k=2 m s^{-1})

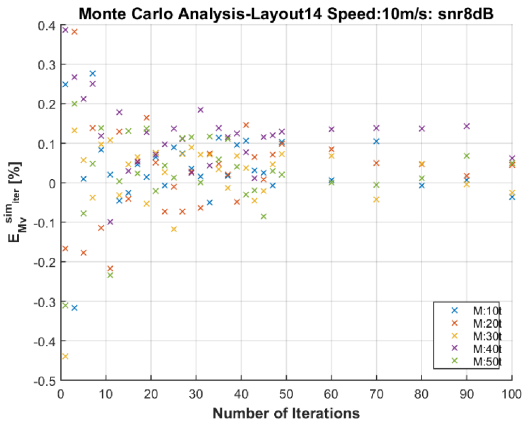

(b) Percentage $E_{v_k}^{sim_{iter}}$ (with k=10 m s^{-1})

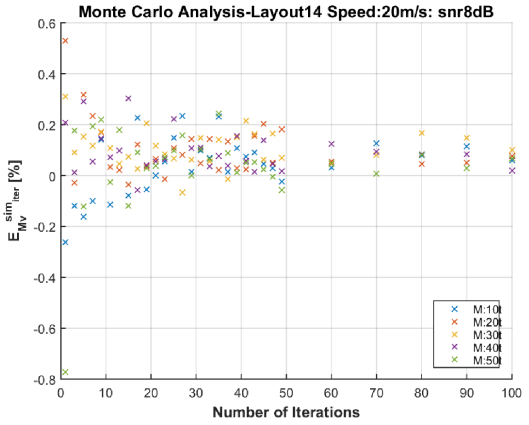

(c) Percentage $E_{v_k}^{sim_{iter}}$ (with k=20 m s^{-1})

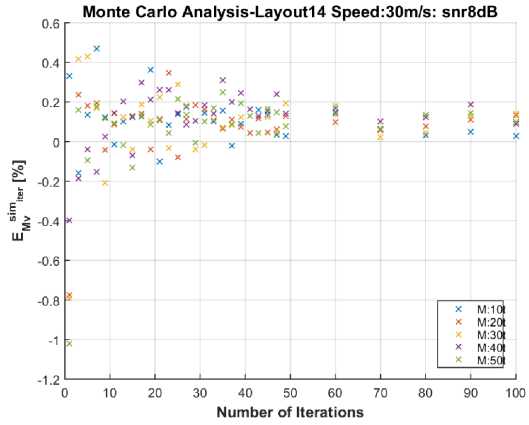

(d) Percentage $E_{v_k}^{sim_{iter}}$ (with k=30 m s^{-1})

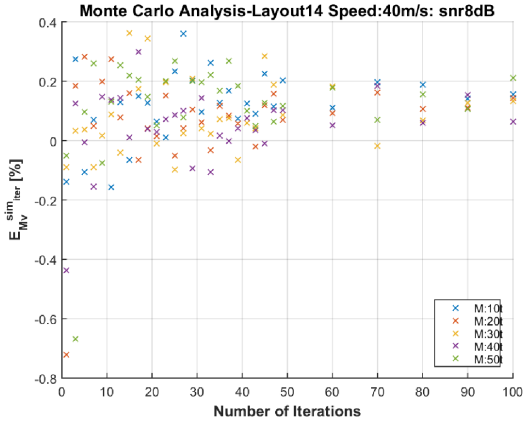

(e) Percentage $E_{v_k}^{sim_{iter}}$ (with k=40 m s^{-1})

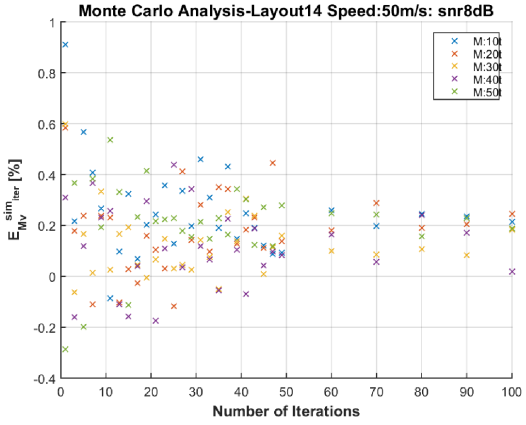

(f) Percentage $E_{v_k}^{sim_{iter}}$ (with k=50 m s^{-1})

Figure B.47: Layout14: Speed Estimation-Monte Carlo Analysis with k=(2-50) m s^{-1}

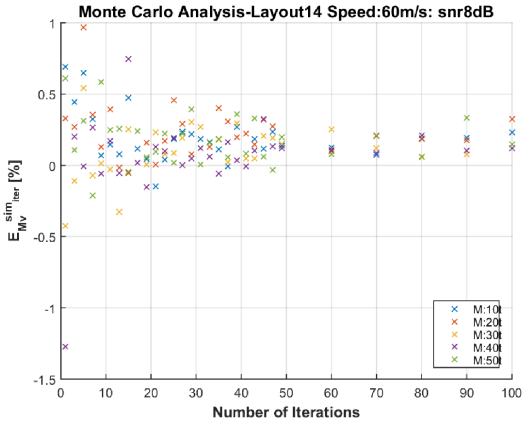

(a) Percentage $E_{v_k}^{sim_{iter}}$ (with k=60 m s^{-1})

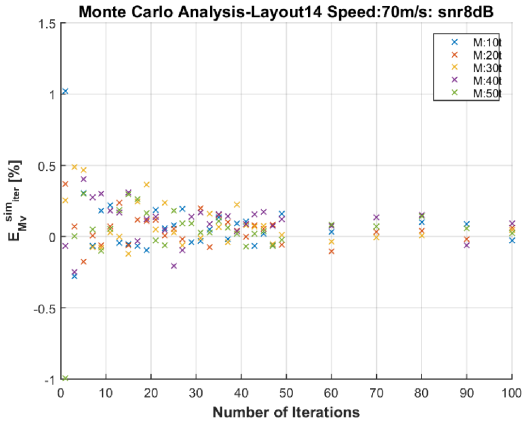

(b) Percentage $E_{v_k}^{sim_{iter}}$ (with k=70 m s^{-1})

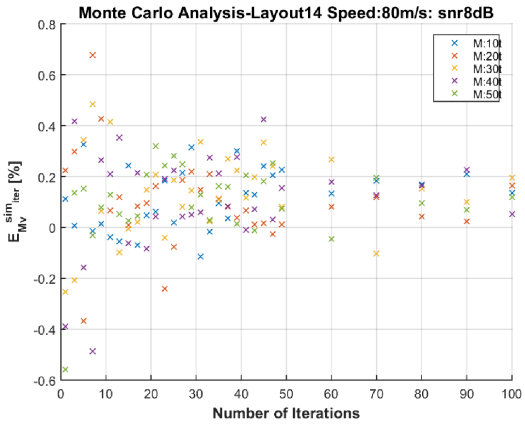

(c) Percentage $E_{v_k}^{sim_{iter}}$ (with k=80 m s^{-1})

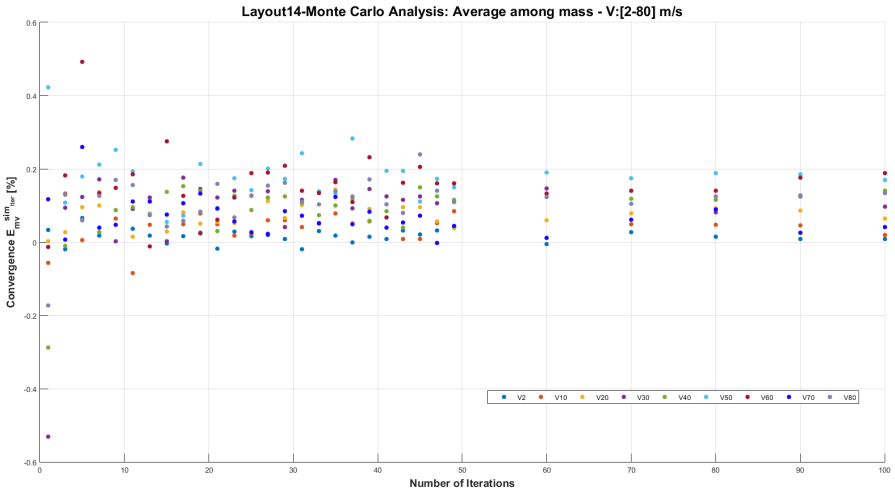

(d) Monte Carlo convergence of $\mathbf{Em}_{v_k}^{sim_{iter}}$ reached at about 30 iteration

Figure B.48: Layout14: Speed Estimation-Monte Carlo Analysis with k=(60-80) m s^{-1} and (d) Monte Carlo convergence

Layout15

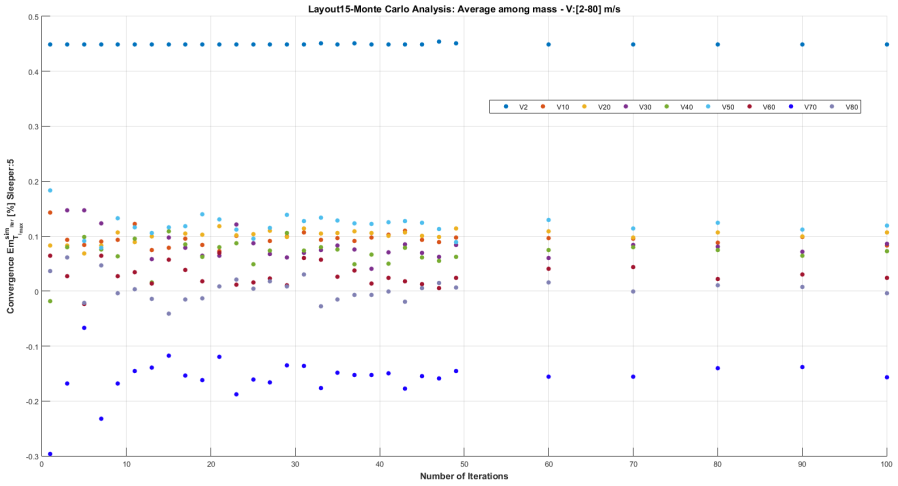

Figure B.49: Layout15: Monte Carlo analysis on the $Em_{T_{i_{max}}}^{sim_{iter}}$: results show as after 49 iterations the convergence is reached

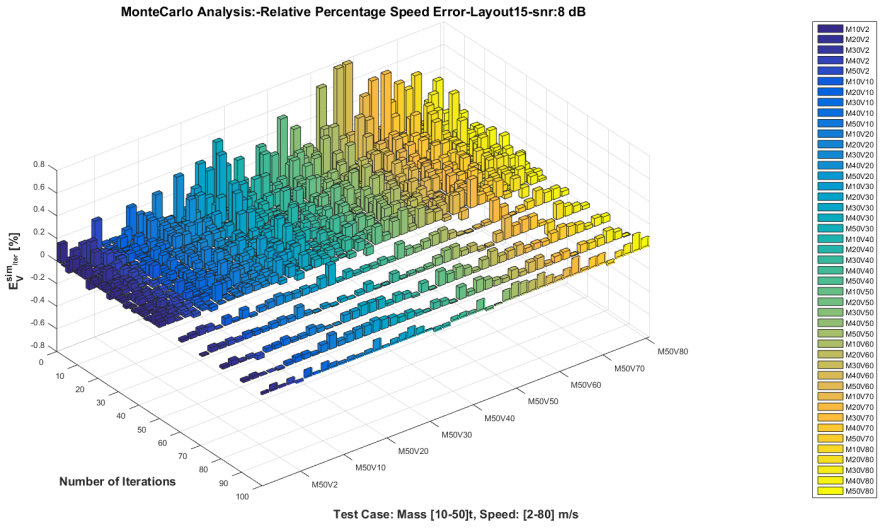

Figure B.50: Layout15: Percentage $E_V^{sim_{iter}}$ trend in all speed and mass range: results highlight how, for each speed, the value of mass vehicle not involves a relevant effect on the errors

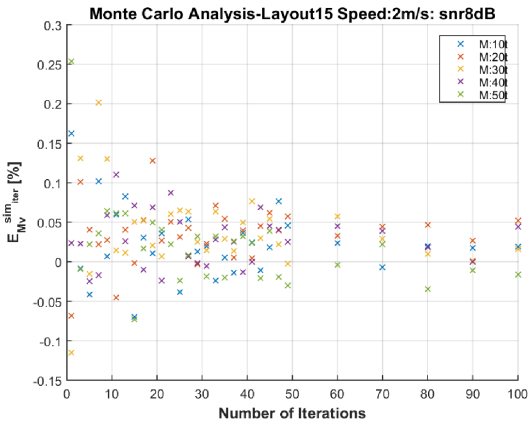

(a) Percentage $E_M{}_{v_k}^{sim_{iter}}$ (with k=2 m s^{-1})

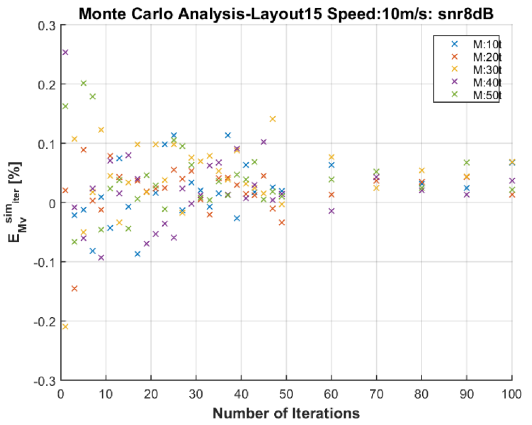

(b) Percentage $E_M{}_{v_k}^{sim_{iter}}$ (with k=10 m s^{-1})

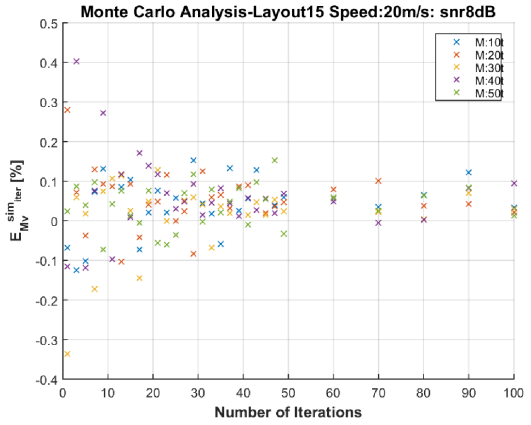

(c) Percentage $E_M{}_{v_k}^{sim_{iter}}$ (with k=20 m s^{-1})

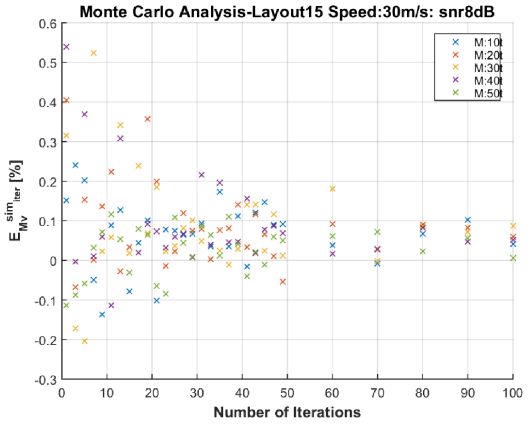

(d) Percentage $E_M{}_{v_k}^{sim_{iter}}$ (with k=30 m s^{-1})

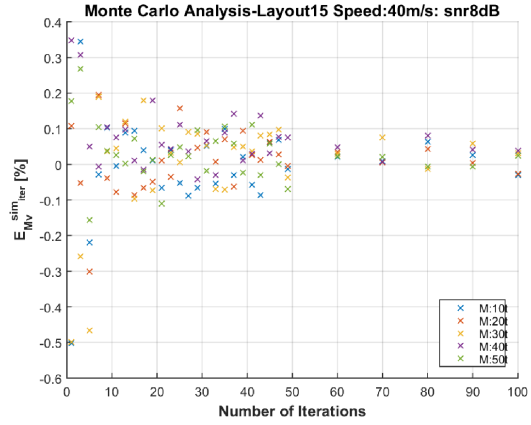

(e) Percentage $E_M{}_{v_k}^{sim_{iter}}$ (with k=40 m s^{-1})

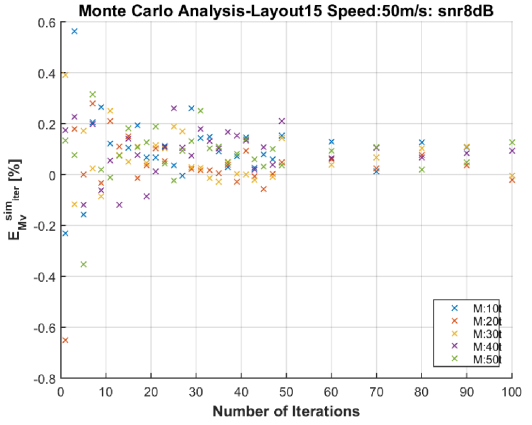

(f) Percentage $E_M{}_{v_k}^{sim_{iter}}$ (with k=50 m s^{-1})

Figure B.51: Layout15: Speed Estimation-Monte Carlo Analysis with k=(2-50) m s^{-1}

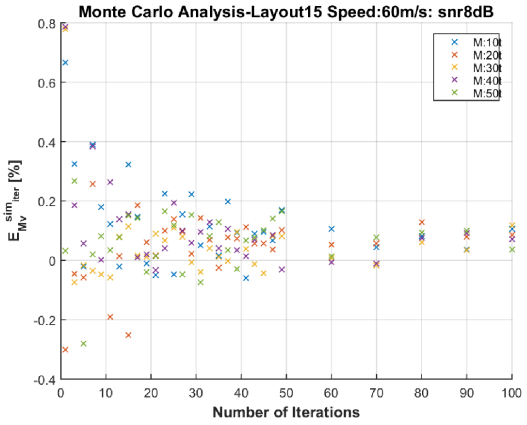

(a) Percentage $E_M{}_{v_k}^{sim_{iter}}$ (with k=60 m s^{-1})

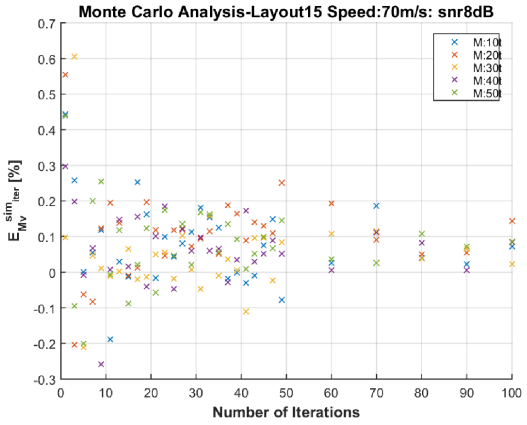

(b) Percentage $E_M{}_{v_k}^{sim_{iter}}$ (with k=70 m s^{-1})

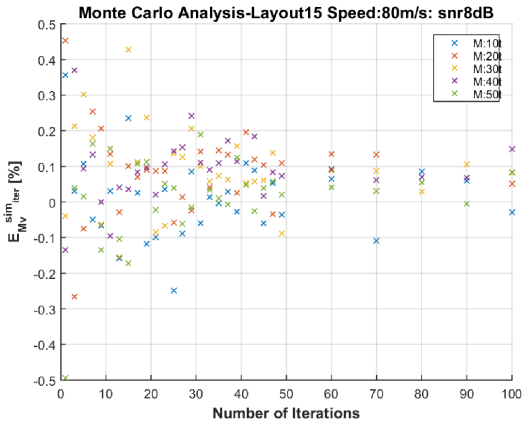

(c) Percentage $E_M{}_{v_k}^{sim_{iter}}$ (with k=80 m s^{-1})

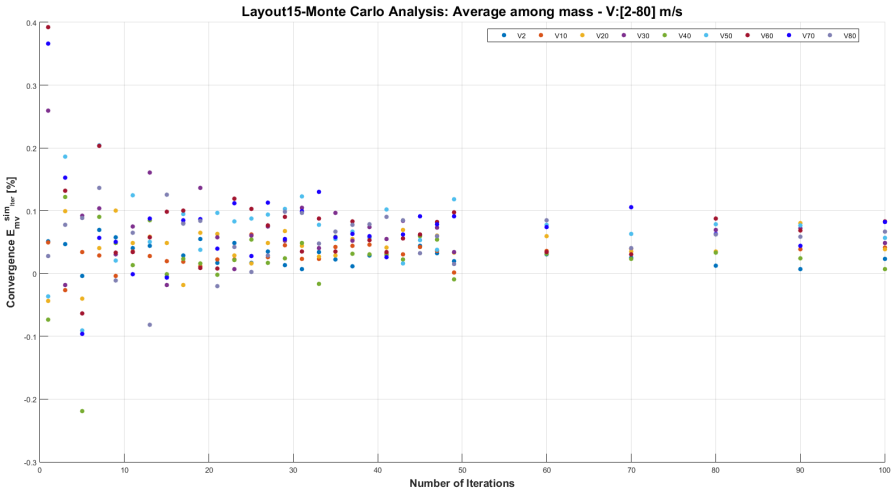

(d) Monte Carlo convergence of $\mathbf{Em}_{v_k}^{sim_{iter}}$ reached at about 49 iteration

Figure B.52: Layout15: Speed Estimation-Monte Carlo Analysis with k=(60-80) m s^{-1} and (d) Monte Carlo convergence

Layout16

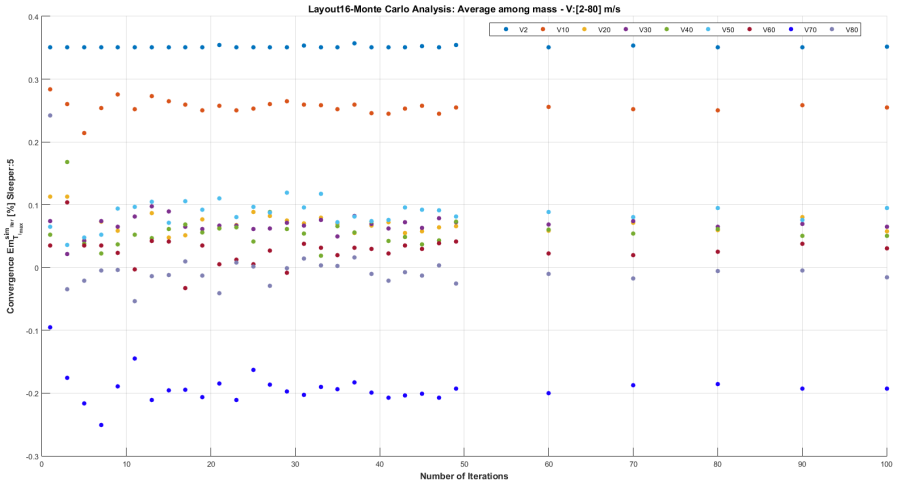

Figure B.53: Layout16: Monte Carlo analysis on the $Em_{T_{i_{max}}}^{sim_{iter}}$: results show as after 49 iterations the convergence is reached

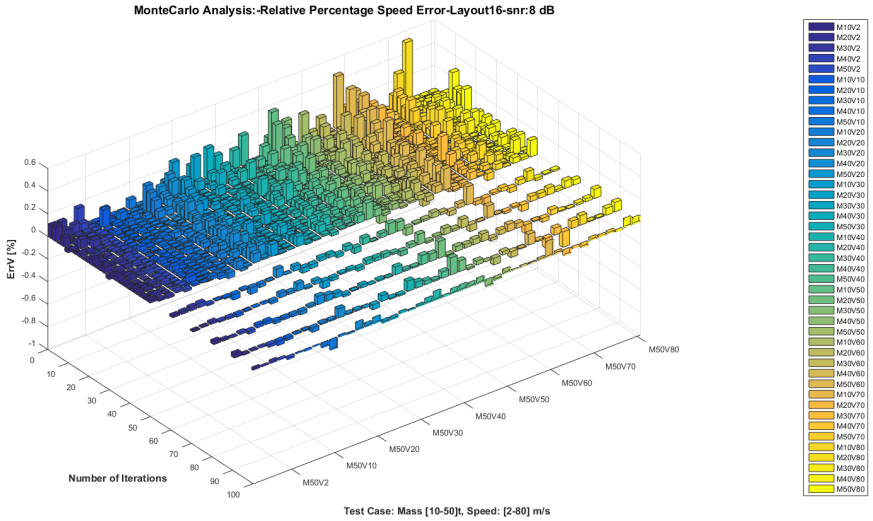

Figure B.54: Layout16: Percentage $E_V^{sim_{iter}}$ trend in all speed and mass range: results highlight how, for each speed, the value of mass vehicle not involves a relevant effect on the errors

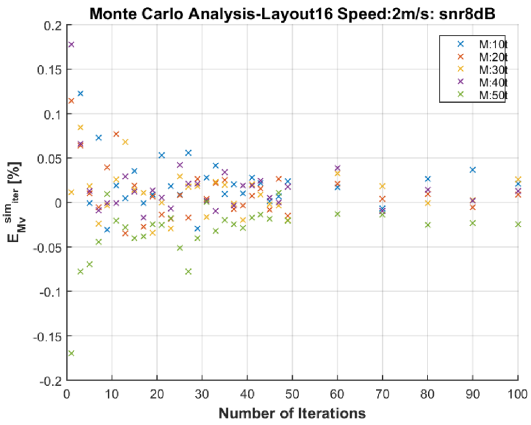

(a) Percentage $E_M{}_{v_k}^{sim_{iter}}$ (with k=2 m s^{-1})

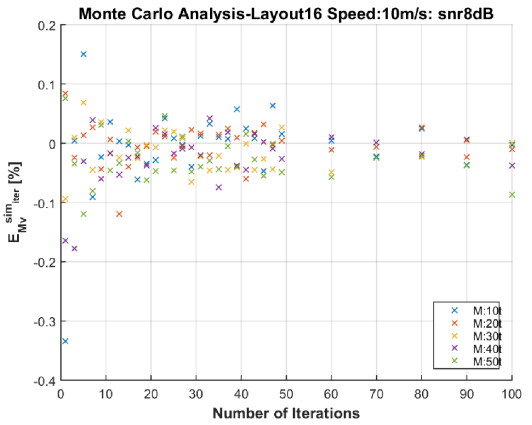

(b) Percentage $E_M{}_{v_k}^{sim_{iter}}$ (with k=10 m s^{-1})

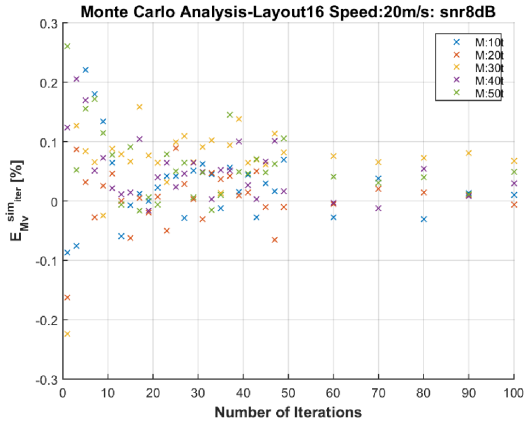

(c) Percentage $E_M{}_{v_k}^{sim_{iter}}$ (with k=20 m s^{-1})

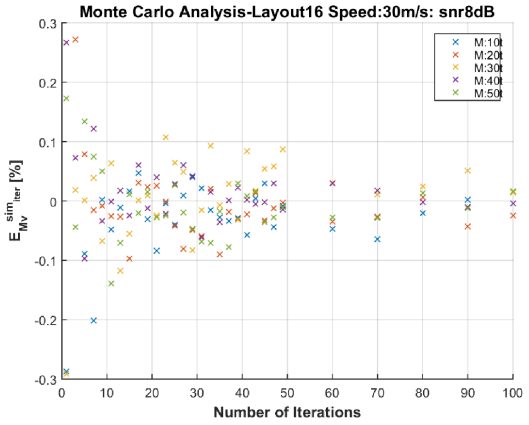

(d) Percentage $E_M{}_{v_k}^{sim_{iter}}$ (with k=30 m s^{-1})

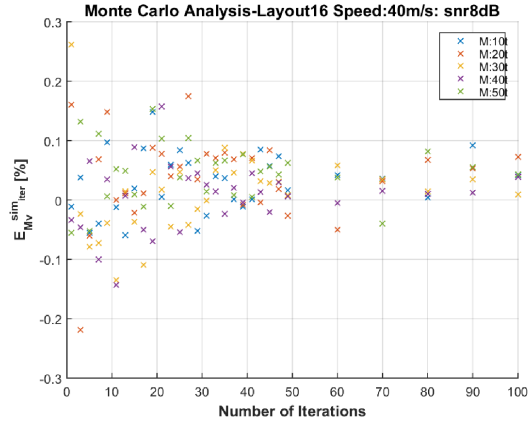

(e) Percentage $E_M{}_{v_k}^{sim_{iter}}$ (with k=40 m s^{-1})

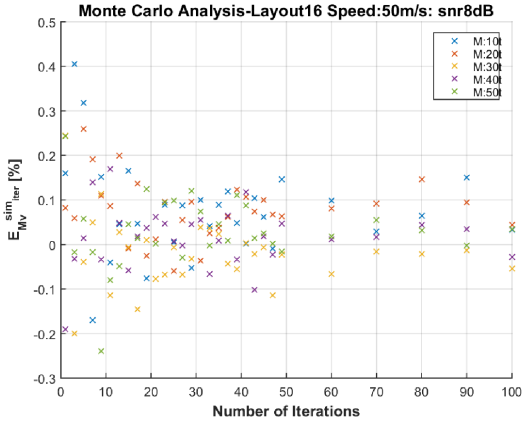

(f) Percentage $E_M{}_{v_k}^{sim_{iter}}$ (with k=50 m s^{-1})

Figure B.55: Layout16: Speed Estimation-Monte Carlo Analysis with k=(2-50) m s^{-1}

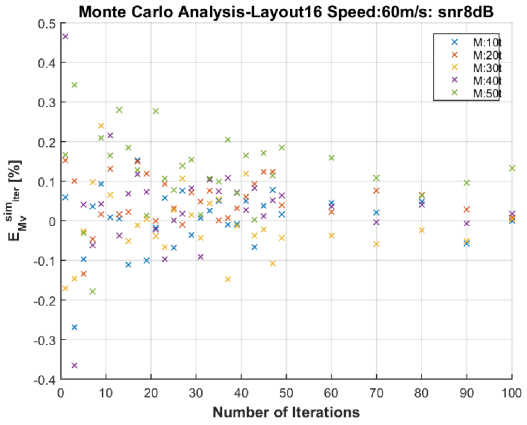

(a) Percentage $E_M{}_{v_k}^{sim_{iter}}$ (with k=60 m s^{-1})

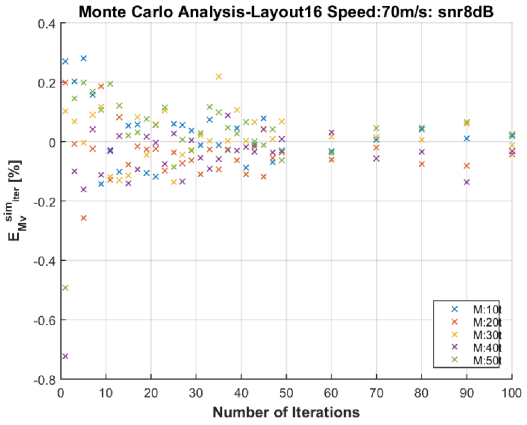

(b) Percentage $E_M{}_{v_k}^{sim_{iter}}$ (with k=70 m s^{-1})

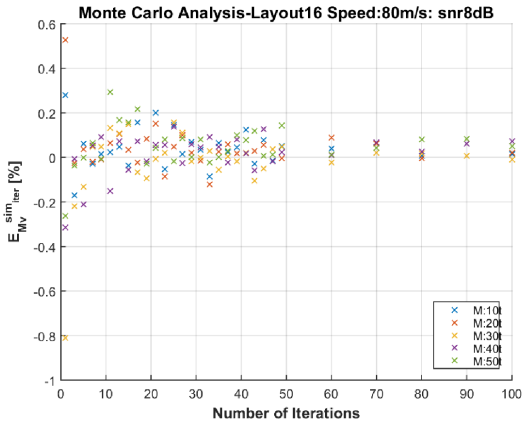

(c) Percentage $E_M{}_{v_k}^{sim_{iter}}$ (with k=80 m s^{-1})

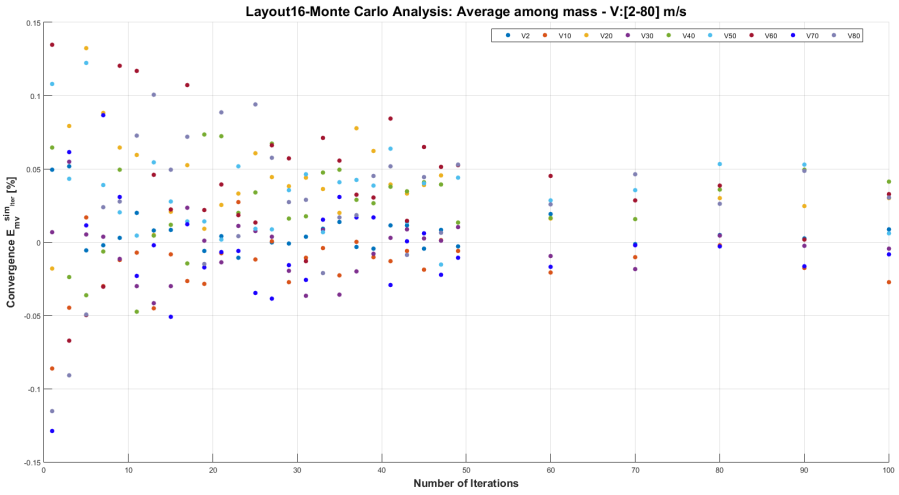

(d) Monte Carlo convergence of $\mathbf{Em}_{v_k}^{sim_{iter}}$ reached at about 30 iteration

Figure B.56: Layout16: Speed Estimation-Monte Carlo Analysis with k=(60-80) m s^{-1} and (d) Monte Carlo convergence

Bibliography

[1] J. Frausher. From track to inductive wheel sensor using a variety of technologies, signal+draht, 2006, volumes 1+2.

[2] M. Rosenberger. Future challenges to wheel detection and axle counting, signal+draht, 2011, volume 9.

[3] Voestalpine. *Diagnostic and Monitoring Technologies*. Voestalpine, 2016.

[4] Frausher. *State of the art in wheel detection*. Frausher, 2012.

[5] Frausher. *Increased availability thanks to the FDS Diagnostic System*. Frausher, 2010.

[6] J. W. Palmer. The need for train detection. In *Railway Signalling and Control Systems (RSCS 2010), IET Professional Development Course on*, Birmingham, UK, 7-11 June 2010.

[7] K.Y. Lee Y.T. Ho K.H. Ho A. Mccusker J.Kam H.Y. Tam S.L.Ho T.K. Ho, S.Y. Liu. An investigation of rail condition monitoring by fibre bragg grating sensors. *Transactions Hong Kong Institution of Engineers*, 16:9–15, 2009.

[8] T. Akio. Development of a trian detection system and a spread spectrum transmission system for track circuit. In *Vehicular Technology Conference*, Phoenix, AZ, 4-7 May. 1997.

[9] S. Midya and R. Thottappillil. An overview of electromagnetic compatibility challenges in europoean rail traffic management system. *Transportation Research PartC: Emerging Technologies*, 16(5):515–534, 2008.

[10] R. Thottappillil S. Midya. An overview of electromagnetic compatibility challenges in european rail traffic management system. *Transportation Research Part C*, 28(16):515–534, 2008.

[11] S. Vlasenko G. Theeg. Railway signalling & interlocking. *Eurailpress, ISBN 978-3-7771-0394-5*.

[12] L. Kinze. Gleisfreimeldesysteme der db ag- aufgaben und funktionen, eisenbahn ingenieur kalender, 2008.

[13] H. J. Patrick M. LeBlanc K. P. Koo C.G. Askins M. A. Putnam A. D. Kersey, M. A. Davis and E. J. Friebele. Fiber grating sensors. *J. Lightw. Technol.*, 15(8):1442–1463, 1997.

[14] R. Bloomfield. Fundamentals of european rail traffic management system-ermts. In *Proceedings of the 11th IET Professional Development Course on Railway Signalling and Control System*, York, England, 5-9 June 2006.

[15] J. Gadja, P. Piwowar, R. Sroka, M. Stencel, and T. Zeglen. Application of inductive loops as wheel detectors. *Transportation Research PartC: Emerging Technologies*, 21(1):57–66, 2012.

[16] S. Zhang, W. K. Lee, and P. W. T. Pong. Train detection by magnetic field measurement with giant magnetoresistive sensors for high-speed railway. *Applied Mechanics and Materials*, 284-287:2102–2114, 2013.

[17] A. Zamani and A. Mirabadi. Optimization of sensor orientation in railway wheel detector, using kriging method. *Journal of Electromagnetic Analysis and Applications*, 3(12):529–536, 2011.

[18] C. Wei, Q. Xin, W. H. Chung, S. Y. Liu, H. Y. Tam, and S. L. Ho. Real-time train wheel condition monitoring by fiber bragg grating sensors. In *Proceedings of the 2010 Joint Rail Conference*, Urbana, IL,USA, 27-29 April 2010.

[19] W. Li, N. Jiang, J. Liu, and Y. Zhang. Train axle counters by bragg and chirped grating techniques. In *19th International Conference on Optical Fibre Sensors*, Perth, Australia, 14 April 2008.

[20] S. J. Buggy, S. W. James, R. Carroll, J. Jaiswal, S. Staines, and R. P. Tatam. Intelligent infrastructure for rail and tramways using optical fibre sensors. *Journal of Sensors*, 2012.

[21] A. K. Chakraborty K. Dasgupta D.K. Bhattacharya M. Majumder, T. K. Gangopadhyay. Fiber bragg gratings in structural health monitoring-present status and applications. *Sensors and Actuators A: Physical*, 147(1):150–164, 2008.

[22] H.Y. Tamb Y.Q.Nia S.Y.Liub W.H. Chungb L.K.Chengc T.H.T. Chan, L.Yu. Fiber bragg grating sensors for structural health monitoring of tsing mabridge: Background and experimental observation. *Engineering Structures*, 28:648–659, 2006.

[23] L. A. Ferreira F.M. Araujo H. Varum A. Costa C. Fernandes C. Barbosa, N. Costa and H. Rodriguesc. Weldable fibre bragg grating sensors for steel bridge monitoring. *Meas. Sci. Technol.*, 19:125–305, 2008.

[24] M. L. Filograno, A. R. Barrios, M. G. Herraez, P. Corredera, S.M. Lopez, M. R. Plaza, and A. A. Alguacil. Real time monitoring of railway traffic using fiber bragg grating sensors. In *Joint Rail Conference*, Urbana, (IL)USA, 27-29 April 2010.

[25] C. L. Wei, C. C. Lai, W. H. Chung, T. K. Ho, H. Y. Tam, S. L Ho, A. McCusker, J. Kam, and K. Y. Lee. A fiber bragg grating sensor system for train axle counting. *Sensors Journal, IEEE*, 10(12):1905–1912, 2010.

[26] A. Laudati N. Mazzino G. Bocchetti A. Cutolo A. Cusano A. Iele, V. Lopez. Fiber optic sensing system for weighing in motion (wim) and wheel flat detection (wfd) in railways assets: The twbcs system. In *8th European Workshop On Structural Health Monitoring (EWSHM 2016*, Spain, Bilbao, 2016.

[27] F. Mennella, A. Laudati, M. Esposito, A. Cusano, A. Cutolo, M. Giordano, S.Campopiano, and G.Breglio. Railway monitoring and train tracking by fiber bragg grating sensors. In *Proc. SPIE 6619, Third European Workshop on Optical Fibre Sensors*, Napoli, Italy, 2 July 2007.

[28] A. Cusano A. Laudati, G. Lanza. Railway monitoring and train tracking by fiber bragg grating sensors: A case study in italy. In *Proc. 4th European Workshop on Structural Health Monitoring*, Poland, 2008.

[29] R. M. da Costa Marques Pimentel, M. C. Beirao Barbosa, N. M. Silva Costa, D. R. Ferreira Ribeiro, L. A. de Almeida Ferreira, F. M. Moita Araujo, and R. A. Bartolo Calcada. Hybrid fiber-optic/electrical measurement system for characterization of railway traffic and its effects on a short span bridge. *IEEE Sensors Journal*, 8(7):289–300, July 2008.

[30] G. James. Analysis of traffic load effects on railway bridges. phd thesis, structural engineering division royal institute of technology, 2003.

[31] A. Johansson and J. Nielsena. Out-of-round railway wheels-wheel-rail contact forces and track response derived from field tests and numerical simulations. *Journal of Rail and Rapid Transit*, 217(2):135–146, 2003.

[32] Gotcha. Wheel flat detection and axle load measurement system. *Technical report, TagMaster*, 2005.

[33] P. D'Adamio. *Studio dello stato dell'arte e selezione della tecnologia di rilevazione del treno e usura contatto ruota rotaia*. ECM-MDM, 2016.

[34] E. Meli L. Pugi A. Rindi P. D'Adamio, L. Marini. Development of a dynamical weigh in motion system for railway applications. *Meccanica*, 271(DOI: 10.1007/s11012-016-0378-2):1–25, 2016.

[35] E. Meli and L. Pugi. Preliminary development, simulation and validation of a weigh in motion system for railway vehicles. *Meccanica*, 48(10):2541–2565, 2013.

[36] S. Iwnicki. *The Manchester Benchmarks for Rail Vehicle Simulators*. Swets and Zeitlinger, Lisse, Netherland, 1999, 2008.

[37] E. Meli, S. Falomi, M. Malvezzi, and A. Rindi. Determination of wheel - rail contact points with semianalytic methods. *Multibody System Dynamics*, 20(4):327–358, 2008.

[38] S. Falomi, M Malvezzi, and E. Meli. Multibody modeling of railway vehicles: innovative algorithms for the detection of wheel-rail contact points. *Wear*, 271(1-2):453–461, 2011.

[39] S. Iwnicki. *Handbook of Railway Vehicle Dynamics*. Taylor and Francis, 2006.

[40] T. Dahlberg. Some railroad settlement models - a critical review. *Journal of Rail and Rapid Transit*, 215:289–300, April 2001.

[41] J. A. Zakeri, H. Xia, and J. J. Fan. Dynamic responses of train-track system to single rail irregularity. *Latin American Journal of Solids and Structures*, 6(2), 2009.

[42] J. J. Kalker. *Three-dimensional Elastic Bodies in Rolling Contact*. Kluwer Academic Publishers, Dordrecht, Netherlands, 1990.

[43] J. J. Kalker. A fast algorithm for the simplified theory of rolling contact. *Veh.Syst.Dyn*, 11:1–13, 1982.

[44] O. Polach. A fast wheel-rail forces calculation computer code. *Veh.Syst.Dyn*, 33:728–739, 1999.

[45] E. Meli L. Marini B. Allotta, P. D'Adamio and L.Pugi. A novel algorithm for train detection using cross-correlation techniques. In *CIVIL-COMP PROCEEDINGS*, Cagliari, Sardegna, 2016.

[46] E. Meli B. Allotta, P. D'Adamio and L. Pugi. Development of a new time domain-based algorithm for train detection and axle counting. *Vehicle System Dynamics*, 53:1850–1875, 2015.

[47] Md. Hanif Ali A.K.M Fazlul Haque and M Adnan Kiber. Improved spectrogram analysis for ecg signal in emergency medical applications. *(IJACSA) International Journal of Advanced Computer Science and Applications*, 1(3):39–44, 2010.

[48] S. A. Fulop and K. Fitz. Algorithms for computing the time-corrected instantaneous frequency (reassigned) spectrogram, with applications. *Acoust. Soc. Am.*, 119(1):360–371, 2009.

[49] S. A. Fulop and K. Fitz. Application of spectrogram in analysing electromyography (emg) signals of manual lifting. *ARPN Journal of Engineering and Applied Sciences*, 11(6):3603–3609, 2016.

[50] Ma. Mustafa. Eeg spectrogram classification employing ann for iq application, 9-11 May 2013.

[51] S.L. Ho K.Y. Lee, K.K. Lee. Exploration of using fbg sensor for axle counter in railway engineering. *International Journal of Distributed Sensor Networks*, 8(1):1âĂŞ25, January 2012.

[52] A. Rindi, L. Pugi, and E. Meli. Weighing in motion of railway vehicles: development and comparison of different identification/measurement techniques. In *European Congress on Computational Methods in Applied Sciences and Engineering (ECCOMAS)*, Vienna, Austria, 10-14 September 2012.

[53] L. F. Shampine and M. W. Reichelt. The matlab ode suite. *SIAM Journal of Scientific Computation*, 18:1–22, 1997.

[54] C. Kelley. *Iterative methods for linear and nonlinear equations*. SIAM, Philadelphia, PA, USA, 1995.

[55] J. Nocedal and S. Wright. *Numerical optimization*. Springer Series in Operation Research, Springer, Berlin, Germany, 1999.